



HAL
open science

Crystal chemistry of polyanion vanadium fluorinated oxy-phosphates: From atomic local structure to electrochemical performance in Na-ion batteries

Long Hoang Bao Nguyen

► **To cite this version:**

Long Hoang Bao Nguyen. Crystal chemistry of polyanion vanadium fluorinated oxy-phosphates: From atomic local structure to electrochemical performance in Na-ion batteries. Material chemistry. Université de Bordeaux, 2019. English. NNT : 2019BORD0356 . tel-03220951

HAL Id: tel-03220951

<https://theses.hal.science/tel-03220951>

Submitted on 7 May 2021

HAL is a multi-disciplinary open access archive for the deposit and dissemination of scientific research documents, whether they are published or not. The documents may come from teaching and research institutions in France or abroad, or from public or private research centers.

L'archive ouverte pluridisciplinaire **HAL**, est destinée au dépôt et à la diffusion de documents scientifiques de niveau recherche, publiés ou non, émanant des établissements d'enseignement et de recherche français ou étrangers, des laboratoires publics ou privés.

THÈSE PRÉSENTÉE
POUR OBTENIR LE GRADE DE

**DOCTEUR DE
L'UNIVERSITÉ DE BORDEAUX**

ÉCOLE DOCTORALE DES SCIENCES CHIMIQUES
SPÉCIALITÉ : PHYSICO-CHIMIE DE LA MATIÈRE CONDENSÉE

Par Long Hoang Bao NGUYEN

**Crystal Chemistry of Polyanion
Vanadium Fluorinated Oxy-phosphates:
From Atomic Local Structure to
Electrochemical Performance in Na-ion Batteries**

Sous la direction de : Laurence CROGUENNEC
co-directeur : Christian MASQUELIER

Soutenue le 12 décembre 2019

Membres du jury :

| | | |
|---------------------------|------------------------------------------------|---------------------------|
| M. STIEVANO, Lorenzo | Professeur, Université de Montpellier | Président |
| Mme. GOWARD, Gillian | Professeure, McMaster University | Rapporteur |
| M. ROUSSEL, Pascal | Directeur de recherche, CNRS/UCCS | Rapporteur |
| M. BOUCHER, Florent | Directeur de recherche, CNRS/IMN | Examineur |
| M. MAGLIONE, Mario | Directeur de recherche, CNRS/ICMCB | Examineur |
| Mme. CROGUENNEC, Laurence | Directrice de recherche, CNRS/ICMCB | Directrice de thèse |
| M. MASQUELIER, Christian | Professeur, Université de Picardie Jules Verne | Co-directeur |
| Mme. CARLIER, Dany | Professeure, Université de Bordeaux | Co-encadrante, Invitée |
| M. OLCHOWKA, Jacob | Chargé de recherche, CNRS/ICMCB | Co-encadrant, Invité |

Titre: Cristallochimie d'Oxyphosphates Fluorés de Vanadium : De l'Etude de leur Structure à leurs Performances en Batteries Na-ion

Résumé:

Les batteries Na-ion se développent comme une nouvelle alternative aux batteries Li-ion. Parmi le grand nombre de matériaux déjà étudiés à l'électrode positive, $\text{Na}_3\text{V}_2(\text{PO}_4)_2\text{F}_3$ et $\text{Na}_3(\text{VO})_2(\text{PO}_4)_2\text{F}$ sont les plus performants grâce à des capacités théoriques élevées, des potentiels d'extraction des ions Na^+ élevés, et la stabilité de la structure lors de cyclages longues durées. De plus, la structure et les propriétés électrochimiques des matériaux $\text{Na}_3\text{V}_2(\text{PO}_4)_2\text{F}_3$ et $\text{Na}_3(\text{VO})_2(\text{PO}_4)_2\text{F}$ peuvent être modulées par un effet de substitution cationique ou anionique. Ce travail de thèse a pour but d'explorer la cristallochimie de nouveaux matériaux dérivés de $\text{Na}_3\text{V}_2(\text{PO}_4)_2\text{F}_3$ et $\text{Na}_3(\text{VO})_2(\text{PO}_4)_2\text{F}$. Dans un premier temps, différents modes de synthèse (voies tout solide, céramique assistée par sol-gel, et broyage mécanique) sont explorées pour réaliser des substitutions cationiques et anioniques. La structure tridimensionnelle à longue distance de ces matériaux est déterminée par diffraction des rayons X synchrotron, tandis que les environnements locaux sont ensuite décrits finement en combinant des techniques de spectroscopies (résonance magnétique nucléaire à l'état solide, absorption des rayons X, et infra-rouge) dont l'interprétation est appuyée par des calculs théoriques. Les diagrammes de phases et les processus d'oxydoréduction impliqués lors des réactions de dés-intercalation et de ré-intercalation des ions Na^+ de la structure hôte sont étudiés pour chacune des compositions, *operando* (cad. lors du fonctionnement de la batterie) en diffraction et absorption des rayons X synchrotron. Une compréhension des mécanismes structuraux et redox impliqués au cours du cyclage permet d'identifier les limitations de ces phases et de nous guider pour proposer des nouveaux matériaux dérivés présentant de meilleures performances.

Mots clés:

Batteries Na-ion

Diffraction des rayons X

Calculs DFT

Matériaux polyanioniques

RMN de l'état solide

Absorption des rayons X synchrotron

Title: Crystal Chemistry of Polyanion Vanadium Fluorinated Oxy-phosphates: From Atomic Local Structure to Electrochemical Performance in Na-ion Batteries

Abstract:

Na-ion batteries are currently developed as a future alternative to the conventional Li-ion batteries. Among all the polyanion materials studied as positive electrodes for Na-ion batteries, $\text{Na}_3\text{V}_2(\text{PO}_4)_2\text{F}_3$ and $\text{Na}_3(\text{VO})_2(\text{PO}_4)_2\text{F}$ are the two promising compositions thanks to their high theoretical capacity, high Na^+ -extraction voltage, and especially the high stability of their structural framework upon long-term cycling. Furthermore, the crystal structure and the electrochemical properties of these materials can be greatly modulated through an effect of cationic or anionic substitution. This PhD work aims at exploring the diversity in crystal chemistry of $\text{Na}_3\text{V}_2(\text{PO}_4)_2\text{F}_3$, $\text{Na}_3(\text{VO})_2(\text{PO}_4)_2\text{F}$ and their derivatives obtained through different synthesis methods. The three-dimensional long range crystal structure of these phases is determined by the use of high resolution synchrotron X-ray powder diffraction whereas their local atomic and electronic structures are investigated through a combination of solid-state nuclear magnetic resonance supported by first-principles theoretical calculations, synchrotron X-ray absorption spectroscopy and infrared spectroscopy. Thereafter, the phase diagram and the redox processes involved in the Na^+ deintercalation and intercalation are established thanks to *operando* synchrotron X-ray diffraction and absorption. An in-depth understanding on the crystal structure as well as the involved redox couples for each composition helps us to determine the limitations of these vanadium fluorinated oxy-phosphates and sheds light to the development of new materials with better performance based on their structure.

Keywords:

Na-ion batteries

Polyanion materials

Synchrotron X-ray diffraction

Solid-state NMR

DFT calculations

Synchrotron X-ray absorption

Institut de Chimie de la Matière Condensée de Bordeaux

ICMBC/CNRS – UPR 9048

87, Avenue du Docteur Schweitzer, 33608 Pessac Cedex

Publications

The material presented in this manuscript is an extended version of the results that was published in the following publications:

[1] M. Bianchini, F. Lalère, H.B.L. Nguyen, F. Fauth, R. David, E. Suard, L. Croguennec, C. Masquelier, $\text{Ag}_3\text{V}_2(\text{PO}_4)_2\text{F}_3$, a new compound obtained by Ag^+/Na^+ ion exchange into the $\text{Na}_3\text{V}_2(\text{PO}_4)_2\text{F}_3$ framework, *J. Mater. Chem. A* **2018**, *6*, 10340-10347.

[2] L.H.B. Nguyen, T. Broux, P. Sanz Camacho, D. Denux, L. Bourgeois, S. Belin, A. Iadecola, F. Fauth, D. Carlier, J. Olchowka, C. Masquelier, L. Croguennec, Stability in water and electrochemical properties of the $\text{Na}_3\text{V}_2(\text{PO}_4)_2\text{F}_3 - \text{Na}_3(\text{VO})_2(\text{PO}_4)_2\text{F}$ solid solution, *Energy Storage Mater.* **2019**, *20*, 324-334.

[3] J. Olchowka, L.H.B. Nguyen, T. Broux, P. Sanz Camacho, E. Petit, F. Fauth, D. Carlier, C. Masquelier, L. Croguennec, Aluminum Substitution for Vanadium in the $\text{Na}_3\text{V}_2(\text{PO}_4)_2\text{F}_3$ and $\text{Na}_3\text{V}_2(\text{PO}_4)_2\text{FO}_2$ type Materials, *Chem. Commun.* **2019**, *55*, 11719-11722.

[4] L.H.B. Nguyen, J. Olchowka, S. Belin, P. Sanz Camacho, M. Duttine, A. Iadecola, F. Fauth, D. Carlier, C. Masquelier, L. Croguennec, Monitoring the Crystal Structure and the Electrochemical Properties of $\text{Na}_3(\text{VO})_2(\text{PO}_4)_2\text{F}$ through Fe^{3+} -Substitution, *ACS Appl. Mater. Interfaces* **2019**, *11* (42), 38808-38818.

[5] L.H.B. Nguyen, P. Sanz Camacho, T. Broux, J. Olchowka, C. Masquelier, L. Croguennec, D. Carlier, DFT-assisted ^{31}P and ^{23}Na MAS-NMR study of the $\text{Na}_3\text{V}_2(\text{PO}_4)_2\text{F}_3 - \text{Na}_3(\text{VO})_2(\text{PO}_4)_2\text{F}$ solid solution: Unravelling the local structure and electronic structure, *Chem. Mater.* **2019**, *31* (23), 9759-9768.

[6] L.H.B. Nguyen, F. Chen, C. Masquelier, L. Croguennec, Book chapter : Polyanion-type compounds as positive electrodes for Sodium-ion batteries, *Elsevier and Wiley Publishers* (International version) and *ISTE Sciences Editions* (French version), *Submitted*.

Acknowledgements

Before getting into the rest, I would like to start thanking the two reviewers, Prof. Gillian Goward (McMaster University, Canada) and Dr. Pascal Roussel (UCCS - CNRS, France), for having accepted to evaluate this thesis. My sincere acknowledgement is also extended to Dr. Florent Boucher (IMN - CNRS, France), Dr. Mario Maglione (ICMCB - CNRS, France) and Prof. Lorenzo Stievano (Université de Montpellier, France) for having taken part in the defense committee and for the great discussion during the defense.

The story of my Ph.D journey should be dated back to October 15th, 2015 when I attended the dissertation defense of the so now Dr. Matteo Bianchini, whose thesis was then supervised by those who are now my advisors, Laurence and Christian. I was immediately impressed by the innovative *operando* techniques developed during this thesis and the inspiring presentation, which promoted me to pursue for a Ph.D degree in the laboratories where he had been trained, hoping to achieve this great level of science. My first contact was with Laurence for a three-year Ph.D at ICMCB. With a great surprise, Laurence told me about an available Ph.D position co-supervised with Christian with a possibility to move back and forth between the two laboratories in Bordeaux and Amiens, and encouraged me to go for it. I was quite hesitate at first, but truly applying for this Ph.D position was the greatest decision in my life and I am now moving the final step of this thesis, writing these acknowledgements without any regrets about my decision.

I want to take a moment to thank my two advisors, Laurence and Christian, for having taken me on as a graduate student and shown me the critical thinking in science. Thanks for always being the inspiring and encouraging sources during the whole Ph.D project. I really appreciate the several opportunities that you have given to me, including the numerous conferences, scientific trainings, experiment at large-scale facilities, joining the RS2E network and especially you have given me an open and flexible project so that I could develop it in a direction which was best suited to my expertise. Through these occasions, you have helped me to have a complete confidence in myself and allowed a total integration into the research society. Thanks a lot for all your personal and scientific advice, which kept me always on the right track and promoted me to go forth for an

academic career. All my appreciation should also be extended to Dany. The ss-NMR spectroscopy and DFT calculations were not completely planned from the beginning of this thesis; nonetheless, you have accepted to get on board and spent a lot of time training me to become an expert in both paramagnetic ss-NMR spectroscopy and DFT calculations. It was a great pleasure to work with you! I would like to express my sincere acknowledgement to Jacob, who miraculously appeared when I was completely stuck with my synthesis. Without you, my thesis cannot go this far! A final thank to all my advisors and co-advisors. We were a great team! Even though I will be soon leaving you for the new horizon, no matter where I will be, I would be proud for having been an ICMCB/LRCS member and for having been your student.

I would like to express my great gratitude to Paula for her help with the ss-NMR measurement and Thibault for having guided me how to use Fullprof and Jana software. I also want to thank my main collaborators at the large-scale facilities for the great experiment that we have performed: François Fauth (ALBA, Spain) for the synchrotron XRD, Stéphanie Belin and Antonella Iadecola (SOLEIL, France) for the synchrotron XAS experiment and Felisa Berenguer (SOLEIL, France) for the coherent diffraction. Cathy, Sabine and Philippe are acknowledged for their support with the daily experiment. Lastly, I want to thank Eric for the XRD acquisition, Mathieu for the Mössbauer spectroscopy, Dominique for the TGA-MS measurement and Lydie for her help with IR.

My daily life and labwork would have not been that great without the presence of my labmates: Yohan, Quentin, Ronan, Adrien, Annie-Kim, Vadim, Tiphaine, Marie, Fatima, Damien, Manu, Edouard, Fan and many other people that the list is so long that I cannot all list here. Many thanks for all your support, for the great sense of humor, for the time spending together, also for the ‘chocolatines’, ‘Schoko-bons’ and the ‘fléchettes’.

I would like to express my special gratitude to the Bernards for having welcomed me to accommodate at their place during my stay in France, which has given me the feeling of having a second family in France. Thanks a lot for showing me the French culture and especially the French hospitality and generosity.

Finally, I want to thank my family: my parents, my aunts and especially my younger brother for having been an unlimited support during my entire life and particularly in these last years.

Résumé de la thèse

Aujourd'hui les batteries Li-ion se développent comme un moyen essentiel pour stocker l'énergie. La naissance des batteries Li-ion remonte aux années 1980s avec la grande contribution de John Goodenough, Stanley Whittingham et Akira Yoshino, et ces travaux ont été récompensés récemment par le Prix Nobel de la Chimie en 2019. Aujourd'hui les batteries Li-ion peuvent être utilisées pour alimenter des téléphones et ordinateurs portables ou encore des voitures électriques. L'intérêt pour des batteries Li-ion est en pleine croissance grâce au développement des énergies renouvelables avec l'objectif de les utiliser pour alimenter des appareils portables par le biais de batteries Li-ion. Malgré ce succès et les avancées de ces dernières années, il existe beaucoup d'inquiétudes sur le futur de la technologie Li-ion. En effet, l'élément lithium est peu abondant, il représente seulement 20 ppm de l'écorce terrestre. Les ressources de Li sont également très mal réparties sur la planète avec 80% et 17% d'entre elles localisées respectivement en Amérique du sud et en Chine. En Europe, il n'y a pas d'importants gisements de Li qui pourraient être utilisés pour la fabrication des batteries Li-ion. Enfin, la plupart des matériaux d'électrode positive pour batteries Li-ion contiennent du cobalt avec 63% des ressources localisées au Congo : la situation très instable de ce pays a conduit récemment à une augmentation considérable de son prix. La criticité de ces éléments a mis la pression sur le développement d'autres technologies de stockage de l'énergie.

Les batteries Na-ion se développent comme une nouvelle alternative aux batteries Li-ion et elles présentent beaucoup d'avantages par rapport à leurs analogues au Li. Le sodium représente environ 2.8% de l'écorce terrestre et est présent partout sur la planète. De plus, les batteries Na-ion peuvent être déchargées à 0 V et donc être stables dans ces conditions pendant une longue durée. Par conséquent, les batteries Na-ion peuvent être stockées longtemps à 0 V sans dégradation de leur capacité, et transportées à 0 V en éliminant tous les risques d'inflammation ou d'explosion.

Une batterie Na-ion se compose d'une électrode négative, d'un électrolyte et d'une électrode positive. Le matériau d'électrode négative utilisé dans les batteries Na-ion est le carbone dur, mais le développement d'autres matériaux de type alliages est également considéré. Un électrolyte classique pour les batteries Na-ion se compose d'un

sel de sodium ion, par exemple NaPF₆, dissous dans un mélange de solvants organiques de type carbonates. Un grand nombre de matériaux est actuellement étudié à l'électrode positive pour batteries Na-ion, et parmi eux les plus intéressants sont des oxydes lamellaires et des matériaux polyanioniques.

Les oxydes lamellaires sont attractifs et sont d'ailleurs actuellement utilisées dans des batteries Na-ion développées par deux start-ups, Faradion (UK) et HiNa (Chine). La capacité délivrée par ces oxydes peut être élevée pour des compositions bien définies en métaux de transition. La mobilité des ions Na⁺ dans cette structure hôte est également excellente dans des domaines de composition en Na⁺, et donc dans des domaines de potentiel bien définis. Néanmoins, ces composés peuvent difficilement être stockés à l'air ou dans un environnement humide. Par contre, les structures polyanioniques sont stables dans des conditions similaires et les potentiels des réactions de dés-intercalation et de ré-intercalation des ions Na⁺ peuvent être modulés par l'effet de polarisation, et parfois dépasser significativement ceux des oxydes lamellaires. La capacité des polyanioniques est par contre plus faible du fait de leur masse molaire élevée, ils ne sont donc pas idéaux pour des applications de type énergie, sauf pour des applications de stockage pour lesquelles le volume n'est pas un critère rédhibitoire.

Ils existent différentes catégories de composés polyanioniques selon la nature de l'anion : phosphates, silicates, sulfates, fluoro-phosphates ... Leur structure peut également être très variable selon leur composition et la connexion entre les polyèdres. Na₃V³⁺₂(PO₄)₂F₃ est le matériau polyanionique le plus performant en batteries Na-ion, grâce à sa capacité théorique élevée, ses potentiels d'extraction des ions Na⁺ élevés, et la stabilité des performances lors de cyclages longues durées et à régimes élevés. Une batterie utilisant Na₃V₂(PO₄)₂F₃ à l'électrode positive peut fonctionner jusqu'à 8000 cycles avec une modeste perte de sa capacité, comme cela a été démontré initialement par le CEA et plus récemment par la start-up française TIAMAT qui développe la technologie C//Na₃V₂(PO₄)₂F₃.

La structure de Na₃V₂(PO₄)₂F₃ est construite par une interconnexion entre des bi-octaèdres V₂O₈F₃ et des tétraèdres PO₄. Chaque bi-octaèdre V₂O₈F₃, ou bien F—VO₄—F—VO₄—F, se compose de deux octaèdres VO₄F₂ tels que les quatre oxygènes sont en plan carré et les deux fluors sur les positions axiales. Les deux octaèdres VO₄F₂ partagent un fluor. Les ions Na⁺ sont localisés dans des tunnels situés dans les plans cristallographiques $z = 0$ et $z = \frac{1}{2}$, et leur distribution varie avec la température. A la

température ambiante, cette distribution impose une distorsion orthorhombique de la structure qui est décrite dans le groupe espace *Amam*. L'augmentation de la température jusqu'à 127°C induit une mobilité croissante des ions Na^+ qui sont distribués sur des anneaux situés dans les tunnels au-dessus et en-dessous des bioctaèdres. Cette redistribution des ions Na^+ s'accompagne d'une transition de phase, la structure de $\text{Na}_3\text{V}_2(\text{PO}_4)_2\text{F}_3$ est alors décrite dans le groupe espace *P4₂/mnm* (maille tétragonale). Concernant des propriétés électrochimiques, deux ions Na^+ peuvent être dés-intercalés à 3.7 et 4.2 V vs. Na^+/Na donnant une capacité de 125 mAh·g⁻¹. En utilisant la diffraction des rayons X (DRX) en mode *operando*, Bianchini *et al.* ont rapporté la complexité et l'existence de plusieurs phases intermédiaires au cours de la charge/décharge entre $\text{Na}_3\text{V}_2(\text{PO}_4)_2\text{F}_3$ et $\text{NaV}_2(\text{PO}_4)_2\text{F}_3$. La formation de ces phases intermédiaires est une conséquence de la réorganisation des ions Na^+ au sein des tunnels dans les phases $\text{Na}_x\text{V}_2(\text{PO}_4)_2\text{F}_3$ ($x = 2.4, 2.2, 2.0, 1.8, 1.3$ et 1.0) pour minimiser les répulsions électrostatiques et leurs énergies totales. Plus particulièrement, un affinement de type Rietveld réalisé sur la phase $\text{NaV}_2(\text{PO}_4)_2\text{F}_3$ a permis de montrer que les environnements locaux des deux vanadiums dans un bi-octaèdre ne sont plus équivalents à la fin de la charge : l'un est symétrique tandis que l'autre est très distordu. Une étude menée *operando* (lors du fonctionnement de la batterie) par spectroscopie d'absorption des rayons X (XAS) associée à la caractérisation de la composition $\text{Na}_{1\pm\delta}\text{V}_2(\text{PO}_4)_2\text{F}_3$ par spectroscopie de résonance magnétique nucléaire (RMN) de ⁵¹V a révélé l'existence de paires $\text{F}-\text{V}^{3+}\text{O}_4-\text{F}-\text{V}^{5+}\text{O}_4-\text{F}$, en bon accord avec les informations obtenues par l'analyse de diffraction des rayons X (environnements et valences des ions vanadium).

Malgré la présence de trois ions Na^+ dans $\text{Na}_3\text{V}_2(\text{PO}_4)_2\text{F}_3$, seulement deux d'entre eux peuvent participer réversiblement aux réactions électrochimiques. En effet, la dés-intercalation et ré-intercalation du troisième ion Na^+ n'a jamais été rapportée, ni par une voie chimique ni par la voie électrochimique. Une instabilité de la structure est observée en batterie à haut potentiel, ou en solution en utilisant un oxydant fort tel que NO_2BF_4 . Des calculs théoriques réalisés par le groupe de Ceder ont également démontré que le potentiel requis pour la des-intercalation du troisième ion Na^+ de $\text{Na}_3\text{V}_2(\text{PO}_4)_2\text{F}_3$ est très élevé, hors du domaine de stabilité des électrolytes actuellement disponibles, et que l'ordre de $\text{Na}^+/\text{lacune}$ est tellement stable qu'il s'accompagne d'une forte diminution de la mobilité des ions au sein de la structure. Par conséquent, une grande énergie d'activation est requise pour casser cet ordre de charge et pour extraire le troisième ion

Na^+ de $\text{Na}_3\text{V}_2(\text{PO}_4)_2\text{F}_3$. La substitution cationique est l'une des voies envisagées, notamment dans le cadre de cette thèse, pour casser cet ordre de charge et ainsi diminuer la valeur de l'énergie d'activation requise pour l'extraction du troisième ion Na^+ . Cette hypothèse est soutenue par les résultats que nous avons obtenus pour les phases $\text{Na}_3\text{V}_2(\text{PO}_4)_2\text{F}_{3-y}\text{O}_y$ ($0 \leq y \leq 2$), dérivées de $\text{Na}_3\text{V}_2(\text{PO}_4)_2\text{F}_3$ avec une substitution partielle de l'oxygène au fluor. Les atomes de fluor terminaux appartenant aux bioctaèdres $\text{V}_2\text{O}_8\text{F}_3$ peuvent être substitués, au contraire du fluor pontant les deux octaèdres. Cette substitution anionique conduit pour la compensation des charges à l'oxydation du vanadium V^{3+} en V^{4+} avec la formation de liaisons vanadyle ($\text{V}^{4+}=\text{O}$). Le potentiel d'extraction des ions Na^+ diminue avec une augmentation du taux de substitution oxygène/fluor, et le potentiel le plus bas est observé pour la phase $\text{Na}_3(\text{VO})_2(\text{PO}_4)_2\text{F}$ pour laquelle tous les ions vanadium sont à l'état tétravalent et engagés dans des liaisons vanadyle. Malgré un grand nombre de publications sur les phases $\text{Na}_3\text{V}_2(\text{PO}_4)_2\text{F}_{3-y}\text{O}_y$, ils restent encore beaucoup de points interrogations spécialement sur la nature des échantillons rapportés dans la littérature, les environnements locaux des atomes et les processus redox impliqués lors des réactions de dés-intercalation et de ré-intercalation. J'ai exploré ce système afin d'établir une connaissance pointue de la relation composition - structure - propriétés et de lever les contradictions rapportées sur le système $\text{Na}_3\text{V}_2(\text{PO}_4)_2\text{F}_{3-y}\text{O}_y$ ($0 \leq y \leq 2$) en comparant leur structure moyenne à longue distance à la structure locale par une approche multi-échelle en combinant des techniques de diffraction à haute résolution et de spectroscopies (XAS, RMN et infrarouge) à des calculs théoriques. Grâce à cette approche, une compréhension complète de la structure et des processus redox mis en jeu lors du fonctionnement de la batterie est accomplie. De plus, différents types de substitution, cationiques et mixtes (cad. simultanément cationiques et anioniques), ont été explorées pour les phases $\text{Na}_3\text{V}^{3+}_2(\text{PO}_4)_2\text{F}_3$ et $\text{Na}_3(\text{V}^{4+}\text{O})_2(\text{PO}_4)_2\text{F}$. Pour chacune des compositions obtenues, les structures moyennes et locales ont été déterminées finement, et les évolutions structurales et processus redox mis en jeu au cours du cyclage ont aussi été étudiés par des techniques avancés. Mon travail de thèse a été consacré à l'exploration à la fois de la richesse et de la complexité de la structure de type $\text{Na}_3\text{V}_2(\text{PO}_4)_2\text{F}_3$, mais aussi à la compréhension de l'influence de la substitution cationique et/ou anionique sur les propriétés physico-chimiques et électrochimiques de $\text{Na}_3\text{V}_2(\text{PO}_4)_2\text{F}_3$.

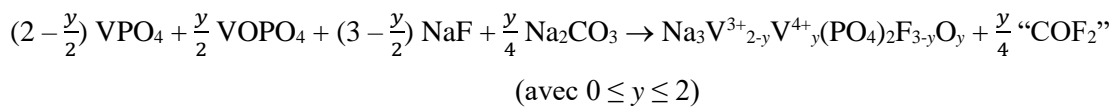
Les résultats obtenus durant ces trois années peuvent être divisés en trois chapitres : (1) Effets de la substitution anionique sur la structure et les propriétés

électrochimiques de $\text{Na}_3\text{V}_2(\text{PO}_4)_2\text{F}_3$, (2) Une étude de la structure atomique et électronique locale de la série de composés appartenant à la famille $\text{Na}_3\text{V}_2(\text{PO}_4)_2\text{F}_3 - \text{Na}_3(\text{VO})_2(\text{PO}_4)_2\text{F}$, en utilisant la spectroscopie de résonance magnétique nucléaire couplée des calculs théoriques et (3) Effets de la substitution cationique sur la structure et les propriétés physico-chimiques et électrochimiques de $\text{Na}_3\text{V}_2(\text{PO}_4)_2\text{F}_3 - \text{Na}_3(\text{VO})_2(\text{PO}_4)_2\text{F}$ en batteries au sodium.

Effets de la substitution anionique sur la structure et les propriétés électrochimiques de $\text{Na}_3\text{V}_2(\text{PO}_4)_2\text{F}_3$

$\text{Na}_3\text{V}_2(\text{PO}_4)_2\text{F}_3$ et $\text{Na}_3(\text{VO})_2(\text{PO}_4)_2\text{F}$ sont les compositions limites d'une famille de matériaux de composition $\text{Na}_3\text{V}_2(\text{PO}_4)_2\text{F}_{3-y}\text{O}_y$ ($0 \leq y \leq 2$) où les atomes de fluor occupant les positions apicales des bi-octaèdres $\text{V}_2\text{O}_8\text{F}_3$ dans la phase $\text{Na}_3\text{V}_2(\text{PO}_4)_2\text{F}_3$ peuvent être substitués par des atomes d'oxygène pour former des liaisons vanadyle très covalentes. Lors de la synthèse de $\text{Na}_3\text{V}_2(\text{PO}_4)_2\text{F}_3$, la substitution de l'oxygène au fluor peut avoir lieu facilement si l'atmosphère de la réaction contient des traces d'oxygène : très souvent, les compositions rapportées dans la littérature comme étant $\text{Na}_3\text{V}_2(\text{PO}_4)_2\text{F}_3$ sont en fait des phases oxygénées $\text{Na}_3\text{V}_2(\text{PO}_4)_2\text{F}_{3-\delta}\text{O}_\delta$, parfois très oxydées. Cette substitution partielle est inévitable, au moins en très faibles proportions. En effet, des analyses thermogravimétriques couplées à la spectrométrie de masse ont été réalisées sur un mélange ($2 \text{VPO}_4 + 3 \text{NaF}$) sous atmosphère d'argon et ont révélé une perte de fluor dès 450°C .

Dans ce travail de thèse, une série de phases oxy-phosphates fluorés de vanadium a été synthétisée par une voie solide selon la réaction :



L'échantillon obtenu contient de faibles teneurs en impuretés qui sont solubles dans l'eau. Par une analyse combinant DRX, RMN et IR, nous avons démontré que toutes les phases $\text{Na}_3\text{V}^{3+}_{2-y}\text{V}^{4+}_y(\text{PO}_4)_2\text{F}_{3-y}\text{O}_y$ sont stables dans l'eau et qu'elles peuvent donc être utilisées pour des formulations d'électrode en voie aqueuse ou encore à l'électrode positive de batteries aqueuses.

A température ambiante, la structure de $\text{Na}_3\text{V}_2(\text{PO}_4)_2\text{F}_3$ est décrite dans le groupe d'espace *Amam* avec une distribution des ions Na^+ sur trois sites cristallographiques différents, à l'origine de la distorsion orthorhombique de la maille. En substituant les atomes de fluor par des atomes d'oxygène, la distribution des ions Na^+ dans les tunnels évolue avec une répartition de ceux-ci sur un anneau, la disparition progressive de la distorsion orthorhombique et une évolution linéaire des paramètres de maille pour la solution solide $\text{Na}_3\text{V}_2(\text{PO}_4)_2\text{F}_3 - \text{Na}_3(\text{VO})_2(\text{PO}_4)_2\text{F}$. Une surstructure a été observée pour la composition $\text{Na}_3(\text{VO})_2(\text{PO}_4)_2\text{F}$, en raison d'un ordre Na^+ /Lacune spécifique. Une maille de symétrie monoclinique décrite dans le groupe d'espace *P2₁/m* combiné à un

vecteur de modulation $q = \frac{1}{2} b^* + \frac{1}{2} c^*$ a été proposée pour décrire la structure de cette phase.

Bien qu'une évolution linéaire des paramètres de maille est observée pour cette famille de matériaux, selon notamment leur état de cristallisation il peut être difficile de les différencier finement et de détecter la distorsion orthorhombique par diffraction des rayons X de laboratoire. La spectroscopie RMN du ^{23}Na et du ^{31}P à l'état solide s'est révélée plus pertinente pour quantifier finement le taux de substitution de l'oxygène au fluor, notamment lorsqu'il s'agit de faibles teneurs. Ces résultats sont détaillés dans le chapitre 2. La spectroscopie IR permet également de détecter directement la présence de liaisons vanadyle car elles sont associées à des bandes intenses dans le domaine de nombres d'onde $900 - 1000 \text{ cm}^{-1}$, selon la covalence de la liaison. Deux bandes de vibration ont été observées pour toutes les compositions intermédiaires $\text{Na}_3\text{V}_2(\text{PO}_4)_2\text{F}_{3-y}\text{O}_y$ ($0 < y < 2$), l'une correspond à celle observée pour $\text{Na}_3(\text{VO})_2(\text{PO}_4)_2\text{F}$ et donc à la vibration de liaisons vanadyle dans le bi-octaèdre $\text{O}=\text{V}^{4+}\text{O}_4-\text{F}-\text{V}^{4+}\text{O}_4=\text{O}$ tandis que l'autre correspondrait à la vibration d'une liaison vanadyle dans un bi-octaèdre $\text{F}-\text{V}^{3+}\text{O}_4-\text{F}-\text{V}^{4+}\text{O}_4=\text{O}$. Cette dernière est d'ailleurs observée pour les faibles taux de substitution, et reflète donc plutôt la présence de défauts isolés de type vanadyle. L'intensité relative entre les deux vibrations permet de réaliser une analyse semi-quantitative pour déterminer le taux de substitution fluor/oxygène.

Deux ions Na^+ peuvent être extraits et ré-intercalés réversiblement dans un domaine de potentiel de $2.5 - 4.3 \text{ V}$ par rapport au couple Na^+/Na pour toutes les compositions $\text{Na}_3\text{V}_2(\text{PO}_4)_2\text{F}_{3-y}\text{O}_y$ ($0 \leq y \leq 2$), et cette réaction met en jeu une série de réactions bi-phasées avec la formation de phases intermédiaires pour les deux compositions extrêmes $\text{Na}_3\text{V}_2(\text{PO}_4)_2\text{F}_3$ et $\text{Na}_3(\text{VO})_2(\text{PO}_4)_2\text{F}$. Pour toutes les autres compositions, des réactions de type solutions solides ont été observées. Le potentiel associé à l'extraction des ions Na^+ est abaissé suite à la substitution fluor/oxygène, le potentiel du couple $\text{V}^{5+}=\text{O}/\text{V}^{4+}=\text{O}$ est donc observé significativement plus bas (à 3.6 et 4.0 V) que celui du couple $\text{V}^{4+}-\text{F}/\text{V}^{3+}-\text{F}$ (à 3.7 et 4.2 V), ce qui s'explique par « l'effet de polarisation inversée » imposé par la formation de la liaison vanadyle sur le site de V^{4+} .

En augmentant le potentiel de la fin de la charge jusqu'à 4.8 V par rapport au couple Na^+/Na , une capacité supplémentaire correspondant à l'extraction partielle du

troisième Na^+ de $\text{Na}_3\text{V}_2(\text{PO}_4)_2\text{F}_3$ a été rapportée par Yan *et al.*, mais seuls deux d'entre eux peuvent être ré-intercalés en décharge dans une structure modifiée irréversiblement. Un suivi *operando* au cours du cyclage de la batterie $\text{Na}/\text{Na}_3\text{V}_2(\text{PO}_4)_2\text{F}_3$ a été réalisé en absorption des rayons X sur la ligne ROCK au synchrotron SOLEIL au cours de ma thèse. Tous les spectres XAS obtenus ont été analysés par chimométrie. Quatre composantes se sont révélées indispensables pour décrire ce système. Une analyse de la structure locale a été réalisée par EXAFS (Extended X-ray Absorption Fine Structure) et a suggéré qu'il n'y aurait pas d'oxydation des ions vanadium à haut potentiel, mais que leur environnement local serait néanmoins largement modifiés du fait d'une forte distorsion, maintenue jusqu'à la ré-intercalation des ions Na^+ jusqu'à un potentiel de fin de décharge de 2.0 V.

Pour les phases $\text{Na}_3\text{V}_2(\text{PO}_4)_2\text{F}_{1.5}\text{O}_{1.5}$ et $\text{Na}_3\text{V}_2(\text{PO}_4)_2\text{F}_2\text{O}$, une capacité supplémentaire (au-delà de la désintercalation de deux ions Na^+) a également été observée à haut potentiel, cette fois, sans impact sur la réversibilité de la réaction électrochimique. Les analyses XAS (XANES et EXAFS) réalisées en mode *operando* ont démontré qu'il n'y a pas d'oxydation des ions vanadium à haut potentiel et pas de modifications structurales à l'échelle locale dans ces conditions « extrêmes ». La substitution partielle de l'oxygène au fluor et la formation des liaisons vanadyle permettent donc de stabiliser ces phases à l'état de surcharge de la batterie.

Une étude de la structure atomique et électronique locale de la série de composés appartenant à la famille $\text{Na}_3\text{V}_2(\text{PO}_4)_2\text{F}_3 - \text{Na}_3(\text{VO})_2(\text{PO}_4)_2\text{F}$, en utilisant la spectroscopie de résonance magnétique nucléaire couplée des calculs théoriques.

Toutes les phases $\text{Na}_3\text{V}_2(\text{PO}_4)_2\text{F}_{3-y}\text{O}_y$ ($0 \leq y \leq 2$) obtenues ont été étudiées par RMN du solide des noyaux ^{23}Na et ^{31}P . Pour la phase $\text{Na}_3\text{V}_2(\text{PO}_4)_2\text{F}_3$, le spectre RMN du ^{31}P montre un seul signal à 6000 ppm qui correspond à l'environnement local $\text{P}(\text{OV}^{3+})_4$ tandis qu'un signal à 0 ppm qui correspond à l'environnement local $\text{P}(\text{OV}^{4+})_4$ a été enregistré pour $\text{Na}_3(\text{VO})_2(\text{PO}_4)_2\text{F}$. Pour toutes les phases de compositions intermédiaires $\text{Na}_3\text{V}_2(\text{PO}_4)_2\text{F}_{3-y}\text{O}_y$ ($0 < y < 2$), cinq résonances du ^{31}P ont été observées à 6000 ppm, 4500 ppm, 3000 ppm, 1500 ppm et 0 ppm et correspondent aux environnements locaux $\text{P}(\text{OV}^{3+})_4$, $\text{P}(\text{OV}^{3+})_3(\text{OV}^{4+})$, $\text{P}(\text{OV}^{3+})_2(\text{OV}^{4+})_2$, $\text{P}(\text{OV}^{3+})(\text{OV}^{4+})_3$, et $\text{P}(\text{OV}^{4+})_4$. La présence d'un ion V^{3+} autour d'un noyau phosphore contribue donc à un déplacement de 1500 ppm

du signal RMN du ^{31}P , et cette hypothèse a pu être confirmée par des calculs théoriques basés sur la théorie de la fonctionnelle de la densité (DFT).

Les résultats de ces calculs théoriques ont démontré que les ions V^{3+} présentent dans ces phases résident dans un environnement octaédrique symétrique et les deux électrons célibataires occupant les orbitales de type t_{2g} participent via les orbitales d_{xz} et d_{yz} à des interactions de type $d_{xz}/d_{yz}(\text{V}^{3+}) - p_{\pi}(\text{O}) - sp^3(\text{P})$ qui permettent un transfert de spins électroniques de V^{3+} au noyau du phosphore. Cette interaction de Fermi induit, à chaque fois, un déplacement de 1500 ppm sur le noyau du phosphore. L'environnement local autour de l'ion V^{4+} est par contre très distordu suite à la formation de la liaison courte de type vanadyle, dans ce cas l'électron célibataire de cet ion localisé dans l'orbitale d_{xy} ne peut pas être transféré sur le noyau de phosphore.

Concernant la RMN du ^{23}Na , pour $\text{Na}_3\text{V}_2(\text{PO}_4)_2\text{F}_3$ un seul signal correspondant à l'environnement local $\text{Na}(\text{OV}^{3+})_2$ a été observé à 140 ppm tandis que pour $\text{Na}_3(\text{VO})_2(\text{PO}_4)_2\text{F}$ un seul signal correspondant à l'environnement local $\text{Na}(\text{OV}^{4+})_2$ a été observé à 80 ppm. Les trois signaux RMN du ^{23}Na observés à 140 ppm, 100 ppm et 80 ppm correspondant donc respectivement aux environnements locaux $\text{Na}(\text{OV}^{3+})_2$, $\text{Na}(\text{OV}^{3+})(\text{OV}^{4+})$ et $\text{Na}(\text{OV}^{4+})_2$ ont été observés pour toutes des phases $\text{Na}_3\text{V}_2(\text{PO}_4)_2\text{F}_{3-y}\text{O}_y$ ($0 < y < 2$). L'intensité relative entre ces signaux RMN du ^{23}Na peut être utilisée pour quantifier le taux de substitution fluor/oxygène.

Effets de la substitution cationique sur la structure et les propriétés physico-chimiques et électrochimiques de $\text{Na}_3\text{V}_2(\text{PO}_4)_2\text{F}_3 - \text{Na}_3(\text{VO})_2(\text{PO}_4)_2\text{F}$ en batteries au sodium

La première partie de ce chapitre est dédiée à la démonstration de la mobilité élevée des ions Na^+ dans la phase $\text{Na}_3\text{V}_2(\text{PO}_4)_2\text{F}_3$ et à la possibilité de transformer cette phase en conducteur des ions Li^+ , K^+ , ou Ag^+ . Les ions Na^+ de $\text{Na}_3\text{V}_2(\text{PO}_4)_2\text{F}_3$ sont très mobiles et peuvent être remplacés facilement par des ions Ag^+ grâce à un échange ionique dans une solution AgNO_3 . Le matériau obtenu, $\text{Ag}_3\text{V}_2(\text{PO}_4)_2\text{F}_3$, adopte la même structure que $\text{Na}_3\text{V}_2(\text{PO}_4)_2\text{F}_3$ et pourrait être utilisé comme matériau actif à l'électrode positive de batteries Ag-ion. Des échanges ioniques Na^+/Li^+ et Na^+/K^+ avaient déjà été rapportés. La structure de type $\text{A}_3\text{V}_2(\text{PO}_4)_2\text{F}_3$ permet donc d'accueillir des ions de tailles très

variables (de 0.72 Å pour Li⁺ à 1.15 Å pour Ag⁺) avec une augmentation du volume de maille et de la distorsion orthorhombique en passant de Li⁺ à Na⁺ puis à Ag⁺.

Dans la deuxième partie, la substitution du Fe³⁺ au vanadium dans la phase Na₃(VO)₂(PO₄)₂F a été réalisée par chimie-douce. Le choix s'est porté sur le fer car c'est un élément abondant qui peut présenter plusieurs états d'oxydation. Le couple redox Fe³⁺/Fe²⁺ est bien connu pour être actifs dans de nombreux matériaux d'électrodes de type oxydes ou polyanioniques, de plus l'activation du couple redox Fe⁴⁺/Fe³⁺ a été récemment rapportée pour NaFeO₂. L'activation du couple redox Fe⁴⁺/Fe³⁺ dépend très fortement du champ cristallin, en effet une « pression » chimique à l'échelle locale est indispensable pour permettre dans certains cas, très rares, de rendre possible l'oxydation des ions Fe³⁺ en Fe⁴⁺ à température ambiante par la voie électrochimique. La structure de type Na₃M₂(PO₄)₂(F,O)₃, qui peut présenter selon sa composition des environnements MO₄(F,O)₂ très distordus, nous semblait propice à l'activation du couple Fe⁴⁺/Fe³⁺. La structure de la phase Na₃Fe(VO)(PO₄)₂F₂ a été décrite dans le groupe espace *P4₂/mnm* avec seulement deux sites cristallographiques pour les ions Na⁺. Un seul ion Na⁺ est extrait lors d'un cyclage dans la fenêtre de potentiel classiquement considérée 2.5 - 4.3 V par rapport au couple Na⁺/Na, associé à l'oxydation de V⁴⁺=O en V⁵⁺=O. La très faible polarisation observée lors de cette réaction électrochimique démontre que cette substitution participe à une augmentation de la mobilité des ions Na⁺ au sein de cette structure hôte. Un suivi de la réaction par diffraction des rayons X synchrotron en mode *operando* au cours du cyclage d'une cellule Na//Na₃Fe(VO)(PO₄)₂F₂ a révélé qu'il n'y avait pas de formation de phases intermédiaires pendant la réaction, ce qui est comme déjà discuté en soi favorable à une mobilité rapide des ions car il n'y a pas d'ordres de charges qui tendent à « figer » les ions et les électrons. En déchargeant la cellule Na//Na₃Fe(VO)(PO₄)₂F₂ à 1.5 V, la réduction des ions Fe³⁺ en Fe²⁺ accompagnée par l'insertion de 0.5 Na⁺ a été mise en évidence, toutefois cette réaction a lieu à un potentiel trop bas et de plus pénalisé par une énorme polarisation, pour pouvoir trouver sa place dans des applications. Néanmoins, c'est la première fois que l'activation du couple redox Fe³⁺/Fe²⁺ a été rapportée dans cette structure.

Dans la troisième partie, la substitution de l'aluminium a été réalisée par chimie-douce dans les structures de Na₃V₂(PO₄)₂F₃ et Na₃(VO)₂(PO₄)₂F. En utilisant les mêmes précurseurs mais en changeant le domaine de pH de la solution, deux familles de matériaux Na₃V_{2-z}Al_z(PO₄)₂F₃ (0 ≤ z ≤ 0.5) et Na₃(VO)_{2-z}Al_z(PO₄)₂F_{1+z} (0 ≤ z ≤ 2) ont été

obtenues. La substitution du V^{3+} par Al^{3+} est observée en milieu acide mais elle est limitée à des taux de substitution de 25% avec la formation de la phase $Na_3V_{1.5}Al_{0.5}(PO_4)_2F_3$. Toutes les compositions obtenues sont décrites dans le groupe d'espace *Amam*, la distorsion orthorhombique étant notamment observée par la séparation des raies de diffraction (400) et (040). Par contre, la substitution $V^{4+}=O$ par $Al^{3+}-F$ a lieu en milieu basique et une solution solide est observée sur tout le domaine de composition avec une évolution linéaire des paramètres de maille. Toutes les phases $Na_3(VO)_{2-z}Al_z(PO_4)_2F_{1+z}$ ($0 < z < 2$) sont décrites dans la maille de symétrie quadratique dans le groupe d'espace *P4₂/mnm*. Dans les phases $Na_3V_{2-z}Al_z(PO_4)_2F_3$ ($0 \leq z \leq 0.5$) et $Na_3(VO)_{2-z}Al_z(PO_4)_2F_{1+z}$ ($0 \leq z \leq 2$), le nombre d'ions Na^+ qui peut participer aux réactions électrochimiques est limité à $(2 - z)$. Evidemment, la présence de l'ion Al^{3+} en grande quantité se fait au détriment de bonnes performances en batteries. Par contre, encore une fois la substitution permet de supprimer toutes les phases intermédiaires observées au cours du cyclage de $Na_3V_2(PO_4)_2F_3$ et $Na_3(VO)_2(PO_4)_2F$. De plus, les potentiels d'extraction des ions Na^+ des phases $Na_3V_{1.5}Al_{0.5}(PO_4)_2F_3$ et $Na_3(VO)_{1.5}Al_{0.5}(PO_4)_2F_{1.5}$ sont similaires respectivement à ceux des phases non substituées, $Na_3V_2(PO_4)_2F_3$ et $Na_3(VO)_2(PO_4)_2F$, ce qui tend à indiquer que l'interaction électronique entre les deux sites métalliques d'un bi-octaèdre est très faible. Malgré l'effet défavorable de la substitution de l'aluminium au vanadium sur les performances électrochimiques de ces matériaux, il sera important de considérer l'impact d'un faible taux de substitution sur la stabilité chimique et thermique à haut potentiel (dans un état de surcharge) des phases $Na_3V_{2-z}Al_z(PO_4)_2F_3$ et $Na_3(VO)_{2-z}Al_z(PO_4)_2F_{1+z}$ car pour certaines compositions cela permettrait d'améliorer le triptyque *potentiel - capacité réversible - stabilité*, essentielle pour l'application.

Table of content

| | |
|-----------------------------------------------------------------------------------------------------------------------------------------------------------------------------------------|-----------|
| Chapter I – General Introduction | 5 |
| I.1. General introduction | 7 |
| I.1.1. Lithium-ion batteries..... | 7 |
| I.1.2. General definitions in batteries | 9 |
| I.2. Sodium-ion batteries | 11 |
| I.2.1. General introduction..... | 11 |
| I.2.2. Negative electrodes for Sodium-ion batteries | 14 |
| I.2.3. Electrolytes for Sodium-ion batteries..... | 15 |
| I.2.4. Positive electrodes for Sodium-ion batteries..... | 16 |
| I.2.4.1. Layered transition metal oxides | 16 |
| I.2.4.2. Polyanionic framework materials..... | 20 |
| I.2.5. $\text{Na}_3\text{V}_2(\text{PO}_4)_2\text{F}_3$ and related materials as positive electrodes for SIBs | 23 |
| I.2.5.1. ‘ NaVPO_4F ’ | 23 |
| I.2.5.2. $\text{Na}_3\text{V}_2(\text{PO}_4)_3$ | 25 |
| I.2.5.3. $\text{Na}_3\text{V}_2(\text{PO}_4)_2\text{F}_3$ | 26 |
| I.2.5.4. $\text{Na}_3(\text{VO})_2(\text{PO}_4)_2\text{F}$ | 32 |
| I.2.5.5. The $\text{Na}_3\text{V}_2(\text{PO}_4)_2\text{F}_3 - \text{Na}_3(\text{VO})_2(\text{PO}_4)_2\text{F}$ system..... | 33 |
| I.2.5.5.1. Crystal structure description | 33 |
| I.2.5.5.2. Characterization techniques | 34 |
| I.2.6. Structural designs and materials derived from $\text{Na}_3\text{V}_2(\text{PO}_4)_2\text{F}_3 - \text{Na}_3(\text{VO})_2(\text{PO}_4)_2\text{F}$ with superior performance | 37 |
| I.2.6.1. Three Na^+ ions extraction at extreme cycling conditions..... | 37 |
| I.2.6.2. Influence of ionic substitution on the electrochemistry of $\text{Na}_3\text{V}_2(\text{PO}_4)_2\text{F}_3$. | 40 |
| I.3. Aim of this work | 43 |

| | |
|-------------------------------------------------------------------------------------------------------------------------------------------------------------------------------------------------------------------------|-----------|
| Chapter II – The Effects of Anionic Substitution on the Crystal Structure and the Electrochemical Properties of $\text{Na}_3\text{V}_2(\text{PO}_4)_2\text{F}_3$ | 45 |
| II.1. Introduction | 47 |
| II.2. Materials synthesis and characterizations | 48 |
| II.2.1. Materials synthesis | 48 |
| II.2.2. Materials characterization | 48 |
| II.3. Results and discussions | 52 |
| II.3.1. The complexity of the synthesis reaction | 52 |
| II.3.2. The stability in water of $\text{Na}_3\text{V}^{3+}_{2-y}\text{V}^{4+}_y(\text{PO}_4)_2\text{F}_{3-y}\text{O}_y$ phases | 56 |
| II.3.3. Crystal structure determination for $\text{Na}_3\text{V}^{3+}_{2-y}\text{V}^{4+}_y(\text{PO}_4)_2\text{F}_{3-y}\text{O}_y$ | 60 |
| II.3.4. Electrochemical properties | 66 |
| II.3.5. <i>Operando</i> X-ray absorption spectroscopy | 70 |
| II.3.6. The paradox of Vanadium redox couple in $\text{Na}_3\text{V}_2(\text{PO}_4)_2\text{F}_{3-y}\text{O}_y$ | 74 |
| II.3.6.1. $\text{Na}_3\text{V}_2(\text{PO}_4)_2\text{F}_3$ | 74 |
| II.3.6.1.1. First charge up to 4.8 V vs. Na^+/Na | 74 |
| II.3.6.1.2. Discharge to 2.5 V vs. Na^+/Na | 78 |
| II.3.6.1.3. Second charge to 4.3 V and then discharge to 2.5 V vs. Na^+/Na | 80 |
| II.3.6.2. The paradox of V redox couple in $\text{Na}_3\text{V}_2(\text{PO}_4)_2\text{F}_{1.5}\text{O}_{1.5}$ & $\text{Na}_3\text{V}_2(\text{PO}_4)_2\text{F}_2\text{O}$ | 81 |
| II.3.6.2.1. $\text{Na}_3\text{V}_2(\text{PO}_4)_2\text{F}_{1.5}\text{O}_{1.5}$ | 83 |
| II.3.6.2.2. $\text{Na}_3\text{V}_2(\text{PO}_4)_2\text{F}_2\text{O}$ | 83 |
| II.3.6.3. A comparison between $\text{Na}_3\text{V}_2(\text{PO}_4)_2\text{F}_3$, $\text{Na}_3\text{V}_2(\text{PO}_4)_2\text{F}_2\text{O}$ and $\text{Na}_3\text{V}_2(\text{PO}_4)_2\text{F}_{1.5}\text{O}_{1.5}$ | 85 |
| II.4. Conclusions | 87 |

| | |
|-----------------------------------------------------------------------------------------------------------------------------------------------------------------------------------------------------------------------------------------------------------------|------------|
| Chapter III – Revealing Atomic Local Environments in $\text{Na}_3\text{V}_2(\text{PO}_4)_2\text{F}_3 - \text{Na}_3(\text{VO})_2(\text{PO}_4)_2\text{F}$ Materials by Solid-State NMR Spectroscopy and First-Principles DFT Calculations | 89 |
| III.1. Introduction | 91 |
| III.2. Principles of NMR measurements and DFT calculations | 94 |
| III.2.1. Samples preparation | 94 |
| III.2.2. NMR measurements | 94 |
| III.2.3. First-principles DFT calculations | 95 |
| III.3. NMR and DFT study on $\text{Na}_3\text{V}_2(\text{PO}_4)_2\text{F}_3 - \text{Na}_3(\text{VO})_2(\text{PO}_4)_2\text{F}$ | 96 |
| III.3.1. ^{31}P NMR signals assignment in $\text{Na}_3\text{V}_2(\text{PO}_4)_2\text{F}_3 - \text{Na}_3(\text{VO})_2(\text{PO}_4)_2\text{F}$ | 96 |
| III.3.2. Vanadium electronic structure in $\text{Na}_3\text{V}_2(\text{PO}_4)_2\text{F}_3 - \text{Na}_3(\text{VO})_2(\text{PO}_4)_2\text{F}$ | 98 |
| III.3.3. Spin Transfer Mechanisms between V^{n+} ions and Phosphorus nuclei | 104 |
| III.3.4. ^{23}Na ss-NMR in $\text{Na}_3\text{V}_2(\text{PO}_4)_2\text{F}_3 - \text{Na}_3(\text{VO})_2(\text{PO}_4)_2\text{F}$ | 109 |
| III.4. NMR study on $\text{Na}_x\text{V}_2(\text{PO}_4)_2\text{F}_3$ and $\text{Na}_x\text{V}_2(\text{PO}_4)_2\text{F}_2\text{O}$ | 116 |
| III.4.1. $\text{Na}_x\text{V}_2(\text{PO}_4)_2\text{F}_3$ | 116 |
| III.4.2. $\text{Na}_x\text{V}_2(\text{PO}_4)_2\text{F}_2\text{O}$ | 121 |
| III.5. Conclusions | 123 |

| | |
|----------------------------------------------------------------------------------------------------------------------------------------------------------------------------------------------------------------------------------------------------|----------------|
| Chapter IV – The Effects of Cationic Substitution on the Crystal Structure and Electrochemistry of Na₃V₂(PO₄)₂F₃ – Na₃(VO)₂(PO₄)₂F | 125 |
| IV.1. Introduction | 127 |
| IV.2. Ag⁺/Na⁺ ion exchange into Na₃V₂(PO₄)₂F₃ | 129 |
| IV.2.1. Samples preparation | 129 |
| IV.2.2. Ag ⁺ /Na ⁺ ion exchange into microcrystalline Na ₃ V ₂ (PO ₄) ₂ F ₃ | 129 |
| IV.2.3. Ag ⁺ /Na ⁺ ion exchange into submicron Na ₃ V ₂ (PO ₄) ₂ F ₃ | 136 |
| IV.3. Fe-substitution into Na₃(VO)₂(PO₄)₂F | 139 |
| IV.3.1. Sample preparation | 139 |
| IV.3.2. Structural characterizations | 141 |
| IV.3.3. Electrochemical properties of Na ₃ (VO)Fe(PO ₄) ₂ F ₂ | 150 |
| IV.3.4. Operando structural characterization | 155 |
| IV.4. Al-substitution in Na₃V₂(PO₄)₂F₃ – Na₃(VO)₂(PO₄)₂F | 160 |
| IV.4.1. Sol-gel synthesis of Na ₃ V ³⁺ _{1.5} Al _{0.5} (PO ₄) ₂ F ₃ | 161 |
| IV.4.1.1. Sample preparation | 161 |
| IV.4.1.2. Atomic and crystal structures characterization | 161 |
| IV.4.2. The Na ₃ (V ⁴⁺ O) _{2-z} Al _z (PO ₄) ₂ F _{1+z} (0 ≤ z ≤ 2) material family | 166 |
| IV.4.2.1. Samples preparation | 166 |
| IV.4.2.2. Phase identification | 167 |
| IV.4.2.3. Structural characterization using high resolution SXRD | 170 |
| IV.4.2.3.1. Na ₃ (VO) _{2-z} Al _z (PO ₄) ₂ F _{1+z} (0 < z < 2) | 170 |
| IV.4.2.3.2. Na ₃ Al ₂ (PO ₄) ₂ F ₃ | 172 |
| IV.4.2.4. Vanadium oxidation state and chemical formula determination | 175 |
| IV.4.2.5. Solid-state NMR characterization | 178 |
| IV.4.2.5.1. Variable temperature ²³ Na and ²⁷ Al <i>ss</i> -NMR of Na ₃ Al ₂ (PO ₄) ₂ F ₃ | 178 |
| IV.4.2.5.2. NMR study of Na ₃ (VO) _{2-z} Al _z (PO ₄) ₂ F _{1+z} solid solution | 179 |
| IV.4.3. Electrochemistry of Al ³⁺ substituted phases | 181 |
| IV.5. Conclusions | 183 |
| Chapter V – General Conclusions | 187 |
| References | 193 |

Chapter I

General Introduction

I.1. General introduction

I.1.1. Lithium-ion batteries

In our modern society, electricity has become an essential part of our daily life. It is not an exaggeration to say that our life quality has been improved significantly since the discovery of electricity. Nowadays, there are several ways of electricity generation, such as fossil fuel (coal, oil, gas), hydroelectric, wind turbines, geothermal, solar energy or nuclear reaction. In France, more than 80% of the electricity production comes from nuclear reaction. Recent researches have focused on the use of sustainable energy generation approaches, such as solar energy, tidal energy or wind energy, however most of these technologies rely significantly on intermittent sources and they should be coupled with an energy storage system. Furthermore, an energy supplier is required for all the mobile devices, including smartphones, laptops and electric cars. Many energy storage systems were developed in recent years in order to supply electricity for mobile devices, such as redox flow batteries, lead-acid accumulators, Ni-Cd accumulators [1–6]. In 1991, Lithium-ion batteries (LIBs) were introduced into the market as an alternative energy storage system and a great interest in the development of LIBs has been observed in the last few years.

The discovery of Lithium element is dated back to 1817 by Johan August Arfwedson. The Swedish chemist reported that the petalite ore ($\text{LiAlSi}_4\text{O}_{10}$) contained a new element whose binary and ternary compounds shared several similarities to that of sodium and potassium. In 1818, the German chemist Christian Gmelin reported that lithium salts gave a bright red color in a flame, however both Arfwedson and Gmelin failed to isolate lithium in its pure form. It was up until 1821 that William Thomas Brande succeeded to obtain lithium metal by electrolysis of lithium oxide. It took more than one century since the discovery of lithium element to the development of the first lithium battery [7].

The first battery using lithium metal as negative electrode was the lithium thionyl chloride battery. This kind of battery used lithium metal as the negative electrode and thionyl chloride (SOCl_2) as the positive electrode. The advantages of the Li- SOCl_2 system are the high energy density and its capacity to operate at temperatures as low as -55°C . However, this kind of batteries is highly toxic and cannot be recharged [8,9].

The development of LIB reached its golden state since the 1980s with the great contributions from the work of John Goodenough, Stanley Whittingham and Akira Yoshino, and these pioneering contributions were recognized by the Nobel Prize in 2019. In his pioneering work, Whittingham has demonstrated the possibility to intercalate and deintercalate Li^+ ions into/from the structure of TiS_2 in an “Li// TiS_2 ” electrochemical cell [10,11] and this was later considered as the first rechargeable lithium battery. The main problems with the “Li// TiS_2 ” electrochemical cell are the formation of Li dendrites upon long-term cycling and the low operating voltage of sulfide materials. Goodenough proposed to replace TiS_2 by LiCoO_2 , whose structure is similar to TiS_2 but the Li^+ intercalation/deintercalation occurs at higher potential as compared to TiS_2 , and this almost doubled the operating voltage of lithium batteries [12]. One of the greatest achievements of LIBs is the use of graphite as negative electrode and lithium ions as the charge carriers to construct a “rocking-chair” battery, which avoids the use of the lithium metal which is highly reactive and can promptly form lithium dendrites upon cycling that can trigger fire or explosion [13]. In 1991, Sony and Asahi Kasei released the first commercialized LIBs. Since then, the development and utilization of LIBs grew up rapidly, and now LIBs can be found in many portable devices, such as mobile phones and laptops. LIBs were also developed to be used in electric vehicles. Many car companies, such as Tesla, Nissan and Toyota, have developed their own electric cars using LIBs as the energy suppliers. In 2019, Nissan introduced the 62 kWh battery package using $\text{Li}_x(\text{Ni},\text{Co},\text{Mn})\text{O}_2$ layered oxide as positive electrode. These batteries can ensure a cruising distance of 458 km and the battery capacity warranty guarantees 160000 km or 8 years [14].

The structure and the operation principle of a LIB are summarized in **Figure 1.1**. A typical LIB is composed of two host networks served as negative and positive electrodes, respectively. The typical negative electrode material for LIB is graphite whereas a wide variety of materials can be used as positive electrode, such as layered oxides and polyanion (mostly phosphate-based) frameworks [15]. An organic electrolyte containing Li^+ salt in a mixture of carbonate organic solvents is usually used as a Li^+ conducting medium. During charge, the Li^+ ions are extracted from the host structure of the positive electrode in parallel to the oxidation of the transition metal ions. Due to the electric field generated by the external system, the Li^+ ions from the positive electrode migrate across the electrolyte and intercalate into the empty space between the graphene layers in graphite structure, which is concomitantly reduced. During the following

discharge, the battery returns to its equilibrium state involving the inverse reactions at both electrodes: The Li^+ ions are extracted from the negative electrode material which is oxidized, then move across the electrolyte and are reinserted into the host structure at the positive electrode which is now reduced.

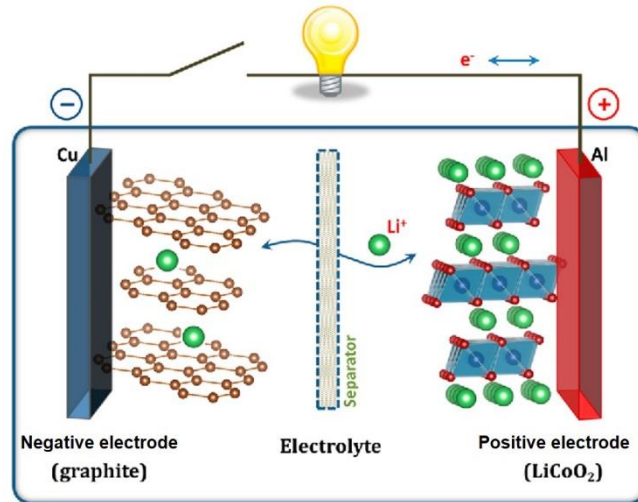


Figure 1.1 : Structure of a Lithium-ion battery (Adapted from [16]).

Even though LIBs have attracted great interest from the scientific community as well as from the growing market, several concerns have been raised about the sustainable development of LIBs in the future as the lithium content in the Earth's crust is rather low (30 ppm) and the lithium resources are not equally distributed all over the world. Several energy storage systems have recently been developed as possible alternatives to LIBs, but before entering into details into the description of these systems, some important definitions used in batteries field will first be given.

I.1.2. General definitions in batteries

Several definitions that are widely used in order to evaluate the performance of electrode materials and batteries:

❖ **Specific capacity** Q_m ($\text{mAh}\cdot\text{g}^{-1}$): corresponds to the amount of electric charges that can be stored/delivered per mass unit of the active material. It can be calculated from the following equation:

$$Q_m = \frac{x \cdot F}{3.6 \cdot M}$$

With x = The number of exchanged electrons

F = The Faraday's constant ($96500 \text{ C}\cdot\text{mol}^{-1}$)

M = The molar mass of the active material ($\text{g}\cdot\text{mol}^{-1}$)

❖ **Open circuit voltage (V)**, also called as **OCV** or **V_{OC}**, is the difference between the Fermi level energy (ΔE_F) of an electron locating in the $1s$ orbital of Lithium metal and another one in the anti-bonding “ nd^* ” states of the transition metal present in the positive electrode material.

$$F \cdot V_{OC} = -\Delta E_F = \mu_{\text{Negative electrode}} - \mu_{\text{Positive electrode}}$$

The Fermi level energy of the positive electrode material depends on the nature of the transition metal ion, its oxidation state as well as its surrounding ligands.

In Sodium-ion batteries, the V_{OC} value is calculated *versus* Sodium metal.

❖ **Electrochemical profile**: This is a plot of the V_{OC} value as a function of the chemical composition (x value) of the electrode materials, which is determined by the first derivative of the Gibbs free energy and obeys the variance rules:

$$V_{OC} = -\frac{1}{F} \left(\frac{dG(x)}{dx} \right) + constant$$

$$v = C + 2 - P$$

The variance, v , is the number of degrees of freedom of the system, C is the number of the components involved in the electrode reaction and P is the number of phases in equilibrium between them. In a $\text{Li}^+(\text{Na}^+)\text{-intercalation}$ or *deintercalation* reaction, the system is composed of two components (Li^+/Na^+ and the host structure) and P can be either 1 or 2 depending on the mechanism of the reaction: *monophasic* (solid solution) or *biphasic*. If the mechanism is *monophasic* ($P = 1$), the degree of freedom of the system is three. On the other hand, the degree of freedom for a *biphasic* reaction ($P = 2$) is two. Nevertheless, when a battery is cycled at ambient conditions (*e.g.* temperature and pressure are constant), two more degrees of freedom are removed from the system. Therefore, under cycling conditions there will be no degree of freedom for a *biphasic* system and the voltage remains unchanged during the alkali ion extraction and reinsertion. The voltage profile ($E = f(x)$) shows the presence of a “plateau” during the whole electrochemical reaction. For a solid solution reaction, the degree of freedom of the

system is one, and hence the voltage profile will evolve continuously during cycling and the $E = f(x)$ profile will be sloping (“S-shape” profile).

❖ **Energy density** ($\text{Wh}\cdot\text{kg}^{-1}$) : For a pure bi-phasic reaction, the energy density is the product between the open circuit voltage and the specific capacity ($E = V_{OC} \cdot Q_m$). In most of the cases, the voltage is not a constant during the overall alkali extraction (reinsertion) reaction and hence the energy density is calculated by the equation:

$$E (\text{Wh} \cdot \text{kg}^{-1}) = \int_{x_{min}}^{x_{max}} \frac{F \cdot V_{OC}(x)}{3.6 \cdot M} dx$$

The energy density value is independent of the time required to charge/discharge the batteries.

❖ **Cycling rate**: By convention, the cycling rate is denoted as C/n meaning that the full capacity is theoretically achieved within n hours. It can also be understood as the exchange of one electron will occur in n hours. For example, a $C/10$ cycling rate means that one Li^+/Na^+ ion is extracted/re-inserted in 10 hours.

❖ **Coulombic efficiency (CE)**, also called as **faradic efficiency** or **current efficiency**, is the ratio of the total charge extracted from the battery to the total charge input into the battery over a full cycle.

I.2. Sodium-ion batteries

I.2.1. General introduction

The booming of electric and hybrid vehicles’ market conjugated to the development of renewable energy technologies in recent years have generated a strong interest in alternative electrochemical energy storage technologies to LIBs, including Sodium-ion batteries (SIBs), potassium-ion batteries, and multivalent-ion batteries (Mg^{2+} , Ca^{2+} , Al^{3+}) [17–22]. Among them, SIBs are considered as the most promising one [23–25] with several battery companies and start-ups working on this technology, such as Natron, Faradion, HiNa and Tiamat [26–29].

Compared to LIBs, SIBs possess several advantages:

- Na resources are equally distributed over the Earth whereas Li resources can be found mainly in Bolivia (43%), Argentina (15%), Chile (24%) and China (17%). There is no big Li deposit in Europe. This unequal Li distribution in the Earth's crust raises the questions about the sustainable and stable development of LIBs.

- Na is a ubiquitous element in the Earth's crust, its abundancy being just behind O, Si, Al, Fe and Ca, which is not the case for Li. The Li concentration in the Earth's crust is just 30 ppm (33th element) which is far behind the concentration of Neodymium (50 ppm). Furthermore, Na precursors are the by-products of the chlorine industry, which ensures a constant supply and reduces the prices of Na precursors. In 2012, the price of Na₂CO₃ was 0.07 - 0.37 dollars·kg⁻¹ comparing to 4.11 - 4.49 dollars·kg⁻¹ for Li₂CO₃ [22].

- In SIBs, Al is used as the current collector for both positive and negative electrodes whereas Al and Cu are used as current collectors for positive and negative electrodes in LIBs, respectively (**Figure 1.2a**). Al cannot be used as the current collector for the negative electrode in LIBs as Li can form an alloy with Al at low voltage and thus destroy the current collector. As no Na-Al is formed at low voltage, Al can be used as current collector at both electrodes in SIBs leading to many advantages:

- ✚ The price of Al is much cheaper than Cu (2000 dollars·ton⁻¹ vs. 8000 dollars·ton⁻¹ in 2004) and thus using Al can reduce significantly the price of the final product.
- ✚ In a LIB, the weight of Cu and Al current collectors accounts for 11% and 5% of the total mass of the cell, respectively (**Figure 1.2b**). As Cu is much heavier than Al, preventing the use of Cu allows reducing the inactive mass in the cell.
- ✚ Thanks to the use of the same current collector for both electrodes, a sodium-ion battery can be discharged down to 0 V and the cell itself can be maintained at this voltage without an external current. The start-up company Faradion reported that SIBs can be stored at 0 V during six months without any capacity degradation. Furthermore, all the prototype cells can be stored and shipped when they are physically shorted meaning that there is no energy storage within the cell and thus prevent the risk of self-ignition or explosion [27].

The main drawback of SIBs is that the redox couple of Na⁺/Na is -2.70 V vs. NHE (Normal Hydrogen Electrode) compared to -3.03 V for Li⁺/Li, meaning that the operating voltage of SIBs would be lower than that of LIBs [30]. Furthermore, the ionic radius of

Na^+ is larger than that of Li^+ (102 ppm vs. 76 ppm) and in some cases the Na^+ diffusion in solid phase would be slower than Li^+ diffusion and thus would limit the cycling performance of SIBs, especially at high cycling rates. Despite these disadvantages, SIBs still find their place in stationary applications, such as grid energy storage, where high operating voltage and cycling rates are not the priorities. The purpose of this is to make a shift from centralized electricity provision system to decentralized one by coupling renewable energy, such as photovoltaic cells, with a grid energy storage system. Nowadays, there are several projects in Spain, such as Estabanell Energia, aiming at electricity provision for 50% of the rural area of the country by combining photovoltaic systems and grid storages. These combinations create the so-called ‘Smart rural grids’ or ‘Island operation’. These ‘islands’ are supposed to be independent in order to ensure a high speed, stable and equal energy provision [31].

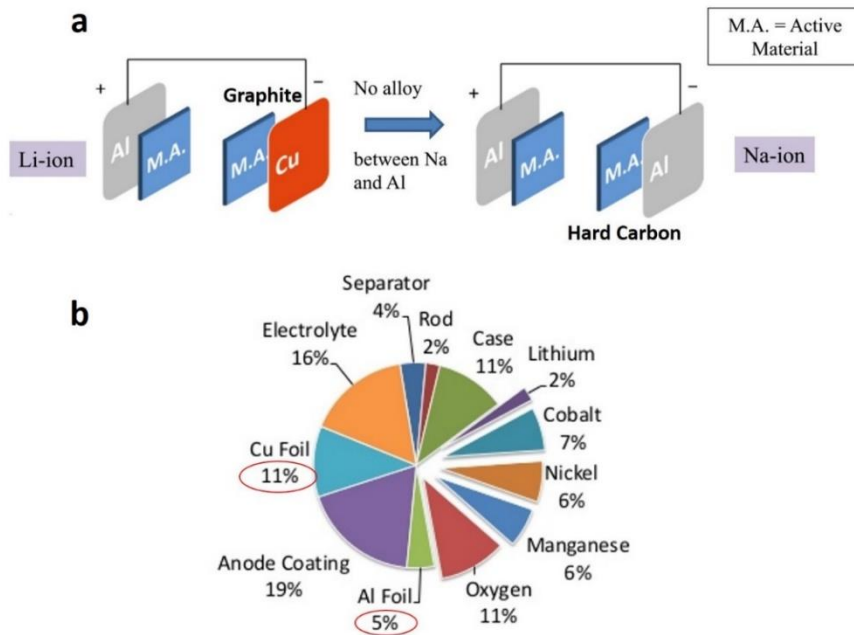


Figure 1.2 : (a) Schematic comparison between the structure of a lithium-ion battery and that of a sodium-ion battery, (b) Composition of a lithium-ion battery (by wt.%) [32].

These mentioned examples have shown the importance and promising applications of SIBs, but there are still several researches that need to be done in order to improve the performance of current SIBs, such as its operating voltage, its capacity, its cycling capability and its durability. This Ph.D work focuses on developing new positive electrode materials for SIBs based on $\text{Na}_3\text{V}_2(\text{PO}_4)_2\text{F}_3$ structural framework with an aim to improve its operating voltage and durability. Nonetheless, before entering into the details of this work, an overview on the structure of a typical SIB and the current development of $\text{Na}_3\text{V}_2(\text{PO}_4)_2\text{F}_3$ will first be given.

I.2.2. Negative electrodes for Sodium-ion batteries

The pre-requisites for a good negative electrode material are high reactivity at low potential, high capacity, reversibility to reaction with Na⁺ ions, fast reaction kinetics, safety, and low cost. Some of the typical negative electrodes for SIBs are:

- **Sodium metal:** With a redox couple value of -2.70 V vs. NHE and a theoretical capacity of 1166 mAh·g⁻¹, sodium metal is an ideal negative electrode for SIBs [33]. Nonetheless, the practical use of sodium metal in commercialized products has little interest at the moment as sodium metal is too reactive and it has a high tendency to form metal dendrites upon cycling which might short-circuit the battery and trigger the self-ignition. Several on-going research efforts aim at developing solid-state electrolytes which might suppress the formation of sodium dendrites upon cycling and promote the use of sodium metal in the prototyped products. Even though sodium metal is currently not used in commercialized batteries, it still holds an important role in fundamental battery testing. A newly discovered negative/positive electrode material is usually cycled versus sodium metal in order to determine its cycling performance. A battery using sodium metal as negative electrode is widely called as a ‘*half-cell*’.

- **Graphite** is a typical negative electrode material for LIBs with reversible Li⁺ insertion/extraction processes, nonetheless, it cannot be used in SIBs as Na⁺ cannot be inserted into the graphite structure even in a chemical way. Na⁺ ions solvated by diglyme (or bis(2-methoxyethyl) ether) can be inserted into the graphite structure according to the following reaction: $C_{20} + 2Na(G2)^+ \rightarrow [Na(G2)]_2C_{20}$ [34,35]. Even though the reaction is reversible, this cannot be used in practice due to the low capacity of the reaction.

- **Hard carbon:** Although Na⁺ ion cannot be intercalated into graphite, it can be inserted and extracted reversibly into hard carbon. Hard carbon is an amorphous material with a non-graphitized structure composed of cross-linking C *sp*³. This material is prepared by the pyrolysis of solid organic precursors, such as celluloses or resins. The Na⁺ storage in this structure involves: (i) The intercalation of Na⁺ ions into the voids of the structure, and (ii) the ion adsorption into the micro-pores. Therefore, the microstructure of hard carbon has an important impact on the practical capacity of this material. The microstructure can be controlled by varying the temperature of the pyrolysis

and the precursor sources. The experimental results revealed that by increasing the temperature, the pore size increases while the number of pores diminishes, as characterized by Small-angle X-ray Scattering (SAXS) [36–39]. Hard carbon is now commonly used in all the commercialized SIBs and an assembled battery using hard carbon as negative electrode is called as a ‘*full-cell*’.

I.2.3. Electrolytes for Sodium-ion batteries

The electrolyte is a non-active material, but it affects the performance of the cell at the beginning of the cell life-time and even when the end of the cell life-time is reached. The most common electrolytes for batteries are liquid and organic-based electrolytes. Usually, a ‘functional electrolyte’ composed of salt(s), solvent(s), and additive(s), is used in batteries. In order to ensure good operation conditions in batteries, an electrolyte must possess high Na⁺ conductivity ($> 1 \text{ mS}\cdot\text{cm}^{-1}$) with no electronic conductivity, high chemical and electrochemical stability, and non-flammability. All of the electrolytes are, in fact, meta-stable due to the high reactivity of the negative electrode material and the solid-electrolyte interface (SEI) formation process. The SEI formation in one way is negative to the performance of the batteries as it results in non-electroactive materials with an irreversible capacity loss in the first few cycles. On the other hand, this SEI formation passivates the negative electrode’s surface and thus prevents it from further attacks by the electrolyte. In LIBs, a typical SEI layer can reach a thickness of 25-30 nm. Normally, the SEI formation in batteries can be engineered by the use of some additives which can promptly react with the negative electrode and then prevent the direct reaction between the negative electrode and electrolyte. A thin layer of decomposed products can also be formed at the positive electrode/electrolyte interface via an oxidation process when the applied potential exceeds 4.5 V. In the case of positive electrode, the passivation layer is called ‘Surface Layer’ (SL) or ‘Solid Permeable Interphase’ (SPI) instead of SEI. The SPI is generally much thinner than the SEI [40–42].

Thanks to the similarities between SIBs and LIBs technologies, the acquired knowledge in the field of LIBs can be transferred to develop new generation of electrolytes for SIBs. Nevertheless, here are some important points in terms of electrolyte that make SIBs superior to LIBs: (i) The Na-containing salts used in SIBs electrolyte are much cheaper than their Li counterpart due to the low of price of Na precursors used in

the synthesis, (ii) Na-salts are less hygroscopic than Li-salts, which makes the purification process much simpler in order to obtain the battery grade products, (iii) the negative electrode material for SIBs is not based on graphite; hence, the use of propylene carbonate (PC), which is inexpensive, as a solvent for the electrolyte can be considered. Some other considerations should also be taken into account in order to develop new electrolytes for SIBs: (i) the electrochemical window of SIBs is moved up 330 mV compared to LIBs; hence, the potential of the SEI-forming additives must be shifted, (ii) unlike LIBs, the SEI layer in SIBs contains mainly inorganic compounds (Na_2CO_3 , NaF, ...) and they are soluble in the electrolyte, which makes the SEI formation occurs continuously during the cycling process. It has been reported that 2-fluoroethylene carbonate (FEC) is an ideal additive for SIBs as it can form stable SEI with negative electrodes and hence stabilize the cycling capacity. Nevertheless, a recent study shows that FEC in fact induces the formation of a stable but resistive SEI, and the use of FEC thus appears only beneficial in electrolytes with a poor tendency of SEI formation [43–46].

Besides the conventional liquid electrolytes, solid-state electrolytes, gel and/or polymer electrolytes are also developed as possible alternatives [47–49].

I.2.4. Positive electrodes for Sodium-ion batteries

The positive electrode is the one where Na^+ ions are extracted during charge and inserted during discharge. The requisites for a good positive electrode material are high reactivity at high potential, high capacity, reversible to Na^+ reaction, long-term cycling, fast reaction kinetics, safe, and low cost. Several compounds have been intensively studied as prospective positive electrode materials for SIBs. Depending on their composition and crystal structure, they are commonly classified into layered oxides, polyanionic based (mostly phosphates), Prussian blue analogues, and organic compounds [30].

I.2.4.1. Layered transition metal oxides

Layered transition metal oxide materials are probably the most appealing ones thanks to their high theoretical capacity and high ionic mobility, with three possible structures (P2, P3 and O3- Na_xMO_2 as defined by Delmas *et al.* [50]) and a great diversity of compositions in transition metal ions. The layered oxides structure is constructed by

always followed by an index indicating the number of repeating MO_2 slabs required to form a unit cell, such as O2, O3 and P2 (**Figure 1.3**). The absolute structure of the Na_xMO_2 composition depends on the Na^+ -content and the nature of the metal ion(s) present in the phase.

In the field of LIBs, the chemistry of Li_xMO_2 is diverse and is intensively explored. For a certain Li_xMO_2 compound, there always exists the Na^+ -containing counterpart, *e.g.* LiCoO_2 *vs.* NaCoO_2 , which can be obtained by direct synthesis or through an ion exchange approach. The main difference between the Li^+ and its Na^+ -containing counterparts is their ion stacking sequence. The Li^+ ion has small ionic radius with a weak screening effect, and thus all the Li_xMO_2 phases always adopt ‘O’-type structures in order to minimize the interslab $\text{O}^{2-}\cdots\text{O}^{2-}$ electrostatic repulsion. On the other hand, Na^+ has a bigger ionic radius with a stronger screening effect which can minimize the interslab $\text{O}^{2-}\cdots\text{O}^{2-}$ repulsion and stabilize the ‘P’-type structures. In Na_xMO_2 , the existence of the ‘O’- and ‘P’-type structures are possible, and the energetically favored structure is determined by the compromise between the interslab $\text{O}^{2-}\cdots\text{O}^{2-}$ repulsion and the intraslab $\text{Na}^+\cdots\text{Na}^+$ repulsion. Furthermore, the Na^+ ion has a bigger size with a greater number of electrons and hence the $\text{Na}^+\cdots\text{Na}^+$ electrostatic repulsion is an important factor determining the stability and the structure of the deintercalated phases. In Na_xMO_2 , several intermediate phases are formed upon cycling as a consequence of the Na^+ /vacancy ordering whereas in their Li_xMO_2 counterparts, the Li^+ -vacancy ordering is thermodynamically unstable and can only be observed in some specific cycling conditions [52–54]. The electrochemical profile of Na_xMO_2 materials is characterized by the presence of several composition-voltage ‘plateaus’ as a result of the Na^+ -vacancy ordering. Some of the promising layered oxides positive electrode materials are $\text{Na}[\text{Ni}_{1/3}\text{Mn}_{1/3}\text{Co}_{1/3}]\text{O}_2$, $\text{Na}_{2/3}[\text{Ni}_{1/3}\text{Mn}_{2/3}]\text{O}_2$ [55,56] and $\text{Na}[\text{Ni}_{2/3}\text{Sb}_{1/3}]\text{O}_2$ [57–59].

In the ‘classical’ layered oxides, the redox center is a “light” transition metal ion, but in some recent studies focusing on the electrochemistry of Na-rich Na_xMO_2 compositions of *4d* and *5d* transition metal ions, such as $\text{Na}[\text{Na}_{1/3}\text{Ru}_{1/2}\text{Sn}_{1/6}]\text{O}_2$ and $\text{Na}[\text{Na}_{1/3}\text{Ru}_{2/3}]\text{O}_2$ (**Figure 1.4**), the electrochemical activity of O^{2-} has been reported [60–62]. These are interesting fundamental studies in the field of solid-state chemistry as they reported that in some specific cases O^{2-} can be oxidized before or at the same time with

M^{n+} and result in a shortening in the O–O distances. Nonetheless, these studies will hardly find any practical applications as (i) the presence of Ru or Ir in these phases increases significantly the price of the products and (ii) the generation of O_2 in the first cycle modifies significantly the surface of the particles, and induces great capacity loss and important hysteresis on the cycling profile [63–66].

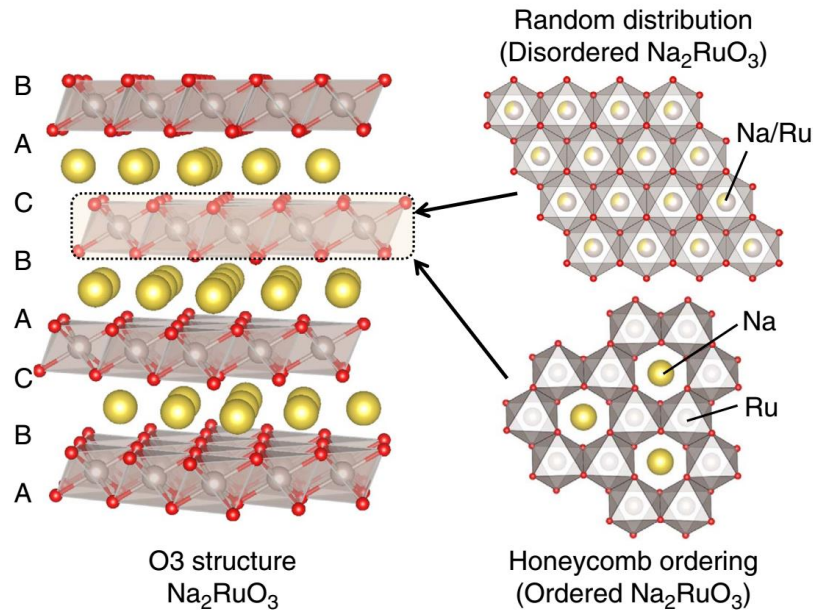


Figure 1.4 : O3 structure of the ordered and disordered Na_2RuO_3 (Adapted from [61]).

These layered oxides can provide high specific capacity and can support high-rate cycling [67], nonetheless, most of them are unstable against moisture as water molecules can penetrate into the empty space between the MO_2 slabs and thus trigger decomposition or irreversible capacity upon cycling. Some recent studies have shown that the presence of Cu-substituent can enhance the stability of the phase, no decomposition or irreversible capacity was detected even though the phase was soaked in water over a long period [68–71]. Another disadvantage of layered oxide materials is that a high cutoff voltage is usually required to achieve a sufficient capacity. Furthermore, the Na/M ratio is usually less than 2/3 for some of the layered oxides, which is a penalizing factor for the capacity of these materials. Last but not least, not all the Na^+ ions present in these layered oxides can participate in the electrochemical reaction as a high deintercalation ratio will lead to a collapse of the structure, or an irreversible structural transformation with a high polarization/hysteresis value [72].

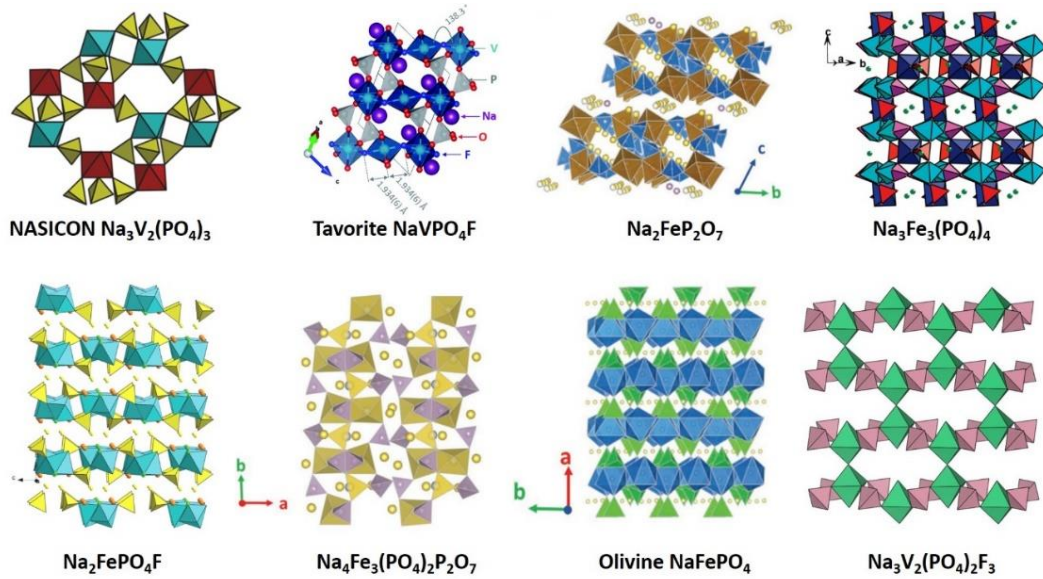


Figure 1.6 : Illustration of the structural frameworks of the main families of polyanionic materials studied as positive electrodes for Na-ion batteries (Figures adapted from [73–85]).

One of the most essential properties of polyanionic materials is the inductive effect, meaning that for a given structural framework, the redox potential of the phase can be tailored easily by changing the nature of the transition metal ions, by changing the anions constituting the network, or just by varying the crystal structure. This concept was first introduced by Manthiram and Goodenough in order to qualitatively illustrate the impact of the nature of the tetrahedral XO_4 groups on the position of the Fe^{3+}/Fe^{2+} redox couple in different $Li_xFe_2(XO_4)_3$ compositions and this was later extended to other Li^+ and Na^+ -containing polyanionic materials [86–88].

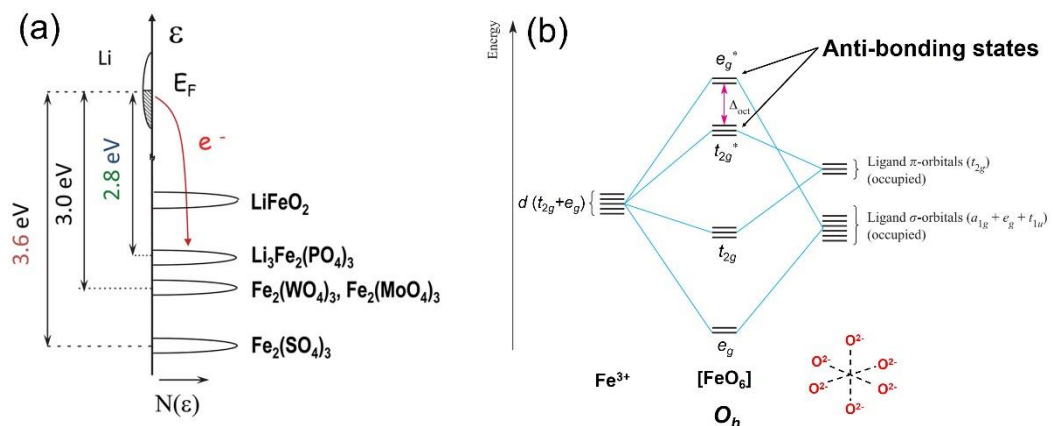


Figure 1.7 : (a) Respective positions of the Fe^{3+}/Fe^{2+} redox couple vs. Li^+/Li in NASICON $A_xFe_2(XO_4)_3$ compositions ($X = P, Mo, W, S$); (b) Molecular diagram illustrates the interaction between $3d$ orbitals in Fe^{3+} and the surrounding O^{2-} ligands. This diagram can further be used to construct the band diagram in $A_xFe_2(XO_4)_3$ compositions. The position of the Fermi level in $A_xFe_2(XO_4)_3$ compositions is determined by the energy of the bands resulted from the interaction of e_g^* or t_{2g}^* levels in extended structures (Adapted from [77,89]).

In $\text{Li}_x\text{Fe}_2(\text{XO}_4)_3$ compositions, the respective position of the $\text{Fe}^{3+}/\text{Fe}^{2+}$ redox couple vs. Li^+/Li is the difference in the energy between the Fermi level of Li metal ($E_F(\text{Li})$) and the “anti-bonding” states in $\text{Li}_x\text{Fe}_2(\text{XO}_4)_3$ ($E_F(\text{Li}_x\text{Fe}_2(\text{PO}_4)_3)$), and these “anti-bonding” states are the results of the interaction between the “ e_g ” states of Fe^{3+} and the “bonding” states of the six surrounding O^{2-} ligands. If the $\text{Fe}^{3+}-\text{O}^{2-}$ bond is more covalent, the resulted “anti-bonding” states will have higher energy and the difference between $E_F(\text{Li})$ and $E_F(\text{Li}_x\text{Fe}_2(\text{PO}_4)_3)$ will be smaller. If the interaction between Fe^{3+} and O^{2-} is more ionic, interaction between the “ e_g ” states of Fe^{3+} and the “bonding” states of O^{2-} ligands is weak, and the energy of these “anti-bonding” states will be less elevated. In this case, the difference between $E_F(\text{Li})$ and $E_F(\text{Li}_x\text{Fe}_2(\text{PO}_4)_3)$ will be greater and the $\text{Fe}^{3+}/\text{Fe}^{2+}$ redox couple will give rise to a higher voltage value. In $\text{Li}_x\text{Fe}_2(\text{XO}_4)_3$, there exist the $\text{Fe}^{3+}-\text{O}-\text{X}$ bond chains and the oxygen ions participate in the chemical bonds with the neighboring X and Fe^{3+} . If the X element possesses a high electronegativity or a high formal charge value, the $\text{O}-\text{X}$ will be more covalent and thus the $\text{Fe}^{3+}-\text{O}$ bond will be more ionic. As a consequence, the $\text{Fe}^{3+}/\text{Fe}^{2+}$ redox couple will have a higher voltage value when X has a high electronegativity and/or a high formal charge value. For instance, the $\text{Fe}^{3+}/\text{Fe}^{2+}$ redox couple (vs. Li^+/Li) varies from ~ 2.8 V for $\text{Li}_3\text{Fe}_2(\text{PO}_4)_3$ [90–92], to 3.0 V for $\text{Fe}_2(\text{MoO}_4)_3$ and $\text{Fe}_2(\text{WO}_4)_3$ [86,93,94], and to 3.6 V for $\text{Fe}_2(\text{SO}_4)_3$ [88,95] when X is replaced by P^{+5} , Mo^{+6} or W^{+6} , and S^{+6} , respectively (Figure 1.7a).

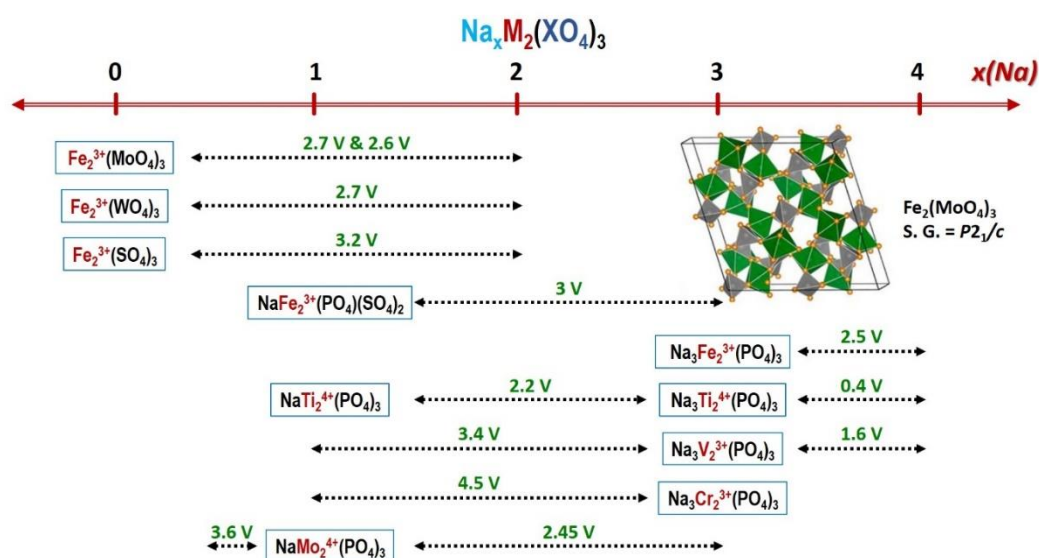


Figure 1.8 : Accessible compositions and the corresponding voltages of the $\text{M}^{n+}/\text{M}^{(n-1)+}$ redox couples (vs. Na^+/Na) involved during Na^+ intercalation and deintercalation in/from NASICON or anti-NASICON $\text{Na}_x\text{M}_2(\text{XO}_4)_3$ structures.

The inductive effect was also observed for Na-containing compounds: isostructural $\text{Na}_3\text{Fe}_2(\text{PO}_4)_3$ and $\text{Fe}_2(\text{SO}_4)_3$ exhibit operating voltages that differ by 0.7 V upon Na^+ intercalation, the latter being lower than the former [96,97]. This inductive effect is illustrated in **Figure 1.8** through the examples of $\text{Na}_x\text{M}_2(\text{XO}_4)_3$ compositions. Furthermore, by monitoring the nature of transition metal ions and anions in the framework, one can tailor the Na^+ -content and thus number of reversible Na^+ ions participating in the electrochemical reaction.

I.2.5. $\text{Na}_3\text{V}_2(\text{PO}_4)_2\text{F}_3$ and related materials as positive electrodes for SIBs

Some of the promising polyanionic materials are the olivine NaFePO_4 , the family of fluorinated oxyphosphates $\text{Na}_3\text{V}_2(\text{PO}_4)_2\text{F}_3$ - $\text{Na}_3(\text{VO})_2(\text{PO}_4)_2\text{F}$, $\text{Na}_2\text{FePO}_4\text{F}$, and the NASICON-related materials including $\text{Na}_3\text{V}_2(\text{PO}_4)_3$ and $\text{Na}_4\text{VMn}(\text{PO}_4)_3$ [75,76,98–104]. Among them, $\text{Na}_3\text{V}_2(\text{PO}_4)_2\text{F}_3$ is the most promising one as it exhibits two reversible Na^+ -extraction processes at relatively high voltage, and high stability upon long-term electrochemical cycling. The crystal structure of $\text{Na}_3\text{V}_2(\text{PO}_4)_2\text{F}_3$ was first determined by Le Meins *et al.* [82] and was later revisited in the work of Bianchini *et al.* [83] by the use of high resolution synchrotron X-ray powder diffraction (SXRD). Despite its well-established crystal structure, $\text{Na}_3\text{V}_2(\text{PO}_4)_2\text{F}_3$ is often confused with ‘ NaVPO_4F ’ and $\text{Na}_3\text{V}_2(\text{PO}_4)_3$.

I.2.5.1. ‘ NaVPO_4F ’

The composition NaVPO_4F first appeared in the work of Barker *et al.* [105]. The authors reported that this novel phase could be obtained by a direct reaction at high temperature between VPO_4 and NaF in the molar ratio 1/1. The crystal structure of the as-obtained ‘ NaVPO_4F ’ was indexed in the $I4/mmm$ space group with $a = b = 6.387(2)$ Å and $c = 10.374(3)$ Å, which was an iso-structure to $\alpha\text{-Na}_3\text{Al}_2(\text{PO}_4)_2\text{F}_3$! The powder was then cycled against a lithium counter electrode in order to generate a new hybrid Li^+/Na^+ -containing compound with the alkali-ion extraction voltage at 3.85 and 4.39 V vs. Li^+/Li . Many later works reported that one Na^+ could be cycled reversibly in a $\text{Na}/\text{‘NaVPO}_4\text{F’}$ half-cell with a Na^+ -extraction voltage at 3.60 vs. Na^+/Na . It is interesting to note that in

all the electrochemical tests reported for ‘NaVPO₄F’, the upper cutoff voltage rarely exceeded 4.0 V vs. Na⁺/Na. In another work, Zhuo and co-workers proposed the formation of monoclinic ‘NaVPO₄F’ indexed in the *C*₂/*c* space group when the structure was doped with chromium [106]. They also claimed that the as-obtained structure was similar to that of α -Na₃Al₂(PO₄)₂F₃, but the absolute crystal structure of ‘NaVPO₄F’ in *I*4/*mmm* or *C*₂/*c* space group has never been reported in the literature. The only thing that one can know about the crystal structure of this material is a vague conclusion of ‘an iso-structure of α -Na₃Al₂(PO₄)₂F₃’ [106–109]. By an in-depth combination between *operando* XRD at high temperature and thermo-gravimetric analysis, Li and co-authors discovered that the *I*4/*mmm* or *C*₂/*c* ‘NaVPO₄F’ was in fact mixture between Na₃V₂(PO₄)₂F₃, Na₃V₂(PO₄)₃, and unreacted VPO₄ [110].

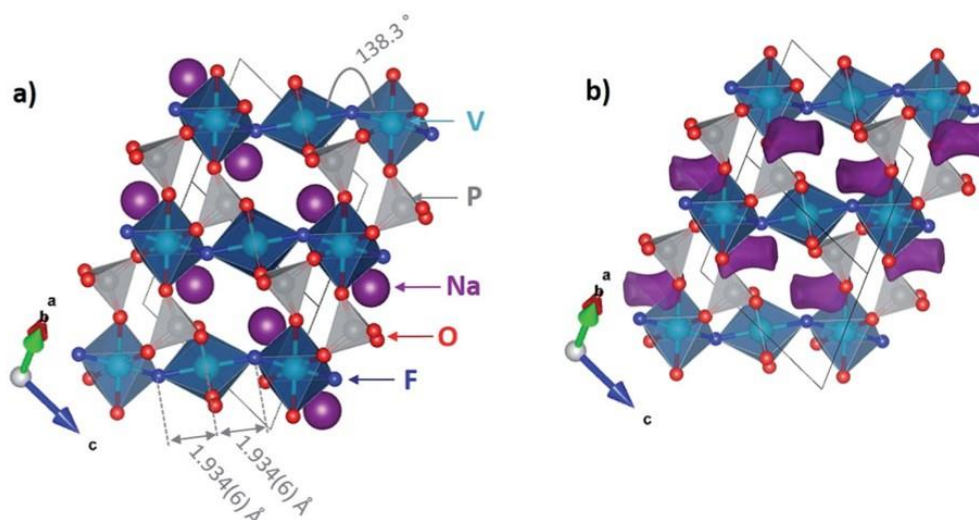


Figure 1.9 : (a) Crystal structure of Tavorite NaVPO₄F. VO₄F₂ octahedra are in dark blue, PO₄ tetrahedra are in grey and Na ions are shown as purple balls, (b) Sodium diffusion pathway calculated thanks to bond valence energy landscape with an energy of 1.6 eV (Adapted from [111]).

Boivin and co-workers have recently reported on the synthesis of monoclinic NaVPO₄F crystallizing in the *C*₂/*c* space group by a hydrothermal approach [111]. The material adopts the Tavorite-structure, which is constructed by infinite [VO₄F₂]_∞ chains running along the [101] direction and joined together by PO₄ groups (**Figure 1.9**). This structure is completely different from that of α -Na₃Al₂(PO₄)₂F₃. The Tavorite NaVPO₄F has no electrochemical interest as only 0.1 Na⁺ can be extracted even at the cycling rate of C/50 [111]!

I.2.5.2. $\text{Na}_3\text{V}_2(\text{PO}_4)_3$

$\text{Na}_3\text{V}_2(\text{PO}_4)_3$ belongs to the NASICON material family whose structure is constructed by ‘lantern units’ made of two VO_6 octahedra joined together by three PO_4 groups with the Na^+ ions occupying the empty space in the structure, thus forming two different crystallographic sites, labelled as Na(1) and Na(2) (**Figure 1.10**) [112]. Depending on the temperature, Na^+ -vacancy ordering can occur and $\text{Na}_3\text{V}_2(\text{PO}_4)_3$ can adopt rhombohedral ($R\bar{3}c$) or monoclinic structure ($C2/c$) with or without an incommensurate vector [74].

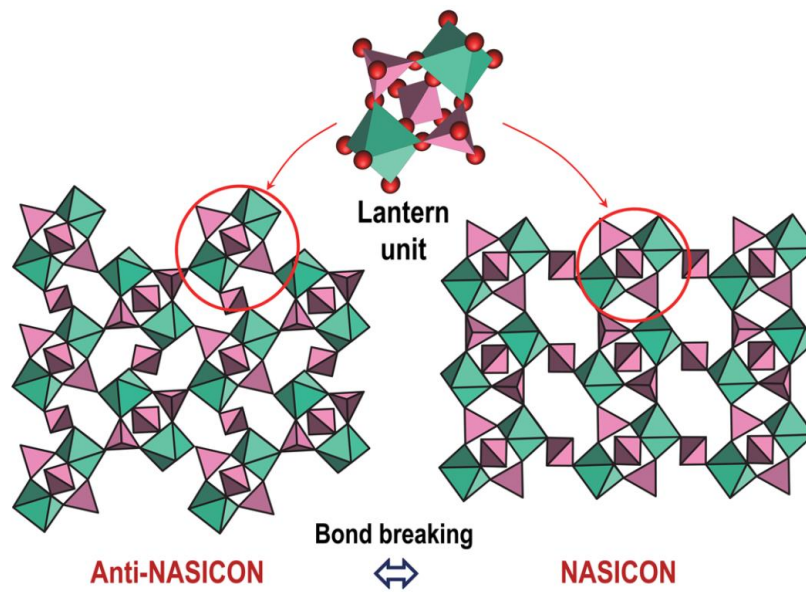


Figure 1.10 : The lantern units and its organization in the three-dimensional space to generate the NASICON and anti-NASICON structures (Adapted from [77]).

$\text{Na}_3\text{V}_2(\text{PO}_4)_3$ is a versatile material which can be used as both negative and positive electrodes for SIBs. At low voltage (~ 1.68 V vs. Na^+/Na), V^{3+} in $\text{Na}_3\text{V}_2(\text{PO}_4)_3$ is reduced into V^{2+} by the insertion of one Na^+ ion per formula unit, thus giving the material a theoretical capacity of $58.8 \text{ mAh}\cdot\text{g}^{-1}$ [113]. In the high voltage region, $\text{Na}_3\text{V}_2(\text{PO}_4)_3$ is a promising positive electrode material for SIBs with two Na^+ ions that can be reversibly extracted/inserted from/into the structure at 3.39 V vs. Na^+/Na according to a biphasic reaction [113–116]. The extraction of the third Na^+ is a priori feasible by chemical means to form $\text{V}_2(\text{PO}_4)_3$ [73] but an electrochemical formation of $\text{V}_2(\text{PO}_4)_3$ has never been reported. One of the most interesting properties of $\text{Na}_3\text{V}_2(\text{PO}_4)_3$ is that the structure can accommodate different kinds of cationic substitutions, such as Fe^{3+} , Ni^{2+} , Mn^{2+} , Ti^{4+} , or Al^{3+} , and this can be employed to modulate the number of reversible Na^+ ions

participating in an electrochemical reaction as well as the Na⁺-extraction voltages [102–104,113,117]. Among them, two interesting compositions are Na₃V_{1.5}Al_{0.5}(PO₄)₃ and Na₄VMn(PO₄)₃. In Na₃V_{1.5}Al_{0.5}(PO₄)₃, 0.5 V⁴⁺ can be oxidized into V⁵⁺ at the end of the end of charge (~ 4.0 V vs. Na⁺/Na) and the presence of the light-weight element, Al, can help to improve the theoretical gravimetric capacity of the phase [113]. In Na₄V³⁺Mn²⁺(PO₄)₃, three Na⁺ ions can be extracted during charge and thus yielding a high gravimetric capacity of 156 mAh·g⁻¹. The Na⁺ removal from Na₄VMn(PO₄)₃ leads to the oxidation of V³⁺ to V⁴⁺ (3.34 V vs. Na⁺/Na), Mn²⁺ to Mn³⁺ (3.58 V) and finally V⁴⁺ to V⁵⁺ (3.86 V). The extraction of the first two Na⁺ ions are highly reversible; however, when a high cutoff value is applied to promote the extraction of the third Na⁺ ion, a huge polarization together with great capacity loss is observed in discharge. Furthermore, the electrochemical profile of the phase was completely modified after the removal of three Na⁺ ions. The reason for the irreversible phase transformation at the high voltage is still now unsolved [102,104].

I.2.5.3. Na₃V₂(PO₄)₂F₃

In 1999, Le Meins *et al.* discovered a family of compounds with the general chemical formula Na₃M₂(PO₄)₂F₃ where M can be V³⁺, Ga³⁺, Al³⁺, Fe³⁺ or Cr³⁺ [82]. In the structure of Na₃V₂(PO₄)₂F₃, each V³⁺ is coordinated by four oxygen atoms in the equatorial plane and two fluorine atoms on the axial positions. Two VO₄F₂ octahedra share one common fluorine vertex to form a bioctahedral unit V₂O₈F₃, F–VO₄–F–VO₄–F (**Figure 1.11a**). These bioctahedral units are connected by PO₄ groups to generate a 3D network (**Figure 1.11a**). The Na⁺ ions occupy and can only diffuse in the channels located at $z = 0$ and $z = \frac{1}{2}$. Furthermore, there is no ion cross-over between two planes localized at different coordinates along the z -axis, indicating that Na₃V₂(PO₄)₂F₃ and all isostructural materials are 2D ionic conductors [118]. The Na⁺ ions distribution depends strongly on the nature of the M metal as well as on the temperature.

At ambient temperature, Na₃V₂(PO₄)₂F₃ was described to crystallize in the tetragonal $P4_2/mnm$ space group with $a = b = 9.047(2)$ Å and $c = 10.705(2)$ Å. The Na⁺ ions are distributed on two different crystallographic sites: the Na(1) site is fully occupied while the Na(2) site is half occupied (**Figure 1.11b**) [82]. Recently, using high resolution

synchrotron X-ray diffraction Bianchini *et al.* revealed an obvious systematic splitting of the (200)/(020) and (400)/(040) diffraction lines (**Figure 1.11c**) for stoichiometric $\text{Na}_3\text{V}_2(\text{PO}_4)_2\text{F}_3$ and thus described the crystal structure using a subtle orthorhombic distortion ($a \neq b$, $b/a = 1.002$) in the space group $Amam$ [83]. This distortion is correlated with the distribution of the Na^+ ions over three different crystallographic sites: Na(1) is fully occupied while Na(2) and Na(3) are partially occupied (**Figure 1.11d**). This subtle orthorhombic distortion and the triangular distribution of Na^+ ions in $\text{Na}_3\text{V}_2(\text{PO}_4)_2\text{F}_3$ allow to minimize the $\text{Na}^+\cdots\text{Na}^+$ electrostatic repulsions, as later on confirmed by the theoretical work of Dacek *et al.* [119].

Upon heating up to 127°C , an order - disorder phase transition occurs. The structure of $\text{Na}_3\text{V}_2(\text{PO}_4)_2\text{F}_3$ above this temperature was then described in the tetragonal $I4/mmm$ space group to take into account the circle-like distribution of the Na^+ ions around the fluorine atoms localized at the extrema of the bioctahedral units $\text{V}_2\text{O}_8\text{F}_3$. The observation of the ‘cationic rings’ reveals the increased mobility of the alkali ions at high temperature [83].

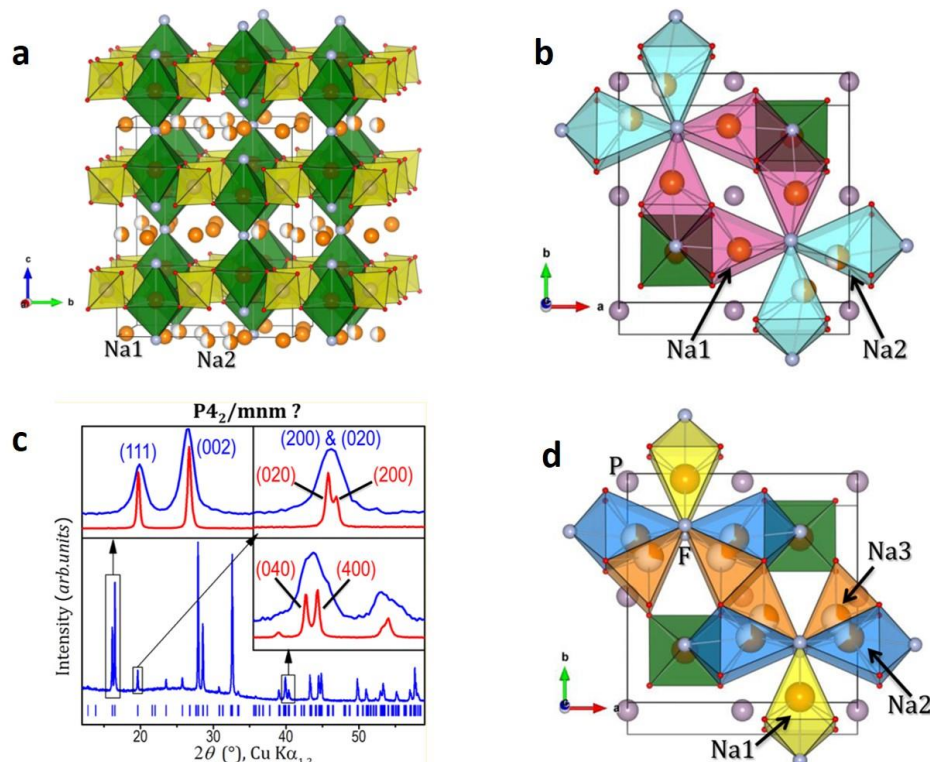


Figure 1.11 : (a) Structural framework of $\text{Na}_3\text{M}_2(\text{PO}_4)_2\text{F}_3$; (b) Distribution of the Na^+ ions in the crystallographic plane localized at $z = 0$ in $\text{Na}_3\text{V}_2(\text{PO}_4)_2\text{F}_3$ as proposed by Le Meins *et al.* (Adapted from [82]); (c) Comparison of the XRD patterns recorded for $\text{Na}_3\text{V}_2(\text{PO}_4)_2\text{F}_3$ using a laboratory $\text{Cu } K\alpha_{1,2}$ diffractometer (Blue) and the high resolution synchrotron X-ray radiation at $\lambda = 0.6687 \text{ \AA}$ (Red); (d) Distribution of the Na^+ ions in the crystallographic plane localized at $z = 0$ in $\text{Na}_3\text{V}_2(\text{PO}_4)_2\text{F}_3$ as proposed by Bianchini *et al.* (Adapted from [83]).

In recent years, $\text{Na}_3\text{V}_2(\text{PO}_4)_2\text{F}_3$ was intensively investigated in particular through cationic and/or anionic substitution in order to tailor the redox potential, the diffusion properties and thus the electrochemical performance. Depending on the nature of the substitution, different goals could be targeted:

✚ **Exchange of the mobile ion:** the great size of the cavities within the crystal structure, together with the high ionic mobility of Na^+ ions making $\text{Na}_3\text{V}_2(\text{PO}_4)_2\text{F}_3$ a good ionic conductor. The Na^+ ions can be replaced easily by other alkali ions, either by a chemical or by an electrochemical ionic exchange reaction. The ionic exchange has been reported for Li^+ , K^+ and Ag^+ [107,120–125], and the obtained compositions can (or could) be used as positive electrode materials in Li^+ , K^+ and Ag^+ -ion batteries, respectively. In $\text{K}_3\text{V}_2(\text{PO}_4)_2\text{F}_3$ and $\text{Ag}_3\text{V}_2(\text{PO}_4)_2\text{F}_3$, the K^+ and Ag^+ ions simply replace the Na^+ ions in the same crystallographic sites of the 3D structural framework and the resulting materials can also be described in the *Amam* space group [125,126].

✚ **Modulation of the redox potential (and thus the number of Na^+ ions reversibly exchanged through ionic substitution):** $\text{Na}_3\text{V}_2(\text{PO}_4)_2\text{F}_3$ contains V^{3+} , which can be oxidized into V^{4+} upon Na^+ extraction, and the electrochemical potential depends on the redox value of the $\text{V}^{3+}/\text{V}^{4+}$ redox couple. The V^{3+} ions can be fully or partially substituted by V^{4+} , Al^{3+} and Ga^{3+} [99,101,127,128]. This cationic substitution modifies the crystal structure and electronic structures, and thus its redox potential and possibly the number of Na^+ ions to be extracted. The other alternative to tailor the redox potential is to employ the polarization effect induced by the anions belonging to the bioctahedral units $\text{V}_2\text{O}_8\text{F}_3$. In $\text{Na}_3\text{V}_2(\text{PO}_4)_2\text{F}_3$, the six oxygen and fluorine ligands in the first coordination sphere of vanadium polarize the energy of the occupied state of V^{3+} and influence the redox potential of the material. By the use of density functional theory (DFT), Xu *et al.* predicted that the terminal fluorine anions could be substituted by oxygen or by other halogen elements, such as chlorine and bromine [129]. Depending on the nature of the substituent, the redox potential of the $\text{V}^{3+}/\text{V}^{4+}$ redox couple in $\text{Na}_3\text{V}_2(\text{PO}_4)_2\text{F}_3$ is lowered when the terminal fluorine is replaced by chlorine or bromine.

Barker *et al.* were the first to propose the use of $\text{Na}_3\text{V}_2(\text{PO}_4)_2\text{F}_3$ as a positive electrode material in rechargeable Li-ion batteries [120]. The first electrochemical signature of a graphite // 1 M LiPF_6 in EC/ DMC (2/1 by weight) // $\text{Na}_3\text{V}_2(\text{PO}_4)_2\text{F}_3$ was reported. Two alkali ions were extracted and reinserted reversibly into the structure of $\text{Na}_3\text{V}_2(\text{PO}_4)_2\text{F}_3$ at 3.88 and

4.43 V vs. Li^+/Li and the full cell showed a very limited capacity fading after 40 cycles performed at a rate of $2C$ [120]. Similar full cells were cycled in a larger potential window, with a cutoff voltage of 5.0 V vs. Li^+/Li , in order to extract the third Na^+ ion. A capacity corresponding to the extraction of three Na^+ ions could be observed in charge, but only two alkali ions could be reinserted on discharge [121]. It was speculated that only a fraction of the third Na^+ could be cycled reversibly. The X-ray diffraction analysis performed *ex situ* on the fully charged sample recovered at 5.0 V revealed that “the full extraction of sodium ion from the $\text{Na}_3\text{V}_2(\text{PO}_4)_2\text{F}_3$ material induced some irreversible structural degradation” [121].

With the recent emergence of SIBs, the use of $\text{Na}_3\text{V}_2(\text{PO}_4)_2\text{F}_3$ as positive electrode materials was reported by several groups [99,130]. The charge-discharge profile obtained for $\text{Na}_3\text{V}_2(\text{PO}_4)_2\text{F}_3$ vs. Na metal in a Na^+ containing organic electrolyte is characterized by two electrochemical voltage domains corresponding to the reversible extraction of two Na^+ ions at 3.70 and 4.20 V vs. Na^+/Na (**Figure 1.12b**) resulting in a reversible capacity of $125 \text{ mAh}\cdot\text{g}^{-1}$.

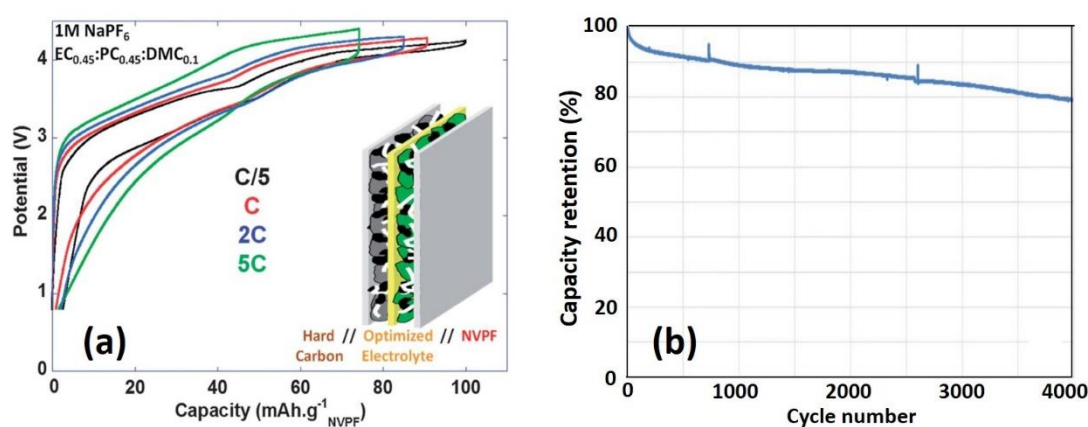


Figure 1.12 : (a) Voltage versus capacity electrochemical curves obtained for a Hard carbon/ $\text{Na}_3\text{V}_2(\text{PO}_4)_2\text{F}_3$ full-cell cycled in an electrolyte containing 1 M NaPF_6 in EC/PC/DMC (0.45/0.45/0.10) at different cycling rates (Adapted from [46]); (b) Long-term cyclability of a Hard carbon/ $\text{Na}_3\text{V}_2(\text{PO}_4)_2\text{F}_3$ $18650 \text{ Wh}\cdot\text{kg}^{-1}$ full cell, cycled at ambient temperature and at a $1C$ cycling rate upon charge and discharge (Adapted from [131]).

Ponrouch *et al.* first reported the electrochemical performance of a Hard carbon/ $\text{Na}_3\text{V}_2(\text{PO}_4)_2\text{F}_3$ coin cell-type full-cell, cycled in an electrolyte containing 1 M NaPF_6 in a mixture of EC/PC/DMC = 0.45/0.45/0.10. The full cell could deliver a capacity of $100 \text{ mAh}\cdot\text{g}^{-1}$ at the cycling rate of $C/5$ [46]. Despite an increased polarization observed at $5C$, a capacity of $70 \text{ mAh}\cdot\text{g}^{-1}$ could still be achieved (**Figure 1.12a**). Broux

et al. have recently reported that an optimized Hard carbon// $\text{Na}_3\text{V}_2(\text{PO}_4)_2\text{F}_3$ 18650 full cell prepared by the CEA (France) and cycled at 1C at ambient temperature could maintain more than 80% of its initial capacity after 4000 cycles (**Figure 1.12b**) [131]. Furthermore, the electrochemical signatures of the cell obtained at C/10 at 25°C and at 0°C and their corresponding *operando* X-ray diffraction patterns were very similar, indicating that Na^+ can maintain high mobility in $\text{Na}_3\text{V}_2(\text{PO}_4)_2\text{F}_3$ even at low temperatures.

The electrochemical signature obtained upon charge and discharge of $\text{Na}_3\text{V}_2(\text{PO}_4)_2\text{F}_3$ vs. Na^+/Na is characterized by the presence of two voltage domains at 3.70 and 4.20 V vs. Na^+/Na (**Figure 1.13**) suggesting the formation of intermediate phases especially at the intermediate mixed valence composition $\text{Na}_2\text{V}^{3+}\text{V}^{4+}(\text{PO}_4)_2\text{F}_3$ corresponding to the potential jump.

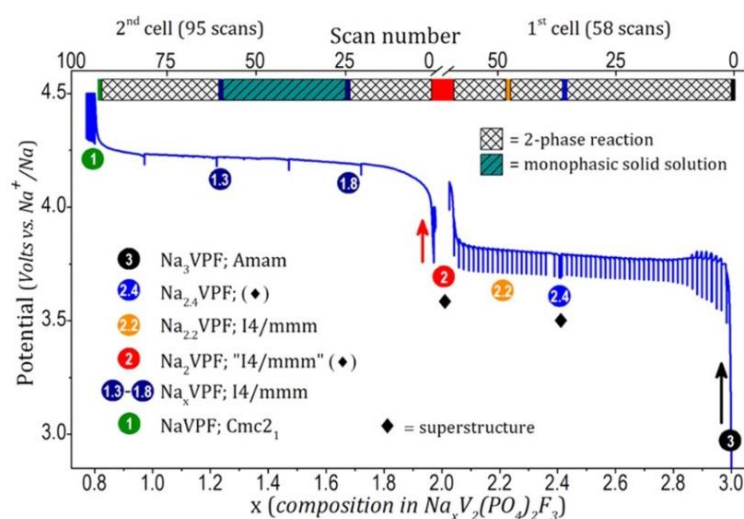


Figure 1.13 : Potential - Composition electrochemical curves obtained upon Na^+ extraction from $\text{Na}_3\text{V}_2(\text{PO}_4)_2\text{F}_3$. Several biphasic and solid solution reactions were observed during the Na^+ extraction process. The regions where the biphasic or the solid solution mechanisms occur are indicated in the upper bar of the figure. The Na-content of the pure intermediate phases isolated during cycling are given in the small circles on the electrochemical profile (Adapted from [132]).

By the use of *operando* SXRD, Bianchini *et al.* identified the succession of several biphasic and monophasic (solid-solution) reactions during the desodiation process from $\text{Na}_3\text{V}_2(\text{PO}_4)_2\text{F}_3$ [132]. A monophasic mechanism was observed only in the composition range $1.3 \leq x \leq 1.8$ in $\text{Na}_x\text{V}_2(\text{PO}_4)_2\text{F}_3$, while biphasic reactions were identified in all the other composition ranges (**Figure 1.13**). Several intermediate phases were detected at $x = 2.4, 2.2, 2.0, 1.8, 1.3,$ and 1.0 . For all of them, the structural framework remains similar

to that of the pristine phase, but a reorganization of the Na^+ ions distribution occurs in order to minimize their mutual electrostatic repulsions. In the pristine composition $\text{Na}_3\text{V}_2(\text{PO}_4)_2\text{F}_3$, the two vanadium sites of the bioctahedral unit are highly symmetric ($6 \times d_{\text{V-F/V-O}} = \sim 2.0 \text{ \AA}$) and crystallographically equivalent [83]. At the end of charge, in $\text{Na}_1\text{V}_2(\text{PO}_4)_2\text{F}_3$, one vanadium site of the bioctahedral unit becomes highly distorted ($4 \times d_{\text{V-O}} = \sim 1.9 \text{ \AA}$, $d_{\text{V-F}} = 2.00 \text{ \AA}$, $d_{\text{V-F}} = 1.67 \text{ \AA}$) while the other remains symmetric ($4 \times d_{\text{V-O}} = \sim 2.0 \text{ \AA}$, $d_{\text{V-F}} = 2.02 \text{ \AA}$, $d_{\text{V-F}} = 1.88 \text{ \AA}$). Combining this observation with bond valence sum analysis, Bianchini *et al.* assigned the distorted site to V^{5+} and the symmetric site to V^{3+} [132].

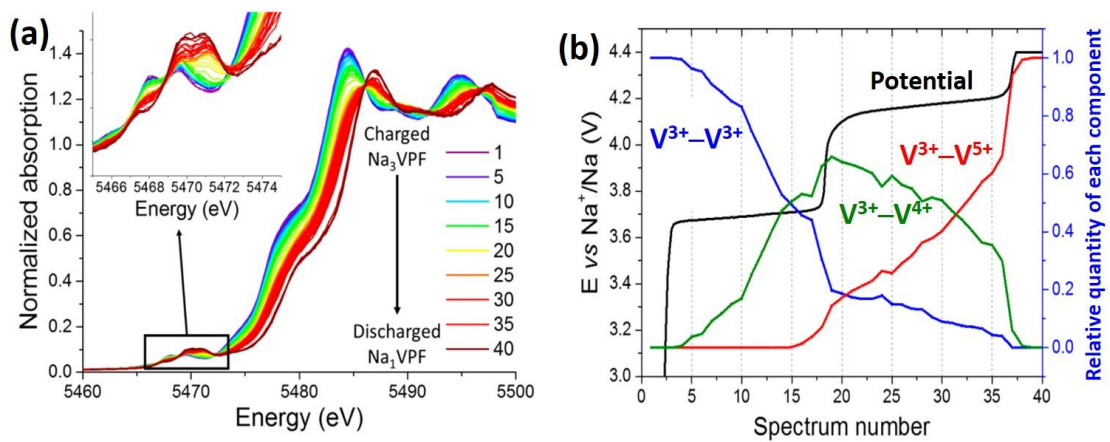


Figure 1.14 : (a) Vanadium K-edge XANES spectra collected *operando* during charge of an $\text{Na}/\text{Na}_3\text{V}_2(\text{PO}_4)_2\text{F}_3$ half-cell cycled at a cycling rate of $C/10$ per Na^+ . Inset shows the evolution of the pre-edge signal; (b) Evolution in the concentration of the three principal components required to describe the whole series of Vanadium K edge XANES data recorded *operando* during the first charge of the battery (Adapted from [133]).

The evolution of vanadium oxidation state in $\text{Na}_3\text{V}_2(\text{PO}_4)_2\text{F}_3$ during charge was followed by *operando* X-ray absorption spectroscopy (XAS) at vanadium K-edge (5465 eV) [133]. **Figure 1.14a** shows the evolution of the *operando* X-ray absorption near edge structure (XANES) spectra recorded at vanadium K edge on an operational $\text{Na}/\text{Na}_3\text{V}_2(\text{PO}_4)_2\text{F}_3$ half-cell. Each XANES spectrum can be divided into the pre-edge and edge regions (**Figure 1.14a**). The pre-edge signal is related to the forbidden $1s \rightarrow 3d$ transition and its intensity can be used to evaluate the local symmetry of the vanadium site. The edge signal is associated to the allowed $1s \rightarrow 4p$ transition and its position and shape are related to the average vanadium oxidation state and to the metal-ligand bond lengths around vanadium.

In the initial stage, the intensity of the pre-edge signal is very weak as all the V^{3+} ions in $Na_3V_2(PO_4)_2F_3$ are in highly symmetric octahedral sites and the $1s \rightarrow 3d$ transition is forbidden. Upon electrochemical oxidation, the intensity of the pre-edge signal increases gradually and shifts towards higher energy (**Figure 1.14a Inset**), figuring the oxidation of the V^{3+} ions together with a distortion in their local environment. This oxidation is also obvious through the linear shift in the edge energy of the *operando* XANES spectra (**Figure 1.14a**).

Three independent components are required to describe the whole system and the concentration profile of each component is given in **Figure 1.14b**. Broux *et al.* did the hypothesis that the first component corresponded to the $V^{3+}-F-V^{3+}$ pairs, as the pristine phase contains only V^{3+} in $V_2O_8F_3$ bioctahedra [133]. Upon charge in the first potential domain, one V^{3+} per pair is oxidized into V^{4+} leading to the formation of $V^{3+}-F-V^{4+}$ pairs (**Figure 1.14b**). In the second potential domain, these $V^{3+}-F-V^{4+}$ pairs are continuously replaced by $V^{3+}-F-V^{5+}$, either through the formation of the transient intermediate state $V^{4+}-F-V^{4+}$ and then a disproportionation ($2V^{4+} \rightarrow V^{3+} + V^{5+}$), or through the direct oxidation of V^{4+} into V^{5+} . Whatever the mechanism, the formation of V^{5+} at the end of charge was detected by ^{51}V solid-state NMR spectroscopy [133] and by *operando* synchrotron X-ray diffraction [132].

I.2.5.4. $Na_3(VO)_2(PO_4)_2F$

In 2002, Massa *et al.* reported on the discovery of a new sodium vanadyl fluorinated phosphate compound with the chemical formula $Na_3(VO)_2(PO_4)_2F$ [134], which can alternatively be written as $Na_3V_2(PO_4)_2FO_2$. The structural framework of this new material is topologically identical to that of $Na_3V_2(PO_4)_2F_3$ where the two terminal fluorine atoms of the bioctahedral units are replaced by two terminal oxygen atoms. The structure is indexed in the $P4_2/mnm$ space group at ambient temperature, and in the $I4/mmm$ space group at temperatures greater than $227^\circ C$ [135]. As in the case of $Na_3V_2(PO_4)_2F_3$, this phase transition is due to the redistribution of the Na^+ ions in the channels of the 3D framework. Sauvage *et al.* demonstrated that two Na^+ ions per formula unit could be extracted electrochemically from $Na_3(VO)_2(PO_4)_2F$ with a poor capacity retention in the high voltage region [136]. This capacity fading was associated to an

increase of the cell polarization due to the formation of a surface layer resulting from the electrolyte degradation; more recently, it was attributed to the presence of impurities in the sample [127]. Indeed, the electrochemical properties of $\text{Na}_3(\text{VO})_2(\text{PO}_4)_2\text{F}$ have recently been revisited by several groups, and an outstanding capacity retention has been demonstrated [39,129,137–140]. Furthermore, $\text{Na}_3(\text{VO})_2(\text{PO}_4)_2\text{F}$ can also be used as active material for hybrid capacitors [141].

I.2.5.5. The $\text{Na}_3\text{V}_2(\text{PO}_4)_2\text{F}_3 - \text{Na}_3(\text{VO})_2(\text{PO}_4)_2\text{F}$ system

I.2.5.5.1. Crystal structure description

Recent studies have shown that $\text{Na}_3\text{V}_2(\text{PO}_4)_2\text{F}_3$ and $\text{Na}_3(\text{VO})_2(\text{PO}_4)_2\text{F}$ are indeed the two end members of a family of materials with the general formula $\text{Na}_3\text{V}^{3+}_{2-y}\text{V}^{4+}_y(\text{PO}_4)_2\text{F}_{3-y}\text{O}_y$ with $0 \leq y \leq 2$ [99,101,142–144]. The partial substitution of oxygen on the terminal fluorine of the bioctahedral units $\text{V}_2\text{O}_8\text{F}_3$ leads to the formation of $\text{Na}_3\text{V}^{3+}_{2-y}\text{V}^{4+}_y(\text{PO}_4)_2\text{F}_{3-y}\text{O}_y$ phases, the vanadium ions bonded to these terminal oxygen atoms being oxidized into V^{4+} with the formation of very covalent vanadyl bonds ($\text{V}=\text{O}$). Comprehensive synthesis protocols for this family of materials have already been reported by different groups [99,101,142].

The crystal structures of all the phases in the $\text{Na}_3\text{V}^{3+}_{2-y}\text{V}^{4+}_y(\text{PO}_4)_2\text{F}_{3-y}\text{O}_y$ family are very similar as they are built on $\text{V}_2\text{O}_{8+y}\text{F}_{3-y}$ bioctahedra and PO_4 groups. Park *et al.* described their structures in a tetragonal $P4_2/mnm$ space group [101]. In fact, a subtle splitting of the (200)/(020) and (400)/(040) diffraction lines is observed for compositions with $y \leq 0.6$ and their structures should then be described in orthorhombic symmetry, using the $Amam$ space group.

A linear evolution of cell parameters with y is reported for $\text{Na}_3\text{V}^{3+}_{2-y}\text{V}^{4+}_y(\text{PO}_4)_2\text{F}_{3-y}\text{O}_y$ ($0 \leq y \leq 2$) [101,138,143,144]. The difference in the cell parameters of these phases is so small that XRD is actually not the most appropriate technique to clearly identify each member of this family of compounds. Instead, spectroscopic techniques can be used to precisely characterize $\text{Na}_3\text{V}^{3+}_{2-y}\text{V}^{4+}_y(\text{PO}_4)_2\text{F}_{3-y}\text{O}_y$ compositions.

I.2.5.5.2. Characterization techniques

The most common technique which can be accessed easily is **infrared (IR) spectroscopy**. This technique can identify the V=O stretching mode in the composition of interest, and then provide information on the composition of the phase thanks to the intensity and position of the V=O vibrational band [144]. The characteristic vibration of the V=O bond can be found at $\sim 920 \text{ cm}^{-1}$ and its corresponding overtone at $\sim 1850 \text{ cm}^{-1}$. As expected, no V=O bond is observed in $\text{Na}_3\text{V}_2(\text{PO}_4)_2\text{F}_3$ (**Figure 1.15a**). On the other hand, in $\text{Na}_3(\text{VO})_2(\text{PO}_4)_2\text{F}$, all the vanadium ions form V=O bonds with the apical oxygen atom as confirmed by intense signals at $\sim 920 \text{ cm}^{-1}$ and $\sim 1840 \text{ cm}^{-1}$ (**Figure 1.15a**). In the intermediate phases ($0 < y < 2$), there are two signals corresponding to V=O stretching modes at $\sim 920 \text{ cm}^{-1}$ (**Figure 1.15a**) and they correspond to the $\text{O}=\text{V}^{4+}-\text{F}-\text{V}^{4+}=\text{O}$ and $\text{O}=\text{V}^{4+}-\text{F}-\text{V}^{3+}-\text{F}$ groups, respectively. The relative intensity between these two signals varies with the y value. The use of IR spectroscopy to identify these vanadium fluorinated oxyphosphates was developed in this Ph.D work and will be discussed in details in **Chapter II**.

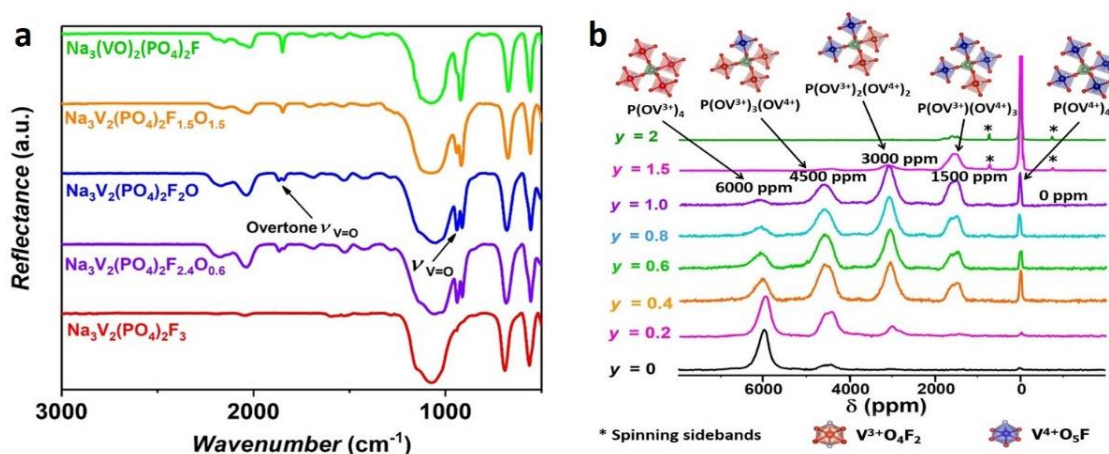


Figure 1.15 : (a) Comparison of the IR spectra of $\text{Na}_3\text{V}_2(\text{PO}_4)_2\text{F}_3$, $\text{Na}_3\text{V}_2(\text{PO}_4)_2\text{F}_{2.4}\text{O}_{0.6}$, $\text{Na}_3\text{V}_2(\text{PO}_4)_2\text{F}_2\text{O}$, $\text{Na}_3\text{V}_2(\text{PO}_4)_2\text{F}_{1.5}\text{O}_{1.5}$ and $\text{Na}_3(\text{VO})_2(\text{PO}_4)_2\text{F}$ powders in the wavenumber range of 500-3000 cm^{-1} ; (b) ^{31}P solid-state NMR spectra of different members of the $\text{Na}_3\text{V}^{3+}_{2-y}\text{V}^{4+}_y(\text{PO}_4)_2\text{F}_{3-y}\text{O}_y$ family collected at 100 MHz, MAS = 30 kHz.

^{23}Na and ^{31}P solid-state NMR spectroscopy. V^{3+} and V^{4+} are not directly probed, but indirectly through their electronic interaction with the ^{23}Na and ^{31}P in their neighbors [101,143]. For instance, ^{31}P NMR spectra recorded for the $\text{Na}_3\text{V}^{3+}_{2-y}\text{V}^{4+}_y(\text{PO}_4)_2\text{F}_{3-y}\text{O}_y$ compositions are given in **Figure 1.15b**. A “single” resonance is recorded at 6000 ppm for $\text{Na}_3\text{V}_2(\text{PO}_4)_2\text{F}_3$, attributed to the $\text{P}(\text{OV}^{3+})_4$ local

environment, while the single resonance detected at ~ 0 ppm for $\text{Na}_3(\text{VO})_2(\text{PO}_4)_2\text{F}$ is attributed to the $\text{P}(\text{OV}^{4+})_4$ local environment. In the mixed valence phases, five resonances recorded at 6000 ppm, 4500 ppm, 3000 ppm, 1500 ppm, and 0 ppm were observed and attributed to the local environments $\text{P}(\text{OV}^{3+})_4$, $\text{P}(\text{OV}^{3+})_3(\text{OV}^{4+})$, $\text{P}(\text{OV}^{3+})_2(\text{OV}^{4+})_2$, $\text{P}(\text{OV}^{3+})(\text{OV}^{4+})_3$, and $\text{P}(\text{OV}^{3+})_4$, respectively. Each V^{3+} in the proximity of the phosphorus nucleus is supposed to contribute to a paramagnetic shift of 1500 ppm [143]. The relative intensities of the five resonances recorded on the ^{31}P NMR spectrum is controlled by the ratio of $\text{V}^{3+}/\text{V}^{4+}$ in the structure. ^{23}Na solid-state NMR can also be used to determine the $\text{V}^{3+}/\text{V}^{4+}$ ratio in the structure as the Fermi contact shift of ^{23}Na nuclei in $\text{Na}_3\text{V}^{3+}_{2-y'}\text{V}^{4+}_{y'}(\text{PO}_4)_2\text{F}_{3-y'}\text{O}_{y'}$ depends on the number of V^{3+} ions in its closest bioctahedron [101,143]. A detailed discussion on the ^{23}Na and ^{31}P NMR of $\text{Na}_3\text{V}^{3+}_{2-y'}\text{V}^{4+}_{y'}(\text{PO}_4)_2\text{F}_{3-y'}\text{O}_{y'}$ ($0 \leq y' \leq 2$) phases will be given in **Chapter III** of this thesis.

Another technique that can directly distinguish V^{3+} and V^{4+} is **electron paramagnetic resonance (EPR)** where the signal can be recorded in perpendicular (\perp) or parallel (\parallel) polarization mode. The V^{4+} ions give rise to a featureless first-differential signal at $g = 1.93$ that can be observed in both perpendicular and parallel polarization modes while the V^{3+} ions generate a broad line shape centered at $g = 4.01$ which is only active in the parallel polarization mode [145]. Li *et al.* have recently developed the use of *ex situ* EPR spectroscopy to study the evolution of V^{3+} and V^{4+} concentration in $\text{Na}_3\text{V}_2(\text{PO}_4)_2\text{O}_{1.6}\text{F}_{1.4}$ during cycling [145]; however, this technique could also be applied to investigate the mixed valence state of vanadium in $\text{Na}_3\text{V}^{3+}_{2-y'}\text{V}^{4+}_{y'}(\text{PO}_4)_2\text{F}_{3-y'}\text{O}_{y'}$.

I.2.5.5.3. Electrochemical properties

All the phases belonging to the $\text{Na}_3\text{V}^{3+}_{2-y'}\text{V}^{4+}_{y'}(\text{PO}_4)_2\text{F}_{3-y'}\text{O}_{y'}$ family can be used as positive electrode materials in SIBs. In the potential range of 2.5 - 4.3 V vs. Na^+/Na , two Na^+ ions can be extracted reversibly for all the compositions [99,101,143,144] and the voltage at which Na^+ -extraction occurs depends strongly on the oxygen-content [101,143,144]. In this series of compositions, $\text{Na}_3\text{V}_2(\text{PO}_4)_2\text{F}_3$ leads to the highest desodiation voltage vs. Na^+/Na and this voltage shifts to a lower value in the mixed valence compositions. The more V^{4+} (or more precisely $\{\text{V}=\text{O}\}^{2+}$ vanadyl bond) present

in the structure, the lower the desodiation voltage value is. The minimum voltage is observed for $\text{Na}_3(\text{VO})_2(\text{PO}_4)_2\text{F}$. In the mixed valence phases, the cycling profile is sloping as the Na^+ extraction/insertion reaction occurs through a solid solution mechanism without the formation of intermediate phases. For the two end members, $\text{Na}_3\text{V}^{3+}_2(\text{PO}_4)_2\text{F}_3$ and $\text{Na}_3(\text{V}^{4+}\text{O})_2(\text{PO}_4)_2\text{F}$, the charge/discharge profiles show the presence of several composition-voltage “plateaus” due to the formation of intermediate phases whose structures were solved using high resolution synchrotron X-ray powder diffraction data [132,146]. Furthermore, analyses by electrochemical impedance spectroscopy revealed that a small amount of oxygen substituted for fluorine helps to increase the ionic conductivity in comparison to that observed in $\text{Na}_3\text{V}_2(\text{PO}_4)_2\text{F}_3$ [147] which could be beneficial to the electrochemical performance.

Importantly, $\text{Na}_3\text{V}_2(\text{PO}_4)_2\text{F}_3$ and all the related phases are stable in aqueous solution. A long immersion in water does not induce any structural degradation as revealed by combining XRD, IR and NMR analyses [144]. Therefore, they can be used to develop aqueous electrode formulation processes or as active materials for aqueous batteries. Kumar *et al.* reported on the use of $\text{Na}_3\text{V}^{3+}_{2-y}\text{V}^{4+}_y(\text{PO}_4)_2\text{F}_{3-y}\text{O}_y$ materials embedded on multi-walled carbon nanotubes (MWCNT) (7.8 wt.%) as positive electrodes in aqueous batteries [148], such electrodes can be electrochemically cycled versus Zn or $\text{NaTi}_2(\text{PO}_4)_3$ as the negative electrode and the full cells exhibit excellent capacity retention upon long term cycling (**Figure 1.16**). Similar results were reported for the $\text{NaTi}_2(\text{PO}_4)_3//\text{Na}_3\text{V}_2(\text{PO}_4)_2\text{F}_3$ full-cell system [149].

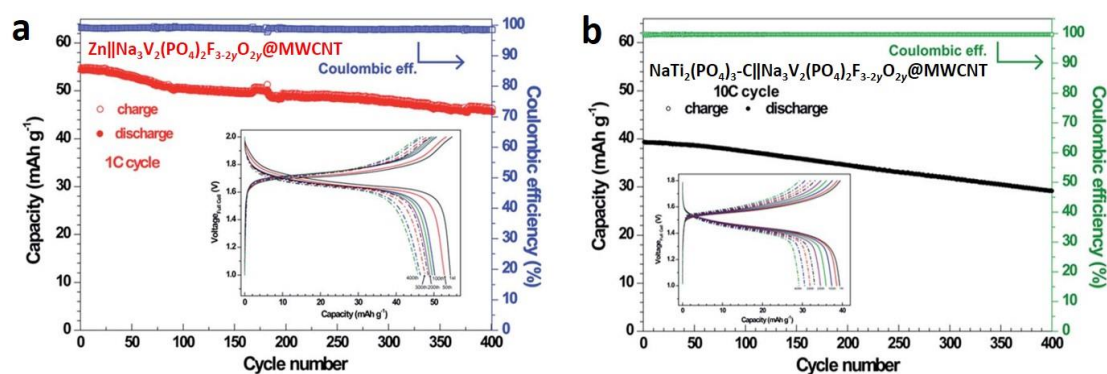


Figure 1.16 : Electrochemical cycling performance and coulombic efficiencies of (a) $\text{Zn}//\text{Na}_3\text{V}_2(\text{PO}_4)_2\text{F}_{3-y}\text{O}_y@MWCNT$ full-cell and (b) $\text{NaTi}_2(\text{PO}_4)_3\text{-C}//\text{Na}_3\text{V}_2(\text{PO}_4)_2\text{F}_{3-y}\text{O}_y@MWCNT$ full-cell cycled in aqueous 10 M NaClO_4 electrolyte. Insets show the corresponding charge-discharge profiles of the given full-cell (Adapted from [148]).

I.2.6. Structural designs and materials derived from $\text{Na}_3\text{V}_2(\text{PO}_4)_2\text{F}_3$ - $\text{Na}_x(\text{VO})_2(\text{PO}_4)_2\text{F}$ with superior performance

Despite the presence of three Na^+ ions in the chemical formula, only two Na^+ ions can apparently be inserted / extracted reversibly for all the $\text{Na}_3\text{V}^{3+}_{2-y}\text{V}^{4+}_y(\text{PO}_4)_2\text{F}_{3-y}\text{O}_y$ compositions. The capacity of these materials could be improved significantly if (i) the third Na^+ ion in the material could be electrochemically cycled reversibly in a practical potential window or (ii) extra Na^+ ions could be inserted reversibly in the structure at lower voltage. Several studies have been made in recent years in order to reach these targets and they will be summarized hereafter.

I.2.6.1. Three Na^+ ions extraction at extreme cycling conditions

Figure 1.17a shows the computed voltage curves in the composition range of $1 \leq x \leq 4$ for $\text{Na}_x\text{V}_2(\text{PO}_4)_2\text{F}_3$ and $\text{Na}_x(\text{VO})_2(\text{PO}_4)_2\text{F}$ [127].

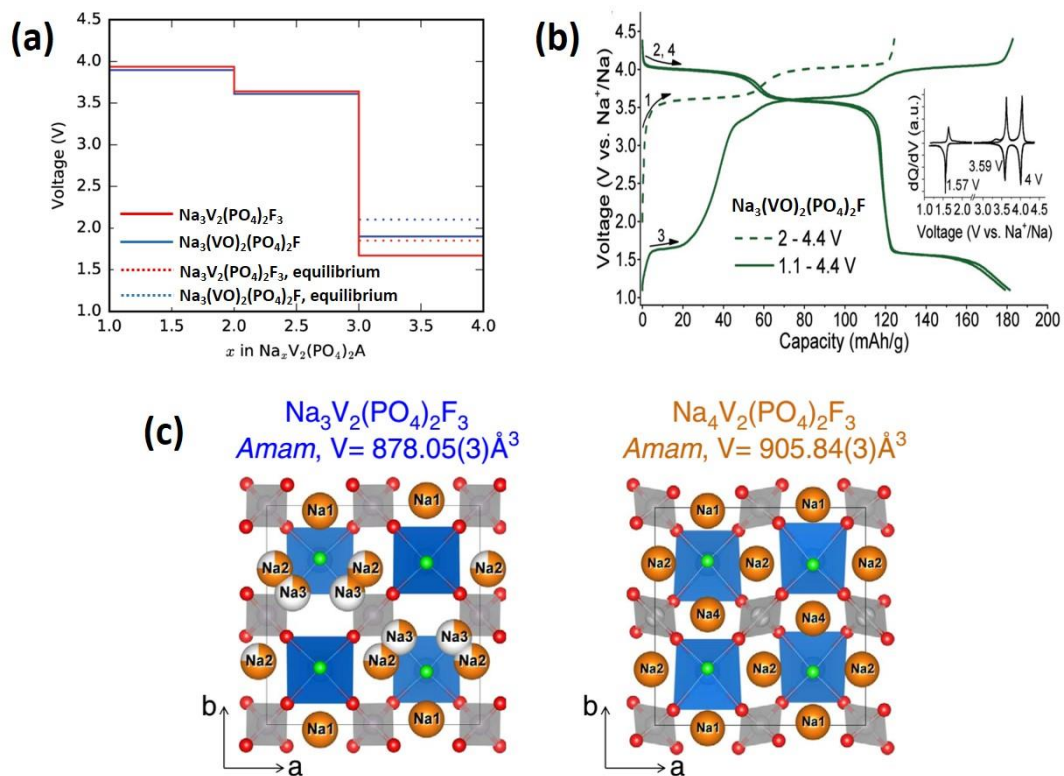


Figure 1.17 : (a) The computed voltage curves in the range of $1 \leq x \leq 4$ for $\text{Na}_x\text{V}_2(\text{PO}_4)_2\text{F}_3$ (red) and $\text{Na}_x(\text{VO})_2(\text{PO}_4)_2\text{F}$ (blue). The dotted curves refer to the average equilibrium potential calculated for the compositions with $3 \leq x \leq 4$, while the full lines are calculated in the region of $3 \leq x \leq 3.125$; (b) Electrochemical charge and discharge curves of $\text{Na}_3(\text{VO})_2(\text{PO}_4)_2\text{F}$ cycled in an electrolyte containing 1 M NaPF_6 in EC/DEC (1/1) at the cycling rate of $C/20$, in the potential range of 1.1 to 4.4 V vs. Na^+/Na (full line) and in the potential range of 2.0 to 4.4 V (dash line). Inset shows the first derivative of the cycling curve between 1.1 and 4.4 V [127]; (c) Comparison between the crystal structure of $\text{Na}_3\text{V}_2(\text{PO}_4)_2\text{F}_3$ and $\text{Na}_4\text{V}_2(\text{PO}_4)_2\text{F}_3$ synthesized by Na reductive ball milling method (Adapted from [127,150]).

A recent theoretical study revealed that one extra Na^+ ion can be inserted into the structure of $\text{Na}_3\text{V}_2(\text{PO}_4)_2\text{F}_3$ and $\text{Na}_3(\text{VO})_2(\text{PO}_4)_2\text{F}$ at 1.67 V and 1.85 V vs. Na^+/Na , respectively [127]. An extra capacity corresponding to the insertion of one Na^+ into the structure of $\text{Na}_3(\text{VO})_2(\text{PO}_4)_2\text{F}$ can be observed experimentally at ~ 1.6 V vs. Na^+/Na when the $\text{Na}/\text{Na}_3(\text{VO})_2(\text{PO}_4)_2\text{F}$ half-cell is cycled between 1.1 V and 4.4 V vs. Na^+/Na (**Figure 1.17b**) [127]. The same authors revealed that no electrochemical Na^+ insertion is observed in the low voltage region for $\text{Na}_3\text{V}_2(\text{PO}_4)_2\text{F}_3$. The insertion of the fourth Na^+ into $\text{Na}_3(\text{VO})_2(\text{PO}_4)_2\text{F}$, with the reduction of V^{4+} into V^{3+} is possible due to the strong screening effect of the oxygen atoms localized on the apical positions of the biocahedral units $\text{V}_2\text{O}_8\text{O}_2\text{F}$, on the contrary to what is observed with fluorine in these positions in $\text{Na}_3\text{V}_2(\text{PO}_4)_2\text{F}_3$. However, the voltage at which this process occurs is too low to hardly find any practical application. Peng *et al.* recently reported long-term cycling of $\text{Na}/\text{Na}_3(\text{VO})_2(\text{PO}_4)_2\text{F}$ half-cells in the voltage window of 1.0 - 4.5 V vs. Na^+/Na and revealed a continuous capacity loss [151], that is most probably associated to electrolyte decomposition at low voltage.

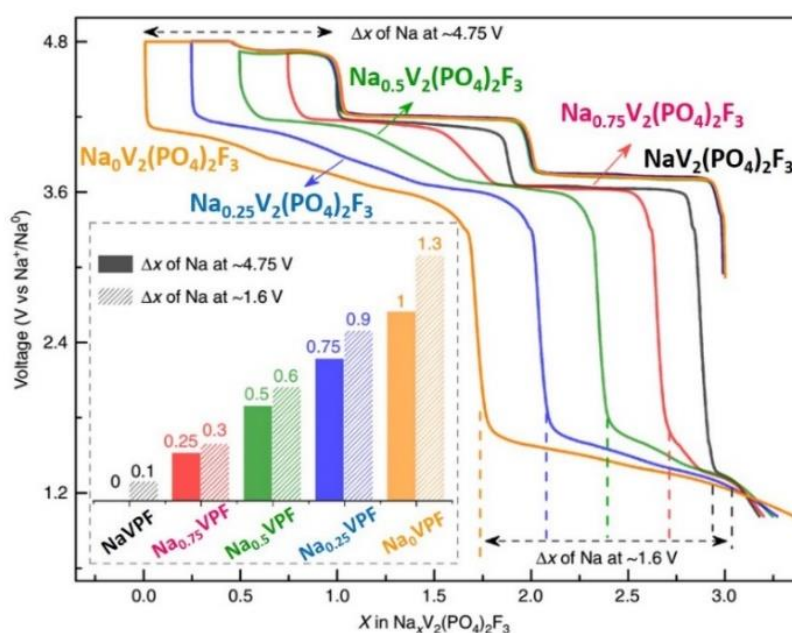


Figure 1.18 : The charge/discharge profile of $\text{Na}_3\text{V}_2(\text{PO}_4)_2\text{F}_3$ with a high cutoff voltage fixed at 4.75 V vs. Na^+/Na with different floating durations. Inset compares the number of Na ions extracted at ~ 4.75 V versus the number of Na ions reinserted into the structure at 1.6 V (Adapted from [152]).

Zhang *et al.* succeeded to synthesize a novel material, $\text{Na}_4\text{V}_2(\text{PO}_4)_2\text{F}_3$, by ball milling $\text{Na}_3\text{V}_2(\text{PO}_4)_2\text{F}_3$ directly with Na metal [150]. Half of the V^{3+} ions in $\text{Na}_3\text{V}_2(\text{PO}_4)_2\text{F}_3$ are reduced into V^{2+} to compensate for the insertion of the fourth Na^+ ion

into the diffusion channels of the structure. The crystal structure of $\text{Na}_4\text{V}_2(\text{PO}_4)_2\text{F}_3$ is similar to that of $\text{Na}_3\text{V}_2(\text{PO}_4)_2\text{F}_3$. The Na^+ ions are distributed on the four corners of a square so as to minimize the electrostatic repulsions between them, and the PO_4 groups are highly distorted (**Figure 1.17c**). The highly distorted structure of $\text{Na}_4\text{V}_2(\text{PO}_4)_2\text{F}_3$ might be a penalizing factor, preventing the reversible electrochemical insertion of the fourth Na^+ into the structure at room temperature. Three Na^+ can be extracted from $\text{Na}_4\text{V}_2(\text{PO}_4)_2\text{F}_3$ during the first charge *vs.* Na metal but only two can then be cycled reversibly. Nevertheless, this irreversible capacity can be - at least partially - sacrificed in the solid-electrolyte interphase (SEI) formation process that always happens at the hard carbon negative electrode during the first cycle. Indeed, it was proposed that the reversible capacity of a ‘Hard carbon// $\text{Na}_3\text{V}_2(\text{PO}_4)_2\text{F}_3$ + $\text{Na}_4\text{V}_2(\text{PO}_4)_2\text{F}_3$ ’ full-cell is higher than that of a ‘Hard carbon// $\text{Na}_3\text{V}_2(\text{PO}_4)_2\text{F}_3$ ’ full-cell.

Park *et al.* reported that “ultrahigh energy” can be obtained from $\text{Na}_3\text{V}_2(\text{PO}_4)_2\text{F}_{1.4}\text{O}_{1.6}$ with the exchange of 1.2 electrons per vanadium ion when the material is cycled in the extended voltage window of 1.5 - 4.6 V *vs.* Na^+/Na [100]. More recently, it was also reported that extra Na^+ can be extracted from $\text{Na}_3\text{V}_2(\text{PO}_4)_2\text{F}_3$ when the upper cutoff voltage is increased up to 4.75 V *vs.* Na^+/Na together with a floating period at the end of charge [152]. The longer the floating time is, the more Na^+ can be extracted: up to three Na^+ ions in total (**Figure 1.18**). These three Na^+ ions can be reinserted into the host structure if the lower cutoff voltage is set at 1.0 V *vs.* Na^+/Na . A reversible capacity of 200 mAh·g⁻¹ was hence announced for $\text{Na}_3\text{V}_2(\text{PO}_4)_2\text{F}_3$ based on the reversible extraction and reinsertion of three Na^+ ions, *i.e.* corresponding to an increase of more than 50% versus the results already reported.

Once the material is deintercalated up to 4.75 V, the discharge profile is completely modified, and the initial electrochemical signature is never recovered regardless the cycling conditions. Indeed, the first charge performed up to 4.75 V is characterized by the succession of three voltage domains, whereas the next discharge and the successive cycles are sloping [152]. The structure undergoes an irreversible modification at high voltage, from the pristine structure described in the space group *Amam* with the Na^+ ions distributed among three sites to a structure similar to the high temperature disordered one described in the space group *I4/mmm* with the Na^+ ions distributed within a ring. The XRD patterns of the samples charged up to 4.75 V and then

discharged to 1.0 V show a large broadening of the diffraction lines and a decrease in the peaks' intensity. Furthermore, ^{31}P solid-state NMR spectra recorded on the same samples also reveal the presence of very broad resonances [152].

In our opinion, the structure would suffer some irreversible degradations, and not only modifications, during the charge up to ~ 4.75 V, as it was also suggested earlier by Barker *et al.* [121]. Furthermore, a contribution of the electrolyte degradation to the capacity is expected at low voltage, as the number of electrons exchanged in charge up to ~ 4.75 V is smaller than that exchanged in discharge down to ~ 1.6 V (**Figure 1.18 Inset**). The result announcing the extraction of the third Na^+ ion from $\text{Na}_3\text{V}_2(\text{PO}_4)_2\text{F}_3$ is really intriguing as all the theoretical works predicted that its extraction would occur at ~ 4.95 V vs. Na^+/Na [119,129] and that the fully desodiated phase $\text{V}_2(\text{PO}_4)_2\text{F}_3$ would be thermodynamically unstable [119].

I.2.6.2. Influence of ionic substitution on the electrochemistry of $\text{Na}_3\text{V}_2(\text{PO}_4)_2\text{F}_3$

As just discussed, above the voltage required to remove the third Na^+ ion is high [119,129], and many theoretical works have thus been conducted in order to predict the possible structure modifications so as to shift this voltage value into the electrochemical window of all the currently available liquid electrolytes. This high voltage value was proposed to be due to the oxidation of V^{4+} to V^{5+} but also to the great activation energy required to break the Na^+ ordering formed at the end of charge [119]. Indeed, Na^+ extraction from $\text{Na}_3\text{V}_2(\text{PO}_4)_2\text{F}_3$ leads to the formation of several intermediate phases with different and quite stable Na^+ orderings, which can slow down the diffusion process.

Figure 1.19 compares the activation energy required to create defects and destabilize the Na^+ ordering observed in $\text{Na}_2\text{V}_2(\text{PO}_4)_2\text{F}_3$ and $\text{NaV}_2(\text{PO}_4)_2\text{F}_3$, the latter being significantly greater (281 meV versus 199 meV). Dacek *et al.* proposed that any factor that could disrupt this Na^+ ordering, such as ionic substitution, could lower the activation energy for the defect formation and reduce the voltage for the Na^+ extraction [119,128]. For instance, Xiong *et al.* showed that the operating voltage of $\text{NaLi}_2\text{V}_2(\text{PO}_4)_2\text{F}_3$, with foreign ions (Li^+) in the diffusion channels, was slightly lower than that of $\text{Na}_3\text{V}_2(\text{PO}_4)_2\text{F}_3$; the voltage profiles of these two materials are different [153].

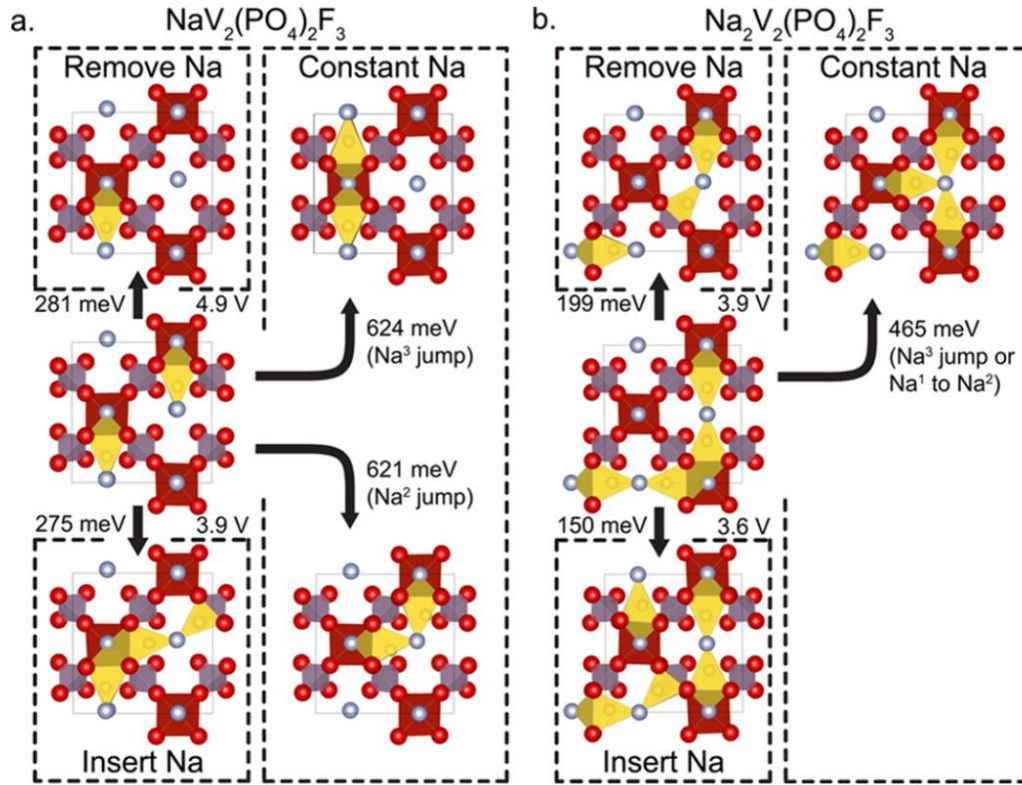


Figure 1.19 : Comparison of the defect formation energies in $\text{NaV}_2(\text{PO}_4)_2\text{F}_3$ and $\text{Na}_2\text{V}_2(\text{PO}_4)_2\text{F}_3$ for the most stable Na^+ ions distributions that allow for bulk diffusion (Adapted from [119]).

In order to understand the role of cationic substitution for vanadium on the redox potential of the $\text{Na}_3\text{V}_2(\text{PO}_4)_2\text{F}_3$ material, Bianchini *et al.* synthesized a series of Al-substituted materials $\text{Na}_3\text{V}_{2-z}\text{Al}_z(\text{PO}_4)_2\text{F}_3$ ($0 \leq z \leq 0.3$) [127]. The redox potential of the $\text{V}^{4+}/\text{V}^{3+}$ couple was unlikely to be affected by the Al-substitution; furthermore, the substitution was shown to be detrimental to the electrochemical performance as the number of Na^+ extracted was shown to be limited to $(2-z)$. The synthesis of $\text{Na}_3\text{VGa}(\text{PO}_4)_2\text{F}_3$ was also reported; however, there was no clear evidence for the activation of the $\text{V}^{4+}/\text{V}^{5+}$ redox couple in the high voltage region [128].

The crystal structure and the electrochemical properties of $\text{Na}_3(\text{VO})\text{Fe}(\text{PO}_4)_2\text{F}_2$ have also been recently reported [154]. The material shows very low polarization which could be due to an enhancement in the Na^+ mobility and a disruption of $\text{Na}^+ - \text{Na}^+$ charge orderings upon cycling. Nevertheless, there is no impact of the substitution on the potential value of the $\text{V}^{5+}/\text{V}^{4+}$ redox couple.

In all the substituted phases, there is no extra diffraction peak corresponding to the V^{3+} –F–M charge ordering in the structure. The interaction between two metal sites in the same bioctahedron seems to be weak, and the V^{3+} and M^{n+} ions tend to distribute randomly over all the bioctahedral units in the structure. This random distribution of the metal ions could be the origin of the absence of Na^+ orderings during cycling.

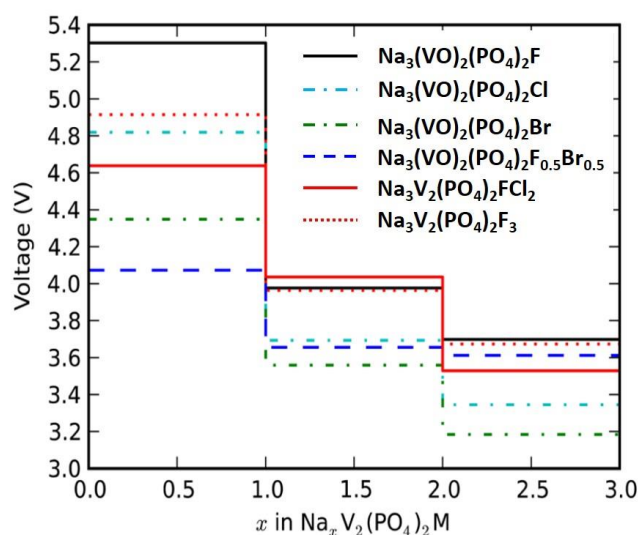


Figure 1.20 : Calculated voltage profiles of $Na_3V_2(PO_4)_2F_3$ with different anionic substitutions (Adapted from [129]).

Each V^{3+} in $Na_3V_2(PO_4)_2F_3$ is coordinated by two fluorine atoms on the axial positions of the octahedron, and these fluorine anions polarize the energy of vanadium orbitals. If the terminal fluorine atom is replaced by other anions such as Cl^- and Br^- , with different electronegativities, it is expected to modify the electronic structure of the material, *i.e.* the energy of the t_{2g} orbitals of V^{3+} , and thus to directly influence the potential of the V^{4+}/V^{3+} redox couple. As shown in **Figure 1.20**, theoretical calculations performed by Xu *et al.* have proposed that chlorine substitution for fluorine should allow a significant decrease of the potential during the extraction of the first and third Na^+ ions, and thus the deintercalation of the three Na^+ ions in the stability window of electrolytes. From these results, it appears that the most attractive phase would be the vanadyl-rich material $Na_3(VO)_2(PO_4)_2F_{0.5}Br_{0.5}$ obtained from a combined substitution of oxygen and bromine for fluorine (**Figure 1.20**). To the best of our knowledge, this phase and all the phases with halogenide substitution for fluorine have never been obtained experimentally, as it may be due to the great mismatch between the ionic radii of F^- ($R_{F^-} = 1.33 \text{ \AA}$) and Cl^-/Br^- ($R_{Cl^-} = 1.81 \text{ \AA}$ and $R_{Br^-} = 1.96 \text{ \AA}$) [155].

I.3. Aim of this work

As was described above, $\text{Na}_3\text{V}_2(\text{PO}_4)_2\text{F}_3$ is an attractive positive electrode material in SIBs thanks to its high theoretical capacity, high operating voltage and the high stability of the structure upon long-term cycling. Nonetheless, the capacity of $\text{Na}_3\text{V}_2(\text{PO}_4)_2\text{F}_3$ is now limited to the reversible extraction/insertion of two Na^+ ions. A simple calculation indicates that its theoretical capacity would be increased by 50% if the third Na^+ ion could also be extracted/re-inserted in a reversible way. Some theoretical studies have demonstrated that an applied voltage value of 5.0 V *vs.* Na^+/Na was required to extract the third Na^+ ions, but this value lies beyond the electrochemical window of all the currently available liquid electrolytes. Furthermore, the structure of $\text{Na}_3\text{V}_2(\text{PO}_4)_2\text{F}_3$ is predicted to be thermodynamically unstable under such an extreme condition.

The theoretical studies also pointed out that the Na^+ -vacancy ordering and slow Na^+ diffusivity in $\text{NaV}_2(\text{PO}_4)_2\text{F}_3$ conjugated to the high polarization effect of the fluorine ligands are the main reasons for the Na^+ extraction voltage at 5.0 V *vs.* Na^+/Na . Nonetheless, the $\text{Na}_3\text{V}_2(\text{PO}_4)_2\text{F}_3$ structure is highly flexible meaning that it can adopt different cationic and/or anionic substitutions. The presence of the foreign ions in the $\text{Na}_3\text{V}_2(\text{PO}_4)_2\text{F}_3$ structural framework is expected to break the Na^+ -vacancy ordering, thus improve the Na^+ diffusivity and decrease the activation energy required for Na^+ diffusion process at the end of charge. In addition to this, an anionic substitution replacing the terminal fluorine ligand by an element with a lower electronegativity will weaken the ligand inductive effect and can also shift down the Na^+ extraction voltage.

This PhD work aims at exploring the crystal structure of $\text{Na}_3\text{V}_2(\text{PO}_4)_2\text{F}_3$, $\text{Na}_3(\text{VO})_2(\text{PO}_4)_2\text{F}$ and their derivatives obtained through different methods. The three-dimensional long range crystal structure of these phases is determined by the use of high resolution synchrotron X-ray powder diffraction whereas their local atomic and electronic structures are investigated through a combination of solid-state nuclear magnetic resonance supported by first-principles theoretical calculations, synchrotron X-ray absorption spectroscopy and infrared spectroscopy. Thereafter, the phase diagram and the redox processes involved in the Na^+ deintercalation and intercalation are established thanks to *operando* synchrotron X-ray diffraction and absorption. An in-depth understanding on the crystal structure evolution as well as the nature of redox couples

involved in the electrochemical reaction of each composition helps us to determine the capacity limitations, and how the ionic substitution can affect the crystal structure and the electrochemical performance of these vanadium fluorinated oxy-phosphates. These findings will help us to construct the ‘*Structure – Compositions – Properties*’ mutual relationship in the vanadium fluorinated oxy-phosphates and shed light to the development of new materials with better performance.

Therefore, the content of this PhD work mainly focuses on:

❖ Synthesizing and characterizing the crystal structure of $\text{Ag}_3\text{V}_2(\text{PO}_4)_2\text{F}_3$, a homologue of $\text{Na}_3\text{V}_2(\text{PO}_4)_2\text{F}_3$, obtained through Ag^+/Na^+ ion exchange into $\text{Na}_3\text{V}_2(\text{PO}_4)_2\text{F}_3$ structure.

❖ Exploring the complexity of the synthesis reactions as well as the effects of oxygen substitution on the crystal structure and electrochemical performance of $\text{Na}_3\text{V}_2(\text{PO}_4)_2\text{F}_3 - \text{Na}_3(\text{VO})_2(\text{PO}_4)_2\text{F}$. Furthermore, an in-depth study on the structure evolution as well as on the nature of the redox couple involved in the electrochemical reaction of these phases will be performed by *operando* synchrotron X-ray diffraction and absorption.

❖ Investigating the sodium and phosphorus local environments in $\text{Na}_3\text{V}_2(\text{PO}_4)_2\text{F}_3 - \text{Na}_3(\text{VO})_2(\text{PO}_4)_2\text{F}$ compositions by the use of solid-state NMR spectroscopy combining with first-principles DFT calculations.

❖ Exploring the effects of cationic substitution on the crystal structure as well as the electrochemical performance of $\text{Na}_3\text{V}_2(\text{PO}_4)_2\text{F}_3 - \text{Na}_3(\text{VO})_2(\text{PO}_4)_2\text{F}$. We here focus on the effects of two different substituents: Al^{3+} and Fe^{3+} .

Chapter II

The Effects of Anionic Substitution on the Crystal Structure and the Electrochemical Properties of $\text{Na}_3\text{V}_2(\text{PO}_4)_2\text{F}_3$

II.1. Introduction

The series of compositions $\text{Na}_3\text{V}^{3+}_{2-y}\text{V}^{4+}_y(\text{PO}_4)_2\text{F}_{3-y}\text{O}_y$ ($0 \leq y \leq 2$) are now widely considered as promising materials for positive electrodes in SIBs thanks to their high operating voltage, high theoretical capacity, high rate performance and their excellent long-term cycling [99,101,131,152]. The two end members, $\text{Na}_3\text{V}_2(\text{PO}_4)_2\text{F}_3$ and $\text{Na}_3(\text{VO})_2(\text{PO}_4)_2\text{F}$, were historically discovered by Le Meins *et al.* and Massa *et al.*, respectively [82,134]; nevertheless, the electrochemical behavior of these phases was first reported in the work of Barker *et al.* [120,121,156] and Sauvage *et al.* [136]. The existence of the fluorinated oxyphosphates family $\text{Na}_3\text{V}^{3+}_{2-y}\text{V}^{4+}_y(\text{PO}_4)_2\text{F}_{3-y}\text{O}_y$ ($0 \leq y \leq 2$) has recently been discovered through the work of Kisuk Kang's and Teofilo Rojo's groups [99,101], and has inspired many following works. Some members of our group have recently revisited the crystal structure and the electrochemical properties of these materials by a combination of several advanced characterization techniques, such as synchrotron X-ray powder diffraction and synchrotron X-ray absorption spectroscopy at Vanadium K-edge energy [83,131,133,143]. Great discrepancies in the literature concerning the crystal description of the phases, the actual chemical formula of the compositions and their corresponding electrochemical profiles were detected. These discrepancies were caused by (i) the resolution of the technique used to characterize the phases, (ii) the complexity in the mechanism of the synthesis reactions, which was not greatly considered in previous studies, and (iii) the difficulty to determine the exact y value in the $\text{Na}_3\text{V}^{3+}_{2-y}\text{V}^{4+}_y(\text{PO}_4)_2\text{F}_{3-y}\text{O}_y$ chemical formula due to the chemical similarity between F^- and O^{2-} as well as between V^{3+} and V^{4+} .

In this study, we aimed at (i) making an in-depth understanding on the complexity of the reactions occurring in the solid-state synthesis process, (ii) correcting the y values and the chemical formulas that had been reported in [143] to reconcile the actual formula of the phases to their observing properties, (iii) developing an easy and reliable method to distinguish all the compositions in the $\text{Na}_3\text{V}^{3+}_{2-y}\text{V}^{4+}_y(\text{PO}_4)_2\text{F}_{3-y}\text{O}_y$ family, (iv) investigating the origin of the extra capacity observed when $\text{Na}_3\text{V}_2(\text{PO}_4)_2\text{F}_3$ is charged up to 4.8 V vs. Na^+/Na , and (v) tracking the vanadium's local structure changes when $\text{Na}_3\text{V}_2(\text{PO}_4)_2\text{F}_3$, $\text{Na}_3\text{V}_2(\text{PO}_4)_2\text{F}_2\text{O}$ and $\text{Na}_3\text{V}_2(\text{PO}_4)_2\text{F}_{1.5}\text{O}_{1.5}$ are charged up to 4.8 V vs. Na^+/Na .

II.2. Materials synthesis and characterizations

II.2.1. Materials synthesis

A series of $\text{Na}_3\text{V}_2(\text{PO}_4)_2\text{F}_{3-y}\text{O}_y$ materials was prepared by a one-step solid-state reaction using stoichiometric amounts of VOPO_4 , VPO_4 , NaF (Sigma-Aldrich; $\geq 99\%$), and Na_2CO_3 (Riedel-de Haën; 99.8%). VPO_4 and VOPO_4 powders were obtained by using the stoichiometric reaction between V_2O_5 (Sigma-Aldrich; $\geq 99.6\%$) and $\text{NH}_4\text{H}_2\text{PO}_4$ (Sigma-Aldrich; $\geq 99.99\%$) as described in details earlier [143]. No coating with carbon was done in order to better control the average oxidation state of vanadium in the samples. The as-prepared $\text{Na}_3\text{V}_2(\text{PO}_4)_2\text{F}_{3-y}\text{O}_y$ powders were washed in distilled water over four days in order to eliminate the impurities formed during the synthesis. The products were then filtered, and finally dried in a Buchi furnace at 80°C [143]. An optimized carbon-coated $\text{Na}_3\text{V}_2(\text{PO}_4)_2\text{F}_3$ powder was used as a reference, the synthesis of which being described in details in a recently accepted patent [157].

II.2.2. Materials characterization

Thermogravimetric analyses were performed on a TGA Setaram TAG 2400 machine coupled with a Balzer ThermoStar mass spectrometer to identify the chemical compounds released by each sample during the thermal treatment. The experiments were carried out under Ar (alpha1) at a heating rate of $5^\circ\text{C}\cdot\text{min}^{-1}$. Special care was taken to work with the best gas quality in order to increase the reproducibility of both the sample surrounding atmosphere and the signals in mass spectrometry during the whole analysis.

Laboratory **X-ray powder diffraction** (XRD) was carried out using a PANalytical Empyrean diffractometer in $\theta - \theta$ configuration and equipped with a $\text{Cu K}_{\alpha 1,2}$ X-ray source. The powder was packed in a 0.5 mm diameter capillary. The acquisition was performed in the 2θ range of $8^\circ - 140^\circ$ with a step size of 0.004° . High angular resolution synchrotron X-ray powder diffraction (SXRD) was performed at the MSPD beamline at ALBA (Barcelona, Spain). The data were recorded by using the MYTHEN detector at a wavelength of 0.8251 \AA , in the 2θ angular range of $1^\circ - 70^\circ$ with a 0.006° step. Diffraction data analysis and Rietveld refinement were performed by utilizing the FullProf Suite and Jana 2006 software [158,159]. The 3D crystal structures of the materials were visualized by using the VESTA software [160].

The **chemical analysis** of the Na, V, and P contents was performed by inductively coupled plasma-optical emission spectroscopy (ICP-OES) using a Varian Model 720-ES spectrometer, after a complete dissolution of the powder into a concentrated hydrochloric acid (HCl) solution.

Scanning electron microscopy (SEM) images were taken on the metallized samples (Pd-deposited) by a Hitachi Model S-4500 microscope.

Fourier transform infrared (FT-IR) spectra were recorded by using a Bruker Equinox 55 spectrometer in the wavenumber range of 400 - 4000 cm^{-1} (mid-IR) with a resolution of 4 cm^{-1} . The samples were finely ground in a mortar with dried KBr in an approximate ratio of 1: 50 (by *wt.*%).

^{23}Na solid-state NMR (ss-NMR) spectra were acquired using a Bruker Avance 500 MHz spectrometer, equipped with a 11.7 T wide bore magnet (operating at Larmor frequency of 132.3 MHz for ^{23}Na). Experiments were performed using conventional 2.5 mm magic-angle spinning (MAS) probes, with 30 kHz MAS rate. Chemical shifts are referenced relative to an aqueous 0.1M NaCl solution at 0 ppm. In each case, a short pulse length of 1.1 μs corresponding to a selective $\pi/8$ pulse determined by using a 0.1 M NaCl aqueous solution was employed. The spectral width was set to 1 MHz and the recycle delay of 0.5 s, which was long enough to avoid T_1 saturation effects. The baseline distortions resulted from the spectrometer dead time (5 - 10 μs) were removed computationally by using a polynomial baseline correction routine. ^{31}P ss-NMR spectra were acquired on a Bruker Avance III 100 MHz spectrometer, equipped with a 2.4 T wide bore magnet (operating at Larmor frequency of 40.6 MHz for ^{31}P) by using a standard Bruker 2.5 mm MAS probe at 30 kHz MAS rate. Chemical shifts are referenced relative to an aqueous H_3PO_4 85% (Sigma-Aldrich) solution at 0 ppm. In each case, a Hahn echo sequence was used with a $\pi/2$ pulse of 1.1 μs and a recycle delay of 0.2 s. The obtained data were processed by TopSpin and DM-fit softwares [161].

Synchrotron X-ray absorption spectroscopy (XAS) was performed at the Vanadium K-edge energy in transmission mode at the ROCK beamline of the SOLEIL synchrotron facility (Saint-Aubin, France) [162]. The storage ring was operated in multibunch top-up at 2.75 GeV with a 450 mA current. The incident beam from the bending magnet was collimated and horizontally focusing by a first toroidal bendable silicon Ir coated mirror. The monochromatization was ensured using the channel-cut Si(111) QuickExafs monochromator [163] and the harmonic rejection was done thanks to the B4C-coated second and third mirrors tilted at 4 mrad. The beam size was 1.5 mm x

0.450 mm (horizontal x vertical). The spectra were collected with an oscillating frequency of 2Hz at V K-edge in transmission utilizing gas ionization chambers as detectors. Three detectors in series allowed to measure during all the experiments a Vanadium metal foil which would be used as reference to calibrate the energy. Several scans (in average 690 scans per spectrum) were recorded in order to ensure the reproducibility and to increase the signal-to-noise ratio. The *ex situ* samples (V^{3+}PO_4 , $\text{LiV}^{4+}\text{PO}_4\text{O}$, and $\text{V}^{5+}\text{OPO}_4$) were prepared by mixing uniformly the active material with cellulose, then pressed into pellets of 13 mm in diameter. Their spectra were recorded during 13 mins.

In order to perform *operando* XAS measurements, the electroactive material was homogeneously mixed with carbon black and polytetrafluoroethylene (PTFE) in the ratio of 30/60/10 (by wt.%) then pressed in a 13 mm pellet die under 10 tons to form self-standing films of $\sim 300 \mu\text{m}$ in thickness. Half-cells were then assembled and used in *operando* experiment with two Beryllium foils as X-ray transparent current collectors [164]. Three different half-cells with $\text{Na}_3\text{V}_2(\text{PO}_4)_2\text{F}_3$, $\text{Na}_3\text{V}_2(\text{PO}_4)_2\text{F}_2\text{O}$, and $\text{Na}_3\text{V}_2(\text{PO}_4)_2\text{F}_{1.5}\text{O}_{1.5}$ as positive electrode were prepared for the *operando* XAS experiments. In order to avoid the strong absorption which might occur due to the high X-ray absorption coefficient of sodium, a tiny hole was made at the negative electrode and the beam size was controlled at $450 \mu\text{m} \times 1.5 \text{ mm}$. The Na// $\text{Na}_3\text{V}_2(\text{PO}_4)_2\text{F}_2\text{O}$ and Na// $\text{Na}_3\text{V}_2(\text{PO}_4)_2\text{F}_{1.5}\text{O}_{1.5}$ half-cells were cycled at C/10 cycling rate from 2.5 V up to 4.8 V vs. Na^+/Na while the Na// $\text{Na}_3\text{V}_2(\text{PO}_4)_2\text{F}_3$ half-cell was cycled at C/5 cycling rate with two consecutive charge-discharge cycles. Thanks to an automatic sample changer, these *operando* cells were measured in parallel with an acquisition time of 6 mins was spent sequentially on each sample. Each spectrum was an average of 690 scans recorded during 6 mins and the time interval between two successive spectra was 12 mins. The energy calibration and normalization were done using graphical interfaces available on the ROCK beamline [165].

The main absorption edge observed at around 5485 eV on the vanadium K edge XANES spectra is due to the $1s \rightarrow 4p$ dipole-allowed transition where the position of the edge can be related to the oxidation state of vanadium in the structure (**Figure 2.1**). The forbidden $1s \rightarrow 3d$ quadrupolar transitions may become allowed thanks to $3d - 4p$ orbital hybridization and lead to contributions in the pre-edge region (**Figure 2.1**). Their position

and intensity are linked to the electronic structure and local environment (coordination number and the nature of the surrounding ligands) of the transition metal ion, here vanadium [133,166–169]. The more distorted the vanadium site, the more intense is the pre-edge signal, versus that observed for highly symmetric environment.

The extended X-ray absorption fine structure (EXAFS) analysis was performed using the Demeter package [170]. Fourier transforms of the k^2 weighted EXAFS oscillations were carried out in the k range from 2.6 - 13.0 \AA^{-1} . Fitting was performed in the R range from 1.0 - 2.2 \AA . EXAFS amplitudes and phase shifts were calculated by FEFF7. The coordination number of each vanadium ($N = 6$), and the attenuation factor ($S_0^2 = 1$) were kept fixed during the fit. In the $\text{Na}_3\text{V}^{3+}_{2-y}\text{V}^{4+}_y(\text{PO}_4)_2\text{F}_{3-y}\text{O}_y$ compounds, each vanadium center is coordinated by six fluorine and oxygen, $\text{V}(\text{O},\text{F})_6$, depending on the oxidation state of the vanadium of interest; however, F^- and O^{2-} are similar X-ray scatterers, we thus simplified the fitting model by assuming that all the six surrounding ligands are just oxygen. The radial distance R_i and the Debye-Waller factor σ^2 were allowed to vary during the fit. A detailed discussion on the number of independent parameters used in the EXAFS fit for each material will be given in the results section. These XAS experiments and the data analysis, including the Principal Component Analysis and EXAFS fit, were done in collaboration with Stéphanie Belin and Antonella Iadecola at the ROCK beamline at SOLEIL synchrotron (Saint Aubin, France).

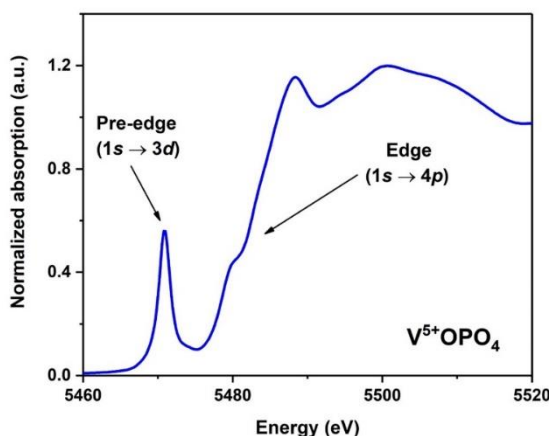


Figure 2.1 : Vanadium K-edge XANES spectrum recorded on VOPO_4 .

Electrochemical tests. The long-term electrochemical performances of the materials were tested in CR2032-type coin cells. The positive electrodes were prepared by the slurry tape casting method, where a slurry containing 80 wt.% active material, 10

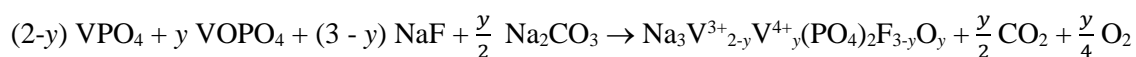
wt.% Carbon black, and 10 wt.% polyvinylidene fluoride (PVDF) dispersed in N-methyl-2-pyrrolidone (NMP) was casted on an Al foil, with a thickness of 150 μm , then dried overnight at 80°C under vacuum. The mass loading of the as-prepared electrodes was around 2.5 $\text{mg}\cdot\text{cm}^{-2}$. A homemade electrolyte containing 1M solution of NaPF_6 (Strem Chemical; 99%) in ethylene carbonate and dimethyl carbonate (EC/DMC = 1/1) with 2 wt.% of fluoroethylene carbonate (FEC) was used in all the electrochemical tests. The assembled cells were cycled in galvanostatic mode, at a $C/10$ cycling rate between 2.5 and 5.0 V vs. Na^+/Na . The rate $C/10$ corresponds to the exchange of 1 Na^+ in 10 hours.

II.3. Results and discussions

II.3.1. The complexity of the synthesis reaction

As already highlighted by Bianchini *et al.* [83] great discrepancies are reported in the literature for the unit cell parameters of $\text{Na}_3\text{V}_2(\text{PO}_4)_2\text{F}_3$. This is not surprising as only a strict control of the synthesis atmosphere (with no traces of oxygen) allows to obtain the stoichiometric phase. Most of the phases claimed in literature to be $\text{Na}_3\text{V}_2(\text{PO}_4)_2\text{F}_3$ are in fact characterized by a partial oxygen substitution for fluorine and thus, as a result of charge compensation, by the presence of V^{4+} according to the formula $\text{Na}_3\text{V}_2(\text{PO}_4)_2\text{F}_{3-y}\text{O}_y$ ($0 < y \leq 2$) [143]. As proposed earlier by our group [143], $\text{Na}_3\text{V}_2(\text{PO}_4)_2\text{F}_{3-y}\text{O}_y$ materials would hence be obtained according to the following reaction (1) with significant amounts of O_2 and CO_2 released:

Equation (1)



We noted that the color of the powders varied gradually from dark grey ($y = 0$) to light green ($y = 0.5$) as the average oxidation state of vanadium was expected to evolve linearly from +3 (for $y = 0$) to +3.25 (for $y = 0.5$). No significant mass loss was recorded during the washing of the powders and a linear evolution of the unit cell parameters had been observed for $0 \leq y \leq 0.5$ [143]. In order to explore more into details on the solid solution $\text{Na}_3\text{V}_2(\text{PO}_4)_2\text{F}_{3-y}\text{O}_y$ with $y > 0.5$, we synthesized in this study several compositions with $y = 0.75, 1.0, 1.5, 1.75$ and 2.0 according to equation (1). Surprisingly,

the unit cell parameters evolved linearly only in the range of $0 \leq y \leq 1$. For $y > 1$, the unit cell parameters remained similar and very close to those reported for $\text{Na}_3(\text{VO})_2(\text{PO}_4)_2\text{F}$ by Tsirlin *et al.* (**Figure 2.2**) [135].

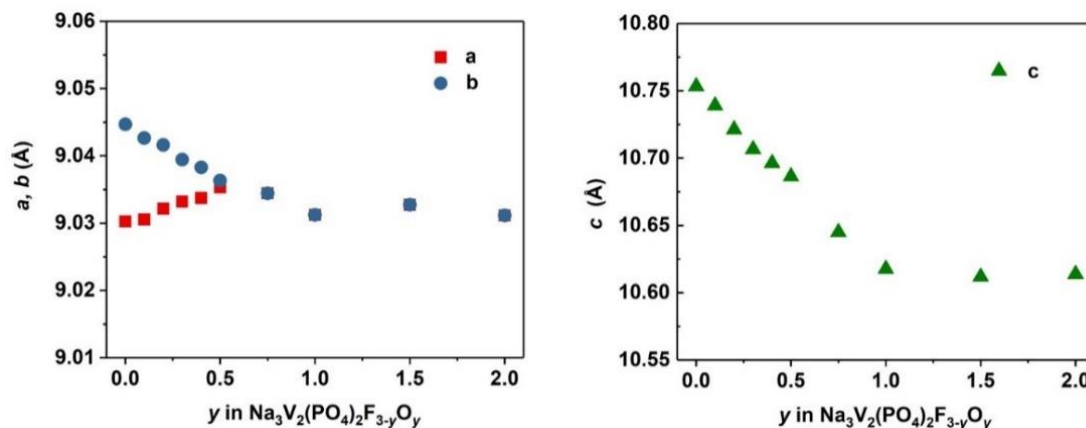


Figure 2.2 : The evolution of the unit cell parameters of the materials synthesized by using Equation (1) in the range of $0 \leq y \leq 2.0$. A linear evolution of the cell parameters was observed for $0 \leq y \leq 1.0$. When $y > 1.0$, there was no further change in the cell parameters.

Furthermore, we observe a significant mass loss for all the samples with $y > 1$ after being washed in water (up to 50 wt.% for $y = 2$). Interestingly, the as-prepared powders ($y > 1$) are dark green, and after washing a color change to bluish green is observed for all the powders. The solution recovered after washing is deep yellow.

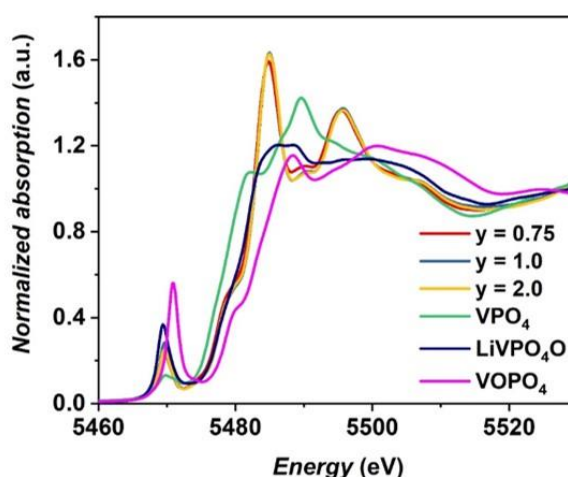


Figure 2.3 : XANES at Vanadium *K* edge of the materials synthesized according to Equation (1) with $y = 0.75$, $y = 1.0$ and $y = 2.0$. The XANES spectra of V^{3+}PO_4 , $\text{LiV}^{4+}\text{PO}_4\text{O}$, and $\text{V}^{5+}\text{PO}_4\text{O}$ are used as external references to determine the oxidation state of Vanadium in the materials of interest. No difference is observed between the spectra recorded for $y = 1.0$ and $y = 2.0$. The position of the absorption edge reveals that both materials contain only V^{4+} .

The comparison of the XAS spectra gathered in **Figure 2.3** confirms that the electronic structure of vanadium ion in all the materials obtained for $y > 1$ is that of vanadium at the tetravalent state. These results revealed, importantly, that equation (1) did not correctly describe the synthesis of $\text{Na}_3\text{V}_2(\text{PO}_4)_2\text{F}_{3-y}\text{O}_y$.

In order to get more insight into the reaction involved in the synthesis of $\text{Na}_3\text{V}_2(\text{PO}_4)_2\text{F}_{3-y}\text{O}_y$, thermogravimetric analyses coupled to mass spectroscopy (TGA-MS) were performed: first on the mixture of $(2\text{VPO}_4 + 3\text{NaF})$ as a reference and then on the mixture $(\text{VPO}_4 + \text{VOPO}_4 + 2\text{NaF} + \frac{1}{2}\text{Na}_2\text{CO}_3)$. The precursors were mixed using ball-milling, and then heated up to 650°C for the former mixture and to 500°C for the latter, at $5^\circ\text{C}\cdot\text{min}^{-1}$ under a continuous Ar flow. For the mixture of $(2\text{VPO}_4 + 3\text{NaF})$, no release of gas was detected before the tiny loss of fluorine ($m/z = 19$) from 450°C (**Figure 2.4a**) that leads to the formation of $\text{Na}_3\text{V}_2(\text{PO}_4)_2\text{F}_{3-\delta}\text{O}_\delta$ ($\delta \sim 0$) with a small amount of oxygen defects. Note that despite several attempts, it was not possible to prevent the presence of oxygen traces during the thermal treatment and thus the formation of defects. Here the fluorine loss corresponds to $\sim 0.5\%$ of the total mass and the δ value is thus expected to be infinitesimally small (**Figure 2.5a**).

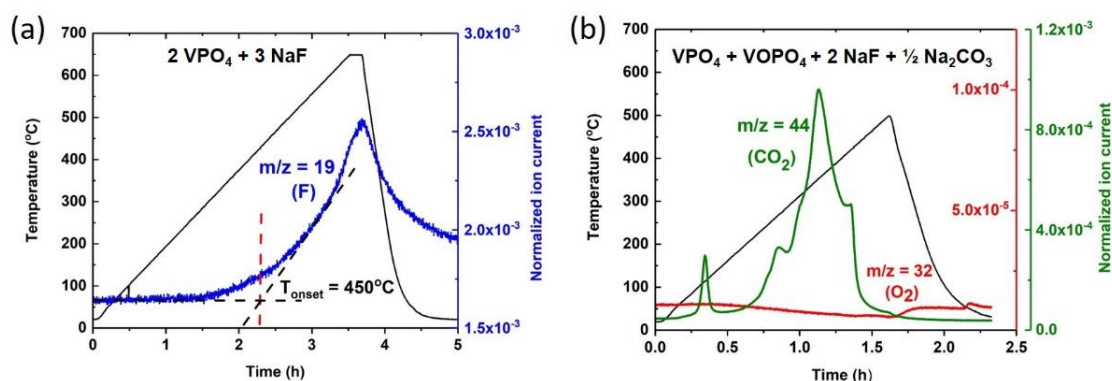
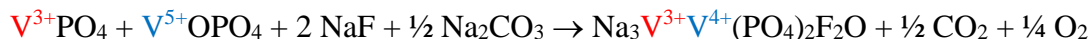


Figure 2.4 : (a) TGA-MS results recorded for a mixture of $(2\text{VPO}_4 + 3\text{NaF})$ heated at $5^\circ\text{C}\cdot\text{min}^{-1}$ between 25°C and 650°C . Fluorine was the only gas released, from 450°C ; (b) TGA-MS results recorded for a mixture of $(\text{VPO}_4 + \text{VOPO}_4 + 2\text{NaF} + \frac{1}{2}\text{Na}_2\text{CO}_3)$ heated at $5^\circ\text{C}\cdot\text{min}^{-1}$ between 25°C and 500°C . No O_2 evolution was detected. CO_2 was the main gas released during the reaction process. Minor loss of Fluorine (not shown) was also observed (Ion current below $2 \cdot 10^{-9}$).

According to equation (1), CO_2 and O_2 should always be released together during the reaction process. From the results obtained for the mixture $(\text{VPO}_4 + \text{VOPO}_4 + 2\text{NaF} + \frac{1}{2}\text{Na}_2\text{CO}_3)$, we can conclude that only CO_2 was detected, and not O_2 (**Figure 2.4b**). This result, combined with the observations made during the synthesis (similar crystalline

phase obtained whatever y for $y > 1$, with an increasing mass loss during washing with increasing y value) revealed that equation (1) proposed earlier by our group is actually not the proper description of the ongoing reaction. Indeed, applying equation (1) for $y = 1$ should have yielded:



into which all the V³⁺ ions from VPO₄ were maintained in their initial oxidation state whereas the V⁵⁺ species from VOPO₄ were reduced to V⁴⁺ through the evolution of O₂, to finally obtain Na₃V³⁺V⁴⁺(PO₄)₂F₂O. Here in this work, we clearly confirm that no O₂ evolution is observed and that only V⁴⁺ is detected in the final product. Therefore, the actual electron exchange occurring during the synthesis reaction thus implies that V³⁺ → V⁴⁺ + 1 e⁻ (for V³⁺ from VPO₄) and V⁵⁺ + 1 e⁻ → V⁴⁺ (for V⁵⁺ from VOPO₄), so that the chemical reaction can be re-written for $y = 1$ as:

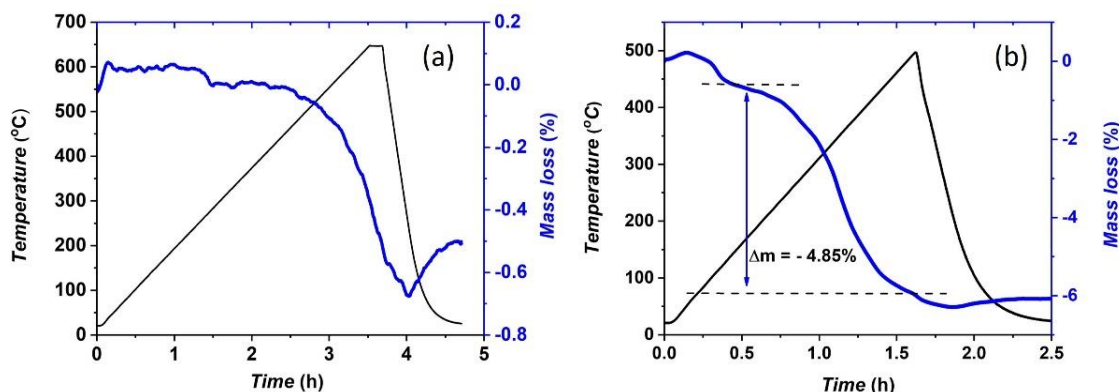
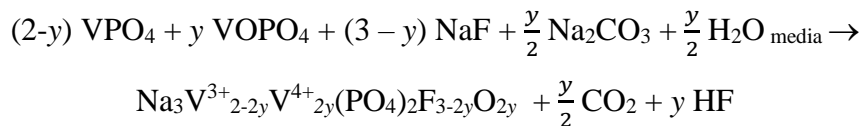


Figure 2.5 : (a) The thermal gravimetric analysis (TGA) curve of a mixture of (2 VPO₄ + 3 NaF) recorded from ambient temperature to 650°C with a heating rate of 5°C·min⁻¹. The minor mass loss (~ - 0.5 wt.%) recorded in this temperature range is due to the release of F ($m/z = 19$), (b) The thermal gravimetric analysis (TGA) curve of a mixture of (VPO₄ + VOPO₄ + 2 NaF + ½ Na₂CO₃) recorded from ambient temperature to 500°C with a heating rate of 5°C·min⁻¹. The mass loss (~ - 4.85 wt.%) recorded in this temperature range is due to the release of CO₂.

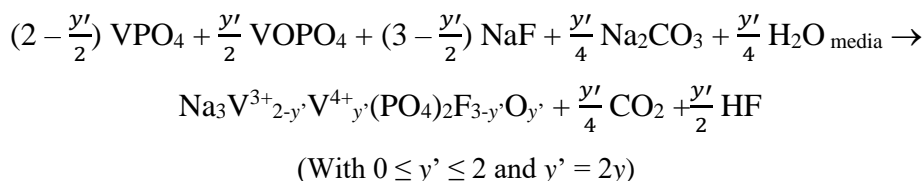
The formation of reactive COF₂ gas was in fact not detected. To explain this discrepancy, our hypothesis was at first to consider the high hygroscopic character of COF₂ which would promptly react with any trace of H₂O to form HF and CO₂. Nevertheless, as these two gases are not detected at the same time (CO₂ is detected first, and only then HF), we propose that Na₂CO₃ is decomposed first and releases CO/CO₂ and then, at higher temperatures, that fluorine is released and reacts with traces of water

to form HF. The general equation (1) can be then re-written with y such as $0 \leq y \leq 1$ and not $0 \leq y \leq 2$:



In order to avoid possible confusion with our previous work, we choose to replace $2y$ by y' throughout this chapter:

Equation (2)



As a conclusion, the general compositions of all the samples synthesized by Broux *et al.* are in fact $\text{Na}_3\text{V}^{3+}_{2-y'}\text{V}^{4+}_{y'}(\text{PO}_4)_2\text{F}_{3-y'}\text{O}_{y'}$ with $0 \leq y' \leq 1$ and not as proposed previously $\text{Na}_3\text{V}^{3+}_{2-y}\text{V}^{4+}_y(\text{PO}_4)_2\text{F}_{3-y}\text{O}_y$ ($0 \leq y \leq 0.5$) [143].

II.3.2. The stability in water of $\text{Na}_3\text{V}^{3+}_{2-y'}\text{V}^{4+}_{y'}(\text{PO}_4)_2\text{F}_{3-y'}\text{O}_{y'}$ phases

As just mentioned, all the as-prepared $\text{Na}_3\text{V}^{3+}_{2-y'}\text{V}^{4+}_{y'}(\text{PO}_4)_2\text{F}_{3-y'}\text{O}_{y'}$ powders were recovered after being washed in water to eliminate impurities such as $\text{Na}(\text{PO}_3)_3$ and $\text{Na}_2\text{V}_2\text{O}_5$. One might question if the phases are fully stable in water, or if water insertion, partial fluorine/hydroxyl exchange or even vanadium oxidation might be observed. The effect of washing with H_2O on the $\text{Na}_3\text{V}^{3+}_{2-y'}\text{V}^{4+}_{y'}(\text{PO}_4)_2\text{F}_{3-y'}\text{O}_{y'}$ ($0 \leq y' \leq 2$) samples will be illustrated through the example of $\text{Na}_3(\text{VO})_2(\text{PO}_4)_2\text{F}$ ($y' = 2$), but the results obtained are representative for the whole series of compounds. The XRD pattern of the as-prepared $\text{Na}_3(\text{VO})_2(\text{PO}_4)_2\text{F}$ ($y' = 2$) reveals the presence of the main phase, of minor amounts of $\text{Na}(\text{PO}_3)_3$ and $\text{Na}_2\text{V}_2\text{O}_5$ and of tiny additional diffraction lines (**Figure 2.6a**). The diffraction peaks corresponding to the impurities fully disappeared after washing as they are soluble in water and, as expected, the mass loss between the samples before and after washing was found to be less than 2 wt.%.

Furthermore, the comparison of the cell parameters determined for $\text{Na}_3(\text{VO})_2(\text{PO}_4)_2\text{F}$ before and after washing reveals no changes and thus supports its stability in water (**Table 2.1**).

Table 2.1 : Comparison of the cell parameters obtained from Cu $K\alpha$ diffractometer for $\text{Na}_3(\text{VO})_2(\text{PO}_4)_2\text{F}$ before and after washing in water.

| | S.G. | a (Å) | b (Å) | c (Å) | V/Z (Å ³) |
|----------------|------------|-----------|-----------|------------|-------------------------|
| Before washing | $P4_2/mnm$ | 9.0317(2) | 9.0317(2) | 10.622(5) | 216.63(2) |
| After washing | $P4_2/mnm$ | 9.0324(1) | 9.0324(1) | 10.6173(2) | 216.55(1) |

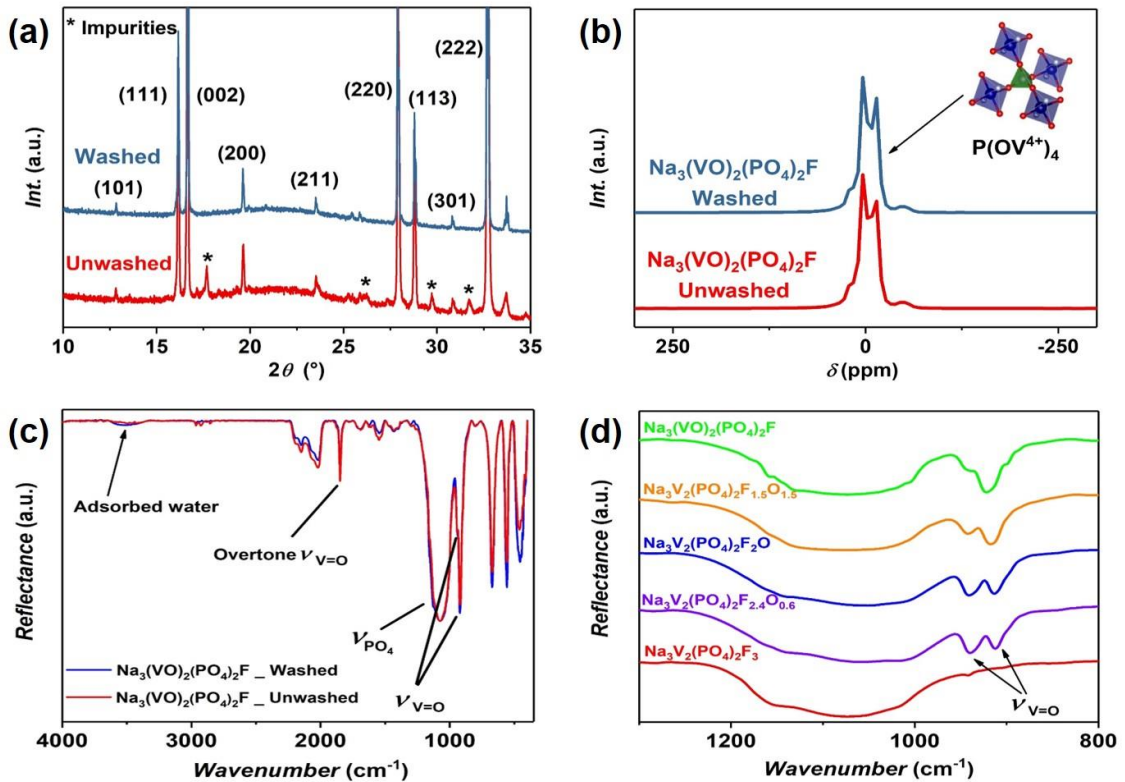


Figure 2.6 : (a) XRD patterns of $\text{Na}_3(\text{VO})_2(\text{PO}_4)_2\text{F}$, collected before and after washing, on a Cu $K\alpha_{1,2}$ diffractometer. The impurities highlighted by * are $\text{Na}(\text{PO}_3)_3$ and $\text{Na}_2\text{V}_2\text{O}_5$, (b) ^{31}P ss-NMR spectra collected for $\text{Na}_3(\text{VO})_2(\text{PO}_4)_2\text{F}$ before and after washing. The spectra were recorded at 100 MHz (MAS = 30 kHz), (c) IR spectra of unwashed and washed $\text{Na}_3(\text{VO})_2(\text{PO}_4)_2\text{F}$ powders in the wavenumber range of 400 - 4000 cm^{-1} , (d) Comparison of the IR spectra of $\text{Na}_3\text{V}_2(\text{PO}_4)_2\text{F}_3$, $\text{Na}_3\text{V}_2(\text{PO}_4)_2\text{F}_{1.5}\text{O}_{1.5}$, $\text{Na}_3\text{V}_2(\text{PO}_4)_2\text{F}_2\text{O}$, $\text{Na}_3\text{V}_2(\text{PO}_4)_2\text{F}_{2.4}\text{O}_{0.6}$, and $\text{Na}_3(\text{VO})_2(\text{PO}_4)_2\text{F}$ powders recovered after washing in the wavenumber range of 800 - 1300 cm^{-1} .

Additionally, ICP-OES analyses confirmed that the stoichiometry in Na/V/P was maintained to 3/2/2 upon washing. $\text{Na}_3(\text{VO})_2(\text{PO}_4)_2\text{F}$ is characterized by agglomerates of particles being less than 1 μm in diameter (**Figure 2.7**), with no apparent extra phases (impurities) at the particles' surface and in the grain boundaries.

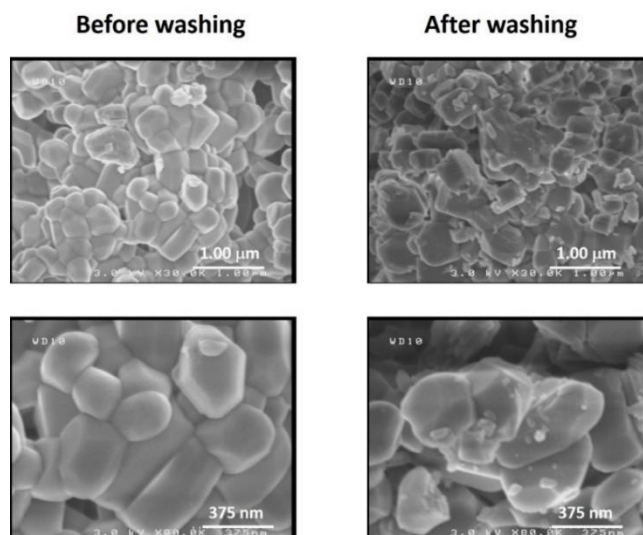


Figure 2.7 : SEM images of $\text{Na}_3(\text{VO})_2(\text{PO}_4)_2\text{F}$ powder before and after washing in water.

The ^{31}P *ss*-NMR spectra recorded for $\text{Na}_3(\text{VO})_2(\text{PO}_4)_2\text{F}$ are identical before and after washing in water (**Figure 2.6b**), showing that there is no change in the phosphorus local environment. The diamagnetic signals centered at ~ 0 ppm correspond to the $\text{P}(\text{OV}^{4+})_4$ local environment in the structure [143] and the splitting of the signals into two different peaks is due to the presence of two inequivalent local environments for phosphorus in $\text{Na}_3(\text{VO})_2(\text{PO}_4)_2\text{F}$ structure.

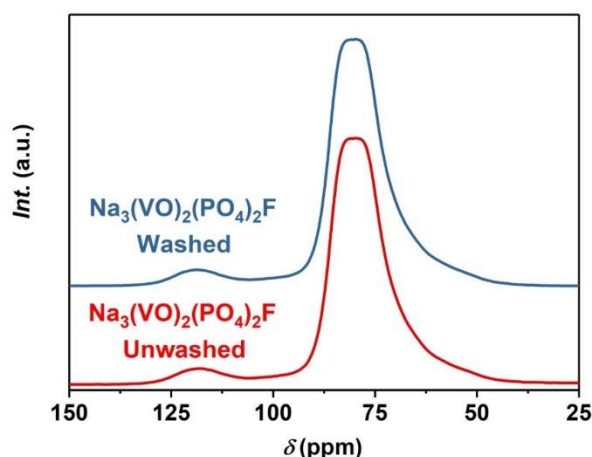


Figure 2.8 : ^{23}Na *ss*-NMR spectra collected for $\text{Na}_3(\text{VO})_2(\text{PO}_4)_2\text{F}$ before and after washing. The spectra were recorded at 500 MHz (MAS = 30 kHz).

^{23}Na *ss*-NMR was also recorded for the washed and unwashed powders in order to get insight into the stability of the phases. The spectra are compared with those of $\text{Na}_3(\text{VO})_2(\text{PO}_4)_2\text{F}$ in **Figure 2.8**. They exhibit two main resonances at 76 ppm and 120 ppm corresponding to Na nuclei interacting with two neighboring V^{4+} ions, and with a

combination of one V^{3+} and one V^{4+} , respectively. These observations show: (i) that there are traces of V^{3+} present in both powders and (ii) the high stability in water as no major changes of the main resonances are observed.

Similar observations were made by IR spectroscopy (**Figure 2.6c**). The characteristic stretching modes of $\text{V}=\text{O}$, and $\text{P}-\text{O}$ (in PO_4^{3-}) bonds were identified in the as-prepared material and remained unchanged after washing. In addition, no signatures revealing the presence of structural (inserted) H_2O molecules and/or of hydroxyl groups due to an exchange with fluorine were detected in the washed sample: they would have been expected as a large band between 2300 and 3500 cm^{-1} and as a narrow band at 3300 cm^{-1} , respectively [171]. The tiny signal recorded in the region of $3000 - 4000\text{ cm}^{-1}$ was attributed to the presence of traces of water adsorbed at the particles' surface. The vibrations observed in the region of $500 - 700\text{ cm}^{-1}$ can be attributed to the stretching mode of $\text{V}-\text{O}/\text{V}-\text{F}$ bonds or to the deformation mode of PO_4 groups in the structure.

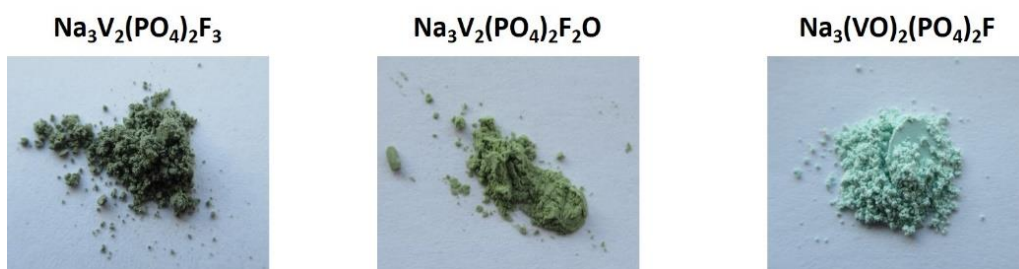


Figure 2.9 : The colors of three samples: $\text{Na}_3\text{V}_2(\text{PO}_4)_2\text{F}_3$, $\text{Na}_3\text{V}_2(\text{PO}_4)_2\text{F}_2\text{O}$, and $\text{Na}_3(\text{VO})_2(\text{PO}_4)_2\text{F}$ obtained after washing in water.

Combining all these illustrated information with additional data measured on the whole range of $0 \leq y' \leq 2$ compositions, we can conclude that the series of compounds $\text{Na}_3\text{V}^{3+}_{2-y'}\text{V}^{4+}_{y'}(\text{PO}_4)_2\text{F}_{3-y'}\text{O}_{y'}$ is stable in water. The washing performed as a final step at the end of the synthesis to remove possible (soluble) impurities is thus not detrimental to the composition and structural integrity of the materials, and as it will be discussed later, to their electrochemical performance. The stability of these phases in aqueous media is indeed a key factor that makes them attractive positive electrode materials for Na-ion batteries as: (i) they can be stored in air for long time without any degradation of their electrochemical performance, (ii) they can be processed in water to develop aqueous electrode formulation and (iii) they can be used as positive electrodes in aqueous rechargeable Na-ion batteries, as recently proposed by Kumar *et al.* [148]

II.3.3. Crystal structure determination for $\text{Na}_3\text{V}^{3+}_{2-y'}\text{V}^{4+}_{y'}(\text{PO}_4)_2\text{F}_{3-y'}\text{O}_{y'}$

Bianchini *et al.* have shown for the first time that the structure of the stoichiometric $\text{Na}_3\text{V}_2(\text{PO}_4)_2\text{F}_3$ phase (i.e. the pure V^{3+} composition) should be described in an orthorhombic space group (*Amam*) due to a specific distribution of the Na^+ ions over three different crystallographic sites within the tunnels of this polyanionic framework, that allows a decrease of the electrostatic interactions between Na^+ ions [83]. Later, Broux *et al.* have shown that the orthorhombic distortion was maintained for partial oxygen substitution for fluorine, despite being less obvious to identify from a simple observation of the synchrotron X-ray diffraction pattern for $0.5 < y' \leq 1$ [143]. Indeed, the clear orthorhombic splitting at the (400) and (040) diffraction lines was no longer observed when $y > 0.3$ (see Figure 2 in [143]). Nevertheless, the orthorhombic distortion was maintained and required, as it was leading to the best calculation of the experimental pattern and to the good description of the structure with regular PO_4 groups as well as to the minimization of the interactions between the Na^+ ions [143]. In the frame of this study, it was thus essential to revisit the structure of $\text{Na}_3\text{V}^{3+}_{2-y'}\text{V}^{4+}_{y'}(\text{PO}_4)_2\text{F}_{3-y'}\text{O}_{y'}$ with y' such as $1 < y' \leq 2$, i.e. for the oxygen-rich compositions. Indeed, up to now, by analogy with the tetragonal structure (*P4₂/mnm*) proposed by Le Meins *et al.* for the phase reported to be $\text{Na}_3\text{V}_2(\text{PO}_4)_2\text{F}_3$ [82], all the compositions (whatever the value of y') were described in *P4₂/mnm* and not in *Amam*.

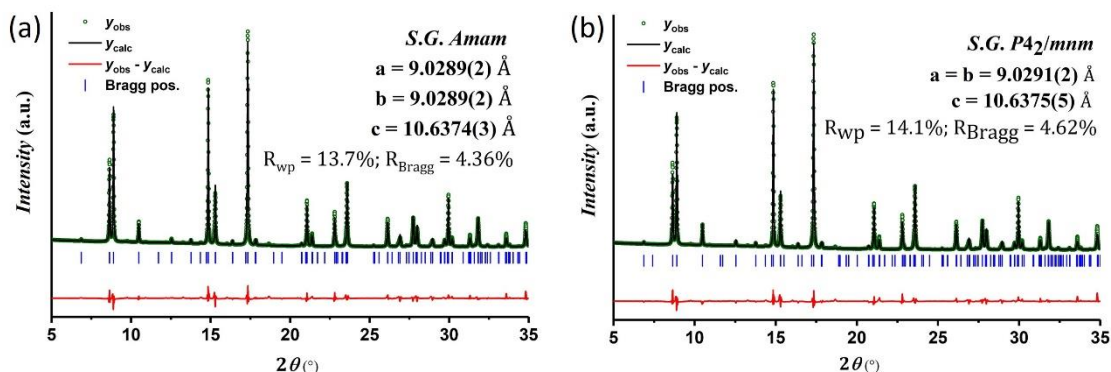


Figure 2.10 : Rietveld refinement results for $\text{Na}_3\text{V}_2(\text{PO}_4)_2\text{F}_{1.5}\text{O}_{1.5}$ in (a) *Amam* space group and (b) *P4₂/mnm* space group at $\lambda = 0.8251 \text{ \AA}$.

The structures of $\text{Na}_3\text{V}_2(\text{PO}_4)_2\text{F}_{1.5}\text{O}_{1.5}$ ($y' = 1.5$) and $\text{Na}_3(\text{VO})_2(\text{PO}_4)_2\text{F}$ ($y' = 2.0$) were analyzed in both *Amam* and *P4₂/mnm* space groups. As shown in **Figure 2.10** and **Figure 2.12** and in good agreement with the observation made already for $\text{Na}_3\text{V}_2(\text{PO}_4)_2\text{F}_2\text{O}$ ($y' = 1.0$) [143], no peak splitting of the (400) and (040) diffraction lines

was observed. In order to discriminate between the two structural hypotheses (the orthorhombic unit cell versus the tetragonal one) for $\text{Na}_3\text{V}_2(\text{PO}_4)_2\text{F}_{1.5}\text{O}_{1.5}$ and $\text{Na}_3(\text{VO})_2(\text{PO}_4)_2\text{F}$, an in-depth analysis of the Fourier difference maps, of the bonds calculated for the PO_4 and $\text{VO}_4(\text{F},\text{O})_2$ polyhedra and of the Na^+-Na^+ distances, was required. Nonetheless, the results of the Fourier difference maps and the bond length analysis of $\text{Na}_3\text{V}_2(\text{PO}_4)_2\text{F}_{1.5}\text{O}_{1.5}$ and $\text{Na}_3(\text{VO})_2(\text{PO}_4)_2\text{F}$ by considering the *Amam* and *P4₂/mnm* space groups are so close and hence it was not easy to decide which is the best structural description for these compositions just by the use of SXRD. Furthermore, the crystal size of these phases was too small for a single crystal XRD study to be performed. Electron diffraction was also performed on these materials, but the Na^+ ions in $\text{Na}_3\text{V}_2(\text{PO}_4)_2\text{F}_{1.5}\text{O}_{1.5}$ were so mobile that under the electron, the high temperature polymorph indexed in the *I4/mmm* space group was detected. In the case of $\text{Na}_3(\text{VO})_2(\text{PO}_4)_2\text{F}$, the phase was unstable and decomposed under the electron beam.

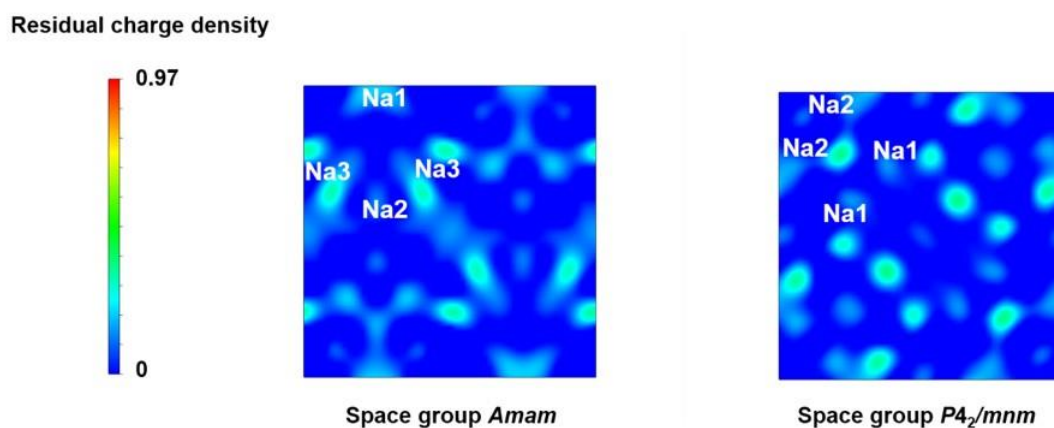


Figure 2.11 : Fourier difference maps calculated for $\text{Na}_3(\text{VO})_2(\text{PO}_4)_2\text{F}$ in *Amam* and *P4₂/mnm* space groups.

In the limit of the data obtained from SXRD, the obtained results suggest that the *Amam* description is the most appropriate one. Indeed, the Fourier difference maps calculated in the *Amam* space group show less charge residue than those calculated in the *P4₂/mnm* space group (**Figure 2.11**). The XRD patterns calculated in the *Amam* space group give a smaller number of diffraction lines (in *P4₂/mnm*, many are calculated with null intensities). Furthermore, longer Na^+-Na^+ distances were obtained in *Amam* and thus allowing a minimization of the electrostatic repulsions within the diffusion channels.

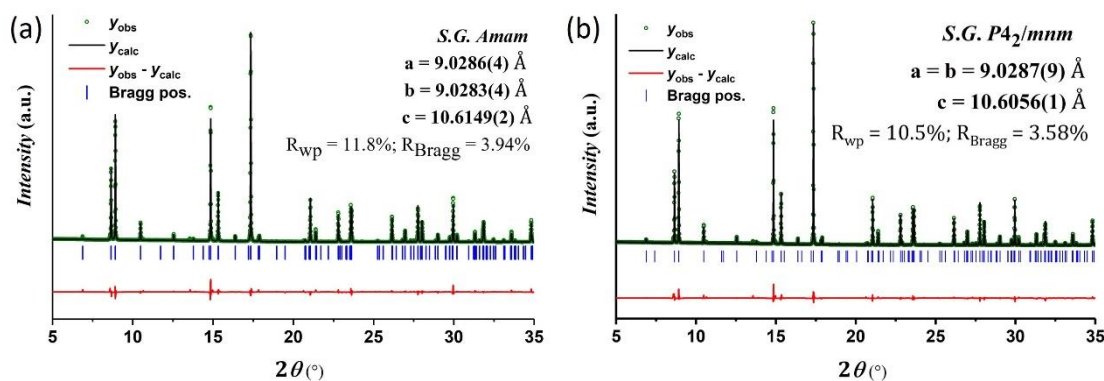


Figure 2.12 : Rietveld refinement results for $\text{Na}_3(\text{VO})_2(\text{PO}_4)_2\text{F}$ in (a) *Amam* space group and (b) *P4₂/mnm* space group at $\lambda = 0.8251 \text{ \AA}$.

The evolution of the cell parameters is given in **Figure 2.13**, in comparison with those reported by Park *et al.* [101], by Serras *et al.* [172] for oxygen-rich composition and by Tsirlin *et al.* [135] for the end member $\text{Na}_3(\text{VO})_2(\text{PO}_4)_2\text{F}$. Note that all these results are consistent and in very good agreement. Indeed, as shown in **Figure 2.13**, a linear decrease of a , b and c is observed with an increasing substitution of oxygen for fluorine: this latter is compensated by the oxidation of V^{3+} into V^{4+} and by the shrinking of the $\text{VO}_4(\text{F},\text{O})_2$ octahedra with the formation of more covalent $\text{V}-\text{O}$ bonds in the square planes and of vanadyl-type bonds along the axis of the bioctahedral units $\text{V}_2\text{O}_8(\text{F},\text{O})_3$. It shows the rather good miscibility between oxygen engaged into a vanadyl-type bond and fluorine, and thus allowing the formation of a solid solution between the two end members $\text{Na}_3\text{V}^{3+}_2(\text{PO}_4)_2\text{F}_3$ and $\text{Na}_3(\text{V}^{4+}\text{O})_2(\text{PO}_4)_2\text{F}$.

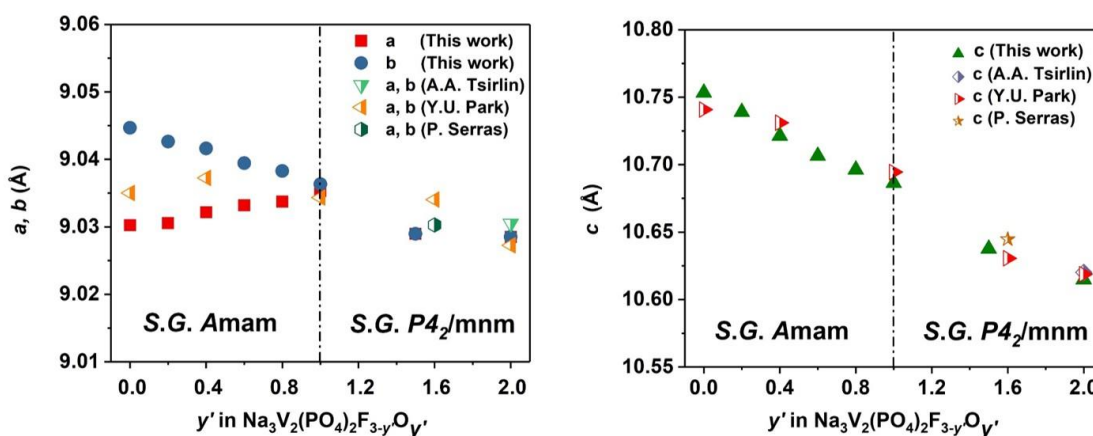


Figure 2.13 : The evolution of the unit cell parameters determined for $\text{Na}_3\text{V}_2(\text{PO}_4)_2\text{F}_{3-y'}\text{O}_{y'}$ ($0 \leq y' \leq 2$) materials obtained in our group (in this work, and by Broux *et al.* [14]), in comparison with those reported in the literature [7,13,30]. All the $\text{Na}_3\text{V}_2(\text{PO}_4)_2\text{F}_{3-y'}\text{O}_{y'}$ phases reported in the literature were indexed in the space group *P4₂/mnm*. By the use of high resolution synchrotron X-ray powder diffraction, a subtle orthorhombic distortion described in the space group *Amam* was detected in the phases such as $y' \leq 1$.

For the specific case of $\text{Na}_3(\text{VO})_2(\text{PO}_4)_2\text{F}$, as highlighted by the enlargements given in **Figure 2.14**, some low intensity diffraction peaks are not indexed in the orthorhombic cell. The doubling of the three unit cell parameters ($2a \times 2b \times 2c$) is required to index all the reflections, and in that case the smaller unit cell required to describe the structure is monoclinic ($P2_1/m$) with a modulation vector of $q = \frac{1}{2} b^* + \frac{1}{2} c^*$ (**Figure 2.14**, bottom) associated to the ordering of the Na^+ ions along the b and c axes. The distribution of the Na^+ ions within the diffusion channels and the modulation waves associated to each Na^+ site are given in **Figure 2.15** and **Table 2.2**. The single PO_4^{3-} anionic group present in the structure is such that the P–O bonds vary between 1.48 and 1.59 Å, whereas two vanadium sites are observed, one with a short V=O vanadyl type bond of 1.53 Å and the other one with a longer V=O vanadyl type bond at 1.71 Å.

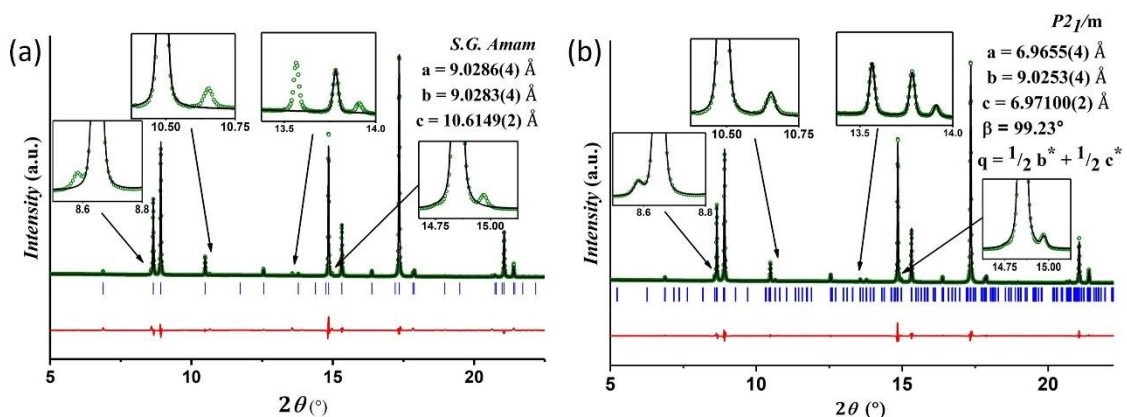


Figure 2.14 : (a) Rietveld refinement of synchrotron powder X-ray diffraction of $\text{Na}_3(\text{VO})_2(\text{PO}_4)_2\text{F}$ (after washing) recorded at $\lambda = 0.8251$ Å in the *Amam* space group. The zooms on the figure show the presence of some low intensity diffraction peaks that are not indexed, (b) The refinement of synchrotron powder X-ray diffraction of $\text{Na}_3(\text{VO})_2(\text{PO}_4)_2\text{F}$ refined in the $P2_1/m$ space group with a modulation vector of $q = \frac{1}{2} b^* + \frac{1}{2} c^*$.

Electron diffraction experiments were performed to try to confirm the monoclinic unit cell and the presence of a modulation vector. Unfortunately, the sample was unstable and decomposed under the electron beam, at ambient and low temperatures.

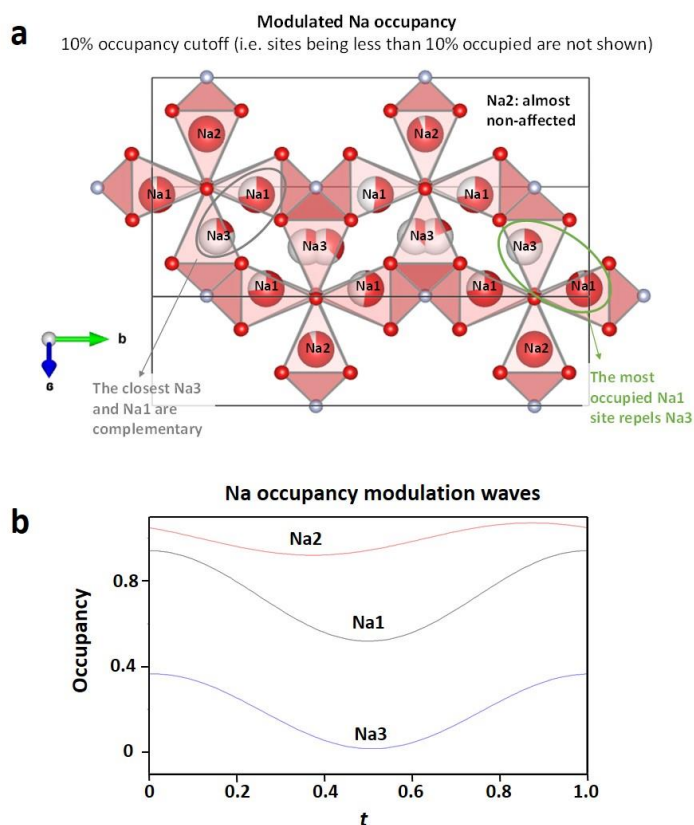


Figure 2.15 : (a) Proposed modulated structure of $\text{Na}_3(\text{VO})_2(\text{PO}_4)_2\text{F}$, and (b) The Na occupancy modulation waves.

Table 2.2 : Atomic positions in $\text{Na}_3(\text{VO})_2(\text{PO}_4)_2\text{F}$ by considering the $P2_1/m$ space group.

| Atoms | x | y | z | Occupancy | B_{iso} |
|---------------|-----------|-----------|-----------|-----------|------------------|
| V (1) | 0.0496(1) | 0.25 | 0.9473(3) | 1 | 0.11(1) |
| V (2) | 0.4474(2) | 0.25 | 0.5487(2) | 1 | 0.11(1) |
| P (2) | 0.2544(4) | 0.0028(3) | 0.2460(5) | 1 | 0.08(1) |
| O (1) | 0.2375(3) | 0.0948(4) | 0.0667(2) | 1 | 0.10(1) |
| O (2) | 0.0594(4) | 0.5898(3) | 0.2426(2) | 1 | 0.10(1) |
| O (3) | 0.4464(3) | 0.5902(4) | 0.2553(5) | 1 | 0.10(1) |
| O (4) | 0.2731(4) | 0.0915(3) | 0.4269(5) | 1 | 0.10(1) |
| O (5) | 0.6010(4) | 0.25 | 0.3807(5) | 1 | 0.10(1) |
| O (6) | 0.9160(5) | 0.25 | 0.1022(3) | 1 | 0.10(1) |
| F (1) | 0.2474(3) | 0.25 | 0.7473(3) | 1 | 0.10(1) |
| Na (1) | 0.7833(4) | 0.0224(3) | 0.2882(3) | 0.73 | 1.0(1) |
| Na (2) | 0.5046(2) | 0.25 | 0.0128(2) | 0.99 | 1.0(1) |
| Na (3) | 0.0195(3) | 0.7008(2) | 0.5351(3) | 0.19 | 1.0(1) |

The cell parameters of all the Na₃V₂(PO₄)₂F_{3-y'}O_{y'} (0 ≤ y' ≤ 2) phases indexed in the *Amam* space group are given in **Table 2.3**. For comparison purpose, the *Amam* space group was applied for Na₃(VO)₂(PO₄)₂F, not the absolute space group *P2₁/m* with the modulation vector.

Table 2.3 : Unit cell parameters of Na₃V₂(PO₄)₂F_{3-y'}O_{y'} (0 ≤ y' ≤ 2). For y' = 1.5 and y' = 2.0, the two unit cells (orthorhombic and tetragonal) could not be clearly discriminated by Rietveld analysis of the diffraction data.

| y' value | Composition | S.G. | a (Å) | b (Å) | c (Å) | V/Z (Å ³) |
|----------|--------------------------------------------------------------------------------------------------|-------------|------------|------------|-------------|-----------------------|
| 0.0 | Na ₃ V ₂ (PO ₄) ₂ F ₃ | <i>Amam</i> | 9.02847(3) | 9.04444(3) | 10.74666(6) | 219.386(6) |
| 0.2 | Na ₃ V ₂ (PO ₄) ₂ F _{2.8} O _{0.2} | <i>Amam</i> | 9.0308(1) | 9.0429(1) | 10.7389(1) | 219.248(1) |
| 0.4 | Na ₃ V ₂ (PO ₄) ₂ F _{2.6} O _{0.4} | <i>Amam</i> | 9.0322(1) | 9.0412(1) | 10.7213(1) | 218.885(1) |
| 0.6 | Na ₃ V ₂ (PO ₄) ₂ F _{2.4} O _{0.6} | <i>Amam</i> | 9.0336(1) | 9.0396(1) | 10.7065(1) | 218.576(1) |
| 0.8 | Na ₃ V ₂ (PO ₄) ₂ F _{2.2} O _{0.8} | <i>Amam</i> | 9.0337(1) | 9.0383(1) | 10.6962(1) | 218.337(1) |
| 1.0 | Na ₃ V ₂ (PO ₄) ₂ F ₂ O | <i>Amam</i> | 9.0353(1) | 9.0375(1) | 10.6863(1) | 218.151(1) |
| 1.5 | Na ₃ V ₂ (PO ₄) ₂ F _{1.5} O _{1.5} | <i>Amam</i> | 9.0289(2) | 9.0289(2) | 10.6374(5) | 216.793(3) |
| 2.0 | Na ₃ (VO) ₂ (PO ₄) ₂ F | <i>Amam</i> | 9.0286(4) | 9.0283(4) | 10.6149(2) | 216.313(2) |

IR spectroscopy was used in order to get a better insight into the formation of the vanadyl-type bonds and their spreading within the framework of Na₃V³⁺_{2-y'}V⁴⁺_{y'}(PO₄)₂F_{3-y'}O_{y'} with y' such as 0 ≤ y' ≤ 2. The comparison of the overall spectra is given in **Figure 2.16** in the wavenumber range of 400 - 3000 cm⁻¹, and the corresponding enlargements in **Figure 2.6d** in the wavenumber range of 800 - 1300 cm⁻¹. The tiny stretching mode observed at ~ 940 cm⁻¹ for Na₃V₂(PO₄)₂F₃ corresponds to the localized V=O vanadyl-type defects present in a fluorine-rich composition [136,173]. Two vibrational bands are observed at ~ 910 cm⁻¹ and ~ 940 cm⁻¹ when oxygen is partially substituted for fluorine in Na₃V³⁺_{2-y'}V⁴⁺_{y'}(PO₄)₂F_{3-y'}O_{y'}, their overtone bands being at ~ 1840 cm⁻¹ and ~ 1870 cm⁻¹, respectively. The intensity of the signal at ~ 910 cm⁻¹ increases while that at ~ 940 cm⁻¹ decreases when the y' value moves from 0 to 2, and the vibration at ~ 940 cm⁻¹ is very similar to the vanadyl stretching mode observed for Na₃V₂(PO₄)₂F₃. The presence of these two signals indicates two different local environments for the vanadyl bond V=O: the one at 940 cm⁻¹ would correspond to vanadyl bonds with a V-F bond opposite along the axis of the bioctahedral unit, and that at 910 cm⁻¹ to vanadyl bonds with a V=O bond opposite along the axis of the bioctahedral unit.

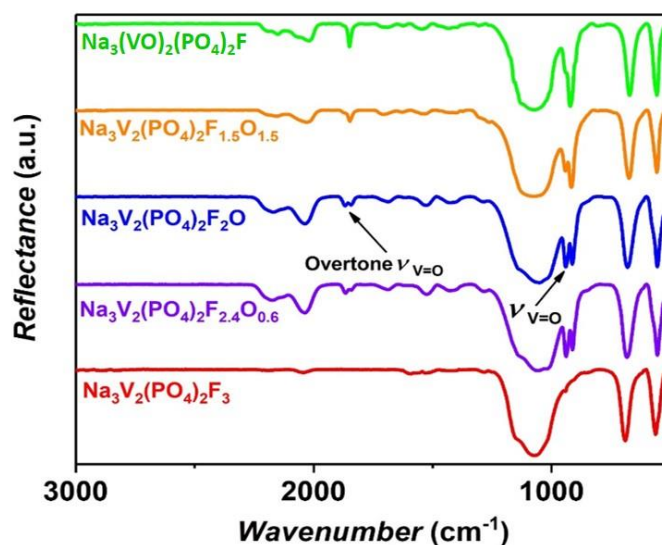


Figure 2.16 : The IR spectra of $\text{Na}_3\text{V}_2(\text{PO}_4)_2\text{F}_3$, $\text{Na}_3\text{V}_2(\text{PO}_4)_2\text{F}_{2.4}\text{O}_{0.6}$, $\text{Na}_3\text{V}_2(\text{PO}_4)_2\text{F}_2\text{O}$, $\text{Na}_3\text{V}_2(\text{PO}_4)_2\text{F}_{1.5}\text{O}_{1.5}$, and $\text{Na}_3(\text{VO})_2(\text{PO}_4)_2\text{F}$ powders recovered after washing in the wavenumber range of 400 - 3000 cm^{-1} . No vibrational frequency of V=O bond was detected in $\text{Na}_3\text{V}_2(\text{PO}_4)_2\text{F}_3$, while the characteristic stretching modes of V=O bond at $\sim 900 \text{ cm}^{-1}$, and $\sim 1800 \text{ cm}^{-1}$ (overtone) were observed in other compounds.

A comparison of the structures of $\text{Na}_3\text{V}_2(\text{PO}_4)_2\text{F}_{1.5}\text{O}_{1.5}$ and $\text{Na}_3(\text{VO})_2(\text{PO}_4)_2\text{F}$ with those we previously reported for $\text{Na}_3\text{V}^{3+}_{2-2y'}\text{V}^{4+}_{y'}(\text{PO}_4)_2\text{F}_{3-y'}\text{O}_{y'}$ ($0 \leq y' \leq 1$) shows that the orthorhombic structural model is the most appropriate one to describe the overall solid solution $\text{Na}_3\text{V}_2(\text{PO}_4)_2\text{F}_3 - \text{Na}_3(\text{VO})_2(\text{PO}_4)_2\text{F}$. In the case of $\text{Na}_3(\text{VO})_2(\text{PO}_4)_2\text{F}$, its absolute structure should be described in the $P2_1/m$ space group with a modulation vector in order to take into account the long-range Na^+ ions ordering.

II.3.4. Electrochemical properties

The electrochemical properties of $\text{Na}_3\text{V}_2(\text{PO}_4)_2\text{F}_2\text{O}$, $\text{Na}_3\text{V}_2(\text{PO}_4)_2\text{F}_{1.5}\text{O}_{1.5}$ and $\text{Na}_3(\text{VO})_2(\text{PO}_4)_2\text{F}$ as positive electrodes in half cells vs. Na are compared in **Figure 2.17** to those of our reference [131], optimized carbon-coated $\text{Na}_3\text{V}_2(\text{PO}_4)_2\text{F}_3$. The electrochemical profiles were obtained at a cycling rate of C/10 per Na^+ in the potential range 2.5 – 4.3 V vs. Na^+/Na . As expected larger polarizations are observed for the oxygen substituted compositions as the materials were not carbon coated. Nevertheless, for all the compositions, about two Na^+ ions can be extracted reversibly in two voltage domains in this potential window: the first Na^+ ion at 3.6 – 3.7 V vs Na^+/Na and the second Na^+ ion at 4.0 – 4.20 V vs Na^+/Na .

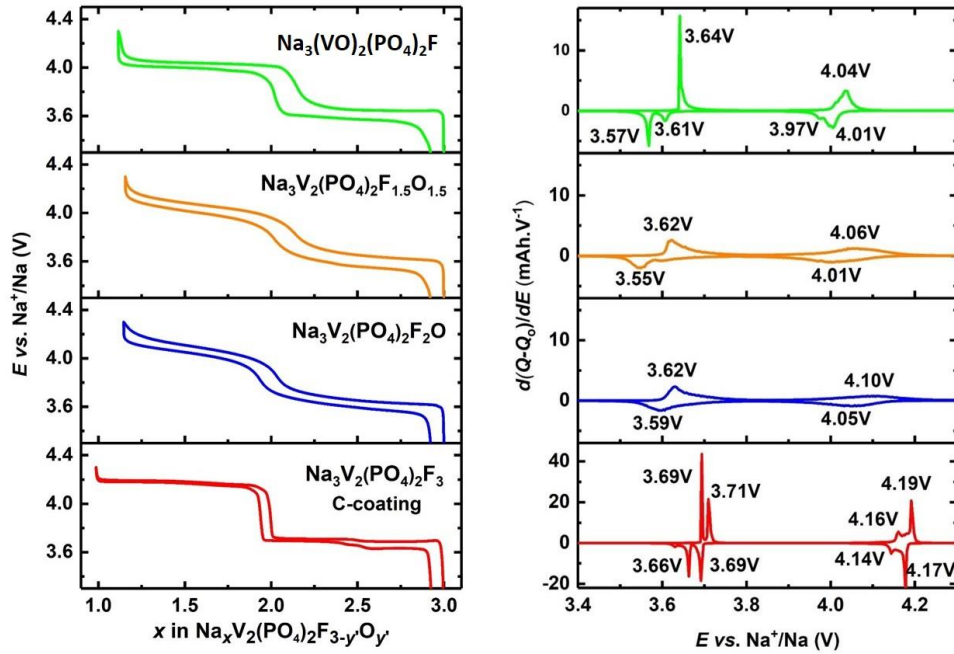


Figure 2.17 : (Left) Comparison of the electrochemical charge/discharge curves obtained for the carbon-coated $\text{Na}_3\text{V}_2(\text{PO}_4)_2\text{F}_3$, $\text{Na}_3\text{V}_2(\text{PO}_4)_2\text{F}_2\text{O}$, $\text{Na}_3\text{V}_2(\text{PO}_4)_2\text{F}_{1.5}\text{O}_{1.5}$ and $\text{Na}_3(\text{VO})_2(\text{PO}_4)_2\text{F}$ in sodium half cells at the cycling rate of $C/10$ per Na^+ ion, (Right) The first derivatives of the corresponding electrochemical curves.

For the two end members $\text{Na}_3\text{V}_2(\text{PO}_4)_2\text{F}_3$ ($y' = 0$) and $\text{Na}_3(\text{VO})_2(\text{PO}_4)_2\text{F}$ ($y' = 2$), voltage-composition “plateaus” can be observed that imply the formation of several intermediate phases during charge/discharge, whose crystal structures were reported by Bianchini *et al.* [132] and Sharma *et al.* [146], respectively. For the compositions corresponding to partial oxygen substitution for fluorine in $\text{Na}_3\text{V}^{3+}_{2-y'}\text{V}^{4+}_{y'}(\text{PO}_4)_2\text{F}_{3-y'}\text{O}_{y'}$, the voltage-composition signatures are sloping indicating solid solution type mechanisms, with a continuous Na^+ deintercalation and re-intercalation from/in the structure during charge/discharge. In these systems, phase transitions - when observed - are associated to charge and/or alkali orderings. In fact, no superstructure was observed in the pristine materials $\text{Na}_3\text{V}^{3+}_{2-y'}\text{V}^{4+}_{y'}(\text{PO}_4)_2\text{F}_{3-y'}\text{O}_{y'}$ ($y' \neq 0, y' \neq 2$) showing that V^{3+} and V^{4+} (as well as the terminal O and F anions in the biocahedral units) are statistically distributed within the framework, and thus not ordered. On the contrary, for the V^{3+} only composition $\text{Na}_3\text{V}_2(\text{PO}_4)_2\text{F}_3$ and for the V^{4+} only composition $\text{Na}_3(\text{VO})_2(\text{PO}_4)_2\text{F}$, charge and alkali orderings can be stabilized, and are indeed observed, as they allow to minimize (i) the strains within the host structure (with the homogeneous distribution of the bond lengths) and (ii) the electrostatic repulsions between the alkali ions within the diffusion channels. It is also interesting to highlight that the average voltage corresponding to Na^+ extraction decreases continuously upon oxygen substitution for fluorine. This decrease is

induced by the formation of strongly covalent vanadyl-type bonds that induce a so-called “reverse inductive effect” and promote the activation of the $\{\text{V}^{5+}=\text{O}\}^{3+}/\{\text{V}^{4+}=\text{O}\}^{2+}$ redox couple at lower voltage.

Theoretically more than two Na^+ ions can be electrochemically extracted per formula unit of $\text{Na}_3\text{V}^{3+}_{2-y}\text{V}^{4+}_y(\text{PO}_4)_2\text{F}_{3-y}\text{O}_y$, up to three Na^+ ions for $\text{Na}_3\text{V}_2(\text{PO}_4)_2\text{F}_3$ with an oxidation of V^{3+} to an average oxidation state of $\text{V}^{4.5+}$. The reversible deintercalation and reintercalation of 3 Na^+ ions would lead to an increase of the capacity delivered by $\text{Na}_3\text{V}_2(\text{PO}_4)_2\text{F}_3$ of 50%. Very recently, a third voltage-composition plateau that would correspond to the extraction of an extra 0.5 Na^+ was observed at 4.75 V vs. Na^+/Na for $\text{Na}_3\text{V}_2(\text{PO}_4)_2\text{F}_3$ [152]. This overall extraction of 2.5 Na^+ ions during the first charge apparently leads to an irreversible transformation of the structure with the formation of a so-called new modification of $\text{Na}_3\text{V}_2(\text{PO}_4)_2\text{F}_3$ described in a disordered tetragonal structure ($I4/mmm$) that allows for the re-insertion of only 1.5 Na^+ in the potential window of interest for applications. It was hence interesting to consider the behavior of oxygen substituted $\text{Na}_3\text{V}^{3+}_{2-y}\text{V}^{4+}_y(\text{PO}_4)_2\text{F}_{3-y}\text{O}_y$ at high voltages.

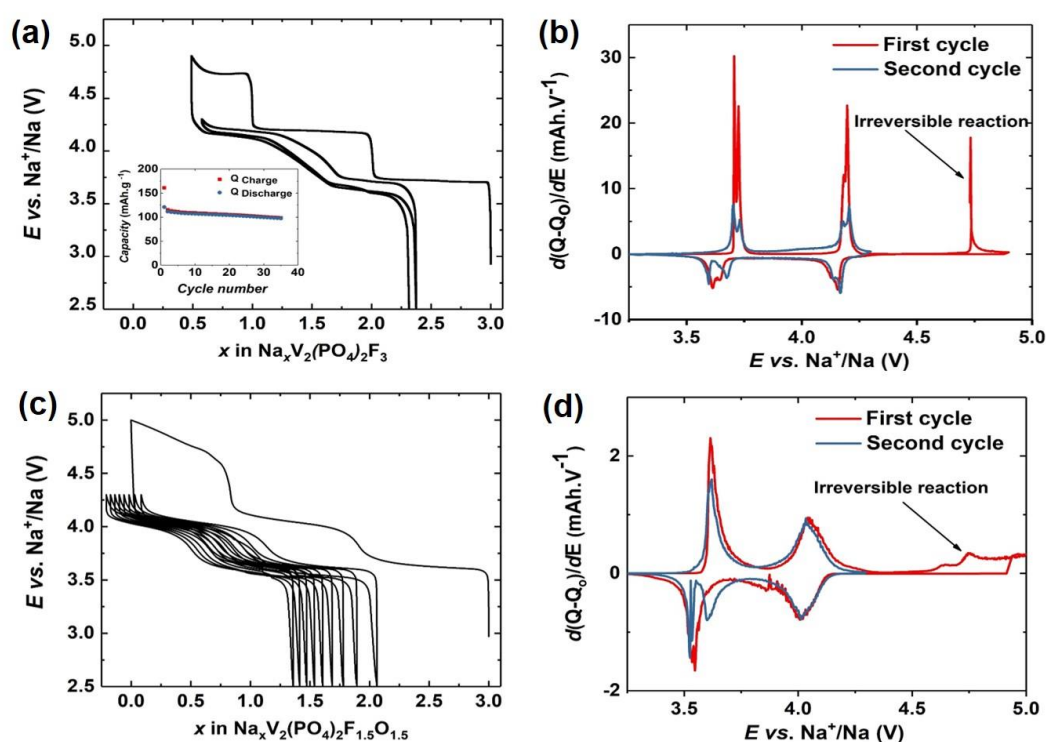


Figure 2.18 : (a) The electrochemical profile recorded for a $\text{Na}/\text{Na}_3\text{V}_2(\text{PO}_4)_2\text{F}_3$ half-cell during the first and the second cycles, the voltage window being widened up to 5.0 V vs. Na^+/Na during the first cycle. The inset gives the corresponding charge/discharge capacities as a function of the cycle number, (b) The corresponding first derivative curves calculated for the first and second cycles. Irreversible reaction is highlighted by an arrow, (c) The electrochemical profile recorded for a $\text{Na}/\text{Na}_3\text{V}_2(\text{PO}_4)_2\text{F}_{1.5}\text{O}_{1.5}$ half-cell during several cycles, the voltage window being widened up to 5.0 V vs. Na^+/Na during the first cycle, (d) The corresponding first derivative curves.

Figure 2.18 gives the comparison of $\text{Na}_3\text{V}_2(\text{PO}_4)_2\text{F}_3$ and $\text{Na}_3\text{V}_2(\text{PO}_4)_2\text{F}_{1.5}\text{O}_{1.5}$ when used as positive electrodes electrochemically cycled up to 5 V vs. Na^+/Na . Theoretically 3 Na^+ ions can be deintercalated from $\text{Na}_3\text{V}_2(\text{PO}_4)_2\text{F}_3$ with the oxidation of vanadium up to an average oxidation state of +4.5 thus being an ion-limited reaction. In the case of $\text{Na}_3\text{V}_2(\text{PO}_4)_2\text{F}_{1.5}\text{O}_{1.5}$, 2.5 Na^+ ions should be extracted with the oxidation of vanadium up to the average oxidation state of +5 and thus a redox-limited reaction. The data plotted in **Figure 2.18** confirm that in continuous galvanostatic cycling conditions at $C/10$ per Na^+ ion, a third plateau is indeed observed during the first charge of $\text{Na}/\text{Na}_3\text{V}_2(\text{PO}_4)_2\text{F}_3$ at high voltage. It corresponds to a voltage jump of 0.5 V after the deintercalation of 2 Na^+ ions from the structure and to an additional exchange of 0.5 extra electrons, in good agreement with the results already reported by Yan *et al.* [152].

The derivative curves of the first and second cycles given in **Figure 2.18b** confirm the irreversible transformation occurring along the third plateau, with sharp peaks associated to successive biphasic reactions during the first charge and then, during the next discharge and cycles, broader peaks showing a drastic change in the reaction mechanism. The inset in **Figure 2.18a** compares the evolution of the charge and discharge capacity upon cycling and highlights that the overcapacity is only observed during the first charge at high voltage and is never recovered then in the potential window practically required for a Na-ion battery developed for applications. For $\text{Na}/\text{Na}_3\text{V}_2(\text{PO}_4)_2\text{F}_{1.5}\text{O}_{1.5}$ a voltage jump of ~ 0.5 V is observed at high voltage, as for $\text{Na}_3\text{V}_2(\text{PO}_4)_2\text{F}_3$, after the deintercalation of 2 Na^+ ions from the structure of $\text{Na}_3\text{V}_2(\text{PO}_4)_2\text{F}_{1.5}\text{O}_{1.5}$. No third plateau is observed but rather a continuous voltage increase when the upper voltage limit is increased to 5 V vs Na^+/Na until the full Na^+ deintercalation from $\text{Na}_x\text{V}_2(\text{PO}_4)_2\text{F}_{1.5}\text{O}_{1.5}$ (**Figure 2.18c**). The “deintercalation” up to a composition of “ $x = 0$ ” is intriguing and unexpected, as the number of transition metal redox centers is such limited that only the exchange of 2.5 Na^+ would be possible. This extra capacity observed in the high-voltage region for $\text{Na}/\text{Na}_3\text{V}_2(\text{PO}_4)_2\text{F}_{1.5}\text{O}_{1.5}$ would thus be associated with the degradation of the electrolyte. This hypothesis is further supported by the fact that, on the contrary to the observation made for $\text{Na}_3\text{V}_2(\text{PO}_4)_2\text{F}_3$, the first charge to high voltage does not induce any modification of the next cycles, as also highlighted by the derivative curves given in **Figure 2.18d**.

II.3.5. *Operando* X-ray absorption spectroscopy

In order to get more insight into the redox processes involved during these first charges to high voltage, analyses were performed *operando*, during the operation of the batteries, by X-ray absorption spectroscopy (XAS) at the Vanadium K-edge. The electrochemical data recorded in the *in situ* electrochemical cells are given in **Figure 2.19a** and **Figure 2.19c** for $\text{Na}/\text{Na}_3\text{V}_2(\text{PO}_4)_2\text{F}_3$ and $\text{Na}/\text{Na}_3\text{V}_2(\text{PO}_4)_2\text{F}_{1.5}\text{O}_{1.5}$ respectively.

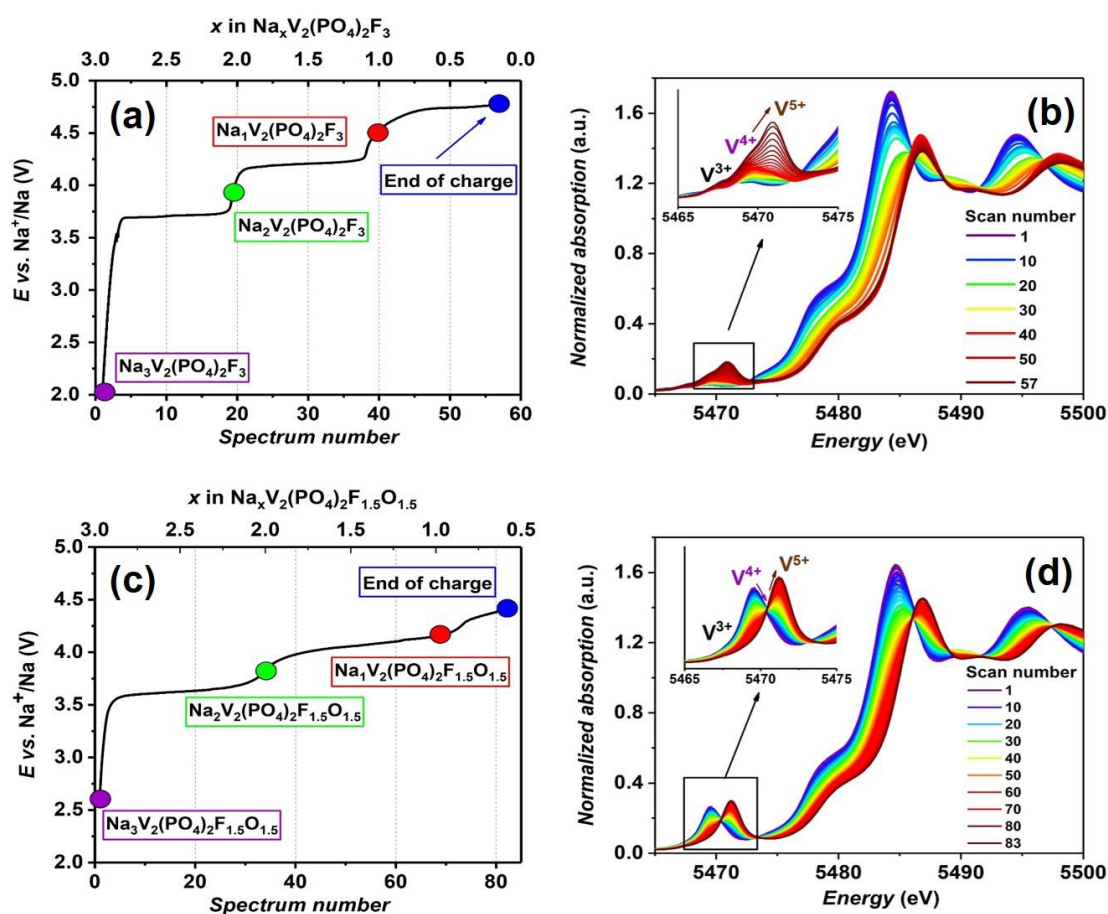


Figure 2.19 : (a) The correlation between the electrochemical profile and the XANES spectra recorded *operando* during the cycling of the cell $\text{Na}/\text{Na}_3\text{V}_2(\text{PO}_4)_2\text{F}_3$ at $C/5$ per Na^+ ion, (b) *Operando* Vanadium K-edge XANES spectra recorded during Na^+ deintercalation from $\text{Na}_3\text{V}_2(\text{PO}_4)_2\text{F}_3$. The inset focuses on the pre-edge region, (c) The correlation between the electrochemical profile and the XANES spectra recorded *operando* during the cycling of the cell $\text{Na}/\text{Na}_3\text{V}_2(\text{PO}_4)_2\text{F}_{1.5}\text{O}_{1.5}$ at $C/10$ per Na^+ ion, (d) *Operando* Vanadium K-edge XANES spectra recorded during Na^+ deintercalation from $\text{Na}_3\text{V}_2(\text{PO}_4)_2\text{F}_{1.5}\text{O}_{1.5}$. The inset focuses on the pre-edge region.

Broux *et al.* have shown, especially by the analysis of the pre-edge of the XAS spectra, that the deintercalation of the first Na^+ ion from $\text{Na}_3\text{V}_2(\text{PO}_4)_2\text{F}_3$ was associated to the formation of $\text{V}^{3+}-\text{V}^{4+}$ pairs in the bioctahedral units. The subsequent

deintercalation of the second Na^+ ion leads to the formation of $\text{V}^{3+}-\text{V}^{5+}$ pairs [133]. Indeed, significant modifications were observed during the oxidation of V^{3+} into V^{4+} and V^{5+} with a global shift to higher energy for the pre-edge and for the edge upon oxidation. The presence of V^{5+} in $\text{Na}_1\text{V}_2(\text{PO}_4)_2\text{F}_3$ at 4.3 V vs. Na^+/Na was supported by the observation of a characteristic signal at 5471 eV [133].

Similar results were obtained in the present study, as shown in **Figure 2.19b**, and as highlighted by the changes observed between the spectra #1, #20 and #40. Surprisingly, upon further Na^+ deintercalation, no shift of the absorption edge is observed between the spectrum #40 corresponding to $\text{Na}_1\text{V}_2(\text{PO}_4)_2\text{F}_3$ and the spectrum #57 recorded at the end of the charge and corresponding to a theoretical composition of $\text{Na}_{-0.15}\text{V}_2(\text{PO}_4)_2\text{F}_3$ (**Figure 2.20a**, and **Figure 2.21** that gives the evolution in the energy of the absorption edge). This result suggests that vanadium does not participate at all into the redox processes in this potential domain (on the third plateau). Indeed, a careful inspection of the XANES results show that only the pre-edge is modified with an increase of the intensity versus that observed for the spectrum #40: this suggests that the local environment around vanadium is increasingly distorted, and thus that significant modification of the vanadium environment is observed, but not of the vanadium oxidation state. Note that similar results are observed in [152] in Figure 7b-c, even if interpreted differently, with a great similarity between the spectra recorded at the Vanadium L-edge and Oxygen K-edge on the compositions assumed to be $\text{Na}_1\text{V}_2(\text{PO}_4)_2\text{F}_3$ and $\text{Na}_{0.25}\text{V}_2(\text{PO}_4)_2\text{F}_3$. These results suggest a drastic reorganization and instability of the structure of $\text{Na}_1\text{V}_2(\text{PO}_4)_2\text{F}_3$ when the battery is overcharged. The XRD and NMR results reported in [152] suggest in fact a strong degradation of the long range atomic structure. At this stage of our understanding, we suggest that the electrons exchanged at high voltage would be associated to the oxidation of the electrolyte, occurring in parallel to the structure degradation. This highly charged state has to be revisited considering this hypothesis, and considering especially the Na/V ratio.

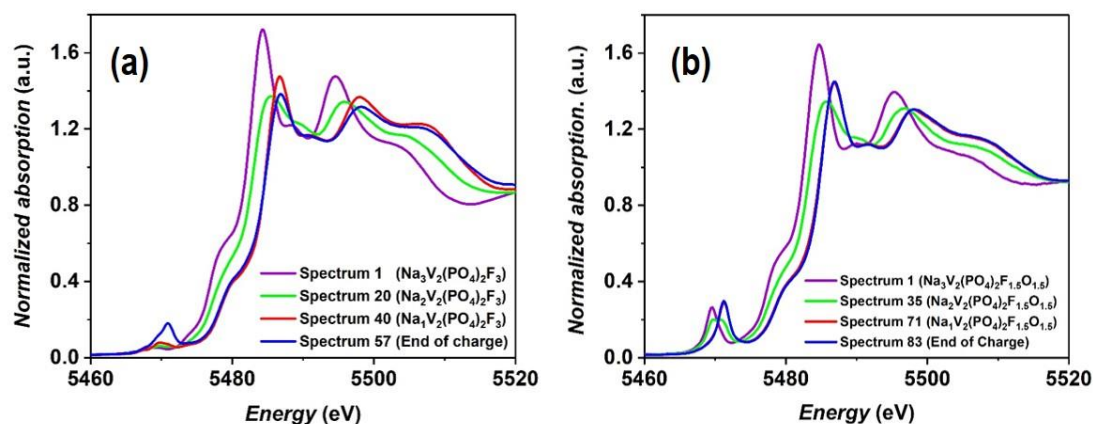


Figure 2.20 : (a) A comparison of the Vanadium K edge XANES spectra recorded for a $\text{Na}/\text{Na}_3\text{V}_2(\text{PO}_4)_2\text{F}_3$ half-cell at some critical points: beginning of the charge (Spectrum #1), at the end of the first plateau on charge (Spectrum #20), at the end of the second plateau on charge (Spectrum #40), and at the end of the third plateau on charge (Spectrum #57), (b) A comparison of the Vanadium K edge XANES spectra recorded on a $\text{Na}/\text{Na}_3\text{V}_2(\text{PO}_4)_2\text{F}_{1.5}\text{O}_{1.5}$ half-cell at some critical points: beginning of the charge (Spectrum #1), formation of $\text{Na}_2\text{V}_2(\text{PO}_4)_2\text{F}_{1.5}\text{O}_{1.5}$ (Spectrum #35), formation of $\text{Na}_1\text{V}_2(\text{PO}_4)_2\text{F}_{1.5}\text{O}_{1.5}$ (Spectrum #70), and at the end of the charge (Spectrum #83). The spectra #71 and #83 are very similar as there is no change in the Vanadium oxidation state and in its local environment.

Interestingly, the XAS spectrum of $\text{Na}_3\text{V}_2(\text{PO}_4)_2\text{F}_{1.5}\text{O}_{1.5}$ is significantly different from that of $\text{Na}_3\text{V}_2(\text{PO}_4)_2\text{F}_3$, with an additional intense signal at 5469.5 eV in the pre-edge region (**Figure 2.19d** and **Figure 2.19b**). Indeed, in this mixed valence composition, the stoichiometry is such that one V^{3+} exists besides three V^{4+} , those being engaged in vanadyl-type bonds $\{\text{V}^{4+}=\text{O}\}^{2+}$. The environments of V^{3+} are ‘quasi’-symmetric $\text{VO}_4(\text{F},\text{O})_2$ sites with six $\text{V}^{3+}-\text{F}/\text{O}$ bond lengths around 1.9 – 2.0 Å, whereas those of V^{4+} are highly distorted $\text{VO}_4\text{O}(\text{F},\text{O})$ sites with a long $\text{V}^{4+}-\text{F},\text{O}$ bond around 2.2 Å and a short and highly covalent $\text{V}^{4+}=\text{O}$ bond around 1.6 Å [83,135,169]. These latter vanadyl-type environments are in fact responsible for the intense signal at 5469.5 eV.

Upon charge, this signal decreases gradually in intensity while a new signal grows at 5471.5 eV (**Figure 2.20b**, spectra #1 to #71). At the same time, a continuous shift of the absorption edge is also observed from 5481.9 eV for the spectrum #1 to 5484.6 eV for the spectrum #70. These evolutions confirm the oxidation of vanadium in the voltage range 3.56 - 4.12 V vs. Na^+/Na . Nevertheless, all the spectra recorded at higher voltage remain identical (see **Figure 2.20b** that compares the spectrum #71 and the final spectrum #83), showing also that the overcapacity observed is not associated with the participation of vanadium to the redox processes, but most probably also to electrolyte decomposition. In that case, on the contrary to the observations made for $\text{Na}_3\text{V}_2(\text{PO}_4)_2\text{F}_3$ no modification of the pre-edge is observed, suggesting that the local structure around vanadium remains the same.

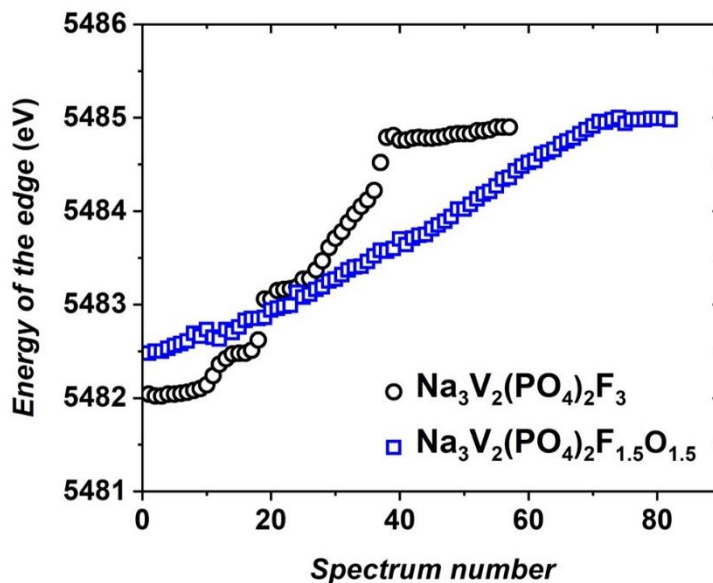


Figure 2.21 : The evolution of the energy of the absorption edge (taken at normalized intensity = 1.0) of *operando* Vanadium K edge XANES spectra recorded for a $\text{Na}/\text{Na}_3\text{V}_2(\text{PO}_4)_2\text{F}_3$ half-cell and a $\text{Na}/\text{Na}_3\text{V}_2(\text{PO}_4)_2\text{F}_{1.5}\text{O}_{1.5}$ half-cell.

It is interesting to highlight that the highly deintercalated $\text{Na}_x\text{V}_2(\text{PO}_4)_2\text{F}_3$ has been predicted to be thermodynamically unstable by theoretical calculations [119,129]. In our opinion it has thus to be considered with careful attention, considering especially the results just discussed. Furthermore, as mentioned earlier, partial oxygen substitution for fluorine could be seen as a stabilizing factor in the overcharge state of the battery. Indeed, the highly deintercalated $\text{Na}_x\text{V}_2(\text{PO}_4)_2\text{F}_{1.5}\text{O}_{1.5}$ appears to be stable, at least over a few cycles. Finally, it is also interesting to mention that, if it occurs or if it should occur, the overcapacity associated with the deintercalation of extra Na^+ ions (*vs.* the “classical” 2 Na^+ ions) should be obtained at lower potential for $\text{Na}_3\text{V}_2(\text{PO}_4)_2\text{F}_{1.5}\text{O}_{1.5}$, as oxygen substitution for fluorine was shown to shift down the average voltage of the reaction. This absence of the third plateau for $\text{Na}_3\text{V}_2(\text{PO}_4)_2\text{F}_{1.5}\text{O}_{1.5}$ is perhaps another argument to question further the origin of the mechanism involved at high voltage.

II.3.6. The paradox of Vanadium redox couple in $\text{Na}_3\text{V}_2(\text{PO}_4)_2\text{F}_{3-y}\text{O}_y$

II.3.6.1. $\text{Na}_3\text{V}_2(\text{PO}_4)_2\text{F}_3$

II.3.6.1.1. First charge up to 4.8 V vs. Na^+/Na

The *operando* Vanadium K-edge XAS data set recorded on the $\text{Na}/\text{Na}_3\text{V}_2(\text{PO}_4)_2\text{F}_3$ half-cell during the first charge up to 4.8 V vs. Na^+/Na (**Figure 2.19b**) was globally analyzed using the chemometric approach, based on a combination of Principal Component Analysis (PCA) and Multivariate-Curve Resolution Alternating Least Squares (MCR-ALS) [174–176]. All the PCA and MCR-ALS analyses in this work were done in collaboration with Stéphanie Belin and Antonella Iadecola at the ROCK beamline at SOLEIL synchrotron facilities (Saint-Aubin, France). PCA allows to determine the minimum number of independent components required to describe the whole *operando* data set obtained during the electrochemical cycling. The number of principal components is then used as the basis for the MCR-ALS analysis [177,178], allowing the reconstruction of the principal orthogonal components needed to interpret the whole data set. In this study, the spectra reconstruction was done using the ‘Pure’ and ‘Evolving Factor Analysis’ (EFA) methods [179–181]. In order to produce chemically and physically meaningful results, the concentration profile of the principal components was constructed by applying the following constraints: (i) non-negative concentration value, (ii) unimodality (the concentration of each principal component can reach the maximum value only once), and (iii) closure (the sum of the concentration of all the components must be equal to one).

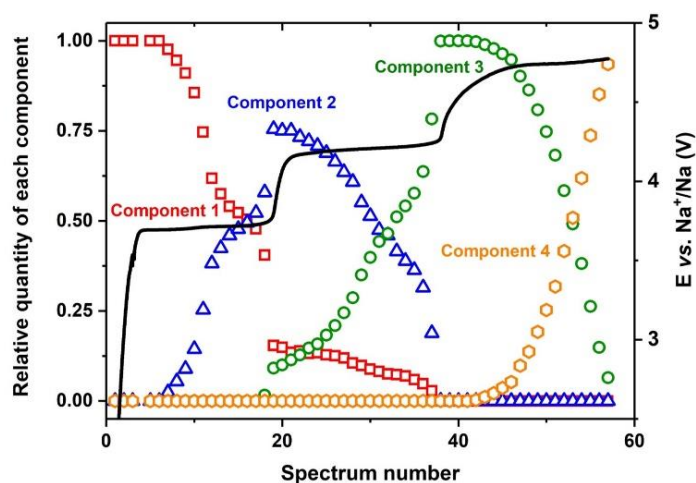


Figure 2.22 : Concentration profile of the four principal components required to describe the *operando* XAS spectra recorded on a $\text{Na}/\text{Na}_3\text{V}_2(\text{PO}_4)_2\text{F}_3$ half-cell upon charging from 2.5 - 4.8 V vs. Na^+/Na .

The variance plot obtained from the PCA analysis performed on the data set given in **Figure 2.19b** shows that four independent components are required to describe the whole system and their corresponding concentration profile is given in **Figure 2.22**. Broux *et al.* have earlier proposed that the natures of the first three principal components observed in the voltage range of 2.5 - 4.3 V *vs.* Na^+/Na are $\text{V}^{3+}\text{-F-V}^{3+}$, $\text{V}^{3+}\text{-F-V}^{4+}$ and $\text{V}^{3+}\text{-F-V}^{5+}$ bioctahedra, respectively [133]. By increasing the upper cutoff voltage to 4.8 V *vs.* Na^+/Na , the fourth component is observed (Orange points in **Figure 2.22**). As illustrated above, there is no change in the oxidation state of vanadium species on the third voltage plateau (**Figure 2.20a**), and hence the nature of this new component is still associated to $\text{V}^{3+}\text{-F-V}^{5+}$ bioctahedra, but the vanadium local structure is now highly distorted as indicated by a great increase in the intensity of the pre-edge signal (**Figure 2.20a**).

The XAS spectra of the principal components are reconstructed by the ‘Pure’ and EFA methods. The reconstructed XAS spectra obtained from the two mentioned methods are identical, and hence only the ‘Pure’ method will further be used to reconstruct the XAS spectra. The Fourier transformation and EXAFS analysis are performed on the reconstructed XAS spectra of the principal components in order to determine changes in vanadium local environments. The EXAFS analysis allows us to determine the metal-ligand distances as well as the Debye-Waller factor of the corresponding ligand. In $\text{Na}_3\text{V}_2(\text{PO}_4)_2\text{F}_3$, there exist $\text{V}_2\text{O}_8\text{F}_3$ bioctahedral units with two vanadium centers, hence there are 12 degrees of freedom for the distances and 11 other degrees of freedom for the Debye – Waller factors (**Figure 2.23**). The number of parameters that can be included in an EXAFS fit, however, is limited by:

$$N = 2 \cdot \Delta k \cdot \Delta R / \pi$$

with N : The number of parameters that can be fit independently

Δk : The k -range used in the forward Fourier transformation

ΔR : The R -range used in the backward Fourier transformation

In this study, the k -range is taken from 2.6 – 11.2 \AA^{-1} and the R -range of 1.0 – 2.1 \AA is generally used, thus a maximum of 5 independent parameters can be included in the EXAFS fit and a simplification of the Vanadium structural model is required. In order to reduce the number of variables, we thus assume that all the surrounding F/O ligands have the same Debye – Waller factor, the energy shift (E^0) and the attenuation factor (S_0^2)

being fixed at 0 and 1 for all the fits, respectively. In the case of $\text{Na}_3\text{V}_2(\text{PO}_4)_2\text{F}_3$, the SXRD data revealed that two V^{3+} sites in the same bioctahedron are equivalent and the V^{3+} local environment is highly symmetric [83,132], thus only one variable is used for all the distances in the EXAFS fit.

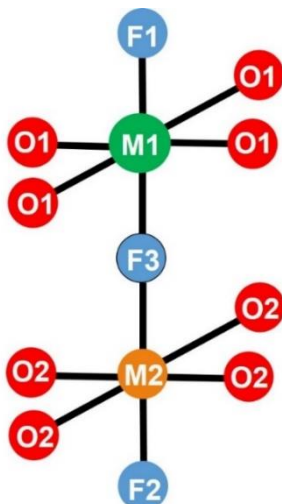


Figure 2.23 : Structure of a bioctahedral unit with its neighboring distances.

The fits of the k^2 -weighted Vanadium K-edge EXAFS spectra Fourier transform (k -range: $2.6 - 11.2 \text{ \AA}^{-1}$, sine window) in the R space and the corresponding fit of the real part of $\chi(q)$ corresponding to the reverse Fourier transform considering only the R -range $1.0 - 2.1 \text{ \AA}$ with $dR = 0 \text{ \AA}$ are shown in **Figure 2.24**. The most appropriate structural results must satisfy two conditions: (i) chemically reasonable and (ii) leading to the best fit in the R - and q -spaces.

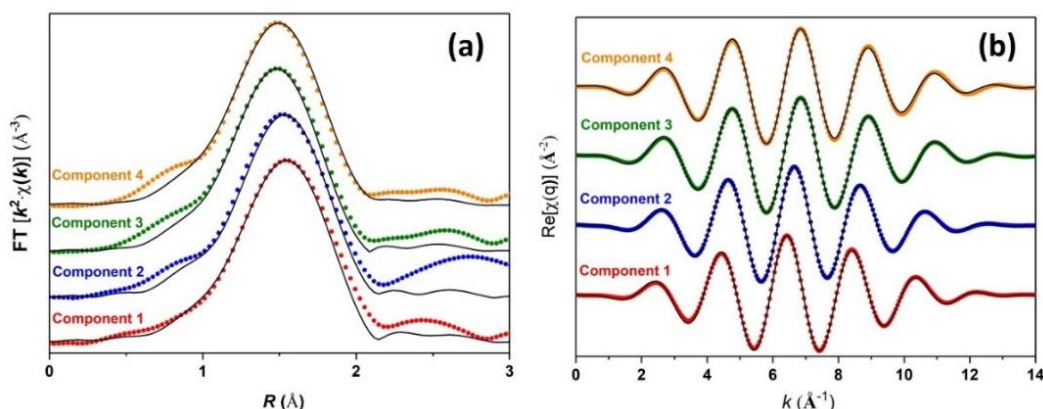


Figure 2.24 : (a) Fit of the k^2 -weighted Vanadium K-edge EXAFS spectra Fourier transform (k -range: $2.6 - 11.2 \text{ \AA}^{-1}$, sine window) in the R space (R -range: $1.0 - 2.1 \text{ \AA}$, $dR = 0$, sine window) for the four components determined by PCA. Their corresponding spectra were reconstructed by MCR-ALS with the 'Pure' method; (b) The corresponding fit of the real part of $\chi(q)$ corresponding to the backward Fourier transform by considering only the R -range $1.0 - 2.1 \text{ \AA}$ with $dR = 0 \text{ \AA}$. The circles represent the experimental data and the solid lines represent the fits.

The EXAFS fit performed on the Fourier transformed spectrum of the first component (pristine Na₃V₂(PO₄)₂F₃) shows that the V³⁺ site is symmetric with six equal V—O/F bond lengths (2.01 Å). These refined values are in agreement to those obtained by SXRD ($d_{V-O(1)} = 2.006(9)$ Å $\times 2$, $d_{V-O(2)} = 1.965(9)$ Å $\times 2$, $d_{V-F(1)} = 1.981(2)$ Å, and $d_{V-F(2)} = 1.968(6)$ Å) [83]. This is also in agreement with the observation of a very weak pre-edge signal on the Vanadium K-edge XANES spectrum recorded for the Na₃V₂(PO₄)₂F₃ phase and also at the beginning of charge.

Upon charging, one of the V³⁺ in the V³⁺—F—V³⁺ bioctahedron is gradually oxidized into V⁴⁺ forming a V³⁺—F—V⁴⁺ bioctahedron (Second component) with a slight contraction of all the surrounding V—O/F bond lengths around the V⁴⁺ center; nonetheless, the V³⁺ site is assumed to retain its octahedral symmetry [133]. The EXAFS data was fit by considering the presence of two different sites in the bioctahedron. The V³⁺ site is completely symmetric and one variable is used to represent its six surrounding V—O/F bonds while a slight distortion might occur on the opposite V⁴⁺ site and three distance variables are required: one for the four equatorial V⁴⁺—O bonds, one for the terminal V⁴⁺—F and one for the sharing V⁴⁺—F bond. One common Debye-Waller factor value was used for all the scatterers. On the second electrochemical plateau, V⁵⁺ is formed in the V³⁺—F—V⁵⁺ bioctahedron (Third component) [133] and the EXAFS spectrum is fit by the use of the same structural model as the one described for V³⁺—F—V⁴⁺ bioctahedron. The V—O/F bond lengths in the vanadium's first coordination sphere obtained from the EXAFS analysis of each principal components are summarized in **Table 2.4**.

Table 2.4 : V—O/F bond lengths in Vanadium's first coordination sphere obtained from the EXAFS analysis performed on the reconstructed XAS spectra of the four principal components required to describe the *operando* data set recorded on a Na/Na₃V₂(PO₄)₂F₃ half-cell upon charging up to 4.8 V vs. Na⁺/Na.

| | Symmetric site | Distorted site | | | σ (Å ²) |
|--------------------|-----------------|-----------------|-----------------|-----------------|----------------------------|
| | $d_{V-F/O}$ (Å) | d_{V-F} (Å) | d_{V-O} (Å) | d_{V-F} (Å) | |
| Component 1 | 2.01×6 | | | | $4.8 \cdot 10^{-3}$ |
| Component 2 | 1.97×6 | 1.91×1 | 1.97×4 | 1.75×1 | $6.0 \cdot 10^{-3}$ |
| Component 3 | 1.92×6 | 1.84×1 | 1.95×4 | 1.80×1 | $6.1 \cdot 10^{-3}$ |
| Component 4 | 1.92×6 | 2.27×1 | 1.95×4 | 1.84×1 | $7.5 \cdot 10^{-3}$ |

When moving to the third voltage plateau, the fourth component is observed, however the absorption energies of the third and the fourth components are the same suggesting that they both correspond to the $\text{V}^{3+}\text{-F-V}^{5+}$ bioctahedra. An intense signal is detected in the pre-edge region of the XANES spectrum of the fourth component implying that at least one of the vanadium local environment is highly distorted. We suggest that the V^{5+} local environment becomes highly distorted at this stage as V^{3+} usually prefers a symmetric environment. The EXAFS data was fit by considering the same model as the one used to describe the second and the third components. Reasonable results were obtained with this model: the assumed V^{3+} site is symmetric with $d_{\text{V}^{3+}\text{-O/F}} = 1.92 \text{ \AA} \times 6$ while the V^{5+} site is greatly distorted with $d_{\text{V}^{5+}\text{-O}} = 1.95 \text{ \AA} \times 4$, $d_{\text{V}^{5+}\text{-F(1)}} = 1.84 \text{ \AA}$ and $d_{\text{V}^{5+}\text{-F(2)}} = 2.27 \text{ \AA}$. Therefore, the oxidation of the $\text{V}^{3+}\text{-F-V}^{4+}$ bioctahedron will first generate the $\text{V}^{3+}\text{-F-V}^{5+}$ bioctahedron with a strong bonding contraction and a slight distortion around V^{5+} . However, the V^{5+} usually prefers to reside in a highly distorted environment, and hence the application of a high voltage value ($\sim 4.8 \text{ V Na}^+/\text{Na}$) will trigger an irreversible structural distortion. The V^{5+} ion will gradually move off the center of the octahedral site together with an elongation of the bond engaged to the bridging F atom while its opposite V-F bond is significantly shortened.

II.3.6.1.2. Discharge to 2.5 V vs. Na^+/Na

After a charge up to 4.8 V vs. Na^+/Na , an irreversible modification of the electrochemical profile of $\text{Na}_3\text{V}_2(\text{PO}_4)_2\text{F}_3$ was observed (**Figure 2.18a**). A discharge down to 2.5 V vs. Na^+/Na was performed on the *operando* half-cell in order to follow the evolution of the vanadium oxidation state in latter cycles. The electrochemical profile of the *operando* $\text{Na}/\text{Na}_3\text{V}_2(\text{PO}_4)_2\text{F}_3$ half-cell is given in **Figure 2.25**.

After a long time holding of the cell at 4.8 V vs. Na^+/Na , a sudden voltage drop was observed due to the electrolyte decomposition reaction (**Figure 2.25**), and hence the cell was forced to switch to discharge with a lower cutoff voltage of 2.5 V vs. Na^+/Na . An irreversible modification of the electrochemical profile was detected as similar to those obtained in a coin cell test (**Figure 2.18a**). In discharge, the edge energy of the XANES spectra shifted down to lower values and the intensity of the pre-edge signal also decreases gradually (**Figure 2.26a and b**). Nevertheless, the XANES pre-edge signal was

still obvious even at the end of discharge at 2.5 V (**Figure 2.26a** and **c**) indicating that the vanadium environment remains significantly distorted and does not recover its initial state. A comparison between the Vanadium K-edge XANES spectrum recorded on the pristine $\text{Na}_3\text{V}_2(\text{PO}_4)_2\text{F}_3$ and the one recorded at the end of the 1st discharge (2.5 V vs. Na^+/Na) reveals that all the vanadium ions present in the reintercalated material are reduced to V^{3+} (**Figure 2.26c**). The structural distortion stabilized on the high voltage plateau is thus irreversible.

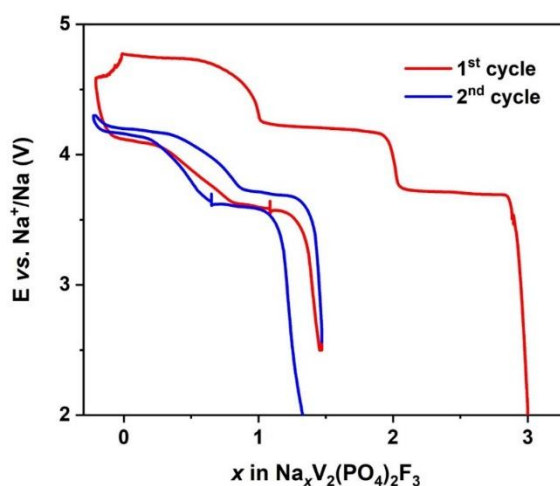


Figure 2.25 : Electrochemical profile of the $\text{Na}/\text{Na}_3\text{V}_2(\text{PO}_4)_2\text{F}_3$ half-cell used in the *operando* XAS experiment. Several cutoff voltage values were applied in order to investigate the evolution of the Vanadium oxidation state at different cycling conditions.

Furthermore, the *operando* Vanadium K-edge XANES spectra recorded in the first charge shows a brutal change between the spectrum #19 and #20 (**Figure 2.19b**), which corresponds to the formation of the intermediate phase $\text{Na}_2\text{V}_2(\text{PO}_4)_2\text{F}_3$, while the obtained data during discharge shows a smooth evolution of all the spectra (**Figure 2.26a**). The PCA analysis reveals the presence of two principal components (components 1' and 2') required to describe the system during a discharge from 4.8 to 2.5 V vs. Na^+/Na which is completely different from the set of four components observed in the first charge from 2.5 to 4.8 V. EXAFS analyses were also performed on the spectra of the two independent components and the obtained results shows that the first component is associated to the highly distorted $\text{V}^{3+}-\text{F}-\text{V}^{5+}$ bioctahedron whose structure has been described above while the second component is a $\text{V}^{3+}-\text{F}-\text{V}^{3+}$ bioctahedron where one V^{3+} site is symmetric with $d_{\text{V}^{3+}-\text{O}/\text{F}} = 2.03 \text{ \AA} \times 6$ while a great distortion is observed for the other site $d_{\text{V}^{3+}-\text{O}} = 1.99 \text{ \AA} \times 4$, $d_{\text{V}^{3+}-\text{F}(1)} = 1.82 \text{ \AA}$ and $d_{\text{V}^{3+}-\text{F}(2)} = 1.59 \text{ \AA}$. The Debye-Waller factor was assumed to be $\sigma = 3.8 \cdot 10^{-3} \text{ \AA}^2$ for all the surrounding ligands.

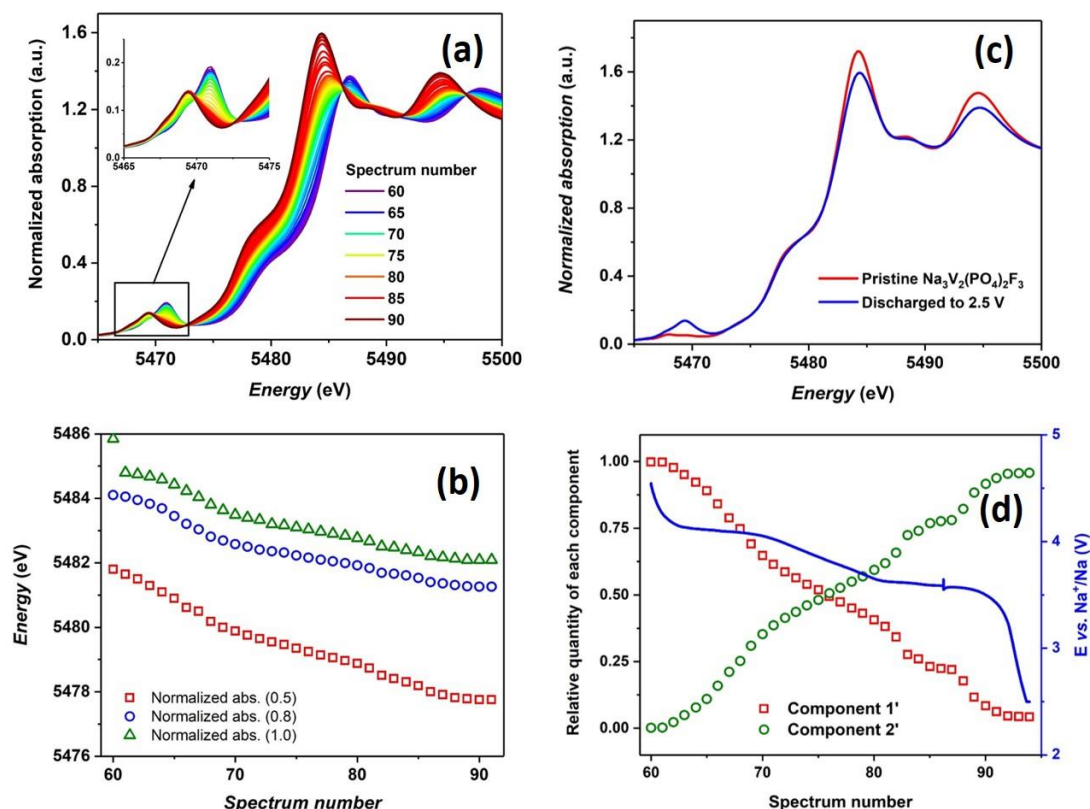


Figure 2.26 : (a) *Operando* Vanadium K edge XANES spectrum recorded on a $\text{Na}/\text{Na}_3\text{V}_2(\text{PO}_4)_2\text{F}_3$ half-cell in its first discharge. The inset focuses on the pre-edge region, (b) Evolution in the edge energy of the Vanadium K-edge XANES spectra recorded on a $\text{Na}/\text{Na}_3\text{V}_2(\text{PO}_4)_2\text{F}_3$ half-cell in its first discharge. The edge energy is taken at the normalized absorption equals to 0.5, 0.8 and 1.0, respectively, (c) Comparison of the Vanadium K-edge XANES spectra recorded for the pristine $\text{Na}_3\text{V}_2(\text{PO}_4)_2\text{F}_3$, after the 1st cycle at the discharged state at 2.5 V vs. Na^+/Na , (d) Concentration profile of the two principal components required to describe the *operando* XAS spectra recorded on a $\text{Na}/\text{Na}_3\text{V}_2(\text{PO}_4)_2\text{F}_3$ half-cell in the 1st discharge step from 4.8 to 2.5 V vs. Na^+/Na .

II.3.6.1.3. Second charge to 4.3 V and then discharge to 2.5 V vs. Na^+/Na

After the first charge to 4.8 V and then discharge to 2.5 V vs. Na^+/Na , a complete charge/discharge cycle in the potential window of 2.5 – 4.3 V was performed on the *operando* cell. In the second cycle, the S-shape of the electrochemical curve is retained with a reversible extraction/re-insertion of two Na^+ ions in the voltage range of 2.5 - 4.3 V vs. Na^+/Na (**Figure 2.25**). The *operando* XAS experiment shows a linear evolution of the spectra both in charge and discharge. The PCA analysis reveals that the system can also be described by a linear combination of two components as given in **Figure 2.26d**. The initial symmetric local environment of V^{3+} ion was not recovered in later cycles.

II.3.6.2. The paradox of V redox couple in $\text{Na}_3\text{V}_2(\text{PO}_4)_2\text{F}_{1.5}\text{O}_{1.5}$ and $\text{Na}_3\text{V}_2(\text{PO}_4)_2\text{F}_2\text{O}$

II.3.6.2.1. $\text{Na}_3\text{V}_2(\text{PO}_4)_2\text{F}_{1.5}\text{O}_{1.5}$

This composition contains 75% V^{4+} and 25% V^{3+} , in which the V^{4+} local environment is greatly distorted due to the formation of the vanadyl bond and the pre-edge signal is quite obvious even in the initial state. The *operando* XANES spectra recorded during the charge of a $\text{Na}/\text{Na}_3\text{V}_2(\text{PO}_4)_2\text{F}_{1.5}\text{O}_{1.5}$ cell (*i.e.* Na^+ deintercalation from $\text{Na}_3\text{V}_2(\text{PO}_4)_2\text{F}_{1.5}\text{O}_{1.5}$) shows a linear evolution of the data (**Figure 2.19d**), including the edge and the pre-edge signals. There is no drastic change in the vanadium local environment for this composition, even in the high-voltage region, and only two Na^+ ions can be extracted up to 4.3 V. There is no further change in the vanadium oxidation state in the higher voltage region. PCA was performed on this data set and three independent compositions are required to describe the whole system during charge. The concentration profile of these components are given in **Figure 2.27a**.

The Fourier transformation and EXAFS analysis were performed on the reconstructed XAS spectra of the principal components in order to determine their vanadium local environments. Among these three components, the reconstructed XAS spectrum of the first component was identical to that recorded on the pristine composition while the reconstructed XAS spectrum of the third component was similar to the one observed at the end of charge. In $\text{Na}_3\text{V}_2(\text{PO}_4)_2\text{F}_{1.5}\text{O}_{1.5}$, there are 75% V^{4+} and 25% V^{3+} or in other words 75% of the terminal fluorine positions observed in $\text{Na}_3\text{V}_2(\text{PO}_4)_2\text{F}_3$ are substituted by oxygen with the formation of vanadyl bonds. DFT calculations showed that the local environment of V^{3+} bonded to the terminal fluorine was symmetric while that of V^{4+} bonded to oxygen was strongly distorted due to the formation of the vanadyl bond [182]. In order to analyze the EXAFS data, we assumed that 25% of the sub-octahedral units in the structure were symmetric $\text{F}-\text{V}^{3+}\text{O}_4-\text{F}$ environments with only one variant to describe all the distances while 75% of the sub-octahedral units were distorted $\text{F}-\text{V}^{4+}\text{O}_4=\text{O}$ environments with three distance parameters associated to the four equatorial $\text{V}^{4+}-\text{O}$ bonds, the $\text{V}^{4+}-\text{F}$ bond and the short vanadyl bond $\text{V}^{4+}=\text{O}$. The fitting model can thus be written as $[6] \times 25\% + [4+1+1] \times 75\%$. The fits of the k^2 -weighted Vanadium K-edge EXAFS spectrum Fourier transform (k -range: $2.7 - 11.6 \text{ \AA}^{-1}$, sine window) in the R space and the corresponding fit of the real part of $\chi(q)$ corresponding to the reverse Fourier transform considering only the R -range : $1.0 - 2.1 \text{ \AA}$ with $dR = 0 \text{ \AA}$ are shown in **Figure 2.27c** and **Figure 2.27d**.

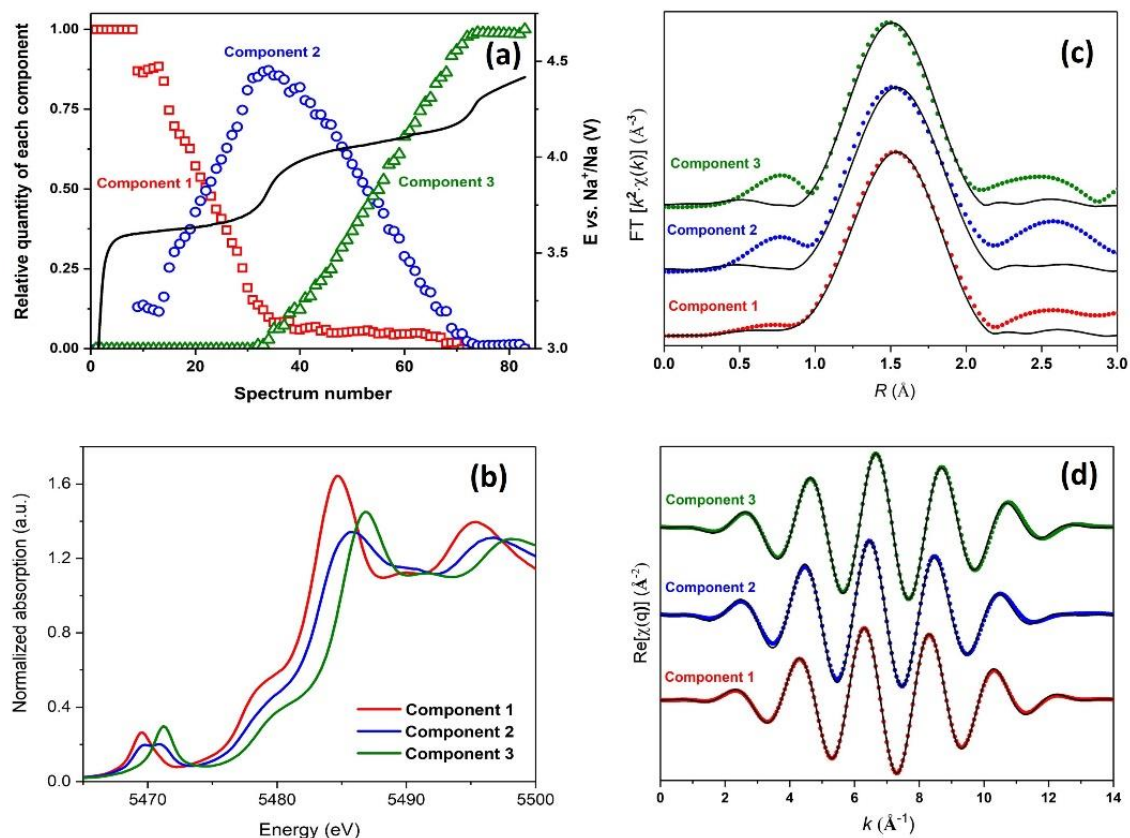


Figure 2.27 : (a) Concentration profile of the three principal components required to describe the *operando* XAS spectra recorded on a $\text{Na}/\text{Na}_3\text{V}_2(\text{PO}_4)_2\text{F}_{1.5}\text{O}_{1.5}$ half-cell upon charging from 2.5 to 4.5 V vs. Na^+/Na . The corresponding electrochemical profile is shown as black solid curve; (b) Reconstructed XANES spectra of the three independent components in the $\text{Na}_3\text{V}_2(\text{PO}_4)_2\text{F}_{1.5}\text{O}_{1.5} - \text{NaV}_2(\text{PO}_4)_2\text{F}_{1.5}\text{O}_{1.5}$ system; (c) Fit of the k^2 -weighted Vanadium K-edge EXAFS spectrum Fourier transform (k -range: 2.7 – 11.6 Å⁻¹, sine window) in the R space (R -range :1.0 – 2.1 Å, $dR = 0$, sine window) for the three components determined for the $\text{Na}_3\text{V}_2(\text{PO}_4)_2\text{F}_{1.5}\text{O}_{1.5} - \text{NaV}_2(\text{PO}_4)_2\text{F}_{1.5}\text{O}_{1.5}$ system. Their corresponding spectra were reconstructed by MCR-ALS with the ‘Pure’ method; (d) The corresponding fit of the real part of $\chi(q)$ corresponding to the backward Fourier transform by considering only the R -range 1.0 – 2.1 Å with $dR = 0$ Å. The circles represent the experimental data and the solid lines represent the fits.

The V–O/F bond lengths obtained from the EXAFS analysis for each principal components are summarized in **Table 2.5**. Upon charge, all the surrounding bonds are contracted gradually due to a decrease in the size of vanadium ions at higher charged state. Comparing the first component (pristine $\text{Na}_3\text{V}_2(\text{PO}_4)_2\text{F}_{1.5}\text{O}_{1.5}$) and the second component, there is a significant change in the local environment surrounding V^{4+} while little changes are observed around V^{3+} . This observation suggests there might be a preferential oxidation of $\{\text{V}=\text{O}\}^{2+}$ to $\{\text{V}=\text{O}\}^{3+}$ in the low-voltage region while the oxidation of $\{\text{V}=\text{O}\}^{2+}$ and V^{3+} –F occurs simultaneously in the high-voltage region, which is in agreement with what was reported earlier by Li *et al.* [145] The formation of the vanadyl bond $\text{V}^{4+}=\text{O}$, with a high covalency, induces the so-called “reserve inductive effect” [169,183], and thus lowers significantly the potential value of the $\text{V}^{5+}/\text{V}^{4+}$ redox

couple. This effect can be understood as following: in the $\{\text{V}=\text{O}\}^{3+}/\{\text{V}=\text{O}\}^{2+}$ redox couple, the V^{4+} ion is doubly bonded to the oxygen atom of the vanadyl bond and the high covalency of this bond will eventually raise up the energy of the “anti-bonding” states of V^{4+} . As was explained in **Figure 1.7a** and **b**, when the energy of the “anti-bonding” states of the transition metal ion is raised up, the difference between the Fermi level of Na metal and the Fermi level of the active material is reduced and thus a lower potential is observed. In the $\{\text{V}=\text{O}\}^{3+}/\{\text{V}=\text{O}\}^{2+}$ redox couple, the vanadyl bond is so covalent that the energy of the “anti-bonding” states of $\text{V}^{4+}=\text{O}$ is raised to the same energy of the “anti-bonding” states of V^{3+} in $\text{V}^{3+}-\text{F}$. Therefore, the $\{\text{V}=\text{O}\}^{3+}/\{\text{V}=\text{O}\}^{2+}$ redox couple can be activated before or simultaneously with the $\text{V}^{4+}-\text{F}/\text{V}^{3+}-\text{F}$ redox couple.

Table 2.5 : V—O/F bond lengths in Vanadium’s first coordination sphere obtained from the EXAFS analysis performed on the reconstructed XAS spectra of the four principal components required to describe the *operando* data set recorded on a Na// $\text{Na}_3\text{V}_2(\text{PO}_4)_2\text{F}_{1.5}\text{O}_{1.5}$ half-cell upon charging up to 4.5 V vs. Na^+/Na .

| | Symmetric site† | Distorted site† | | | σ (\AA^2) |
|--------------------|--------------------------------------------|------------------------------------------|------------------------------------------|------------------------------------------|-----------------------------|
| | $d_{\text{V}-\text{F/O}}$ (\AA) | $d_{\text{V}-\text{F}}$ (\AA) | $d_{\text{V}-\text{O}}$ (\AA) | $d_{\text{V}=\text{O}}$ (\AA) | |
| Component 1 | 1.94×6 | 1.85×1 | 2.06×4 | 1.63×1 | $2.0 \cdot 10^{-4}$ |
| Component 2 | 1.91×6 | 1.76×1 | 2.02×4 | 1.59×1 | $4.0 \cdot 10^{-3}$ |
| Component 3 | 1.86×6 | 1.77×1 | 1.98×4 | 1.58×1 | $1.6 \cdot 10^{-3}$ |

† 25% of Vanadium sites are assumed to be symmetric while 75% are distorted

II.3.6.2.2 $\text{Na}_3\text{V}_2(\text{PO}_4)_2\text{F}_2\text{O}$

In the case of $\text{Na}_3\text{V}_2(\text{PO}_4)_2\text{F}_2\text{O}$, a linear evolution of the *operando* Vanadium K-edge XANES spectra was also observed upon electrochemical cycling (**Figure 2.28a**) and three independent components are also required to describe the recorded spectra (**Figure 2.28b**).

There are 50% of V^{3+} and 50% of V^{4+} in the pristine composition, $\text{Na}_3\text{V}_2(\text{PO}_4)_2\text{F}_2\text{O}$, with 50% of the terminal fluorine atoms substituted by oxygen and we assume that all the bioctahedra can be averagely depicted as $\text{FO}_4\text{V}^{3+}-\text{F}-\text{V}^{4+}\text{O}_4=\text{O}$, where V^{3+} site is assumed to be symmetric while the V^{4+} site is highly distorted. Four different populations of bond lengths were used for the EXAFS fit: one for all the $\text{V}^{3+}-\text{F/O}$ bonds in the symmetric site, one for the vanadyl $\text{V}^{4+}=\text{O}$ bond, one common variable for the four

equatorial $\text{V}^{4+}-\text{O}$ bonds and one parameter for the sharing $\text{V}^{4+}-\text{F}$. This can be depicted as a $[6] + [4 + 1 + 1]$ fitting model. One common Debye-Waller factor is used for all the ligands. The $\text{V}-\text{O}/\text{F}$ bond lengths obtained from the EXAFS analysis for each principal component are summarized in **Table 2.6**. As similar to $\text{Na}_3\text{V}_2(\text{PO}_4)_2\text{F}_{1.5}\text{O}_{1.5}$, a gradual decrease in the bond length values was also observed upon charge.

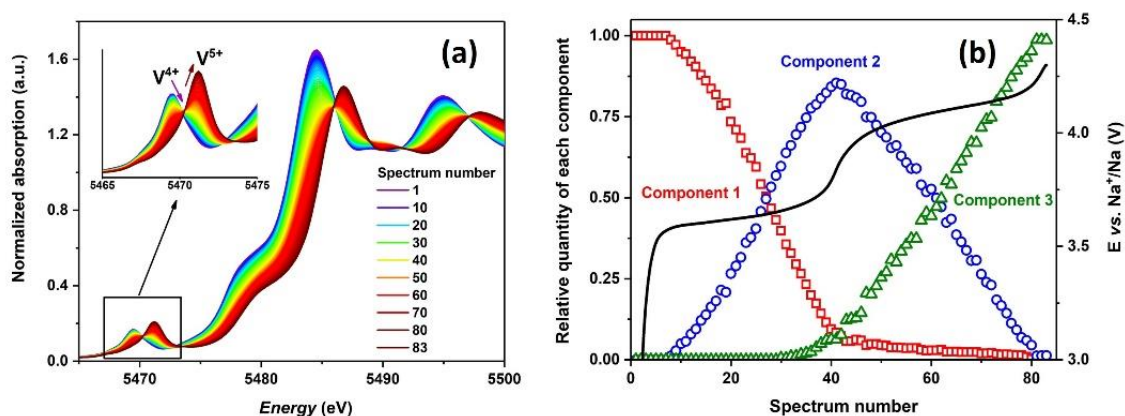


Figure 2.28 : (a) *Operando* Vanadium K edge XANES spectra recorded on a $\text{Na}/\text{Na}_3\text{V}_2(\text{PO}_4)_2\text{F}_2\text{O}$ half-cell from 2.5 – 4.5 V vs. Na^+/Na . The inset focuses on the pre-edge region; (b) Concentration profile of the three principal components required to describe the *operando* XAS spectra recorded on a $\text{Na}/\text{Na}_3\text{V}_2(\text{PO}_4)_2\text{F}_2\text{O}$ half-cell upon charging from 2.5 - 4.5 V vs. Na^+/Na . The corresponding electrochemical profile is shown as black solid curve.

Table 2.6 : $\text{V}-\text{O}/\text{F}$ bond lengths in Vanadium's first coordination sphere obtained from the EXAFS analysis performed on the reconstructed XAS spectra of the four principal components required to describe the *operando* data set recorded on a $\text{Na}/\text{Na}_3\text{V}_2(\text{PO}_4)_2\text{F}_2\text{O}$ half-cell upon charging up to 4.5 V vs. Na^+/Na .

| | Symmetric site | Distorted site | | | σ (\AA^2) |
|--------------------|-------------------------------------|-----------------------------------|-----------------------------------|-----------------------------------|-----------------------------|
| | $d_{\text{V-F/O}}$ (\AA) | $d_{\text{V-F}}$ (\AA) | $d_{\text{V-O}}$ (\AA) | $d_{\text{V=O}}$ (\AA) | |
| Component 1 | 2.03×6 | 1.85×1 | 2.00×4 | 1.63×1 | $3.6 \cdot 10^{-3}$ |
| Component 2 | 1.97×6 | 1.72×1 | 1.97×4 | 1.60×1 | $8.0 \cdot 10^{-3}$ |
| Component 3 | 1.90×6 | 1.73×1 | 1.99×4 | 1.56×1 | $3.6 \cdot 10^{-3}$ |

In $\text{Na}_3\text{V}_2(\text{PO}_4)_2\text{F}_2\text{O}$, all the bioctahedral units can be written as $\text{FO}_4\text{V}^{3+}-\text{F}-\text{V}^{4+}\text{O}_5$, and during the removal of the first Na^+ ion, several scenarios can occur: (i) exclusive oxidation of $\text{V}^{3+}-\text{F}$ to form $\text{FO}_4\text{V}^{4+}-\text{F}-\text{V}^{4+}\text{O}_4=\text{O}$, (ii) exclusive oxidation of $\text{V}^{4+}=\text{O}$ to form $\text{FO}_4\text{V}^{3+}-\text{F}-\text{V}^{5+}\text{O}_4=\text{O}$ and (iii) simultaneous oxidation of $\text{V}^{3+}-\text{F}$ and $\text{V}^{4+}=\text{O}$. The EXAFS analysis results shows an important change in the bond length values for both symmetric and distorted sites (**Table 2.6**). Furthermore, the reconstructed XANES

spectrum of the second component shows the presence of both V^{4+} and V^{5+} ions in the pre-edge signals (**Figure 2.29**). These observations reveal that both $\text{V}^{3+}\text{-F}$ and $\text{V}^{4+}\text{=O}$ can be activated in the low-voltage region in $\text{Na}_3\text{V}_2(\text{PO}_4)_2\text{F}_2\text{O}$. The “reverse inductive effect” also occurs in this compositions, but it is not strong enough to completely lower the voltage value of the $\{\text{V=O}\}^{3+}/\{\text{V=O}\}^{2+}$ redox couple below the $\text{V}^{4+}\text{-F}/\text{V}^{3+}\text{-F}$ redox couple.

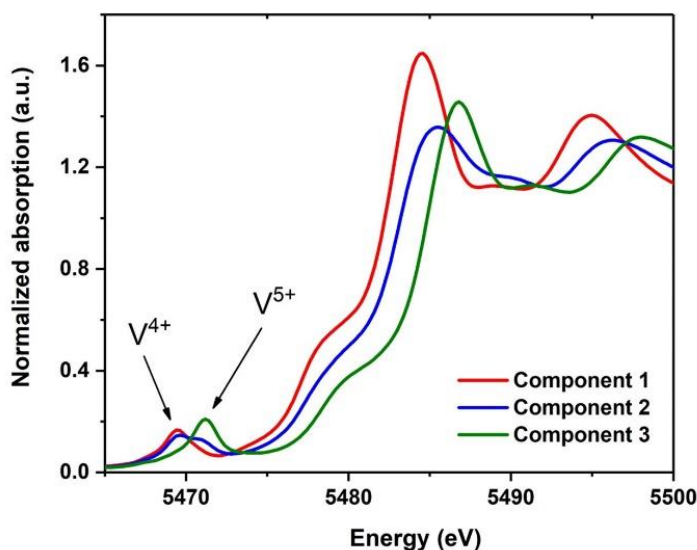


Figure 2.29 : Reconstructed XANES spectra at Vanadium K-edge of the three independent components of the $\text{Na}_3\text{V}_2(\text{PO}_4)_2\text{F}_2\text{O} - \text{NaV}_2(\text{PO}_4)_2\text{F}_2\text{O}$ system.

II.3.6.3. A comparison between $\text{Na}_3\text{V}_2(\text{PO}_4)_2\text{F}_3$, $\text{Na}_3\text{V}_2(\text{PO}_4)_2\text{F}_2\text{O}$ and $\text{Na}_3\text{V}_2(\text{PO}_4)_2\text{F}_{1.5}\text{O}_{1.5}$

The three investigated compositions possess the same structural framework but different $\text{V}^{3+}/\text{V}^{4+}$ ratios. In $\text{Na}_3\text{V}_2(\text{PO}_4)_2\text{F}_3$, there is no V^{4+} while in $\text{Na}_3\text{V}_2(\text{PO}_4)_2\text{F}_2\text{O}$ and $\text{Na}_3\text{V}_2(\text{PO}_4)_2\text{F}_{1.5}\text{O}_{1.5}$, 50% and 75% of the vanadium ions are V^{4+} , respectively. The presence of V^{4+} increases the average oxidation state of the vanadium ions and hence the absorption energy of the edge shifts to a higher value when moving from $\text{Na}_3\text{V}_2(\text{PO}_4)_2\text{F}_3$ to $\text{Na}_3\text{V}_2(\text{PO}_4)_2\text{F}_{1.5}\text{O}_{1.5}$ through $\text{Na}_3\text{V}_2(\text{PO}_4)_2\text{F}_2\text{O}$ (**Figure 2.30a**). Furthermore, V^{4+} resides in a distorted octahedral site while the local environment of V^{3+} is completely symmetric. Hence, the presence of V^{4+} induces a significant signal in the pre-edge. The higher the V^{4+} content, the more intense is the pre-edge region (**Figure 2.30a**). The same

phenomenon was also observed for the spectra recorded after the extraction of the first Na^+ ion (**Figure 2.30b**). Surprisingly, after the extraction of two Na^+ ions, the edge energy of the three desodiated phases are similar despite a difference in their average oxidation state (**Figure 2.30c**). Nevertheless, the difference in the intensity of their pre-edge signals is quite obvious. It could be possible that the absorption energy of V^{4+} in $\text{F}-\text{V}^{4+}\text{O}_4-\text{F}$ and that of V^{5+} in $\text{F}-\text{V}^{5+}\text{O}_4=\text{O}$ are so close that they do not show any difference on the XANES spectra. In these cases, a comparison between the pre-edge signals would be more appropriate and more precise than comparing the absorption energy of the edge.

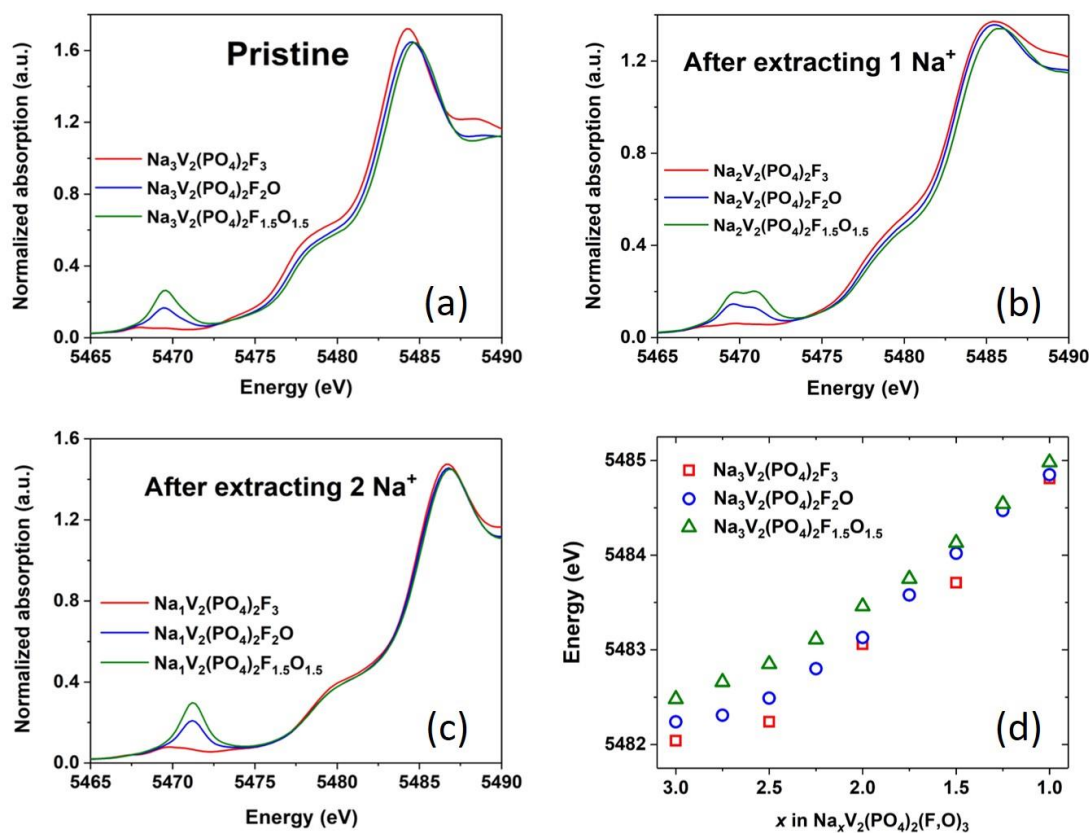


Figure 2.30 : A comparison between the Vanadium K-edge XANES spectra of $\text{Na}_3\text{V}_2(\text{PO}_4)_2\text{F}_3$, $\text{Na}_3\text{V}_2(\text{PO}_4)_2\text{F}_2\text{O}$ and $\text{Na}_3\text{V}_2(\text{PO}_4)_2\text{F}_{1.5}\text{O}_{1.5}$ at (a) Initial state, (b) After extracting one Na^+ , (c) After extracting two Na^+ , and (d) Evolution in the edge energy of $\text{Na}_3\text{V}_2(\text{PO}_4)_2\text{F}_3$, $\text{Na}_3\text{V}_2(\text{PO}_4)_2\text{F}_2\text{O}$ and $\text{Na}_3\text{V}_2(\text{PO}_4)_2\text{F}_{1.5}\text{O}_{1.5}$ in the first charge from 2.5 to 4.5 V vs. Na^+/Na . The edge energy value was taken at the position where the normalized abs. equaled to 1.0.

II.4. Conclusions

A series of compounds $\text{Na}_3\text{V}^{3+}_{2-y'}\text{V}^{4+}_{y'}(\text{PO}_4)_2\text{F}_{3-y'}\text{O}_{y'}$ ($0 \leq y' \leq 2$) was obtained through solid-state reaction and the complexity of the reaction in the solid phase was examined through the use of thermogravimetric analysis coupled with mass spectroscopy. These vanadium fluorinated oxyphosphates were proven to be completely stable in water. Indeed, a wash in water can be used to remove soluble and undesirable impurities formed during the synthesis, without any detrimental impact on their electrochemical performance in batteries. It is thus possible to develop aqueous electrode formulations or even to use these vanadium fluorinated oxyphosphates at the positive electrode in aqueous batteries [148,149]. The orthorhombic structural model appears as the most appropriate one to describe the overall solid solution $\text{Na}_3\text{V}_2(\text{PO}_4)_2\text{F}_3 - \text{Na}_3(\text{VO})_2(\text{PO}_4)_2\text{F}$. In the vanadyl-rich composition, $\text{Na}_3(\text{VO})_2(\text{PO}_4)_2\text{F}$, the long-range Na^+ -vacancy ordering was detected and a modulated structure is required to describe the distribution of the Na^+ ions. The minimization of the electrostatic repulsions within the diffusion channels throughout the framework appears as the main driving force for the formation of the long-range Na^+ ordering. The two characteristic stretching modes of vanadyl bond in this structural framework were detected at $\sim 920 \text{ cm}^{-1}$ with their corresponding overtones at $\sim 1840 \text{ cm}^{-1}$. These vibrations can be used as fingerprint in order to distinguish different members in the $\text{Na}_3\text{V}_2(\text{PO}_4)_2\text{F}_3 - \text{Na}_3(\text{VO})_2(\text{PO}_4)_2\text{F}$ series.

Extra capacity can be obtained for $\text{Na}_3\text{V}_2(\text{PO}_4)_2\text{F}_3$ and oxygen substituted $\text{Na}_3\text{V}_2(\text{PO}_4)_2\text{F}_{3-y'}\text{O}_{y'}$ compositions by increasing the upper cutoff voltage to 5.0 V *vs.* Na^+/Na ; however, this capacity is irreversible. Whatever the compositions, the vanadium redox center appears not to be involved beyond the deintercalation of 2 Na^+ ions per formula unit. Nevertheless, for the fluorine-rich compositions, the overcharge leads to a drastic modification of the structure with the formation of a highly disordered structure: the local environment of the vanadium ions is modified, despite their oxidation state is not. On the contrary, the oxygen-rich compositions are stable during the overcharge as the local environment of vanadium nor its oxidation state are modified. The presence of the oxygen substitution for fluorine and the formation of vanadyl-type bonds seems to have a stabilizing effect on the structure at high voltage.

The EXAFS analysis of the XAS spectra recorded on a $\text{Na}/\text{Na}_3\text{V}_2(\text{PO}_4)_2\text{F}_3$ half-cell at high voltage (~ 4.8 V) reveals the formation of a highly distorted vanadium local environment. Each bioctahedral unit is now composed of one symmetric $\text{V}^{3+}\text{O}_4\text{F}_2$ octahedron and one distorted $\text{V}^{5+}\text{O}_4\text{F}_2$ octahedron, and this structural distortion is retained even in discharge. This irreversible structural distortion is the origin of the permanent modification of the electrochemical profile.

By the use of *operando* XAS at Vanadium K-edge on $\text{Na}_3\text{V}_2(\text{PO}_4)_2\text{F}_2\text{O}$ and $\text{Na}_3\text{V}_2(\text{PO}_4)_2\text{F}_{1.5}\text{O}_{1.5}$ upon cycling, we have discovered that the $\{\text{V}=\text{O}\}^{3+}/\{\text{V}=\text{O}\}^{2+}$ redox couple was activated simultaneously with the $\text{V}^{4+}-\text{F}/\text{V}^{3+}-\text{F}$ redox couple, which is due to the presence of the “reverse inductive effect” caused by the formation of a highly covalent vanadyl bond on V^{4+} . This phenomenon is similar to what has been reported in the vanadyl-containing “ $\text{LiVPO}_4\text{F} - \text{LiVOPO}_4$ ” system in our group [169,183,184]. In the parental composition, LiVPO_4F , $\text{V}^{3+}\text{O}_4\text{F}_2$ octahedral units exist and these building units are joined together by sharing the two fluorine atoms, leading to the formation of the infinite $[\text{F}-\text{V}^{3+}\text{O}_4-\text{F}]_\infty$ chains running along the [101] direction. The two fluorine atoms can be partially or fully substituted by oxygen, and thus generate the $\text{LiVPO}_4\text{F}_{1-y}\text{O}_y$ phases. In the substituted compositions, the “reverse inductive effect” was so strong that the $\{\text{V}=\text{O}\}^{3+}/\{\text{V}=\text{O}\}^{2+}$ redox couple was activated at a lower voltage than $\text{V}^{4+}-\text{F}/\text{V}^{3+}-\text{F}$. In $\text{LiVPO}_4\text{F}_{1-y}\text{O}_y$ phases, the V^{3+} and V^{4+} ions are not homogeneously distributed in the structure and there exist the “vanadyl-rich” and “vanadyl-poor” regions. When the $\{\text{V}=\text{O}\}^{3+}/\{\text{V}=\text{O}\}^{2+}$ redox couple is activated, the delithiation process occurs through a solid solution mechanism, however when the $\text{V}^{4+}-\text{F}/\text{V}^{3+}-\text{F}$ redox is triggered at the high-voltage region, the reaction occurs through bi-phasic mechanism with the formation of Li^+ -vacancy ordering. In “ $\text{Na}_3\text{V}_2(\text{PO}_4)_2\text{F}_3 - \text{Na}_3(\text{VO})_2(\text{PO}_4)_2\text{F}$ ”, the V^{3+} and V^{4+} are homogeneously distributed over all the lattice as evidenced by (i) no significant broadening was observed on the diffraction lines, (ii) the binomial distribution of the ^{23}Na and ^{31}P NMR signals and (iii) DFT calculations results [185]. Except the two ending members of the system $\text{Na}_3\text{V}^{3+}_{2-y'}\text{V}^{4+}_{y'}(\text{PO}_4)_2\text{F}_{3-y'}\text{O}_{y'}$, the desodiation reactions occur through solid solution mechanism.

Chapter III

Revealing Atomic Local Environments in

$\text{Na}_3\text{V}_2(\text{PO}_4)_2\text{F}_3 - \text{Na}_3(\text{VO})_2(\text{PO}_4)_2\text{F}$

Materials by Solid-State NMR

Spectroscopy and First-Principles DFT

Calculations

III.1. Introduction

In recent years, the use of solid-state nuclear magnetic resonance (NMR), especially paramagnetic solid-state NMR, has increased significantly in the field of LIBs and SIBs. For instance, $^6/7\text{Li}$ NMR was used extensively to study the lithium atomic local environments in LiCoO_2 -related materials, LiMn_2O_4 , and LiFePO_4 [186–191]. ^7Li solid-state NMR was especially used as the key tool to detect the presence of local defects in LiVPO_4F [169,184,192,193]. *Operando* NMR techniques have also been developed to investigate dynamic processes occurring in batteries upon cycling. Despite of several challenges, many encouraging results were recently reported [194–199].

For paramagnetic materials, the observed resonances are usually broad and highly shifted due to the electron-nuclear spin interaction, which is also known as hyperfine shift [191,200]. The hyperfine shift can occur (*i*) through space by the electron-nuclear dipolar coupling, which broadens the line shape of the observed resonances, and (*ii*) through chemical bonds (Fermi contact), which results in a highly shifted resonant value [187,200]. The Fermi contact can be classified into spin delocalization and spin polarization mechanisms. The former contact leads to a positive Fermi contact shift while the latter induces a negative value. A schematic description of the spin delocalization and spin polarization mechanisms in transition metal oxides was reported by Carlier *et al.* [187], which could also be used to predict the sign of the observed resonances in similar structures. In paramagnetic polyanionic materials, the spin transfer can still occur through the Fermi contact, but the spin interaction pathways are usually not obvious to apprehend and it is difficult to make a general formalism due to the variety of polyanionic frameworks. Therefore, the interpretation of paramagnetic NMR signals is usually complicated and required the help from density functional theory (DFT) calculations. Nevertheless, an insightful study and a detailed interpretation of the paramagnetic signals can provide important information on the electronic and atomic local environment of the nuclei of interest, such as the coordination number, the oxidation state and the number of unpaired electrons of the transition metal ions which are adjacent to it.

A systematic study on the ^{23}Na and ^{31}P solid-state NMR of $\text{Na}_3\text{V}_2(\text{PO}_4)_2\text{F}_3$ and its corresponding desodiated phases $\text{Na}_x\text{V}_2(\text{PO}_4)_2\text{F}_3$ ($0 < x \leq 3$) was reported by Liu *et al.* [201]. For $\text{Na}_3\text{V}_2(\text{PO}_4)_2\text{F}_3$, the authors observed two different ^{31}P MAS NMR resonances

at 6000 ppm and 4500 ppm, and thus assigned them to two different phosphorus crystallographic sites, P1 and P2, existing in the $\text{Na}_3\text{V}_2(\text{PO}_4)_2\text{F}_3$ structure indexed in the space group $P4_2/mnm$. By following the evolution of the ^{23}Na NMR signals and the Na^+ diffusion coefficients observed in desodiated phases, these authors also discovered that the Na^+ ions present in the deintercalated phases have higher ionic mobility than in the initial state.

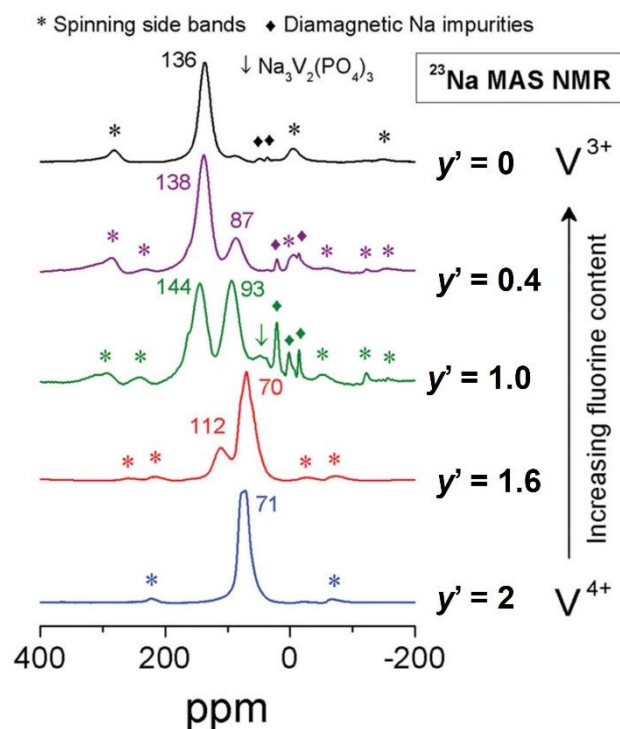


Figure 3.1 : ^{23}Na MAS NMR recorded on the $\text{Na}_3\text{V}^{3+}_{2-y}\text{V}^{4+}_y(\text{PO}_4)_2\text{F}_{3-y}\text{O}_{y'}$ ($0 \leq y' \leq 2$) compositions reported by Park *et al.* (Adapted from [101]).

The ^{23}Na and ^{31}P MAS NMR spectra of $\text{Na}_3\text{V}^{3+}_{2-y}\text{V}^{4+}_y(\text{PO}_4)_2\text{F}_{3-y}\text{O}_{y'}$ ($0 \leq y' \leq 2$) compositions were studied by Park *et al.* [101]. The authors pointed out that the Na^+ ions are influenced by a strong Fermi contact with the two vanadium ions in their closest bioctahedral unit and the observed ^{23}Na NMR shift depends on whether the Na^+ is in contact with two V^{4+} , two V^{3+} , or a combination of one V^{3+} and one V^{4+} (**Figure 3.1**). A series of ^{31}P MAS NMR spectra was also reported, the authors however only focused on the ^{31}P resonances observed at ~ 0 ppm despite of the fact that these compositions contained paramagnetic ions, *i.e.* V^{3+} and V^{4+} , and the ^{31}P NMR signals are expected to be highly shifted due to the strong hyperfine contact between these ions and the phosphorus nuclei.

Broux *et al.* have recently revisited the ^{31}P MAS NMR signatures of some compositions between $\text{Na}_3\text{V}_2(\text{PO}_4)_2\text{F}_3$ and $\text{Na}_3\text{V}_2(\text{PO}_4)_2\text{F}_2\text{O}$, and they reported that each phosphorus nucleus in these structures is in contact with four neighboring vanadium ions and thus generates the $\text{P}(\text{OV}^{n+})_4$ local environments where V^{n+} can be V^{3+} or V^{4+} . Five different ^{31}P MAS NMR resonances were detected at 6000 ppm, 4500 ppm, 3000 ppm, 1500 ppm, and ~ 0 ppm in all the oxygen-substituted phases, and it was speculated that they are originated from the $\text{P}(\text{OV}^{3+})_3(\text{OV}^{4+})$, $\text{P}(\text{OV}^{3+})_2(\text{OV}^{4+})_2$, $\text{P}(\text{OV}^{3+})(\text{OV}^{4+})_3$, and $\text{P}(\text{OV}^{4+})_4$ local environments, respectively [143]. What was unclear is that the authors hypothesized that V^{4+} ions in this structure would cause no Fermi contact with its neighboring phosphorus nuclei despite the fact that V^{4+} possessed one unpaired electron.

In this chapter, we will investigate the electronic structure of V^{3+} and V^{4+} in $\text{Na}_3\text{V}_2(\text{PO}_4)_2\text{F}_3 - \text{Na}_3(\text{VO})_2(\text{PO}_4)_2\text{F}$ and related compositions with the help of DFT calculations. Furthermore, we aim at confirming the ^{31}P MAS NMR resonance assignment, which had been proposed earlier by Broux *et al.*, through a careful consideration of the orbital interaction between $\text{V}^{3+}/\text{V}^{4+}$ ions and the phosphorus nuclei in the structure. As a local probe, an insightful analysis of the ^{23}Na and ^{31}P MAS NMR will also allow us to discuss whether the $\text{V}^{3+}/\text{V}^{4+}$ ions are randomly distributed in the lattice or not. Last but not least, we will compare the ^{23}Na and ^{31}P MAS NMR spectra of two series of materials $\text{Na}_x\text{V}_2(\text{PO}_4)_2\text{F}_3$ and $\text{Na}_x\text{V}_2(\text{PO}_4)_2\text{F}_2\text{O}$ ($0 \leq x \leq 3$), whose electrochemical behaviors are very different: the former one is characterized by the presence of several Na^+ -vacancy orderings upon charging while in the latter case there is no formation of intermediate charge ordering, in order to understand the influence of the Na^+ -vacancy ordering on the behavior of the resulted NMR spectra as well as the Na^+ ion diffusion properties in the diffusion channels. These experiments also help us to follow the evolution in the strength of the Fermi contact between $\text{V}^{3+}/\text{V}^{4+}$ and Na/P nuclei upon cycling.

III.2. Principles of NMR measurements and DFT calculations

III.2.1. Samples preparation

The $\text{Na}_3\text{V}^{3+}_{2-y}\text{V}^{4+}_y(\text{PO}_4)_2\text{F}_{3-y}\text{O}_y$ ($0 \leq y \leq 2$) compositions were obtained by the solid-state synthesis route as described in details in the Experimental part in **Chapter II**.

Desodiated compositions, $\text{Na}_x\text{V}_2(\text{PO}_4)_2\text{F}_3$ and $\text{Na}_x\text{V}_2(\text{PO}_4)_2\text{F}_2\text{O}$ ($0 \leq x \leq 3$), were obtained by galvanostatic electrochemical Na^+ extraction from $\text{Na}_3\text{V}_2(\text{PO}_4)_2\text{F}_3$ and $\text{Na}_3\text{V}_2(\text{PO}_4)_2\text{F}_2\text{O}$, respectively. Several $\text{Na}/\text{Na}_3\text{V}_2(\text{PO}_4)_2\text{F}_3$ and $\text{Na}/\text{Na}_3\text{V}_2(\text{PO}_4)_2\text{F}_2\text{O}$ half-cells were prepared and cycled in an electrolyte containing 1 M NaPF_6 in EC/DMC (1/1) with 2% of FEC at the cycling rate of $C/10$ per Na^+ ion. A time limitation was applied in order to control the amount of extracted Na^+ . The materials after cycling were recovered, washed with DMC in order to remove the electrolyte traces, and then dried under vacuum before being subjected to ^{23}Na , ^{31}P MAS NMR measurement, and XRD. In some cases, the amount of powder recovered after washing was so little that it was well mixed with KBr prior to NMR and XRD measurements.

III.2.2. NMR measurements

^{31}P *ss*-NMR spectra were acquired on a Bruker Avance III spectrometer with a 2.35T magnetic field at a resonance frequency of 40.6 MHz by using a standard Bruker 2.5 mm magic-angle spinning (MAS) probe with a 30 kHz spinning frequency. A Hann echo sequence was applied with a 90° pulse 1.1 μs and a recycle delay of 1 s. H_3PO_4 85% (Sigma-Aldrich) was used as external reference for 0 ppm chemical shift.

^{23}Na *ss*-NMR spectra were acquired using a Bruker Avance 500 MHz spectrometer, equipped with a 11.7 T wide bore magnet (operating at Larmor frequency of 132.3 MHz for ^{23}Na). Experiments were performed using conventional 2.5 mm MAS probe, with 30 kHz MAS rate. Chemical shifts are referenced relative to an aqueous 0.1M NaCl solution at 0 ppm. In each case, a short pulse length of 1.1 μs corresponding to a selective $\pi/8$ pulse determined by using a 0.1 M NaCl aqueous solution was employed. The spectral width was set to 1 MHz and the recycle delay of 0.5 s, which was long enough to avoid T_1 saturation effects. The baseline distortions resulted from the spectrometer dead time (5 - 10 μs) were removed computationally by using a polynomial baseline correction routine.

III.2.3. First-principles DFT calculations

First-principles calculations were performed within the DFT framework, and the calculations using projector augmented wave (PAW) method were computed with the Vienna *ab initio* simulation package (VASP) code [202]. A wave plane cutoff energy of 600 eV and a *k*-mesh of 2x2x2 were applied. The experimental crystal structure of the materials was used as input model and the calculations were spin polarized type with ferromagnetic ordering, which is appropriate to take into account the Fermi contact interaction as discussed in [187]. The energy minimization and electron density on each atom were calculated by using the generalized gradient approximation (GGA) and GGA+U approaches, where the Hubbard type interaction is added to the latter method to localize *d* electrons. In this study, the U value of 3.0, 4.0, and 5.0 eV were tested.

In order to quantify the Fermi contact interaction, the VASP code can compute the hyperfine coupling contact by considering the contribution of valence and core electrons:

$$A_{iso} = \frac{2}{3} \frac{\mu_0 \gamma_e \gamma_N}{\langle S_N \rangle} \int \delta_T(r) \rho_s(r + R_I) dr \quad (\text{Equation 3.1})$$

where ρ_s is the difference of the population between the spin-up and spin-down energy levels at a specific nucleus where the hyperfine coupling constant is being calculated and ρ_s is usually known as “electronic spin density”, μ_0 is the magnetic susceptibility of free space, γ_e is the electronic gyromagnetic ratio, γ_N is the nuclear gyromagnetic ratio of the nucleus being studied, R_I is the nucleus radius, and $\langle S_N \rangle$ is the expectation value of the *z*-component of the total electron spin. $\delta_T(r)$ is a smeared out of δ function, as described in the literature [203].

The spin density surrounding the nucleus of interest ($\rho^i(0)$) can further be calculated from the A_{iso} value by the following equation:

$$\rho^i(0) = \frac{A_{iso} S(Tot)}{\gamma_N} \quad (\text{Equation 3.2})$$

where S(Tot) is the total magnetic moment in the cell, γ_N is the nuclear gyromagnetic ratio of the nuclear of interest, and A_{iso} is the hyperfine coupling constant as described in Equation 3.2.

The isotropic shift of a specific nucleus due to Fermi contact can then be quantified from the electron spin density:

$$\delta_{iso}^i = \frac{1}{3SN_A} \rho^i(0) \chi_M(T) \quad (\text{Equation 3.3})$$

where S is the spin quantum number of the paramagnetic ion, $\rho^i(0)$ is the computed spin density on the i nucleus, and $\chi_M(T)$ is the molar magnetic susceptibility at the temperature where the NMR spectrum was recorded. The temperature (T) was chosen to be 320K, which is the approximate temperature inside the rotor at a spinning rate of 30 kHz.

The following nuclear gyromagnetic ratio ($\text{MHz}\cdot\text{T}^{-1}$) were used for the calculations: 11.215 (^{51}V), 17.2538 (^{31}P), 11.271 (^{23}Na), 40.078 (^{19}F), and 5.775 (^{17}O). The Curie temperature was assumed to be 0K for all compounds and the theoretical value of molar magnetic susceptibility calculated by Curie law was used for the Fermi contact shift calculations.

The partial density of states on vanadium ions were calculated by considering the ionic radius of V^{3+} equals to 0.55 Å [204]. The 3D charge density and electronic spin density distribution maps were visualized by utilizing VESTA software [160].

III.3. NMR and DFT study on $\text{Na}_3\text{V}_2(\text{PO}_4)_2\text{F}_3 - \text{Na}_3(\text{VO})_2(\text{PO}_4)_2\text{F}$

III.3.1. ^{31}P NMR signals assignment in $\text{Na}_3\text{V}_2(\text{PO}_4)_2\text{F}_3 - \text{Na}_3(\text{VO})_2(\text{PO}_4)_2\text{F}$

Figure 3.2 shows the ^{31}P *ss*-NMR spectra already reported by Broux *et al.* in [143] for the samples $\text{Na}_3\text{V}^{3+}_{2-y}\text{V}^{4+}_y(\text{PO}_4)_2\text{F}_{3-y}\text{O}_y$, belonging to a limited range of compositions of $0 < y' \leq 1$, and a comparison with those recorded recently for the more oxidized compositions $\text{Na}_3\text{V}_2(\text{PO}_4)_2\text{F}_{1.5}\text{O}_{1.5}$ ($y' = 1.5$) and $\text{Na}_3(\text{VO})_2(\text{PO}_4)_2\text{F}$ ($y' = 2$). This set of spectra allows to get an insight into the origin of the ^{31}P *ss*-NMR spectra of the whole composition range. For $\text{Na}_3\text{V}_2(\text{PO}_4)_2\text{F}_3$ ($y' = 0$) the main ^{31}P resonance was observed at ~ 6000 ppm and was assigned to the $\text{P}(\text{OV}^{3+})_4$ unit, which was the dominant phosphorus local environment. In addition to the main signal, a second resonance at around 4500 ppm

was also detected due to the presence of oxygen defects in the structure leading to the formation of the $\text{P}(\text{OV}^{3+})_3(\text{OV}^{4+})$ local environment [143]. In the $\text{Na}_3\text{V}^{3+}_{2-y'}\text{V}^{4+}_{y'}(\text{PO}_4)_2\text{F}_{3-y'}\text{O}_{y'}$ ($0 < y' \leq 2$) series, in addition to the 6000 ppm signal, four new resonances were observed at 4500 ppm, 3000 ppm, 1500 ppm and ~ 0 ppm, whose intensity varies as a function of the oxygen content. It has been speculated that these signals could be originated from different phosphorus local environments in the structure by considering the first vanadium coordination sphere: $\text{P}(\text{OV}^{3+})_3(\text{OV}^{4+})$, $\text{P}(\text{OV}^{3+})_2(\text{OV}^{4+})_2$, $\text{P}(\text{OV}^{3+})(\text{OV}^{4+})_3$, and $\text{P}(\text{OV}^{4+})_4$. [143]. The broadening and the asymmetry of some signals can be resulted from various ^{31}P environments if one considers also the second vanadium coordination sphere, *i.e.* the second vanadium site of the bioctahedron. Among those signals, it was really surprising to observe a very narrow signal at ~ 0 ppm corresponding to the $\text{P}(\text{OV}^{4+})_4$ local environment, as V^{4+} are paramagnetic ions.

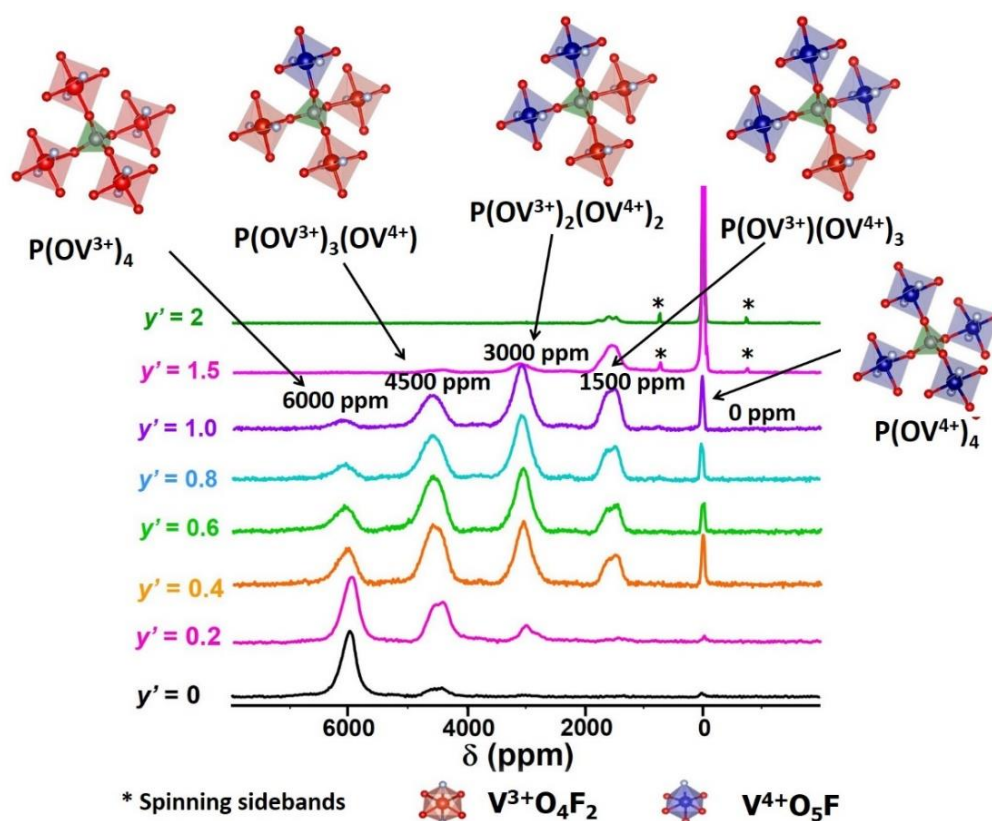


Figure 3.2 : Hahn echo ^{31}P MAS NMR spectra of the $\text{Na}_3\text{V}^{3+}_{2-y'}\text{V}^{4+}_{y'}(\text{PO}_4)_2\text{F}_{3-y'}\text{O}_{y'}$ ($0 \leq y' \leq 2$) samples ($B_0 = 2.35\text{T}$; $\nu_R = 30\text{ kHz}$). The spinning sidebands are marked with asterisks. The PO_4 tetrahedral units are in green while $\text{V}^{3+}\text{O}_4\text{F}_2$ and $\text{V}^{4+}\text{O}_5\text{F}_1$ octahedral units are in red and blue, respectively.

In fact, for the $\text{Na}_3(\text{VO})_2(\text{PO}_4)_2\text{F}$ ($y' = 2$) composition, where $\text{P}(\text{OV}^{4+})_4$ is the only permitted phosphorus environment, the main and highly intense resonance is recorded nearby 0 ppm (**Figure 3.2**). This latest finding confirms thus the hypothesis proposed earlier in [143], and proves that there is no electron-nuclear spin interaction between the unpaired electron of V^{4+} and phosphorus nuclei in $\text{P}(\text{OV}^{4+})_4$ local environment, which gives rise to a ^{31}P NMR shift value in the diamagnetic regime. First-principles calculations were performed on $\text{Na}_3\text{V}^{3+}_2(\text{PO}_4)_2\text{F}_3$, $\text{Na}_3(\text{V}^{4+}\text{O})_2(\text{PO}_4)_2\text{F}$, and $\text{Na}_3\text{V}^{3+}\text{V}^{4+}(\text{PO}_4)_2\text{F}_2\text{O}$ in order to understand the electronic structure of the existing vanadium ions as well as the mechanism of the electron-nuclear spin interaction between the unpaired electron(s) of $\text{V}^{3+}/\text{V}^{4+}$ and the phosphorus nuclei in these structures.

III.3.2. Vanadium electronic structure in $\text{Na}_3\text{V}_2(\text{PO}_4)_2\text{F}_3 - \text{Na}_3(\text{VO})_2(\text{PO}_4)_2\text{F}$

In order to perform DFT calculations, we aimed at using the experimental structure of $\text{Na}_3\text{V}_2(\text{PO}_4)_2\text{F}_3$ as input model. However, it contains three different Na crystallographic sites, Na1, Na2, and Na3, in which Na1 is fully occupied whereas the other two have a partial occupancy (**Figure 3.3**) [83]. An approximate model structure has thus to be considered in our DFT calculations. Considering the close proximity (0.90 Å) between the two partially occupied Na sites, *i.e.* Na2 and Na3, an approximate input model was created by placing a fully occupied Na2' site on the barycenter between Na2 and Na3. This input model was then used in the structural relaxation step. The DFT optimized structure is compared to the experimental one in **Figure 3.3**.

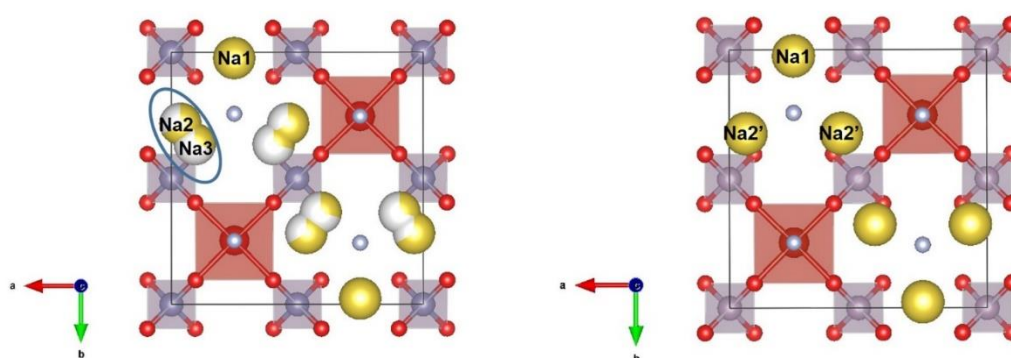


Figure 3.3 : (Left) Experimental structure of $\text{Na}_3\text{V}_2(\text{PO}_4)_2\text{F}_3$ determined by synchrotron X-ray powder diffraction [83], and (Right) Input model used for DFT calculations where a fully occupied Na site represents the partial occupied Na2 and Na3 sites in the actual structure.

Since here we focus on the Fermi contact shift calculation between vanadium ions and ^{31}P nuclei, we do not expect a strong influence of Na positions on the strength of the Fermi contact. The structure was first relaxed using GGA or GGA+U methods. The optimized structures of $\text{Na}_3\text{V}_2(\text{PO}_4)_2\text{F}_3$ crystallizes in an orthorhombic system, which is in good agreement with the experimental space group, *Amam* (**Table 3.1**). The optimized cell parameters (*a*, *b*, and *c*) calculated by GGA method are in the error range of 1% in comparison to those obtained by SXRD. Using GGA+U (here $U = 3 \text{ eV}$, 4 eV , and 5 eV), a greater deviation from the experimental data is observed (**Table 3.1**) suggesting that GGA method is a better choice to study this material.

Table 3.1 : Calculated unit cell parameters of $\text{Na}_3\text{V}_2(\text{PO}_4)_2\text{F}_3$ after geometry optimization using GGA and GGA+U methods compared to the experimental ones.

| | SXRD | GGA | GGA + 3eV | GGA + 4eV | GGA + 5eV |
|--------------|-------------|--------|-----------|-----------|-----------|
| <i>a</i> (Å) | 9.02847(3) | 9.096 | 9.126 | 9.150 | 9.178 |
| <i>b</i> (Å) | 9.04444(3) | 9.156 | 9.193 | 9.215 | 9.235 |
| <i>c</i> (Å) | 10.74666(6) | 10.758 | 10.890 | 10.895 | 10.902 |
| α | 90° | 90° | 90° | 90° | 90° |
| β | 90° | 90° | 90° | 90° | 90° |
| γ | 90° | 90° | 90° | 90° | 90° |

For $\text{Na}_3(\text{VO})_2(\text{PO}_4)_2\text{F}$, the situation is more complex. The crystal structure of $\text{Na}_3(\text{VO})_2(\text{PO}_4)_2\text{F}$ had been studied in details by Tsirlin *et al.* and had been reported to crystallize in the $P4_2/mnm$ space group, which contained a fully occupied Na1 site and a half occupied Na2 site with a distance of 2.374 \AA between the two closest Na2 sites (**Figure 3.4**) [135].

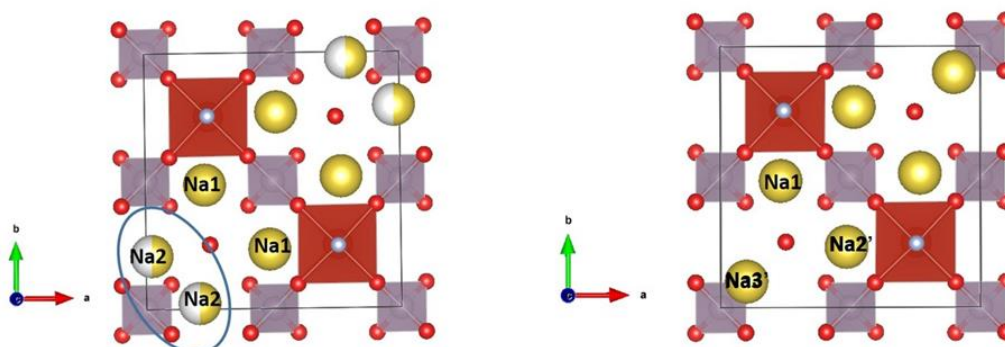


Figure 3.4 : (Left) Experimental structure of $\text{Na}_3(\text{VO})_2(\text{PO}_4)_2\text{F}$ determined by single crystal diffraction reported by Tsirlin *et al.* [135], and (Right) Input model used for DFT calculations where a fully occupied Na3' site represents the half occupied Na2 sites in the actual structure.

We have recently revisited the crystal structure of this material by high resolution SXRD and we have in fact shown that the structure is even more complex: it should be described in a monoclinic cell with a modulation vector of $q = \frac{1}{2} b^* + \frac{1}{2} c^*$ in the $P2_1/m$ space group that takes into account a long range ordering of Na^+ ions on three different sites Na1, Na2 and Na3, where all these Na sites are partially occupied. As in the case of $\text{Na}_3\text{V}_2(\text{PO}_4)_2\text{F}_3$, partially occupied sites cannot be taken into account in DFT calculations, we therefore retained the structural description reported by Tsirlin *et al.* where a fully occupied Na3' site was placed at the barycenter between two Na2 sites in the structure despite of the great distance between the two actual sites (**Figure 3.4**). The input model relaxes into a tetragonal cell whose unit cell parameters are in agreement with those reported by Tsirlin *et al.* As for $\text{Na}_3\text{V}_2(\text{PO}_4)_2\text{F}_3$, upon increasing the U values, the cell parameters deviate from the experimental ones (**Table 3.2**).

Table 3.2 : Calculated unit cell parameters of $\text{Na}_3(\text{VO})_2(\text{PO}_4)_2\text{F}$ after geometry optimization using GGA and GGA+U methods compared to the experimental ones.

| | SXRD | GGA | GGA + 3eV | GGA + 4eV | GGA + 5eV |
|----------|------------|--------|-----------|-----------|-----------|
| a (Å) | 9.0285(1) | 9.092 | 9.138 | 9.152 | 9.167 |
| b (Å) | 9.0285(1) | 9.092 | 9.138 | 9.152 | 9.167 |
| c (Å) | 10.6149(2) | 10.624 | 10.591 | 10.587 | 10.569 |
| α | 90° | 90° | 90° | 90° | 90° |
| β | 90° | 90° | 90° | 90° | 90° |
| γ | 90° | 90° | 90° | 90° | 90° |

The optimized V–O and V–F distances and the density of states (DOS) calculation of vanadium ions in $\text{Na}_3\text{V}_2(\text{PO}_4)_2\text{F}_3$ both agree with the presence of V^{3+} ion a symmetric octahedral site formed by four oxygen atoms in the basal plane of the octahedron and two fluorine atoms on the axial positions, one of which being shared with the neighboring V^{3+} site (**Figure 3.5a**), which has been reported experimentally [82,83]. The difference between the experimental and the calculated V–O, V–F, and P–O distances is less than 1% with GGA (**Figure 3.5a**). Despite the difference in the nature of fluorine and oxygen, the V^{3+} site is ‘quasi’-symmetric as the six surrounding bond lengths are nearly similar (~ 2.0 Å) (**Figure 3.5a**).

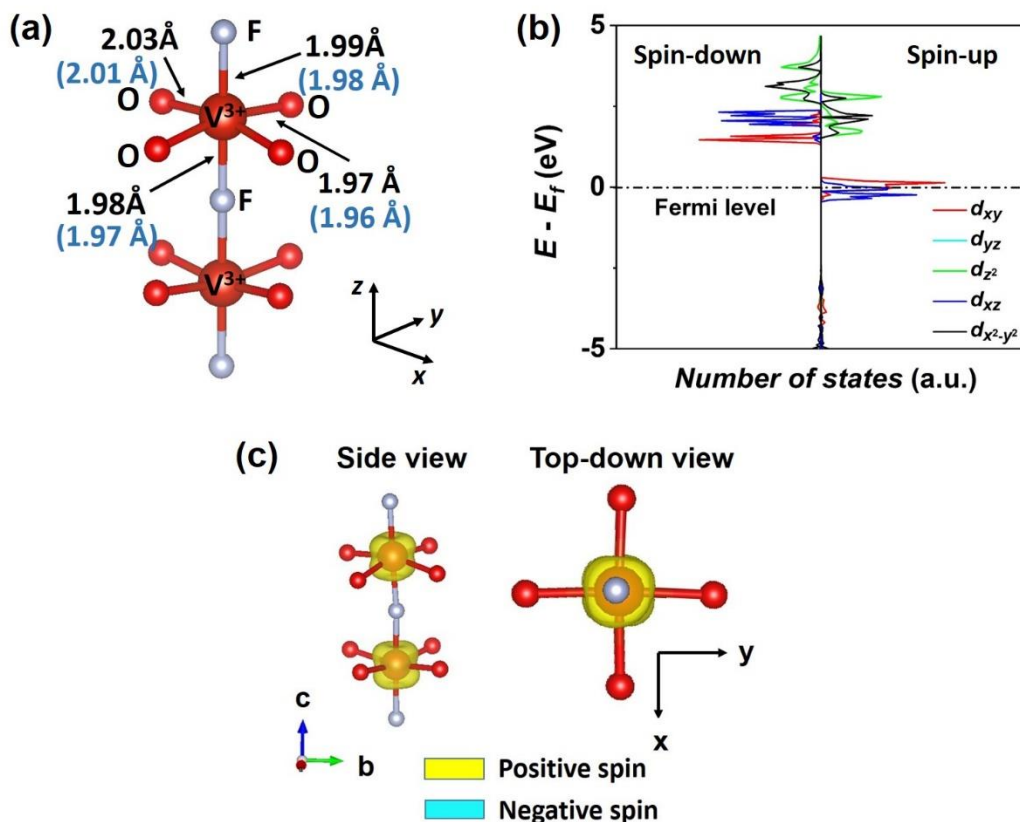


Figure 3.5 : (a) The local environment of V^{3+} in $\text{Na}_3\text{V}_2(\text{PO}_4)_2\text{F}_3$ with the optimized distances comparing to the experimental ones given in parentheses, (b) Calculated partial DOS around the vanadium ions in $\text{Na}_3\text{V}_2(\text{PO}_4)_2\text{F}_3$ using the GGA method, (c) Calculated spin distribution map surrounding a $\text{V}_2\text{O}_8\text{F}_3$ bioctahedral unit. A $8 \cdot 10^{-3}$ electron-Å $^{-2}$ iso-surface value was used for this plot. The positive and negative electron spin are represented in yellow and blue, respectively.

The partial DOS around V ions in $\text{Na}_3\text{V}_2(\text{PO}_4)_2\text{F}_3$ indicates that the two unpaired electrons of V^{3+} ions are partially located in the three d_{xy} , d_{xz} , and d_{yz} (t_{2g}) orbitals (**Figure 3.5b**). The x , y , and z directions used to define the orientation of the orbitals are chosen to run along the ‘ligand – V^{n+} ’ interatomic axes: x and y axes running along the V–O bonds in the basal plane while the z axis orienting along the bioctahedron axis, all of them are independent of the a , b , and c crystallographic directions of the unit cell. **Figure 3.5c** shows the 3D electronic spin distribution map calculated for $\text{Na}_3\text{V}_2(\text{PO}_4)_2\text{F}_3$, which allows to visualize the local spin distribution in the t_{2g} orbitals. The two V^{3+} ions in the bioctahedral units of $\text{Na}_3\text{V}_2(\text{PO}_4)_2\text{F}_3$ exhibit a similar spin distribution, with maximum spin concentration in lobes pointing in-between the two V–O bonds in the basal plane or in-between the V–O and V–F bonds in the (xz) and (yz) planes, thus confirming the partial occupancy of the three t_{2g} orbitals.

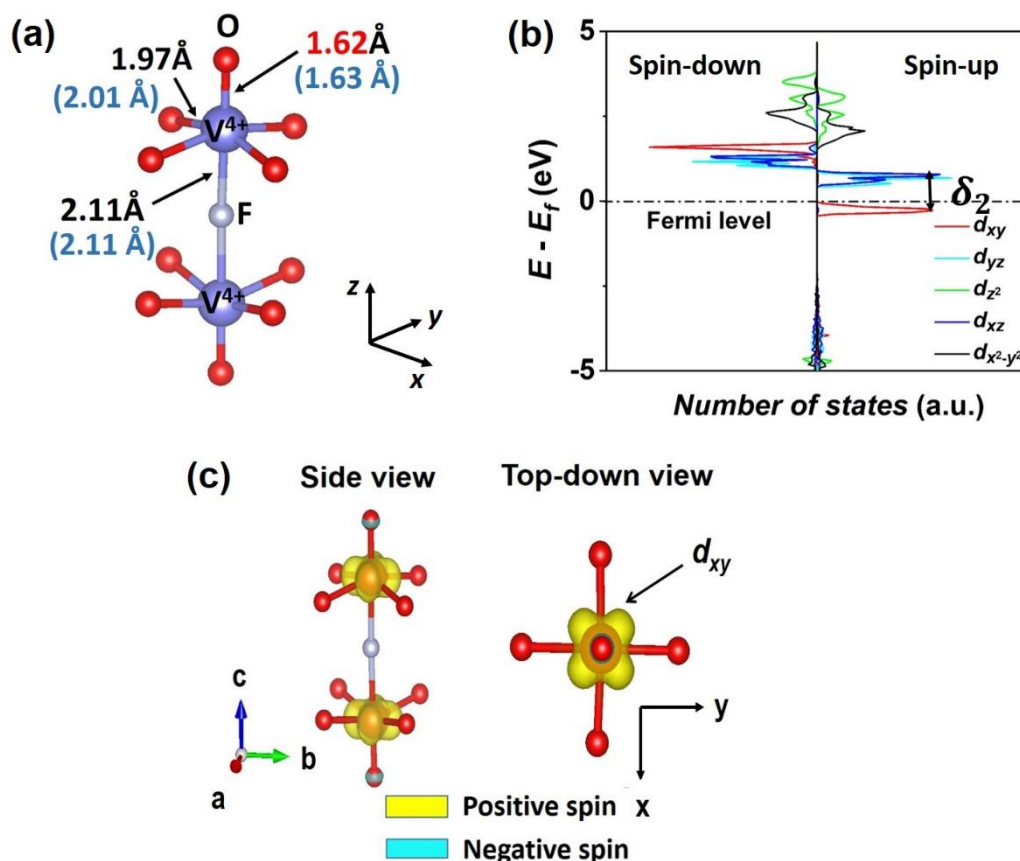


Figure 3.6 : (a) The local environment of V^{4+} in $\text{Na}_3(\text{VO})_2(\text{PO}_4)_2\text{F}$ with the optimized distances as compared to the experimental ones given in parentheses, (b) The DOS diagram of V^{4+} in $\text{Na}_3(\text{VO})_2(\text{PO}_4)_2\text{F}$ calculated by GGA method. Only the ‘spin-up’ state of d_{xy} orbital is occupied, (c) Calculated spin distribution map surrounding a $\text{V}_2\text{O}_{10}\text{F}$ bi-octahedral unit. A $2 \cdot 10^{-2}$ electron- \AA^{-2} iso-surface value was used for this plot. The single electron of V^{4+} occupies the d_{xy} orbital uniquely.

For $\text{Na}_3(\text{VO})_2(\text{PO}_4)_2\text{F}$, the vanadium ions reside in octahedral sites formed by four equal V–O bonds (1.97 \AA) in the basal plane, a very short V=O bond (1.62 \AA), and a long V–F bond (2.1 \AA), where the fluorine is shared with another vanadium ion in the axial position (**Figure 3.6a**). The calculated partial DOS on V shows that vanadium ions are in the +4 oxidation states as expected, and that the single unpaired electron is located only in the d_{xy} orbital which is perpendicular to the bi-octahedron axis (**Figure 3.6b**). Due to the presence of a short vanadyl bond, a distortion occurs on all VO_5F sites, lowering the O_h symmetry to C_{4v} locally. As a consequence, the t_{2g} orbitals of V^{4+} are split into b_2 (d_{xy}) and e (d_{xz} , d_{yz}) sub-groups while the e_g orbitals will be split further into b_2 ($d_{x^2-y^2}$) and a_1 (d_{z^2}). The splitting scheme and the relative energy of the orbitals in this case are shown in **Figure 3.7**. The orbital d_{xy} has therefore the lowest energy value and is occupied by the single electron of V^{4+} , the δ_2 splitting energy of 0.426 eV, which is higher than the kT energy at ambient temperature (25 meV) (**Figure 3.6b**). The 3D spin density map plotted

for a bioctahedron in $\text{Na}_3(\text{VO})_2(\text{PO}_4)_2\text{F}$ confirms the localization of the spin density only in lobes pointing in-between two V–O bonds in the basal plane, which is perpendicular to the bioctahedron axis (**Figure 3.6c**).

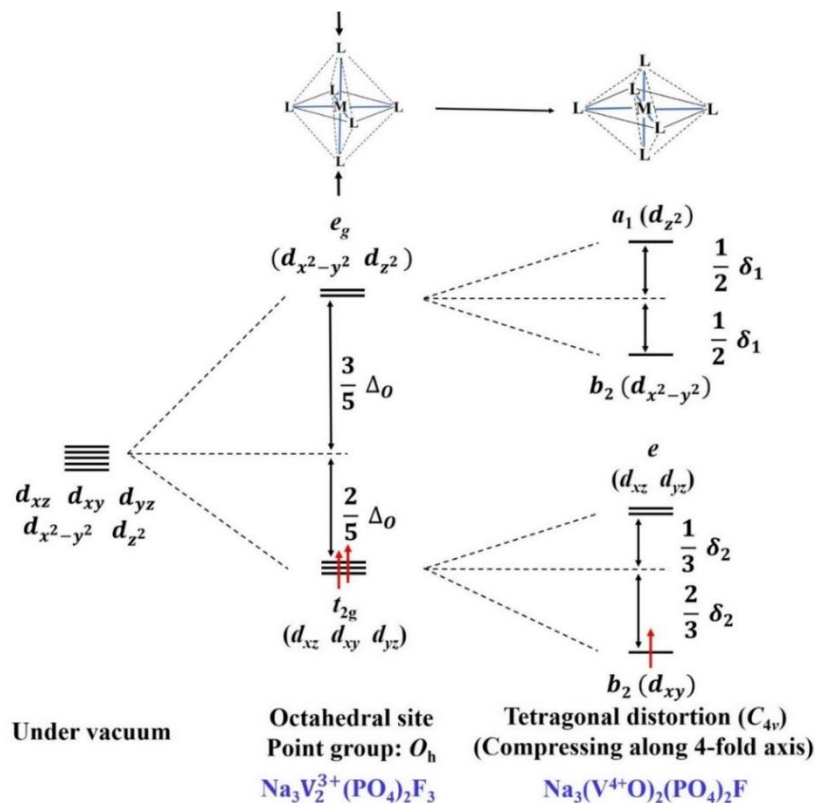


Figure 3.7 : The degeneracy of five 3d orbitals under vacuum and the splitting scheme of these orbitals in $\text{Na}_3\text{V}_2(\text{PO}_4)_2\text{F}_3$ and in $\text{Na}_3(\text{VO})_2(\text{PO}_4)_2\text{F}$.

Our DFT calculations also provide an approximate value of the electron spin density on the nuclei in the structures, thus allowing to compute the expected Fermi contact shifts for ^{31}P and ^{23}Na nuclei by using equations (1), (2) and (3) given in the experimental part.

Table 3.3 : Calculated ^{31}P Fermi contact NMR shifts (in ppm) in $\text{Na}_3\text{V}_2(\text{PO}_4)_2\text{F}_3$ and $\text{Na}_3(\text{VO})_2(\text{PO}_4)_2\text{F}$ using GGA and GGA+U methods, compared to the experimental ones.

| $\text{Na}_3\text{V}_2(\text{PO}_4)_2\text{F}_3$ | | | | | |
|---------------------------------------------------|-------------------|----------|----------|----------|----------|
| | Experimental data | GGA | GGA+3eV | GGA+4eV | GGA+5eV |
| P1 | ~ 6000 ppm | 6562 ppm | 4580 ppm | 3943 ppm | 3334 ppm |
| P2 | | 6534 ppm | 4598 ppm | 3942 ppm | 3336 ppm |
| $\text{Na}_3(\text{VO})_2(\text{PO}_4)_2\text{F}$ | | | | | |
| P1 | ~ 0 ppm | 96 ppm | 163 ppm | 117 ppm | 66 ppm |
| P2 | | 79 ppm | 124 ppm | 77 ppm | 22 ppm |

Each unit cell of $\text{Na}_3\text{V}_2(\text{PO}_4)_2\text{F}_3$ or $\text{Na}_3(\text{VO})_2(\text{PO}_4)_2\text{F}$ contains two groups of ^{31}P nuclei with different Fermi contact shifts. As seen in **Table 3.3**, the difference in the calculated shifts for these two groups is however negligible. For $\text{Na}_3\text{V}_2(\text{PO}_4)_2\text{F}_3$, the ^{31}P *ss*-NMR Fermi contact shifts computed either by GGA or GGA+U are positive and large, which is in agreement with the strong interaction expected between V^{3+} ions and P nuclei. As also expected, as the U value increases, the unpaired electrons are more localized on the t_{2g} orbitals of V^{3+} and therefore less delocalized to the neighboring phosphorus nuclei, leading to lower computed shifts [205]. Fermi contact shifts computed within the GGA method are in better agreement with the experimental one. For $\text{Na}_3(\text{VO})_2(\text{PO}_4)_2\text{F}$, whatever the method (GGA or GGA+U), all the calculated ^{31}P *ss*-NMR Fermi contact shifts are very weak and fall in the typical range of shifts for ^{31}P in diamagnetic compounds, which is also in agreement with the experimental observation (**Table 3.3**). This implies that there should be almost no electron spin transfer from the paramagnetic V^{4+} ions to phosphorus nuclei. As both the optimized structures and the computed Fermi contact shifts obtained using the GGA method are in good agreement with the experimental data, and in much better agreement than the GGA+U methods, hence only the GGA results will further be discussed in the following parts.

III.3.3. Spin Transfer Mechanisms between V^{n+} ions and Phosphorus nuclei

In order to investigate the spin transfer mechanism in $\text{Na}_3\text{V}_2(\text{PO}_4)_2\text{F}_3$, 3D electronic spin distribution maps are plotted using different iso-surface values and different local orientation. The electron spin transfer occurs through the so-called spin delocalization mechanism, which results from the overlap between t_{2g} orbitals of the V^{3+} ions (**Figure 3.5c** and **Figure 3.8a**), with the p_π orbitals of its neighboring O also hybridized with the sp^3 orbitals of P (**Figure 3.8a**). Among the three partially filled t_{2g} orbitals of V^{3+} ions, it appears that d_{xz} and d_{yz} are the two orbitals mostly involved in the spin transfer, as properly oriented to the π -overlap with O p_π orbital that is also overlapping with the sp^3 orbital of P, resulting in a $d_{xz}(\text{V}^{3+}) - p_\pi(\text{O}) - sp^3(\text{P})$ hybridization with a 135.8° V–O–P angle as schematized in **Figure 3.8b**. In $\text{Na}_3\text{V}_2(\text{PO}_4)_2\text{F}_3$, each phosphorus is surrounded by four V^{3+} ions and each of them contributes to a Fermi contact shift of around 1500 ppm through the $d_{xz}/d_{yz}(\text{V}^{3+}) - p_\pi(\text{O}) - sp^3(\text{P})$ interaction. In **Figure 3.8c**, the overall electron spin density map viewed along the c direction shows a strong

and positive spin density present on the P site, which is the origin of the highly shifted resonance (6000 ppm) observed on ^{31}P *ss*-NMR.

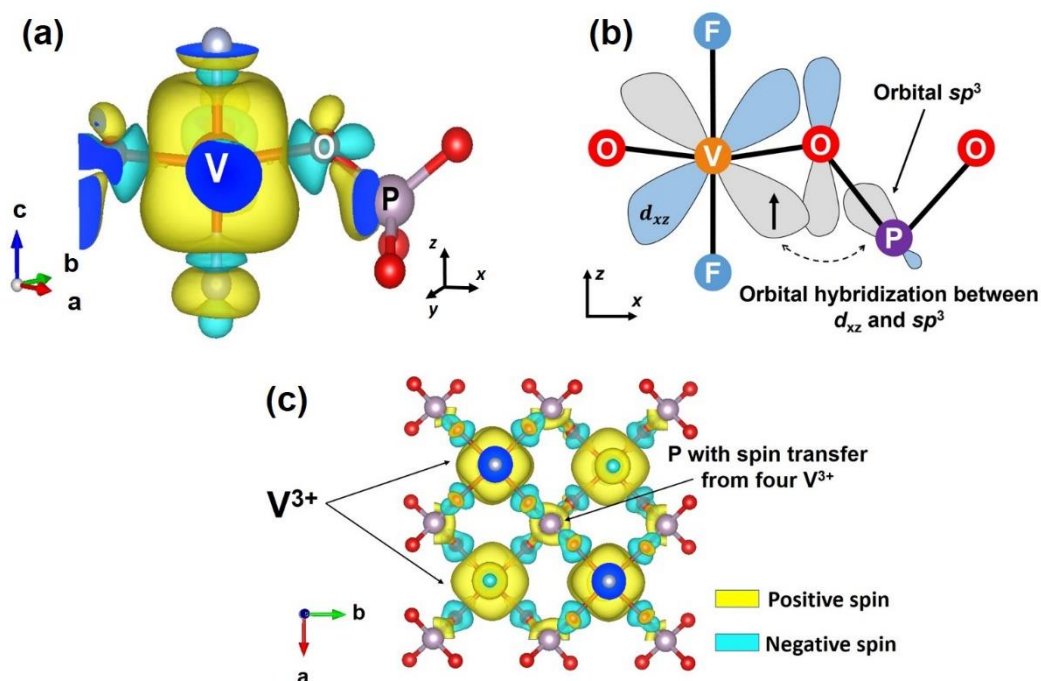


Figure 3.8 : (a) 3D calculated spin density map showing the electron spin transfer mechanism from a V^{3+} ion to a neighboring Phosphorus ($8 \cdot 10^{-4}$ electron· \AA^{-2} iso-surface value), (b) Schematic representation of the spin transfer mechanism from V^{3+} to P by orbital hybridization model, (c) 3D calculated spin density map ($8 \cdot 10^{-4}$ electron· \AA^{-2} iso-surface value) showing that each phosphorus nucleus in $\text{Na}_3\text{V}_2(\text{PO}_4)_2\text{F}_3$ receives the electron spin from four neighboring V^{3+} ions.

The spin transfer mechanism was also analyzed for $\text{Na}_3(\text{VO})_2(\text{PO}_4)_2\text{F}$. As previously discussed, the two V^{4+} ions of the biocahedral units are similar and exhibit one unpaired electron localized only in the d_{xy} orbital perpendicular to the biocahedron axis (**Figure 3.6c** and **Figure 3.9a**). As seen in **Figure 3.9b**, no orbital overlap is involving this V d_{xy} orbital and the P sp^3 one. The V d_{xy} orbital is only π -hybridized with one O $2p$ orbital that does not overlap with the P orbitals and the V–O–P angle is equal to 131.9° . However, as can be seen also in **Figure 3.9b**, another O $2p$ orbital, perpendicular to this π -bond, is negatively polarized as no overlapping occurs with Vanadium d_{xy} . One could have actually expected a negative Fermi contact shift for ^{31}P in $\text{Na}_3(\text{VO})_2(\text{PO}_4)_2\text{F}$, but the participation of the P sp^3 orbitals in the negatively deep polarized level should be very weak. This explains why we recorded a ^{31}P signal nearby 0 ppm for $\text{Na}_3(\text{VO})_2(\text{PO}_4)_2\text{F}$ despite the presence of paramagnetic V^{4+} ions around P (**Figure 3.9c**).

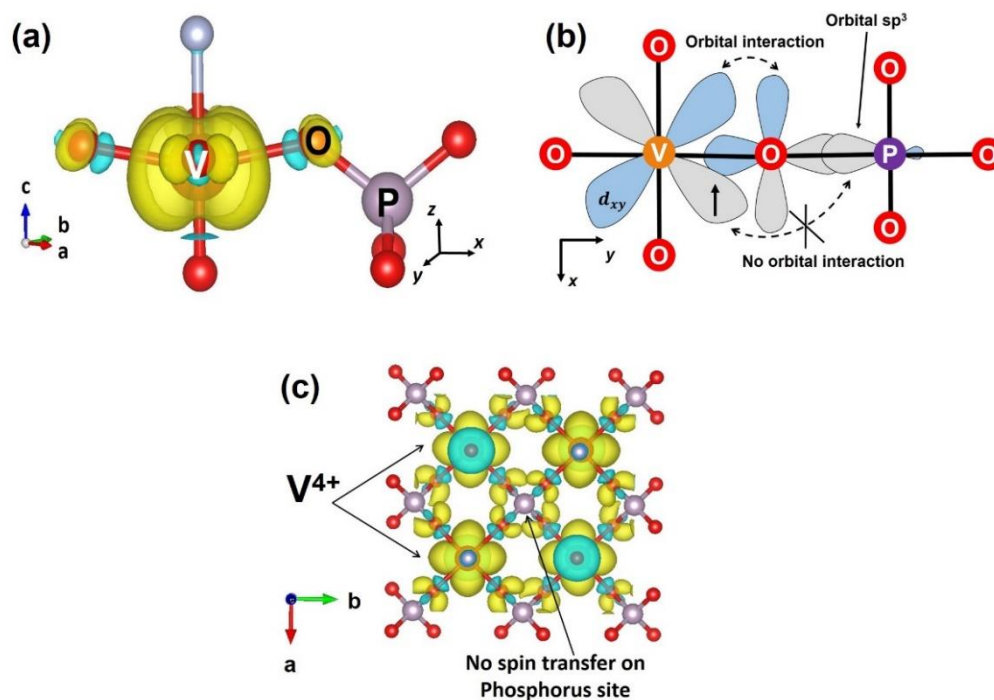


Figure 3.9 : (a) 3D calculated spin density map showing the electron spin density surrounding a V^{4+} ion in $\text{Na}_3(\text{VO})_2(\text{PO}_4)_2\text{F}$ ($2 \cdot 10^{-3}$ electron $\cdot\text{\AA}^{-2}$ iso-surface value), (b) A 2D projection of the V–O–P chemical bond on the (xy) plane of the octahedral unit. The single electron of V^{4+} occupies the d_{xy} orbital, which orients along the diagonal lines of the (xy) plane while the V–O–P bond is formed along the x/y direction, (c) The spin distribution map calculated at $8 \cdot 10^{-4}$ electron $\cdot\text{\AA}^{-2}$ revealing that there is no spin transfer between V^{4+} ions and phosphorus nuclei in $\text{Na}_3(\text{VO})_2(\text{PO}_4)_2\text{F}$ due to the lack of orbital overlap.

We further calculated the spin distribution map for some intermediate compositions in the $\text{Na}_3\text{V}_2(\text{PO}_4)_2\text{F}_3 - \text{Na}_3(\text{VO})_2(\text{PO}_4)_2\text{F}$ system. In $\text{Na}_3\text{V}^{3+}\text{V}^{4+}(\text{PO}_4)_2\text{F}_2\text{O}$ ($y' = 1.0$), for example, half of the vanadium ions are expected to be $+3$ and half $+4$. The terminal oxygen ions could be distributed differently in the crystal structure leading to a different distribution of $\text{V}^{3+}/\text{V}^{4+}$ ions over the vanadium sites. In order to study the relationship between the $\text{V}^{3+}/\text{V}^{4+}$ distribution in the structure and the observed ^{31}P ss-NMR shifts, we generated four different input models for $\text{Na}_3\text{V}_2(\text{PO}_4)_2\text{F}_2\text{O}$ with four different terminal O-distribution. We assumed that the Na^+ ordering in this case was similar to the one used for $\text{Na}_3\text{V}_2(\text{PO}_4)_2\text{F}_3$. The structures of the input models are given in **Figure 3.10**.

The as-mentioned models were relaxed until the structure reached its minimum energy. As no significant differences in the total energies (E) of all the calculated structural models were detected, we concluded that they exhibit similar stability; hence, from DFT calculations, we predict that V^{3+} or V^{4+} ions are randomly distributed over all the vanadium sites. The oxygen distribution on the terminal positions and hence the

$\text{V}^{3+}/\text{V}^{4+}$ distribution may be controlled solely by statistics leading to a random formation of $\text{V}^{3+}-\text{F}-\text{V}^{3+}$, $\text{V}^{4+}-\text{F}-\text{V}^{4+}$ and $\text{V}^{3+}-\text{F}-\text{V}^{4+}$ bioctahedra. This aspect will be further discussed in the following part. Nevertheless, our different models allow to compute the expected Fermi contact shifts for different $\text{V}^{3+}/\text{V}^{4+}$ phosphorus local environments. In all models, the vanadium ions are found in the +3 state with the same local electronic structure as in $\text{Na}_3\text{V}^{3+}_2(\text{PO}_4)_2\text{F}_3$ when they are localized in VO_4F_2 octahedral sites. On the contrary, they are found in the +4 oxidation state with the same local electronic structure as in $\text{Na}_3(\text{V}^{4+}\text{O})_2(\text{PO}_4)_2\text{F}$ when localized in VO_5F octahedral sites. Therefore, one expects the same spin transfer mechanisms as described above for each ion.

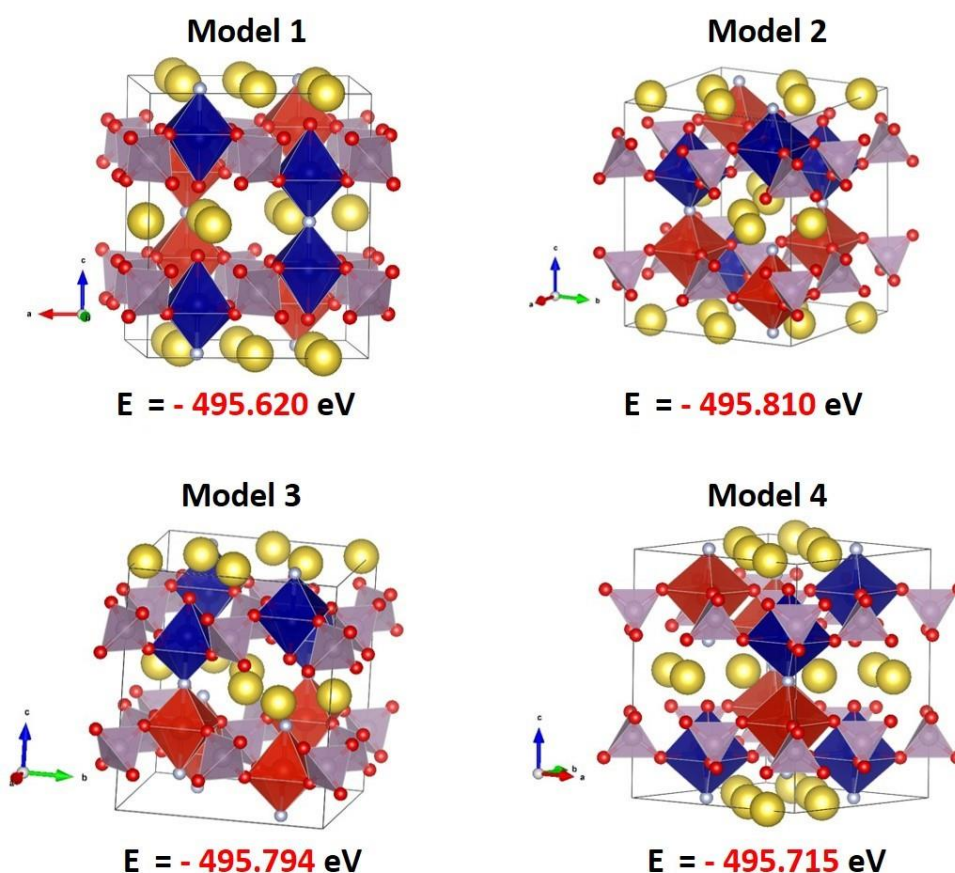


Figure 3.10 : Different ways to distribute V^{3+} and V^{4+} in $\text{Na}_3\text{V}_2(\text{PO}_4)_2\text{F}_2\text{O}$ ($y' = 1.0$) structure. $\text{V}^{3+}\text{O}_4\text{F}_2$ and $\text{V}^{4+}\text{O}_5\text{F}_1$ units are depicted as red and blue octahedra, respectively. The corresponding total energies of each configuration are given below the models.

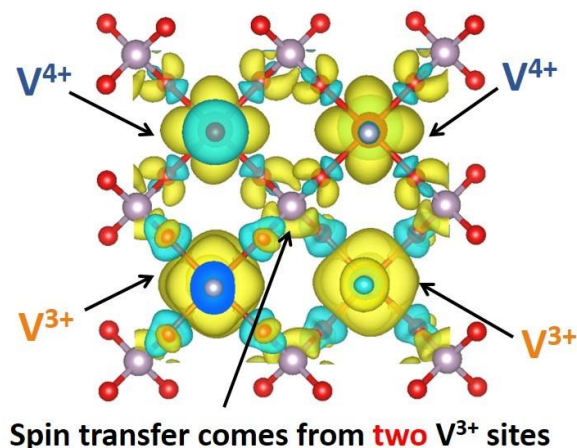


Figure 3.11 : The spin distribution map showing $\text{P}(\text{OV}^{3+})_2(\text{OV}^{4+})_2$ local environment in Model 1 of $\text{Na}_3\text{V}_2(\text{PO}_4)_2\text{F}_2\text{O}$.

As shown in **Figure 3.11** for model 1 ($\text{P}(\text{OV}^{3+})_2(\text{OV}^{4+})_2$ environment), a spin transfer mechanism does occur only from the two V^{3+} ions leading to computed ^{31}P Fermi contact shifts in the 3282 - 3285 ppm range (**Table 3.4**). 3D spin density maps of the other considered models can be found in **Figure 3.12**. In **Table 3.4**, we summarize the computed Fermi contact shifts depending on the P environments. DFT calculations allow to rationalize that in the $\text{Na}_3\text{V}_2(\text{PO}_4)_2\text{F}_3 - \text{Na}_3(\text{VO})_2(\text{PO}_4)_2\text{F}$ solid solution, each V^{3+} ions located in the proximity of the P contributes for about ~1500 ppm to the Fermi contact shift whereas a V^{4+} ion does not lead to a significant shift. This confirms the signal assignments proposed earlier [143].

Table 3.4 : Phosphorus local environments generated from DFT calculations and their respective Fermi contact shifts in comparison to those observed experimentally.

| | DFT calculations | | Experimental shift (ppm) |
|-------------------------|------------------------------------------------|------------------------|--------------------------|
| | Local environment | Calculated shift (ppm) | |
| Model 3 | $\text{P}(\text{OV}^{3+})_4$ | 5800 – 5900 | 6000 |
| Model 2 | $\text{P}(\text{OV}^{3+})_3(\text{OV}^{4+})$ | 4200 – 4600 | 4500 |
| Model 1/ Model 4 | $\text{P}(\text{OV}^{3+})_2(\text{OV}^{4+})_2$ | 3282 – 3285 | 3000 |
| Model 2 | $\text{P}(\text{OV}^{3+})(\text{OV}^{4+})_3$ | 1700 – 2100 | 1500 |
| Model 3 | $\text{P}(\text{OV}^{4+})_4$ | 665 | ~ 0 |

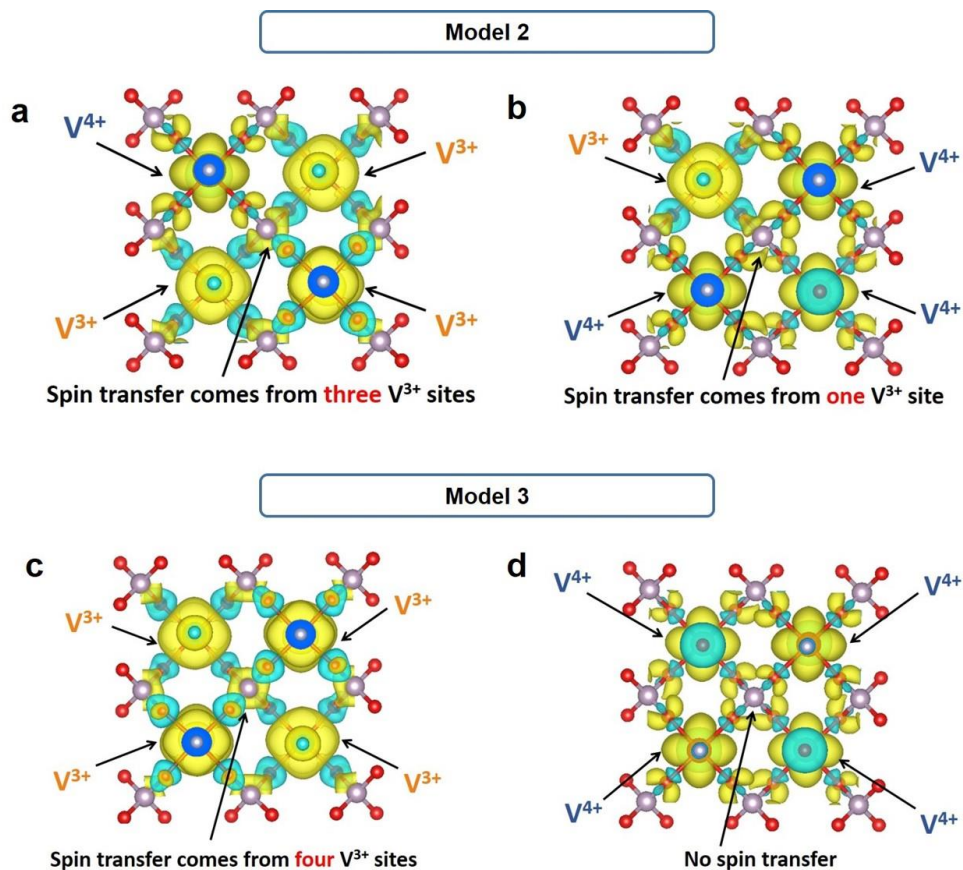


Figure 3.12 : (a and b) The spin distribution map showing $\text{P}(\text{OV}^{3+})_3(\text{OV}^{4+})$ and $\text{P}(\text{OV}^{3+})(\text{OV}^{4+})_3$ local environments in Model 2 of $\text{Na}_3\text{V}_2(\text{PO}_4)_2\text{F}_2\text{O}$; (c and d) The spin distribution map showing $\text{P}(\text{OV}^{3+})_4$ and $\text{P}(\text{OV}^{4+})_4$ local environments in Model 3 of $\text{Na}_3\text{V}_2(\text{PO}_4)_2\text{F}_2\text{O}$.

III.3.4. ^{23}Na ss-NMR in $\text{Na}_3\text{V}_2(\text{PO}_4)_2\text{F}_3 - \text{Na}_3(\text{VO})_2(\text{PO}_4)_2\text{F}$

The ^{23}Na ss-NMR properties of $\text{Na}_3\text{V}^{3+}_{2-y}\text{V}^{4+}_y(\text{PO}_4)_2\text{F}_{3-y}\text{O}_y$ ($0 \leq y \leq 2$) phases have been studied in details by Park *et al.* [101]. The authors proposed that there were eight different paths to transfer the electron spin from the neighboring vanadium sites to Na^+ , but only two of them are the strong 90° interactions which can really give rise to a significant Fermi contact shift [101]. There are three different Na sites in the crystal structure of $\text{Na}_3\text{V}^{3+}_{2-y}\text{V}^{4+}_y(\text{PO}_4)_2\text{F}_{3-y}\text{O}_y$ phases [83,143], and the local environments of these Na sites are given in **Figure 3.13**. Depending on the positions of the Na^+ ions in the channel, the spin diffusion paths can slightly vary; nevertheless, the two most dominant spin transfer mechanism always comes from the $t_{2g}(\text{V}) - p_\pi(\text{F1}) - s(\text{Na})$ orbital overlaps, and the ^{23}Na ss-NMR Fermi contact shift depends on the number of $\text{V}^{3+}/\text{V}^{4+}$ in its closest bioctahedral unit [101].

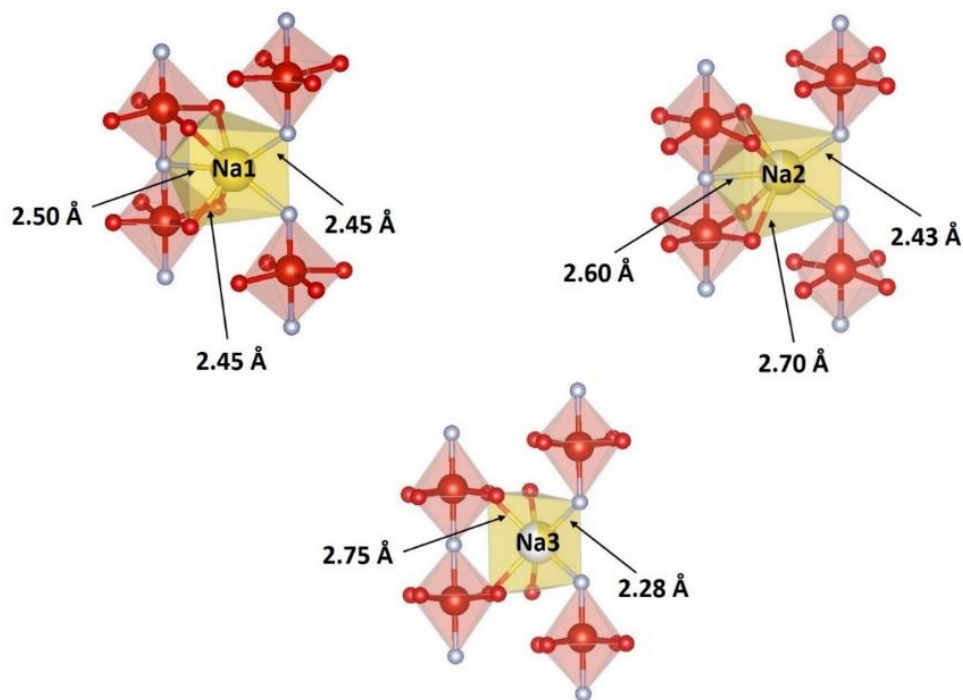


Figure 3.13 : Local environments of different Na sites in $\text{Na}_3\text{V}_2(\text{PO}_4)_2\text{F}_3$ material. Oxygen atoms are depicted in red and fluorine atoms are depicted in light grey.

In this previous study, the authors ignored the local distortion and peculiar local electronic structure of the V^{4+} ions involved in a vanadyl bond [101]. Actually by considering the partial t_{2g} orbital occupation for V^{3+} ions (**Figure 3.5b** and **c**) and the d_{xz} occupation for V^{4+} ions (**Figure 3.6b** and **c**), the electronic spin transfer mechanism between $\text{V}^{3+}/\text{V}^{4+}$ and the Na nuclei can be described differently. In $\text{Na}_3\text{V}^{3+}_2(\text{PO}_4)_2\text{F}_3$, among all the partially occupied t_{2g} orbitals, the d_{xz} one is properly oriented to form a π bond with F $2p_x$ that is pointing towards orbital $3s$ of a nearby Na^+ in the channel, leading to a $3d_{xz}(\text{V}^{3+}) - 2p_x(\text{F}) - 3s(\text{Na})$ hybridized orbital suitable for the spin transfer through a delocalization mechanism (**Figure 3.14a**). As a result, a positive Fermi contact shift is observed for ^{23}Na . In $\text{Na}_3(\text{V}^{4+}\text{O})_2(\text{PO}_4)_2\text{F}$, the single $3d_{xy}$ occupied orbital of the V^{4+} ions (**Figure 3.6b** and **c**) cannot strongly overlap with the $2p_x$ orbital of F1 and the $3s$ orbital of Na (**Figure 3.14b**) resulting in weaker Fermi contact shifts. In the oxygen-substituted phases, $\text{Na}_3\text{V}_{2-y}(\text{PO}_4)_2\text{F}_{3-y}\text{O}_y$, V^{3+} and V^{4+} co-exist and they are distributed randomly over all vanadium sites in the structure. This random distribution will create a third Na local environment, in which the Na nucleus resides next to a bioctahedron containing one V^{3+} and one V^{4+} . The value of the ^{23}Na NMR shift in this case is expected to be between the shift values observed in $\text{Na}_3\text{V}_2(\text{PO}_4)_2\text{F}_3$ and in $\text{Na}_3(\text{VO})_2(\text{PO}_4)_2\text{F}$.

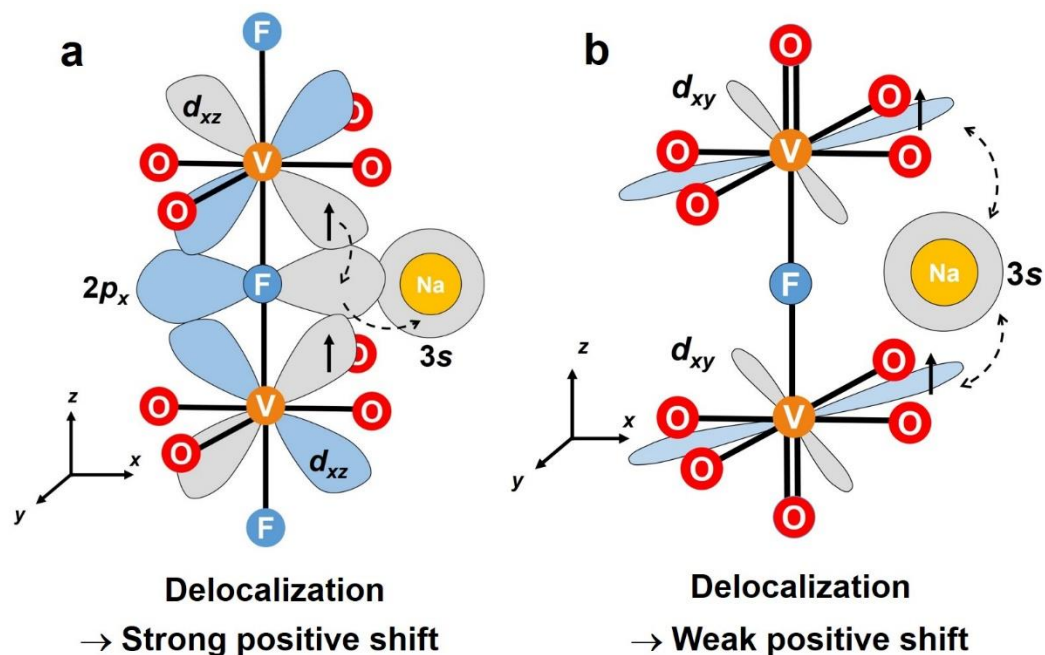


Figure 3.14: (a) The strong delocalization interaction between the spin electron on orbital $3d_{xz}$ (V^{3+}) and Na nuclei in $\text{Na}_3\text{V}_2(\text{PO}_4)_2\text{F}_3$, (b) The weak delocalization interaction between the spin electron on orbital $3d_{xy}$ (V^{4+}) and Na nuclei in $\text{Na}_3(\text{VO})_2(\text{PO}_4)_2\text{F}$.

Table 3.5 : The ^{23}Na ss-NMR chemical shifts (in ppm) calculated by GGA and GGA+U methods for sodium nuclei in $\text{Na}_3\text{V}_2(\text{PO}_4)_2\text{F}_3$ and $\text{Na}_3(\text{VO})_2(\text{PO}_4)_2\text{F}$ structures.

| $\text{Na}_3\text{V}_2(\text{PO}_4)_2\text{F}_3$ | | | | | |
|---------------------------------------------------------------------|--------------------------|---------------|----------------|----------------|----------------|
| | Experimental data | GGA | GGA+3eV | GGA+4eV | GGA+5eV |
| Na1 (x4) | ~ 139.6 ppm | 270 - 273 ppm | 166 ppm | 152 ppm | 131 ppm |
| Na2 (x8) | | 205 - 258 ppm | 133 ppm | 118 ppm | 102 ppm |
| $\text{Na}_3(\text{VO})_2(\text{PO}_4)_2\text{F}$ | | | | | |
| Na1 (x4) | ~ 80 ppm | 77 ppm | 6 ppm | -31 ppm | -65 ppm |
| Na2 (x8) | | 94 ppm | 59 ppm | 32 ppm | 2 ppm |

Note that in our study, we had to consider different Na-vacancy orderings or intermediate positions in order to model compounds with partial site occupancy. Therefore, the calculated Fermi contact shifts summarized in **Table 3.5** do not reflect the exact positions of the sodium ions and will not be further discussed here. Nevertheless, our approach allow to confirm the signal assignment presented in **Figure 3.14**.

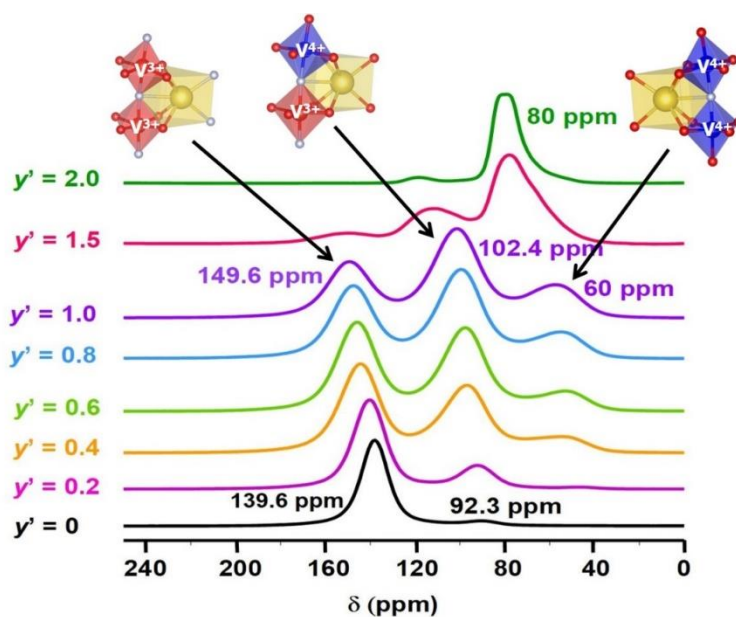


Figure 3.15 : Selective single pulse ^{23}Na MAS NMR spectra of $\text{Na}_3\text{V}^{3+}_{2-y'}\text{V}^{4+}_{y'}(\text{PO}_4)_2\text{F}_{3-y'}\text{O}_{y'}$ ($0 \leq y' \leq 2$) samples ($B_0 = 11.7\text{T}$; $\nu_R = 30\text{ kHz}$). The Na sites are in yellow and $\text{V}^{3+}\text{O}_4\text{F}_2$ and $\text{V}^{4+}\text{O}_5\text{F}_1$ octahedral units in red and blue, respectively.

III.3.5. $\text{V}^{3+}/\text{V}^{4+}$ distribution and the relative intensity of ^{23}Na and ^{31}P NMR

As the ^{23}Na and ^{31}P NMR signals assignments were confirmed by our DFT calculations, one can analyze the relative intensities of the ^{31}P and ^{23}Na signals in order to discuss the local electronic structures of the series. If V^{3+} and V^{4+} ions are distributed randomly over the whole structure, the probability of occurrence of each phosphorus or sodium local environment can be estimated using a binomial distribution:

$$C(n, k)p^k(1-p)^{(n-k)} = \left(\frac{n!}{k!(n-k)!} \right) p^k(1-p)^{(n-k)}$$

In the case of phosphorus, $n = 4$, i.e. the number of surrounding vanadium sites, $k = 0, 1, 2, 3$, or 4 , i.e. the number of V^{4+} among the vanadium sites, and $p =$ the percentage of V^{4+} for a given composition. In $\text{Na}_3\text{V}_{2-y'}(\text{PO}_4)_2\text{F}_{3-y'}\text{O}_{y'}$ compositions, $p = y'/2$.

In the case of sodium, $n = 2$ as the shift of each sodium is influenced by two neighboring vanadium sites, and $k = 0, 1$, or 2 .

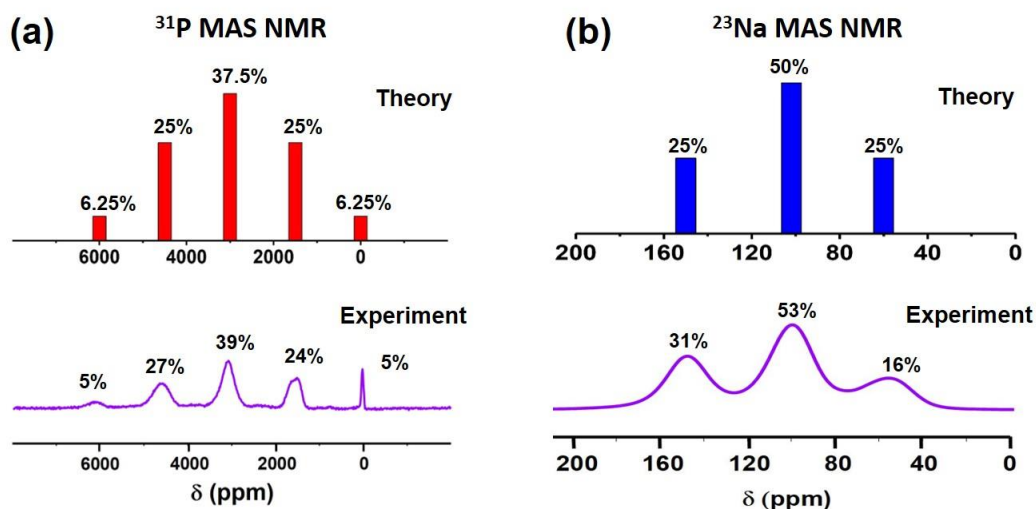


Figure 3.16 : Comparison between theoretical and experimental relative intensity of (a) ^{31}P ss-NMR and (b) ^{23}Na ss-NMR resonances recorded on $\text{Na}_3\text{V}_2(\text{PO}_4)_2\text{F}_2\text{O}$.

Figure 3.16a compares the experimental and theoretical relative intensities between the five ^{31}P ss-NMR resonances observed for $\text{Na}_3\text{V}_2(\text{PO}_4)_2\text{F}_2\text{O}$, characterized by half vanadium ions in the +4 state and half in the +3 state. The experimental values are in good agreement with those expected from the binomial distribution supporting the assumption that F and O are distributed randomly in the whole structure. In a previous publication, Broux *et al.* stated that ‘the experimental intensities distribution does not follow the theoretical one if the repartition of V^{3+} and V^{4+} ions would have been statistical around each phosphorus: phosphorus nuclei appear to be experimentally surrounded by more V^{4+} than expected’ [143]; in fact, the chemical formulas announced in [143] were not correct and there were indeed more V^{4+} than the expected values. With a correction of the chemical formula of these compounds in **Chapter II**, the theoretical and experimental relative intensities of ^{31}P NMR resonances recorded on $\text{Na}_3\text{V}_2(\text{PO}_4)_2\text{F}_2\text{O}$ are in good agreement with each other. Note that the ^{31}P ss-NMR spectrum of $\text{Na}_3\text{V}_2(\text{PO}_4)_2\text{F}_2\text{O}$ is quite broad with resonances ranging from 0 ppm to 6000 ppm (**Figure 3.16a**), and depending on the position of the off-set of the excitation pulse, their relative intensity can vary significantly. This observation is demonstrated in **Figure 3.17**, where the off-set of the excitation was placed at 800 ppm, 2978 ppm, and 5000 ppm, the intensities of resonances close to the off-set are enhanced while those far away are underestimated.

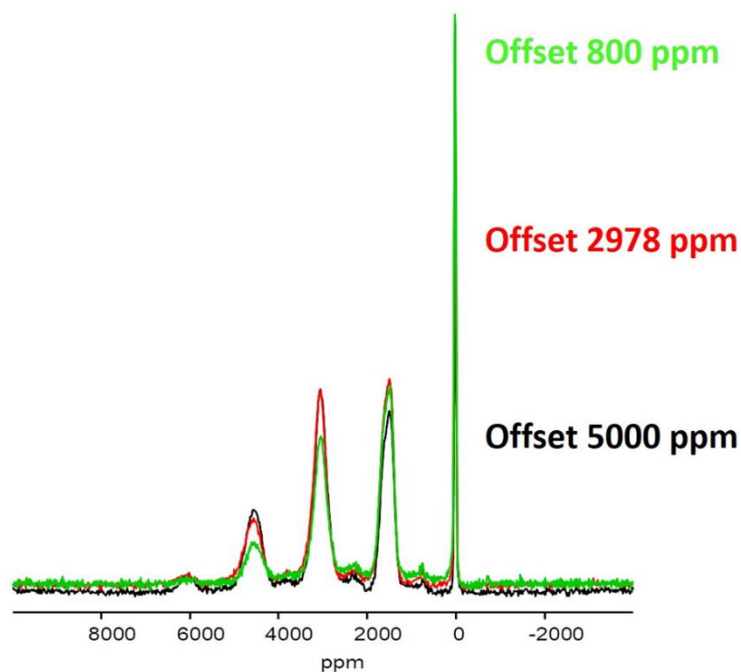


Figure 3.17 : The evolution of the relative intensity between different ^{31}P *ss*-NMR resonances in $\text{Na}_3\text{V}_2(\text{PO}_4)_2\text{F}_2\text{O}$ as the function of the off-set positions (800 ppm, 2978 ppm, and 5000 ppm).

Furthermore, the resonances observed in $\text{Na}_3\text{V}_2(\text{PO}_4)_2\text{F}_2\text{O}$ have different relaxation times. When the refocalization delay of the echo acquisition is varied, the intensities of some peaks can be underestimated or overestimated (**Figure 3.18**). Therefore, the ^{31}P *ss*-NMR experimental measurements on $\text{Na}_3\text{V}_2(\text{PO}_4)_2\text{F}_2\text{O}$ are just semi-quantitative.

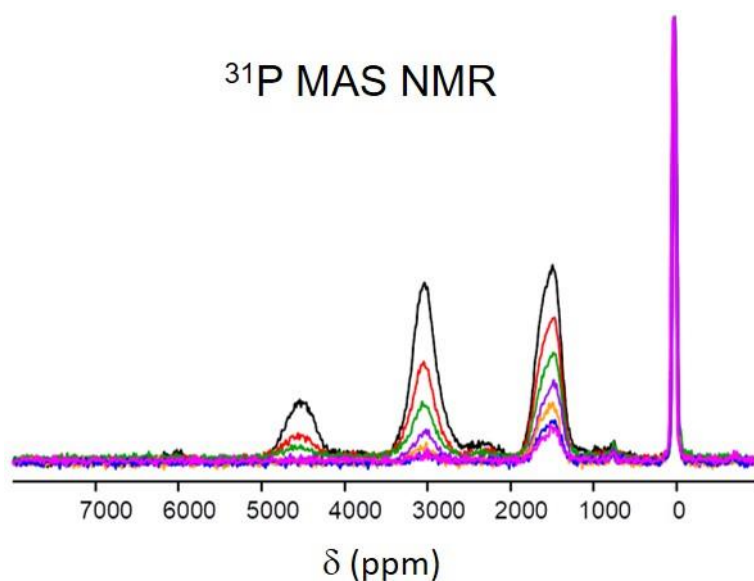


Figure 3.18 : The change in the relative intensity between different ^{31}P *ss*-NMR resonances in $\text{Na}_3\text{V}_2(\text{PO}_4)_2\text{F}_2\text{O}$ at different refocalization delays ranging from 1s (black spectrum) to 7s (pink spectrum).

The theoretical relative intensities between ^{23}Na NMR resonances can also be calculated by the binomial equation by considering the $\text{V}^{3+}/\text{V}^{4+}$ distribution on two closest vanadium sites. The relative intensity of ^{23}Na NMR signals can be extracted from the calculated area of peaks by using DM-fit software with the pseudo-Voigt peak shape function. All the observed ^{23}Na NMR resonances in the $\text{Na}_3\text{V}_{2-y}(\text{PO}_4)_2\text{F}_{3-y}\cdot\text{O}_y$ compositions can be fit with a pseudo-Voigt peak shape function, except the resonance at 80 ppm in $\text{Na}_3(\text{VO})_2(\text{PO}_4)_2\text{F}$ composition, which requires two peak functions to describe it. This could imply a Na ordering in the structure leading to two Na local environments which are slightly different from each other [101]. Nevertheless, the intensity of this resonance is considered to be equal to the sum of the area of these two signals. The theoretical and observed relative intensities between ^{23}Na NMR resonant lines for $\text{Na}_3\text{V}_2(\text{PO}_4)_2\text{F}_2\text{O}$ composition are given in **Figure 3.16b** as an example. The results for other compositions can be found in **Table 3.6**.

The resonant region of ^{23}Na *ss*-NMR signals is quite narrow; therefore, there is no influence of the off-set position on the relative intensity of the signal and ^{23}Na *ss*-NMR measurement is quantitative. In this case, the binomial equation gives results which are in good agreement with the experimental ones proving that $\text{V}^{3+}/\text{V}^{4+}$ are randomly distributed in these structures. The relative intensity between ^{23}Na resonances can be used to estimate the *y*' value in a $\text{Na}_3\text{V}_{2-y}(\text{PO}_4)_2\text{F}_{3-y}\cdot\text{O}_y$ composition.

Table 3.6 : A comparison of the experimental and theoretical relative intensities between the three main ^{23}Na *ss*-NMR resonances observed for the $\text{Na}_3\text{V}_2(\text{PO}_4)_2\text{F}_3 - \text{Na}_3(\text{VO})_2(\text{PO}_4)_2\text{F}$ solid-solution.

| | Calculated | | | Observed | | |
|--------------------------------------------------------------------|-------------------------------|---------------------------------------------|-------------------------------|-------------------------------|---------------------------------------------|-------------------------------|
| | $\text{Na}(\text{OV}^{3+})_2$ | $\text{Na}(\text{OV}^{3+})(\text{OV}^{4+})$ | $\text{Na}(\text{OV}^{4+})_2$ | $\text{Na}(\text{OV}^{3+})_2$ | $\text{Na}(\text{OV}^{3+})(\text{OV}^{4+})$ | $\text{Na}(\text{OV}^{4+})_2$ |
| $\text{Na}_3\text{V}_2(\text{PO}_4)_2\text{F}_3$ | 100% | | | 95% | 5% | |
| $\text{Na}_3\text{V}_2(\text{PO}_4)_2\text{F}_{2.8}\text{O}_{0.2}$ | 81% | 18% | 1% | 81% | 19% | |
| $\text{Na}_3\text{V}_2(\text{PO}_4)_2\text{F}_{2.6}\text{O}_{0.4}$ | 64% | 32% | 4% | 53% | 40% | 7% |
| $\text{Na}_3\text{V}_2(\text{PO}_4)_2\text{F}_{2.4}\text{O}_{0.6}$ | 49% | 42% | 9% | 47% | 45% | 8% |
| $\text{Na}_3\text{V}_2(\text{PO}_4)_2\text{F}_{2.2}\text{O}_{0.8}$ | 36% | 48% | 16% | 39% | 49% | 11% |
| $\text{Na}_3\text{V}_2(\text{PO}_4)_2\text{F}_2\text{O}$ | 25% | 50% | 25% | 31% | 53% | 16% |
| $\text{Na}_3\text{V}_2(\text{PO}_4)_2\text{F}_{1.5}\text{O}_{1.5}$ | 6.25% | 37.5% | 56.25% | 7% | 24% | 69% |
| $\text{Na}_3(\text{VO})_2(\text{PO}_4)_2\text{F}$ | | | 100% | | 3% | 97% |

III.4. NMR study on $\text{Na}_x\text{V}_2(\text{PO}_4)_2\text{F}_3$ and $\text{Na}_x\text{V}_2(\text{PO}_4)_2\text{F}_2\text{O}$

III.4.1. $\text{Na}_x\text{V}_2(\text{PO}_4)_2\text{F}_3$

All the desodiated phases were first studied by ^{23}Na MAS NMR, then by ^{31}P MAS NMR. The XRD patterns were recorded on the recovered powder in order to confirm their structures and compositions. The XRD patterns of the desodiated phases and their corresponding cell parameters obtained from Le Bail fits are summarized in **Figure 3.19** and **Table 3.7**.

For most of the recovered powder, the XRD patterns show well defined peaks, except for $\text{NaV}_2(\text{PO}_4)_2\text{F}_3$. The diffraction peaks of $\text{NaV}_2(\text{PO}_4)_2\text{F}_3$ are significantly broadened and the global intensity of all the diffracted peaks is significantly low suggesting that the structure might become highly disordered at the high applied voltage. The intensity of the diffraction peaks in $\text{NaV}_2(\text{PO}_4)_2\text{F}_3$ is so low that a Le Bail fit performed on the obtained XRD pattern did not give any meaningful information.

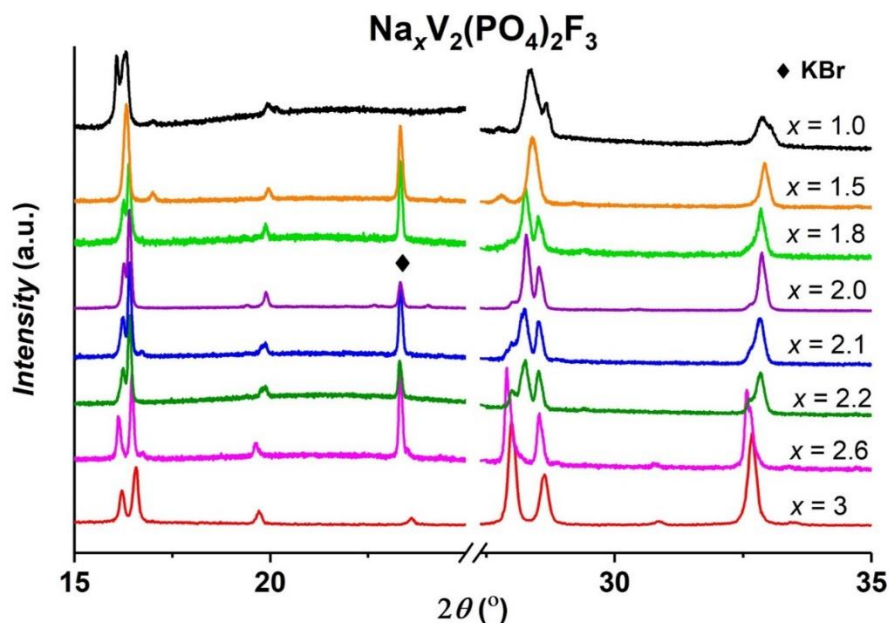


Figure 3.19 : XRD patterns of $\text{Na}_x\text{V}_2(\text{PO}_4)_2\text{F}_3$ powders recorded with $\text{Cu K}\alpha$ radiation. The 2θ angular region of $25 - 27.375^\circ$ was excluded from the patterns due to the presence of the intense diffraction peaks of KBr. The intensities of all the diffraction peaks were normalized to the range of 0 – 1.

Table 3.7 : Cell parameters of $\text{Na}_x\text{V}_2(\text{PO}_4)_2\text{F}_3$ ($1.5 \leq x \leq 3$) materials determined from Le Bail fits. († The XRD patterns reveal the presence of two phases with the $Amam$ and $P4_2/mnm$ space groups, respectively. ‡ All the observed reflection peaks can be observed by the use of a supercell with the $Pmmm$ space group as reported in [132]. Nevertheless, the actual structure of the supercell is still unknown).

| | Space group | a (Å) | b (Å) | c (Å) | V/Z (Å ³) |
|--------------------|-------------|-----------|------------|------------|-------------------------|
| $x = 3$ | $Amam$ | 9.0288(6) | 9.0426(6) | 10.7402(5) | 219.22 |
| $x = 2.6$ | $Amam$ | 9.020(1) | 9.0433(6) | 10.7549(6) | 219.33 |
| $x = 2.2^\dagger$ | $Amam$ | 9.035(1) | 8.9777(5) | 10.7825(6) | 218.66 |
| | $I4/mmm$ | 6.3139(3) | 6.3139(3) | 10.791(1) | 215.10 |
| $x = 2.1^\dagger$ | $Amam$ | 9.0197(8) | 8.9771(3) | 10.7794(4) | 218.20 |
| | $I4/mmm$ | 6.3179(3) | 6.3179(3) | 10.7981(8) | 215.51 |
| $x = 2.0^\ddagger$ | $Pmmm$ | 25.296(1) | 12.6097(1) | 21.597(1) | 215.28 |
| $x = 1.8$ | $I4/mmm$ | 6.3125(5) | 6.3125(5) | 10.796(1) | 215.10 |
| $x = 1.5$ | $I4/mmm$ | 6.2879(4) | 6.2879(4) | 10.832(2) | 214.13 |

The XRD results reveal that the patterns recorded for $\text{Na}_3\text{V}_2(\text{PO}_4)_2\text{F}_3$ and $\text{Na}_{2.6}\text{V}_2(\text{PO}_4)_2\text{F}_3$ can be indexed with a single phase within the $Amam$ space group (**Table 3.7**). All the samples with $2.0 < x < 2.6$ were in fact a mixture of two phases indexed in the $Amam$ and $I4/mmm$ space groups, respectively (**Figure 3.19** and **Table 3.7**). In $\text{Na}_2\text{V}_2(\text{PO}_4)_2\text{F}_3$, the recorded XRD pattern reveals the appearance of several extra diffraction peaks which are due to the formation of a new supercell, indexed in the $Pmmm$ space group (**Figure 3.20**); nonetheless, the actual structure of this supercell has not been determined yet even with the help of SXRD [132]. When the x value is less than 2.0, the recorded XRD patterns can be indexed in the $I4/mmm$ space group (**Table 3.7**).

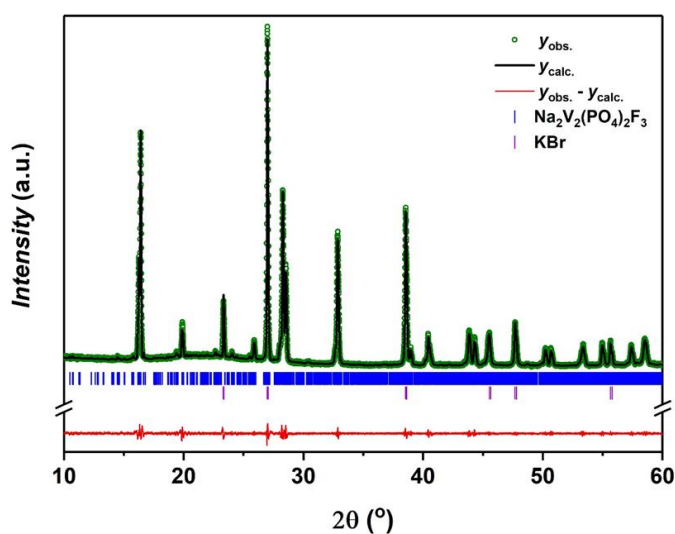


Figure 3.20 : Le Bail fit of $\text{Na}_2\text{V}_2(\text{PO}_4)_2\text{F}_3$ performed by the use of a supercell within the $Pmmm$ space group with $a = 25.221$ Å, $b = 12.599$ Å and $c = 21.586$ Å.

A change in the space group indexations from *Amam* to *Pmmm* and *I4/mmm* is a consequence of the Na^+ -vacancy ordering that occurs during the desodiation process. At the atomic local scale, the phosphorus atoms in these structures reside in the PO_4 group, which is always in interaction with its four neighboring vanadium ions, $\text{P}(\text{OV}^{\text{n}+})_4$. The atomic positions of the Na^+ ions in the diffusion channels vary during the electrochemical cycling as a result of the Na^+ -vacancy ordering; nonetheless, the strongest Fermi contact between $\text{V}^{\text{n}+}$ ions and the Na nucleus always comes from the two $\text{V}^{\text{n}+}$ ions in the closest bioctahedral unit. Therefore, the origin of ^{23}Na MAS NMR resonances observed in $\text{Na}_x\text{V}_2(\text{PO}_4)_2\text{F}_3$ desodiated phases can also be interpreted by the distribution of $\text{V}^{3+}/\text{V}^{4+}/\text{V}^{5+}$ ions in the $\text{Na}(\text{OV}^{\text{n}+})_2$ units.

As already discussed, the ^{23}Na MAS NMR spectrum of the pristine phase, $\text{Na}_3\text{V}_2(\text{PO}_4)_2\text{F}_3$, shows the main resonance at 140 ppm corresponding to the $\text{Na}(\text{OV}^{3+}-\text{F})_2$ local environment where the Na nucleus receives the electron spins from the two neighboring V^{3+} thanks to the strong $3d_{xz}(\text{V}^{3+}) - 2p_x(\text{F}) - 3s(\text{Na})$ orbital interaction [101,143,182]. The tiny signal at 92 ppm is due the $\text{Na}(\text{OV}^{3+}-\text{F})(\text{OV}^{4+}=\text{O})$ local environment as a result of the presence of oxygen defects (**Figure 3.21a**). Upon electrochemical charging, Na^+ ions are extracted from the structure together with the oxidation of V^{3+} into V^{4+} to form the $\text{Na}_x\text{V}_2(\text{PO}_4)_2\text{F}_3$ ($0 \leq x \leq 3$) compositions. A single ^{23}Na NMR resonance at 140 ppm is observed for $\text{Na}_{2.6}\text{V}_2(\text{PO}_4)_2\text{F}_3$ (**Figure 3.21a**), which is similar to the case of $\text{Na}_3\text{V}_2(\text{PO}_4)_2\text{F}_3$. This resonance is also assigned to the $\text{Na}(\text{OV}^{3+}-\text{F})_2$ local environment. The resonance at 92 ppm was completely diminished which could be due to a preferential extraction of Na^+ ions close to V^{4+} ions bonded to the O-defect.

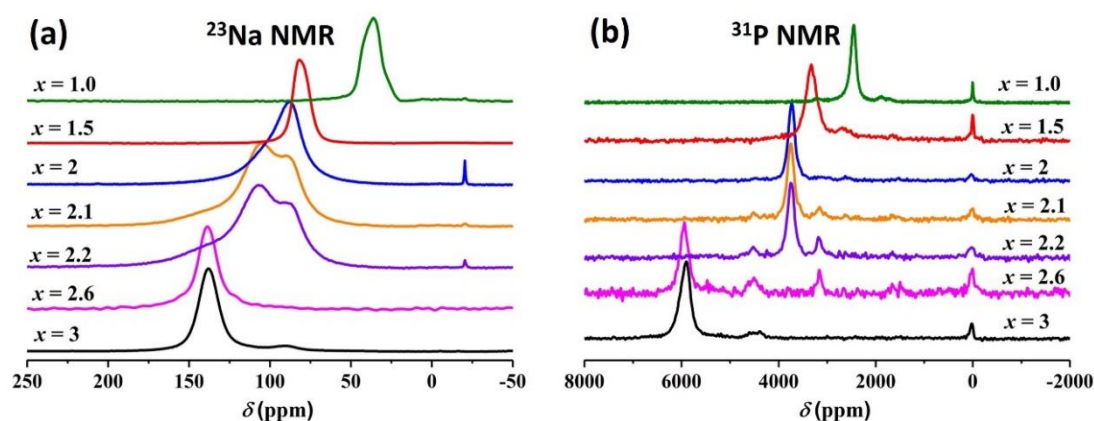


Figure 3.21 : (a) ^{23}Na MAS NMR spectra of $\text{Na}_x\text{V}_2(\text{PO}_4)_2\text{F}_3$ phases recorded at $B_0 = 11.7$ T with $\nu_R = 30$ kHz, (b) ^{31}P MAS NMR spectra of $\text{Na}_x\text{V}_2(\text{PO}_4)_2\text{F}_3$ phases recorded at $B_0 = 2.35$ T with $\nu_R = 30$ kHz.

The ^{31}P spectrum of pristine phase, $\text{Na}_3\text{V}_2(\text{PO}_4)_2\text{F}_3$, shows a main signal at 6000 ppm, which is attributed to the dominant $\text{P}(\text{OV}^{3+}\text{-F})_4$ local environment [143]. The tiny resonance at 4500 ppm is attributed to the $\text{P}(\text{OV}^{3+}\text{-F})_3(\text{OV}^{4+}=\text{O})_{\text{vanadyl}}$ unit as a result of the presence of oxygen defects [143]. In $\text{Na}_{2.6}\text{V}_2(\text{PO}_4)_2\text{F}_3$, the main ^{31}P NMR resonance at 6000 ppm corresponding to the $\text{P}(\text{OV}^{3+}\text{-F})_4$ local environment can be observed clearly, and the resonances at 4500 ppm, 3000 ppm and 1500 ppm corresponding to $\text{V}^{4+}=\text{O}$ defects are still obvious.

Up to now, we have distinguished two different V^{4+} local environments in this structure:

i) V^{4+} involved in a vanadyl-type bond, $\text{F-V}^{4+}\text{O}_4=\text{O}$, which is formed due to the presence of the oxygen defects or oxygen substitution in the structure. This V environment is highly distorted due to the presence of a strongly covalent vanadyl bond ($d_{\text{V}=\text{O}} = 1.62 \text{ \AA}$). As a consequence, the unpaired electron of V^{4+} is localized in the $3d_{xy}$ orbital, which cannot be extended to the neighboring phosphorus nuclei to induce the Fermi contact.

ii) V^{4+} in the slightly distorted $\text{F-V}^{4+}\text{O}_4\text{-F}$ local environment: In the pristine material, $\text{Na}_3\text{V}_2(\text{PO}_4)_2\text{F}_3$, most of the V^{3+} ions reside in the ‘quasi’-symmetric octahedral site $\text{F-V}^{3+}\text{O}_4\text{-F}$; upon charge, the V^{3+} in this octahedral site is oxidized and thus generates the $\text{F-V}^{4+}\text{O}_4\text{-F}$ group with a contraction on the surrounding bond lengths. The terminal V-F in this unit is shortened to $\sim 1.88 \text{ \AA}$; nevertheless, this length shortening is not strong enough to induce a significant compressed tetragonal distortion on this octahedral site and the three t_{2g} orbitals of V^{4+} are still degenerated. Therefore, the unpaired electron on V^{4+} in $\text{F-V}^{4+}\text{O}_4\text{-F}$ partially occupies these t_{2g} orbitals and can thus induce the Fermi contact with the neighboring phosphorus.

In order to distinguish the two different kinds of V^{4+} ions that can exist in the structure upon charging, we labelled the V^{4+} formed by oxygen substitution as “ $\text{V}^{4+}=\text{O}$ ” and its interaction with the phosphorus nucleus is denoted as $\text{P}(\text{OV}^{4+}=\text{O})$ in order to stress the presence of the highly covalent vanadyl bond that induces the great local distortion on this site. The V^{4+} ion formed through the oxidation of $\text{F-V}^{3+}\text{O}_4\text{-F}$ during charge is labelled as “ $\text{V}^{4+}\text{-F}$ ” and its Fermi interaction with the neighboring phosphorus is denoted as $\text{P}(\text{OV}^{4+}\text{-F})$. The presence of O in the $\text{P}(\text{OV}^{4+}\text{-F})$ notation stresses that the Fermi

contact between $\text{V}^{3+}/\text{V}^{4+}$ and the adjacent phosphorus nucleus occurs through the shared oxygen. These notations will be used in the following parts in order to explain the origin of the ^{23}Na and ^{31}P NMR resonances detected in $\text{Na}_x\text{V}_2(\text{PO}_4)_2\text{F}_3$ desodiated phases.

In $\text{Na}_{2.2}\text{V}_2(\text{PO}_4)_2\text{F}_3$ and $\text{Na}_{2.1}\text{V}_2(\text{PO}_4)_2\text{F}_3$, three different ^{23}Na signals are detected at 140 ppm, 110 ppm and 80 ppm (**Figure 3.21a**). By analogy to the study of the oxygen substituted $\text{Na}_3\text{V}_2(\text{PO}_4)_2\text{F}_{3-y}\text{O}_y$ phases, these ^{23}Na NMR resonances are attributed to the $\text{Na}(\text{OV}^{3+}-\text{F})_2$, $\text{Na}(\text{OV}^{3+}-\text{F})(\text{OV}^{4+}-\text{F})$ and $\text{Na}(\text{OV}^{4+}-\text{F})_2$ local environments, respectively. As mentioned above, the $\text{V}^{4+}-\text{F}$ groups are generated from the oxidation of $\text{V}^{3+}-\text{F}$ groups during the desodiation. This oxidation leads to a decrease in the total electron spin density in the unit cell, and thus weakens the Fermi contact between V^{n+} ions and Na nuclei. The relative intensities between $\text{Na}(\text{OV}^{3+}-\text{F})_2$, $\text{Na}(\text{OV}^{3+}-\text{F})(\text{OV}^{4+}-\text{F})$ and $\text{Na}(\text{OV}^{4+}-\text{F})_2$ resonances does not follow a binomial distribution expected for a statistical repartition of $\text{V}^{3+}/\text{V}^{4+}$ in the bioctahedra, which could be due to the fact that (i) the co-existence of *Amam* and *I4/mmm* phases (**Table 3.7**) and each of these phases has different preference towards the formation of $\text{V}^{3+}-\text{F}$ or $\text{V}^{4+}-\text{F}$, or (ii) the oxidation of $\text{V}^{3+}-\text{F}$ into $\text{V}^{4+}-\text{F}$ does not occur randomly in these compositions, but through a $\text{V}^{3+}-\text{F}/\text{V}^{4+}-\text{F}$ charge ordering and hence the $\text{V}^{3+}-\text{F}/\text{V}^{4+}-\text{F}$ distribution does not obey the statistics anymore.

The ^{31}P NMR spectra recorded for $\text{Na}_{2.2}\text{V}_2(\text{PO}_4)_2\text{F}_3$ and $\text{Na}_{2.1}\text{V}_2(\text{PO}_4)_2\text{F}_3$ show a main resonance at 3700 ppm while the signatures of $\text{V}^{4+}=\text{O}$ defects at 4500 ppm and 3000 ppm are still visible. One would have expected the presence of multiple ^{31}P NMR signals in these compositions due to a statistical repartition of $\text{V}^{3+}-\text{F}$ and $\text{V}^{4+}-\text{F}$ groups. Nonetheless, the presence of a main signal at 3700 ppm indicates that only one ^{31}P local environment is observed and the oxidation of $\text{V}^{3+}-\text{F}$ into $\text{V}^{4+}-\text{F}$ occurs through a charge ordering process around the phosphorus nuclei that all the phosphorus local environments are the identical. For $x = 2.2$ and 2.1 , we expect roughly the same amount of V^{3+} and V^{4+} ions, and the main signal could then be assigned to the $\text{P}(\text{OV}^{3+}-\text{F})_2(\text{OV}^{4+}-\text{F})_2$ local environment.

When moving from $\text{Na}_2\text{V}_2(\text{PO}_4)_2\text{F}_3$ to $\text{Na}_1\text{V}_2(\text{PO}_4)_2\text{F}_3$, only one ^{23}Na MAS NMR resonance is detected and its position shifts gradually from 80 ppm to 35 ppm. This observation indicates that (i) the Na^+ ions in the highly desodiated phases can possess higher mobility than in its initial state that they can hop freely between different Na sites

in the diffusion channels and hence only one average signal can be detected on the NMR timescale, or (ii) there could be a rapid electronic hopping between two vanadium sites in the same bioctahedral unit and this electronic hopping can occur in all bioctahedra that all the vanadium sites are now equivalent in terms of spin, which would result in a unique ^{23}Na NMR resonance. Finally, the unique ^{23}Na NMR signal shifts gradually toward a lower resonant frequency as the electron spin density in the unit cell decreases when the desodiation occurs and this weakens the Fermi contact between vanadium ions and Na nuclei.

One ^{31}P MAS NMR resonance is also observed in all the compositions between $\text{Na}_2\text{V}_2(\text{PO}_4)_2\text{F}_3$ to $\text{Na}_1\text{V}_2(\text{PO}_4)_2\text{F}_3$, thus confirming the fast electronic hopping between vanadium sites in the same bioctahedral units and all the vanadium ions are now equivalent in terms of electron spin. The ^{31}P NMR resonances also shifts toward a lower resonant frequency due to a decrease in the total spin density upon charge.

In the case of $\text{Na}_1\text{V}_2(\text{PO}_4)_2\text{F}_3$, several ^{31}P MAS NMR measurements were performed on this composition, and in some cases the obtained signals were greatly broadened. Some ^{31}P MAS NMR studies on $\text{NaV}_2(\text{PO}_4)_2\text{F}_3$ reported in the literature also showed very broad and featureless signals [152,201], the broadening and the featureless of the signals at the high voltage region could be linked to the disorder of the phase as indicated by broadening of the diffraction lines or it could also be linked to the instability of the highly desodiated samples.

III.4.2. $\text{Na}_x\text{V}_2(\text{PO}_4)_2\text{F}_2\text{O}$

By the use of *operando* XAS, we have discovered that the $\text{V}^{4+}\text{-F}/\text{V}^{3+}\text{-F}$ and $\{\text{V}^{5+}=\text{O}\}^{3+}/\{\text{V}^{4+}=\text{O}\}^{2+}$ redox couples can be activated simultaneously in this composition (**Chapter II**); hence, upon charge we can expect the co-existence of different vanadium species: $\text{V}^{3+}\text{-F}$, $\text{V}^{4+}\text{-F}$, $\text{V}^{4+}=\text{O}$ and $\text{V}^{5+}=\text{O}$, which might complicate the interpretation of the recorded ^{23}Na and ^{31}P NMR spectra.

The ^{23}Na spectrum of $\text{Na}_3\text{V}_2(\text{PO}_4)_2\text{F}_2\text{O}$ shows three different resonances at 150 ppm, 102 ppm and 60 ppm (**Figure 3.22a**), which are assigned to $\text{Na}(\text{OV}^{3+}\text{-F})_2$, $\text{Na}(\text{OV}^{3+}\text{-F})(\text{OV}^{4+}=\text{O})$ and $\text{Na}(\text{OV}^{4+}=\text{O})_2$ local environments, respectively

[101,143,182]. In the desodiated phases, only one broad ^{23}Na resonance is observed which could be due to the fact that there is no formation of Na^+ -vacancy ordering upon cycling and the Na^+ mobility in the desodiated phases is greater than in the pristine material, $\text{Na}_3\text{V}_2(\text{PO}_4)_2\text{F}_2\text{O}$. Therefore, the Na^+ ions in the desodiated phases can be hopping freely between different Na sites leading to the observation of an average Na resonance. The ^{23}Na resonances in the desodiated phases shift continuously to the lower value as the Fermi contact is weakened when more and more vanadium ions are oxidized into higher oxidation states. The ^{23}Na NMR resonance observed at -20 ppm could be due to the electrolyte residue that contained NaPF_6 .

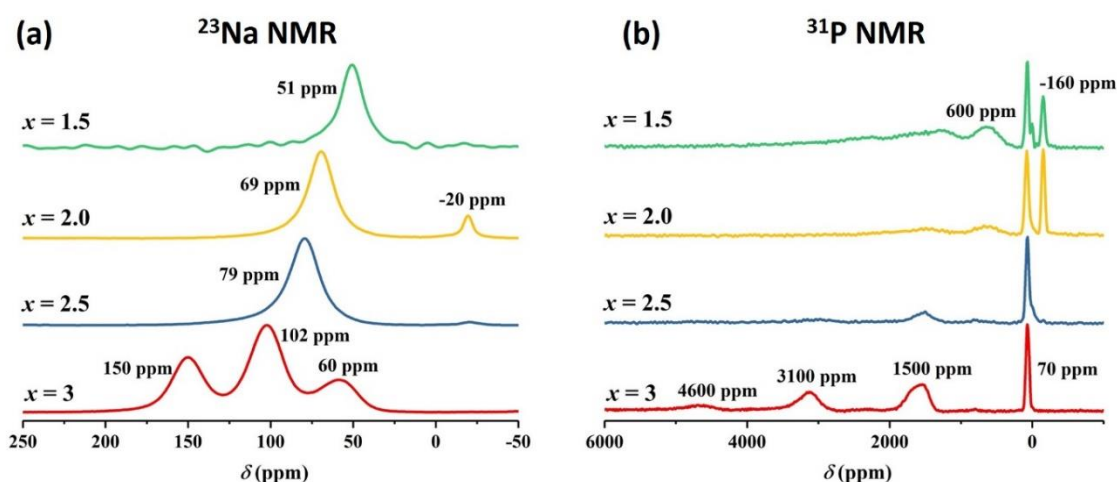


Figure 3.22 : (a) ^{23}Na MAS NMR spectra of $\text{Na}_x\text{V}_2(\text{PO}_4)_2\text{F}_2\text{O}$ phases recorded at $B_0 = 11.7$ T with $\nu_R = 30$ kHz, and (b) ^{31}P MAS NMR spectra of $\text{Na}_x\text{V}_2(\text{PO}_4)_2\text{F}_2\text{O}$ phases recorded at $B_0 = 2.35$ T with $\nu_R = 30$ kHz.

As it was explained earlier, the ^{31}P spectrum of $\text{Na}_3\text{V}^{3+}\text{V}^{4+}(\text{PO}_4)_2\text{F}_2\text{O}$ shows five different resonances at 6000 ppm, 4500 ppm, 3000 ppm, 1500 ppm and 0 ppm (**Figure 3.22b**) corresponding to the $\text{P}(\text{V}^{3+}-\text{F})_4$, $\text{P}(\text{V}^{3+}-\text{F})_3(\text{OV}^{4+}=\text{O})$, $\text{P}(\text{V}^{3+}-\text{F})_2(\text{OV}^{4+}=\text{O})_2$, $\text{P}(\text{V}^{3+}-\text{F})(\text{OV}^{4+}=\text{O})_3$ and $\text{P}(\text{OV}^{4+}=\text{O})_4$ local environments, respectively. In $\text{Na}_{2.5}\text{V}_2(\text{PO}_4)_2\text{F}_2\text{O}$, all the paramagnetic resonances with a shift higher than 3000 ppm decrease in intensity, which is a clear evidence of the oxidation of $\text{V}^{3+}-\text{F}$ into $\text{V}^{4+}-\text{F}$. A diamagnetic signal observed at -160 ppm for $\text{Na}_2\text{V}_2(\text{PO}_4)_2\text{F}_2\text{O}$ and $\text{Na}_{1.5}\text{V}_2(\text{PO}_4)_2\text{F}_2\text{O}$ could be originated from the electrolyte residue. In the $\text{Na}_{1.5}\text{V}_2(\text{PO}_4)_2\text{F}_2\text{O}$ composition, we observed a growth of the ^{31}P MAS NMR resonances at 600 ppm and 2 ppm, which are now assigned to the $\text{P}(\text{V}^{4+}-\text{F})(\text{OV}^{5+}=\text{O})_3$ and $\text{P}(\text{OV}^{5+}=\text{O})_4$ local environments generated during the desodiation process. Nonetheless, the ^{31}P NMR spectra of

$\text{Na}_x\text{V}_2(\text{PO}_4)_2\text{F}_2\text{O}$ compositions are really complex that we do not fully understand the origin of all the observed resonances and the DFT calculations are required in order to make a better understanding on this system.

Through a systematic study on the ^{23}Na and ^{31}P MAS NMR spectra recorded on the $\text{Na}_x\text{V}_2(\text{PO}_4)_2\text{F}_3$ and $\text{Na}_x\text{V}_2(\text{PO}_4)_2\text{F}_2\text{O}$ systems, we have discovered that the Na^+ ions in the desodiated phases might possess a higher diffusion coefficient than in the initial state that their ^{23}Na NMR resonances can quickly merge into one signal. In the oxygen substituted phases, $\text{Na}_3\text{V}_{2-y}(\text{PO}_4)_2\text{F}_{3-y}\text{O}_y$, there exist V^{4+} ions, but these V^{4+} ions are strongly bonded to the oxygen atom forming the highly covalent vanadyl bond $\text{V}^{4+}=\text{O}$. The local environment of V^{4+} engaged in a vanadyl bond is highly distorted that its unpaired electron is localized in the $3d_{xy}$ orbital with no spin transfer to its neighboring P nuclei. Starting from $\text{Na}_3\text{V}_2(\text{PO}_4)_2\text{F}_3$, V^{4+} ions can also be generated by an electrochemical oxidation of $\text{F}-\text{V}^{3+}\text{O}_4-\text{F}$ groups. The EXAFS analyses performed on the *operando* XAS data show that the local environment of V^{4+} ions in $\text{F}-\text{V}^{4+}\text{O}_4-\text{F}$ groups is just slightly distorted (**Chapter II**) and its unpaired electron can partially occupy all the t_{2g} orbitals. An V^{4+} in this local environment can still engage in the Fermi contact with its neighboring P nuclei.

III.5. Conclusions

The local atomic and electronic structures of the compositions belonging to the solid solution $\text{Na}_3\text{V}_2(\text{PO}_4)_2\text{F}_3 - \text{Na}_3(\text{VO})_2(\text{PO}_4)_2\text{F}$ have been investigated by a combination of ^{23}Na and ^{31}P MAS NMR and DFT calculations. The experimental ^{31}P NMR Fermi contact shift values are in agreement with those calculated using the PAW approach implemented in the VASP code considering a Curie-Weiss law. The V^{3+} ions in $\text{Na}_3\text{V}_2(\text{PO}_4)_2\text{F}_3$ reside in a ‘quasi’-symmetric octahedral site with its electron spins spreading out to the four neighboring phosphorus nuclei through the orbital overlap between its $3d_{xz}/3d_{yz}$ orbitals and the sp^3 hybridized orbital of phosphorus atoms via the O $2p$ orbital. The presence of a V^{3+} ion in the proximity of a phosphorus nucleus contributes to the Fermi contact shift of 1500 ppm. Once oxygen substitution occurs, the

vanadium ion bonded to this oxygen is oxidized to V^{4+} and forms a vanadyl-type bond with a very peculiar electronic structure (d_{xy}^1). This highly covalent bond distorts the local structure of the vanadium ion, imposes further orbital splitting where $3d_{xy}$ orbital of V^{4+} has the lowest energy and can be occupied by the unpaired electron of V^{4+} . This peculiar electronic structure of V^{4+} ion thus suppresses the spin transfer to their neighboring phosphorus nuclei and hence the $\text{P}(\text{OV}^{4+}=\text{O})_4$ environment with a shift in the diamagnetic ppm region. The observation of the resonance close to 0 ppm for the $\text{P}(\text{OV}^{4+})_4$ environment is a surprising finding in the field of paramagnetic *ss*-NMR, which shows the importance role of orbital overlap in the Fermi contact shift. The ^{23}Na MAS NMR signals assignment was also confirmed and illustrated by the orbital overlap model. In the case of ^{23}Na NMR, the direct Fermi contact between $\text{V}^{3+}/\text{V}^{4+}$ and the Na nucleus is rather weak. The spin transfer on Na nuclei occurs mainly through the sharing fluorine atom between the two vanadium ions. An analysis of the relative intensity of the ^{31}P and ^{23}Na NMR signals shows there is no segregation of V^{4+} ions in the $\text{Na}_3\text{V}_2(\text{PO}_4)_2\text{F}_3 - \text{Na}_3(\text{VO})_2(\text{PO}_4)_2\text{F}$ electrode materials, unlike what was suspected for the $\text{LiVPO}_4\text{F} - \text{LiVPO}_4\text{O}$ series [192,193].

^{23}Na and ^{31}P *ss*-NMR were also studied for the $\text{Na}_x\text{V}_2(\text{PO}_4)_2\text{F}_3$ and $\text{Na}_x\text{V}_2(\text{PO}_4)_2\text{F}_2\text{O}$ ($1 \leq x \leq 3$) desodiated phases and the obtained results show a gradual shift to lower resonant frequencies of the ^{23}Na and ^{31}P signals as a consequence of a decrease in the materials' electron spin density upon charge. In the $\text{Na}_x\text{V}_2(\text{PO}_4)_2\text{F}_3$ series, new ^{23}Na resonances were observed upon charge which could be due to the formation of Na^+ -vacancy ordering in the diffusion channels whereas a continuous evolution of the unique ^{31}P resonance implies a possible electron hopping between the two vanadium sites in the same bioctahedral unit. In the case of $\text{Na}_x\text{V}_2(\text{PO}_4)_2\text{F}_2\text{O}$, three ^{23}Na NMR resonances were observed in the initial state, however they quickly merged into one signal once the desodiation started implying an increase in the Na^+ mobility in the desodiated phases.

Chapter IV

The Effects of Cationic Substitution on the Crystal Structure and Electrochemistry of $\text{Na}_3\text{V}_2(\text{PO}_4)_2\text{F}_3 - \text{Na}_3(\text{VO})_2(\text{PO}_4)_2\text{F}$

IV.1. Introduction

$\text{Na}_3\text{V}_2(\text{PO}_4)_2\text{F}_3$ and other related structures are widely considered as promising materials for SIBs thanks to their high operating voltage, high theoretical capacity and excellent long-term cycling. Furthermore, many recent studies have shown that the Na^+ ions in $\text{Na}_3\text{V}_2(\text{PO}_4)_2\text{F}_3$ are relatively mobile and that they can be easily replaced by Li^+ ions and the resulting material can also be used as positive electrode in LIBs [105,122–124,153]. Lin *et al.* have also shown that the Na^+ ions in $\text{Na}_3\text{V}_2(\text{PO}_4)_2\text{F}_3$ can be exchanged with K^+ ions leading to the formation of $\text{K}_3\text{V}_2(\text{PO}_4)_2\text{F}_3$, which is a suitable positive electrode for potassium-ion batteries with good cycling performance [126].

Even though $\text{Na}_3\text{V}_2(\text{PO}_4)_2\text{F}_3$ shows several interesting properties as a positive electrode for SIBs, it also possesses many drawbacks that need to be improved in order to develop a new generation of electrodes with superior electrochemical performances. Firstly, the electronic conductivity of the phase is rather slow and a carbon coating process is usually required in order to improve the material's electrochemical performance, especially for high cycling rates [131]. Secondly, there are many Na^+ -vacancy orderings occurring upon cycling and many theoretical studies have suggested that the formation of these Na^+ -vacancy orderings might increase significantly the activation energy required for the Na^+ diffusion process. It was also proposed that the substitution of V^{3+} by a foreign ion, isovalent or aliovalent, will disrupt the charge ordering and thus promote greatly the ionic diffusion [119,128]. Other experimental researches also demonstrated that when the V^{3+} in $\text{Na}_3\text{V}_2(\text{PO}_4)_2\text{F}_3$ is partially substituted by yttrium or manganese ion, the charge transfer resistance will be reduced [206,207]. Last but not least, there are two V^{3+} ions per formula unit of $\text{Na}_3\text{V}_2(\text{PO}_4)_2\text{F}_3$ and vanadium can reach the maximum oxidation state of +5, thus the electrochemical performance of $\text{Na}_3\text{V}_2(\text{PO}_4)_2\text{F}_3$ is 'alkali ion-limited' [128], meaning that the maximum number of exchanged electrons exceeds the number of available Na^+ . In reality, only two Na^+ ions can participate in the reversible electrochemical reaction together with an exchange of two electrons. Therefore, there are two different approaches in order to improve the electrochemical performance of the phase by (i) replacing one V^{3+} ion in the structure by a lightweight and eco-friendly ion, *i.e.* Al^{3+} , to increase the theoretical capacity of the material or (ii) introducing a structural distortion into the phase so as to promote the extraction of the third Na^+ as predicted in the theoretical work of Ceder's group [119,127,128].

This chapter is devoted to the exploration of the effects of cationic substitution on the crystal structure and electrochemical behaviors of $\text{Na}_3\text{V}_2(\text{PO}_4)_2\text{F}_3$ and $\text{Na}_3(\text{VO})_2(\text{PO}_4)_2\text{F}$. This chapter is divided into three sub-chapters and each of them focuses on the different nature of the substituents and the properties of the resulting phases:

✚ Ag^+/Na^+ ion exchange into $\text{Na}_3\text{V}_2(\text{PO}_4)_2\text{F}_3$ phase: The purpose of this study is to develop a facile method to obtain $\text{Ag}_3\text{V}_2(\text{PO}_4)_2\text{F}_3$, which is a potential material that can be further used as positive electrode for silver-based batteries.

✚ Fe^{3+} -substituted $\text{Na}_3(\text{VO})_2(\text{PO}_4)_2\text{F}$: In this study, a novel composition, $\text{Na}_3(\text{VO})\text{Fe}(\text{PO}_4)_2\text{F}_2$ was obtained through an original sol-gel method. The phase exhibits good electrochemical cycling performance with very low polarization even without carbon-coating, implying that the Na^+ mobility is greatly improved by Fe^{3+} substitution. Furthermore, the electrochemical activity of the $\text{Fe}^{3+}/\text{Fe}^{2+}$ redox couple as well as the ^{57}Fe Mössbauer signals of Fe ions in this structural framework have been observed for the first time.

✚ Al^{3+} -substituted $\text{Na}_3\text{V}_2(\text{PO}_4)_2\text{F}_3$ and Al^{3+} -substituted $\text{Na}_3(\text{VO})_2(\text{PO}_4)_2\text{F}$ phases: This study aims at a partial substitution of the vanadium ion by Al^{3+} , which is expected to increase the material capacity and to induce a subtle structural distortion that might promote the extraction of the third Na^+ at high voltage. By varying the reaction conditions, new material compositions with the general formula $\text{Na}_3\text{V}_{2-z}\text{Al}_z(\text{PO}_4)_2\text{F}_3$ ($0 \leq z \leq 0.5$) and $\text{Na}_3(\text{VO})_{2-z}\text{Al}_z(\text{PO}_4)_2\text{F}_{1+z}$ ($0 \leq z \leq 2$) were successfully achieved.

IV.2. Ag^+/Na^+ ion exchange into $\text{Na}_3\text{V}_2(\text{PO}_4)_2\text{F}_3$

IV.2.1. Samples preparation

Two batches of $\text{Na}_3\text{V}_2(\text{PO}_4)_2\text{F}_3$ powders were used in this ionic exchange experiment. The first batch contains a $\text{Na}_3\text{V}_2(\text{PO}_4)_2\text{F}_3$ microcrystalline powder with the particle size of $\sim 1 \mu\text{m}$ without any carbon coating at the surface of the particles. A second batch of $\text{Na}_3\text{V}_2(\text{PO}_4)_2\text{F}_3$ was also prepared in order to reduce the particle size. In this case, VPO_4 coated with carbon was used as an intermediate precursor, and thus the resulting $\text{Na}_3\text{V}_2(\text{PO}_4)_2\text{F}_3$ powder has the particle size of the order of hundreds of nm and coated with carbon. The synthesized $\text{Na}_3\text{V}_2(\text{PO}_4)_2\text{F}_3$ powders were then stirred for a variable time in an aqueous solution of AgNO_3 0.36 M to exchange sodium ions by silver ions. The obtained powders after ion exchange were washed several times with water and acetone and dried at 50°C under vacuum before being subjected to any characterization.

IV.2.2. Ag^+/Na^+ ion exchange into microcrystalline $\text{Na}_3\text{V}_2(\text{PO}_4)_2\text{F}_3$

The ion-exchange study started by following, through XRD, the amount of Ag^+/Na^+ substitution in $\text{Na}_3\text{V}_2(\text{PO}_4)_2\text{F}_3$ as a function of time.

Figure 4.1 shows the XRD patterns collected at different times after the ion exchange process started. One can observe that the exchange of Na^+ for Ag^+ starts quickly, as after 15 minutes Bragg peaks' positions (*e.g.* (113), (222)) and intensities (*e.g.* (220), (211)) are already modified, indicative of the initial substitution (the volume of unit cell describing the material increases from 219.2 \AA^3 to 220 \AA^3). A long ion exchange time of 20 hours results in a significantly different diffraction pattern, indicating that the material has become significantly Ag-rich. However, only a small variation is observed between 20 and 60 hours of exchange and the volume of the unit cell increases only slightly from 223.8 to 224.3 \AA^3 , respectively. Although this could indicate that the exchange is at this point complete, SEM-EDX after the longest ion exchange reaction time (60 h) shows that some sodium remains in the structure (approximately 0.38 $\text{Na}^+/\text{f.u.}$). The global composition reached is close to $\text{Ag}_{2.71(6)}\text{Na}_{0.3(2)}\text{V}_2(\text{PO}_4)_2\text{F}_3$, still containing some Na^+ but significantly Ag-rich. This composition, in rather good agreement with SEM-EDX, is obtained from the Rietveld refinement described in the

following (**Figure 4.2**). We suggest that the incomplete exchange is due to limited kinetics because of the large particles size of our $\text{Na}_3\text{V}_2(\text{PO}_4)_2\text{F}_3$.

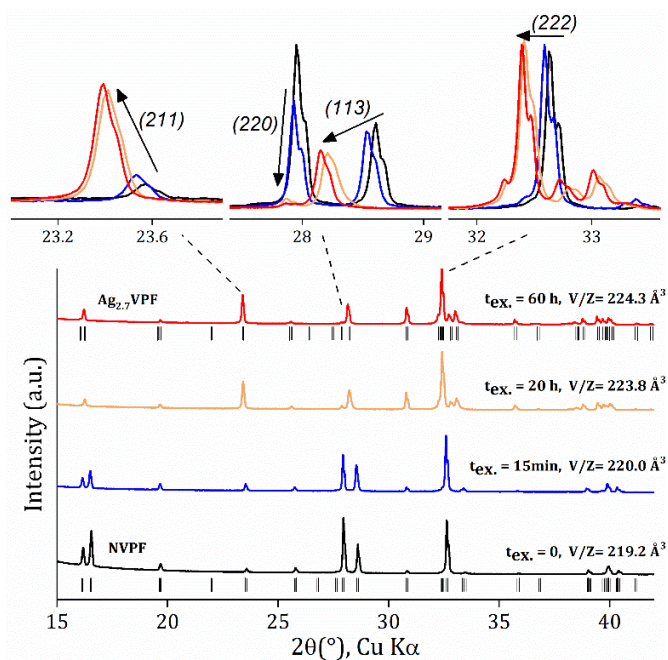


Figure 4.1 : Evolution of the XRD patterns of $\text{Na}_3\text{V}_2(\text{PO}_4)_2\text{F}_3$ with the larger size particles as the Ag^+/Na^+ ion exchange proceeds. The different positions of selected Bragg peaks, indexed in the orthorhombic $Amam$ space group, are highlighted at the top. The unit cell volume obtained from Rietveld refinement is also indicated.

The crystal structure of $\text{Ag}_{2.71(6)}\text{Na}_{0.3(2)}\text{V}_2(\text{PO}_4)_2\text{F}_3$ obtained after ion exchange was studied by high angular resolution SXRD, while the complete Rietveld structural refinement was carried out combining this with neutron diffraction data from the D2B diffractometer at ILL (**Figure 4.2**). A combined approach was chosen because the XRD pattern is dominated by the “heavy” silver and vanadium atoms while neutrons are helpful to better localize the lighter atoms O, F, P and the residual Na. The Bragg reflections in the SXRD pattern have slightly modified angular positions as compared to those measured from $\text{Na}_3\text{V}_2(\text{PO}_4)_2\text{F}_3$, although the most important differences are found on the reflections' intensities, as expected by the higher atomic weight of silver with respect to sodium. Indexation quickly revealed the compatibility of all Bragg positions with the $Amam$ space group of $\text{Na}_3\text{V}_2(\text{PO}_4)_2\text{F}_3$. As all the diffraction peaks are properly indexed, no doubt is left about the presence of a single phase after our ionic exchange. We mention nonetheless the presence of few small peaks (in the synchrotron data only) that are actually unindexed, but being significantly broader than those of the main phase, we attribute them at this stage to impurities resulting from the ion exchange reaction.

The pure Na parent compound has the peculiarity of an extremely small orthorhombic distortion in the a - b plane. The distortion is found to significantly increase in $\text{Ag}_{2.71(6)}\text{Na}_{0.3(2)}\text{V}_2(\text{PO}_4)_2\text{F}_3$, where $a = 9.0843(1) \text{ \AA}$ and $b = 9.0303(1) \text{ \AA}$ ($b < a$ now and $a/b = 1.006$). This implies that while the b unit cell parameter slightly decreases, a increases ($< 1\%$). The c axis, perpendicular to the 2-D planes of (Na/Ag) lengthens more significantly, from $c = 10.741(3) \text{ \AA}$ to $c = 10.9942(1) \text{ \AA}$. It is interesting to note that this directly confirms and further strengthens the recent attribution of an orthorhombic Amm space group for $\text{Na}_3\text{V}_2(\text{PO}_4)_2\text{F}_3$. The Ag/Na substitution respects such a symmetry constraint and the space group can be more clearly and undoubtedly confirmed in reason of the presence of Ag, which has two effects: it distorts more the a - b plane, making the Bragg peaks' splitting easier to observe, and it is a stronger scatterer of X-ray ($Z = 47$ vs. $Z = 11$ for Na), thus dominating the intensity of reflections and clearly marking its position in the structure.

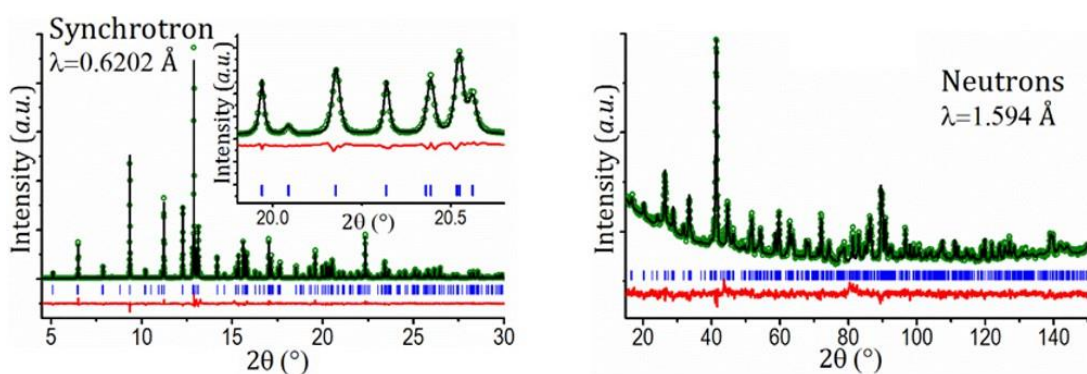


Figure 4.2 : Combined Rietveld refinement of SXRD and NPD of $\text{Ag}_{2.71(6)}\text{Na}_{0.3(2)}\text{V}_2(\text{PO}_4)_2\text{F}_3$. Measured data are shown as green dots, Rietveld fit as a black line, their difference as a red line and Bragg positions as blue marks.

Based on the combined Rietveld refinement of synchrotron and neutron diffraction patterns (**Figure 4.2** and **Table 4.1**), the crystal structure of $\text{Ag}_{2.71(6)}\text{Na}_{0.3(2)}\text{V}_2(\text{PO}_4)_2\text{F}_3$ was obtained and is displayed in **Figure 4.3**. The basic structural framework of $\text{Na}_3\text{V}_2(\text{PO}_4)_2\text{F}_3$, consisting of $\text{V}_2\text{O}_8\text{F}_3$ bioctahedra bridged by corner-sharing PO_4 tetrahedra, is preserved. The large 2D tunnels are also preserved, hence the relative ease of ion exchange with silver without consequent disruption of the 3D framework of the material is not a surprise.

Table 4.1 : Structural parameters obtained from combined Rietveld refinement of the structure of $\text{Ag}_{2.71(6)}\text{V}_2(\text{PO}_4)_2\text{F}_3$ by SXRD and neutrons diffraction data. The occupancy of Na3 site is found to be slightly negative, and is thus set to 0. The sum of Ag and Na ions was constrained so that it equaled 3.00(1).

| $\text{Ag}_{2.71(6)}\text{Na}_{0.3(2)}\text{V}_2(\text{PO}_4)_2\text{F}_3$ | | | | | | |
|------------------------------------------------------------------------------------------|------------------|-----------------|-----------|---------------|----------|------------------|
| Space group : $Amam$; $Z = 4$ | | | | | | |
| $a = 9.0843(1) \text{ \AA}$, $b = 9.0303(1) \text{ \AA}$, $c = 10.9442(1) \text{ \AA}$ | | | | | | |
| $V = 897.796(1) \text{ \AA}^3$, $V/Z = 224.449(1) \text{ \AA}^3$ | | | | | | |
| Combined $\chi^2 = 6.56$ | | | | | | |
| Synchrotron $R_{\text{Bragg}} = 7.87\%$, Synchrotron $R_{\text{wp}} = 16.7\%$ | | | | | | |
| Neutrons $R_{\text{Bragg}} = 12.6\%$, Neutrons $R_{\text{wp}} = 18.9\%$ | | | | | | |
| Atom | Wyckoff position | Atomic position | | | Occ. | B_{iso} |
| | | x/a | y/b | z/c | | |
| V | 8g | $\frac{1}{4}$ | 0.2526(6) | 0.1820(4) | 1 | 0.5(1) |
| P | 8e | 0 | 0 | 0.2396(9) | 1 | 0.7(1) |
| O1 | 16h | 0.099(1) | 0.094(1) | 0.156(1) | 1 | 0.7(2) |
| O2 | 16h | 0.093(1) | 0.402(1) | 0.175(1) | 1 | 0.7(2) |
| F1 | 4c | $\frac{1}{4}$ | 0.265(2) | 0 | 1 | 0.8(3) |
| F2 | 8g | $\frac{1}{4}$ | 0.742(2) | 0.140(1) | 1 | 1.0(3) |
| Ag1 | 4c | $\frac{1}{4}$ | 0.9610(5) | 0 | 0.93(4) | 2.1(1) |
| Ag2 | 8f | 0.9598(7) | 0.792(1) | $\frac{1}{2}$ | 0.51(4) | 1.2(2) |
| Ag3 | 8f | 0.942(1) | 0.856(2) | $\frac{1}{2}$ | 0.38(2) | 1.6(3) |
| Na1 | 4c | $\frac{1}{4}$ | 0.9610(5) | 0 | 0.03(17) | 2.1(1) |
| Na2 | 8f | 0.9598(7) | 0.792(1) | $\frac{1}{2}$ | 0.14(17) | 1.2(2) |

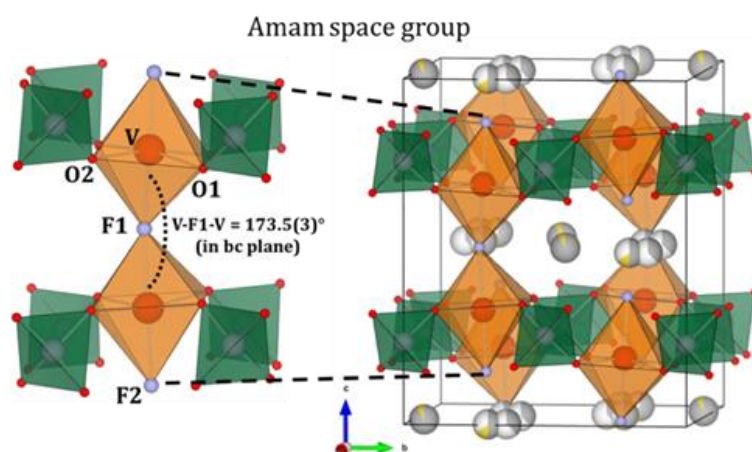


Figure 4.3 : Crystal structure of $\text{Ag}_{2.71(6)}\text{Na}_{0.3(2)}\text{V}_2(\text{PO}_4)_2\text{F}_3$ obtained by ion exchange from $\text{Na}_3\text{V}_2(\text{PO}_4)_2\text{F}_3$. The space group $Amam$ is retained, but a more pronounced orthorhombic distortion is induced (a/b from 1.002 to 1.006).

The increase of the unit cell dimensions can be explained by steric effects of the bigger Ag^+ ions with respect to Na^+ . As reviewed by Shannon [155], the effective ionic radii for 6-coordinated Na^+ and Ag^+ are 1.02 Å and 1.15 Å, respectively. This unit cell increase is in line with what is observed for the Na/Ag substitution in other materials families, such as alluaudites [208] and materials of composition $\text{Ag}_{7-x}\text{Na}_x\text{Fe}_3(\text{X}_2\text{O}_7)_4$ ($\text{X} = \text{P}, \text{As}$) [209–211].

In $\text{Na}_3\text{V}_2(\text{PO}_4)_2\text{F}_3$, sodium ions are found in planes at $z = 0$ and $z = 1/2$, distributed on a "triangular" arrangement of three crystallographic sites Na(1), Na(2) and Na(3). The first one is fully occupied, while Na(2) and Na(3) have partial occupancies close to 2/3 and 1/3, respectively. We found that Ag^+ ions choose to place themselves on the exact same sites as the Na^+ ions in $\text{Na}_3\text{V}_2(\text{PO}_4)_2\text{F}_3$. Relative occupations are also similar (**Table 4.1**). **Figure 4.4** gathers Na^+ and Ag^+ distributions in the $z = 0$ plane. Since from SEM-EDX it was found that the ion exchange was not complete we used this information and included both Ag and Na cations in the Rietveld refinement. We observe that the remaining Na^+ cations are localized in Na(1) (0.03(17) / f.u.) and mainly Na(2) (0.28(17) / f.u.) sites, but not in the Na(3) one, where the site occupancy factor (SOF) converged to a negligible (slightly negative) value, and was thereafter set to zero. We can conclude that Ag-Ag distances (**Figure 4.4**) are very similar to Na-Na ones in $\text{Na}_3\text{V}_2(\text{PO}_4)_2\text{F}_3$, except for Ag(3)–Ag(3) which are farther away (Na(3)–Na(3) = 2.84 Å in $\text{Na}_3\text{V}_2(\text{PO}_4)_2\text{F}_3$ whereas Ag(3)–Ag(3) = 3.50 Å in $\text{Ag}_{2.71(6)}\text{Na}_{0.3(2)}\text{V}_2(\text{PO}_4)_2\text{F}_3$).

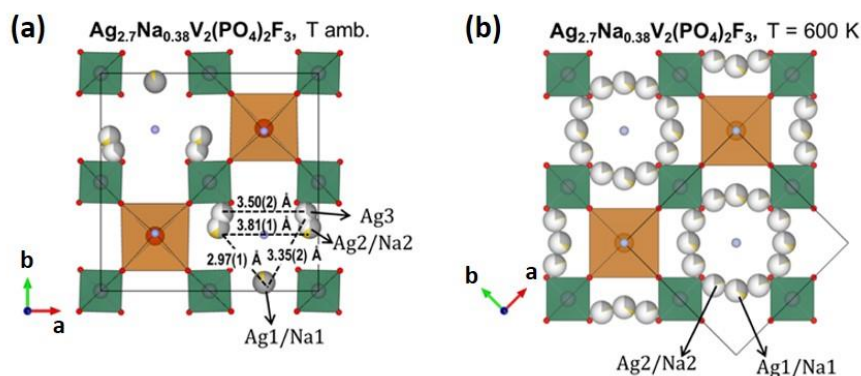


Figure 4.4 : Sodium distribution in $\text{Ag}_{2.71(6)}\text{Na}_{0.3(2)}\text{V}_2(\text{PO}_4)_2\text{F}_3$ for the room-temperature (*Amam*) and high-temperature (*I4/mmm*) polymorphs.

Both $\text{Na}_3\text{V}_2(\text{PO}_4)_2\text{F}_3$ and its oxidized relative $\text{Na}_3(\text{VO})_2(\text{PO}_4)_2\text{F}$ are known to undergo an order-disorder phase transition upon heating at 100°C and 200°C, respectively

[82,83,135]. The disordering of sodium cations results in a tetragonal unit cell, smaller by a factor of 2 and rotated by 45° with respect to the room-temperature one (**Figure 4.4**). To assess the behavior of the Ag^+ ion-substituted compound, we realized an *in situ* synchrotron temperature-controlled SXR D experiment. The sample we used was $\text{Ag}_{2.71(6)}\text{Na}_{0.3(2)}\text{V}_2(\text{PO}_4)_2\text{F}_3$ obtained from $\text{Na}_3\text{V}_2(\text{PO}_4)_2\text{F}_3$, as the larger crystallite size allows a better resolution in the *in situ* experiment. **Figure 4.5** shows the evolution of the diffracted peaks during the cooling process, *i.e.* the sample $\text{Ag}_{2.71(6)}\text{Na}_{0.3(2)}\text{V}_2(\text{PO}_4)_2\text{F}_3$ was heated offline to 350°C and then measured in the beamline upon cooling. We can observe that the transition occurs at a temperature $300^\circ\text{C} < T < 325^\circ\text{C}$ (**Figure 4.5**), significantly higher than the one observed for $\text{Na}_3\text{V}_2(\text{PO}_4)_2\text{F}_3$.

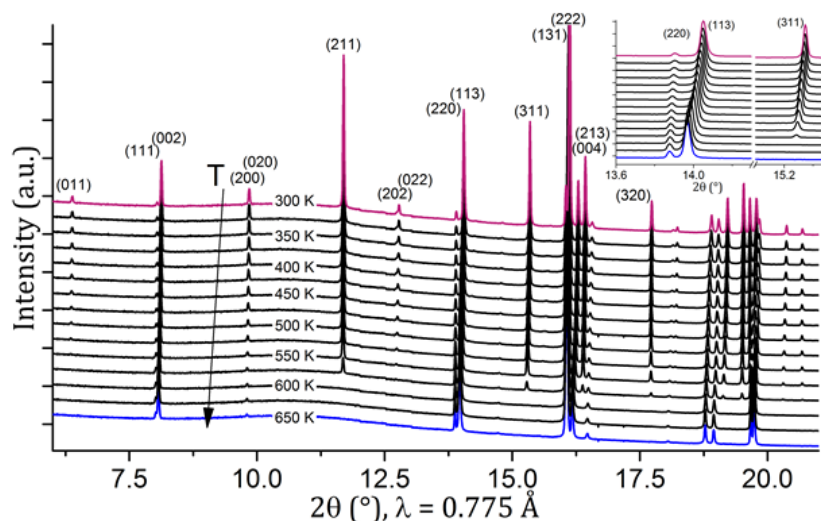


Figure 4.5 : SXR D data measured as a function of temperature upon cooling. The order-disorder phase transition of $\text{Ag}_{2.71(6)}\text{Na}_{0.3(2)}\text{V}_2(\text{PO}_4)_2\text{F}_3$ is observed close to $T = 600$ K. The inset zooms on the 13.6-15.4° angular domain.

The SXR D pattern measured at $\sim 350^\circ\text{C}$ (625K) was used for a detailed structural refinement by the Rietveld method. The results of the structural analysis are reported in **Table 4.2**. Firstly one should note that the Ag amount is independently refined and, as in the RT case, it yields 2.72(2) Ag/f.u. $\text{Ag}_{2.71(6)}\text{Na}_{0.3(2)}\text{V}_2(\text{PO}_4)_2\text{F}_3$ follows the same disordering scheme than reported for $\text{Na}_3\text{V}_2(\text{PO}_4)_2\text{F}_3$. Thus, no significant differences are present within the skeleton of the compound between the RT and the high temperature phases. The main difference is just a change in the position and the arrangement of the monovalent cations within the $z = 0$ and $z = 1/2$ planes. They disorder in a circular arrangement around the fluorine that terminates the bioctahedra. This in turn induces a homogeneous electrostatic repulsion along the a and b axes, and thus favors the tetragonal symmetry of the structure.

Table 4.2 : Structural parameters obtained from Rietveld refinement of SXRD of $\text{Ag}_{2.71(6)}\text{Na}_{0.3(2)}\text{V}_2(\text{PO}_4)_2\text{F}_3$ at 350°C. 0.3 Na/f.u. are included in the refinement, as obtained in the RT case. Only site Na1 is included because it is Wyckoff position 8*h*, corresponding to both Na1 and Na2 sites in the RT *Amam* space group.

| $\text{Ag}_{2.72(2)}\text{Na}_{0.3}\text{V}_2(\text{PO}_4)_2\text{F}_3$ (350°C) | | | | | | |
|------------------------------------------------------------------------------------------|------------------|-----------------|-----------|-----------|----------|------------------|
| Space group : <i>I4/mmm</i> ; <i>Z</i> = 2 | | | | | | |
| $a = 6.4176(1) \text{ \AA}$, $b = 6.4176(1) \text{ \AA}$, $c = 11.0198(1) \text{ \AA}$ | | | | | | |
| $V = 453.856(3) \text{ \AA}^3$, $V/Z = 226.928(1) \text{ \AA}^3$ | | | | | | |
| Combined $\chi^2 = 4.09$ | | | | | | |
| Synchrotron $R_{\text{bragg}} = 9.61\%$, Synchrotron $R_{\text{wp}} = 11.3\%$ | | | | | | |
| Atom | Wyckoff position | Atomic position | | | Occ. | B_{iso} |
| | | x/a | y/b | z/c | | |
| V | 4 <i>e</i> | 0 | 0 | 0.1819(3) | 1 | 1.0(1) |
| P | 4 <i>d</i> | ½ | 0 | ¼ | 1 | 1.6(1) |
| O | 16 <i>n</i> | 0.3082(9) | 0 | 0.1651(5) | 1 | 1.4(1) |
| F1 | 2 <i>a</i> | 0 | 0 | 0 | 1 | 1.7(4) |
| F2 | 4 <i>e</i> | 0 | 0 | 0.3568(9) | 1 | 1.9(3) |
| Ag1 | 8 <i>h</i> | 0.2871(5) | 0.2871(5) | 0 | 0.30(1) | 2.8(2) |
| Ag2 | 16 <i>l</i> | 0.409(1) | 0.210(1) | 0 | 0.19(1) | 3.8(3) |
| Na1 | 8 <i>h</i> | 0.2871(5) | 0.2871(5) | 0 | 0.075(-) | 2.8(2) |

DFT calculations by Matts *et al.* shed light on the migration barriers of sodium into the structure of $\text{Na}_3\text{V}_2(\text{PO}_4)_2\text{F}_3$ [128]. In particular, they calculated a very low migration barrier for sodium within the rings with the order of 20 meV. This is of the same order of the thermal energy at room T, usually estimated as 25 meV, which can well explain why the orthorhombic structure features sodium ions in partial occupancy positions. Bringing the temperature to 100°C in $\text{Na}_3\text{V}_2(\text{PO}_4)_2\text{F}_3$ (corresponding to 35 meV) is sufficient to trigger the complete sodium disordering within such rings, in rather good agreement with Matts *et al.* The fact that the disordering does not happen until 300°C in $\text{Ag}_{2.71(6)}\text{Na}_{0.3(2)}\text{V}_2(\text{PO}_4)_2\text{F}_3$ is an indication that the migration barriers for Ag are higher than for Na. One should also note that the Na hops within the rings are non-percolating, hence do not result in macroscopic sodium diffusion. A much higher energy barrier is calculated for Na hops between neighboring rings, of the order of 0.6 eV and above [128]. These hops are required for macroscopic diffusion; in fact, recently the activation energy for Na conduction in $\text{Na}_3\text{V}_2(\text{PO}_4)_2\text{F}_3$ was measured by Impedance Spectroscopy and reported to be 680 meV (or even greater) [128,212] in good agreement with the calculations.

IV.2.3. Ag^+/Na^+ ion exchange into submicron $\text{Na}_3\text{V}_2(\text{PO}_4)_2\text{F}_3$

Given the fact that the ion exchange does not proceed to completion even after 60 hours in the $\text{Na}_3\text{V}_2(\text{PO}_4)_2\text{F}_3$ powder with the particle size of 1 μm , we prepared a new batch of $\text{Na}_3\text{V}_2(\text{PO}_4)_2\text{F}_3$ with the particle size in the range of a few hundreds of nm. We then repeated the ion exchange procedure, but with more intermediate characterization steps. **Figure 4.6** shows the evolution of the SXRD patterns as the ionic exchange proceeds, while **Table 4.3** summarizes the evolution of unit cell parameters.

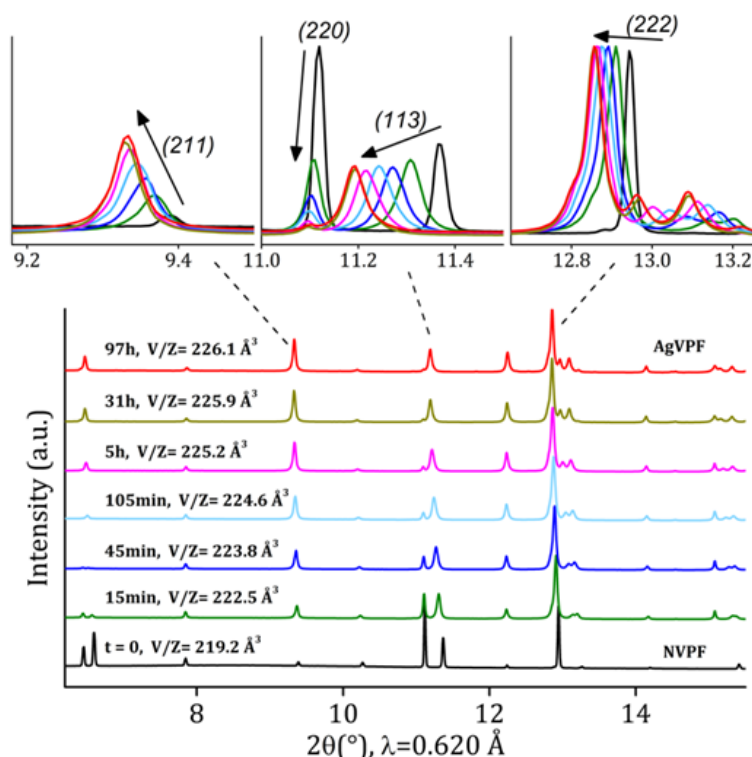


Figure 4.6 : Evolution of the SXRD patterns of $\text{Na}_3\text{V}_2(\text{PO}_4)_2\text{F}_3$ as the Ag^+/Na^+ ion exchange proceeds. The different positions of selected Bragg peaks, indexed in the orthorhombic $Amam$ space group, are highlighted at the top. The unit cell volume obtained from Rietveld refinement is also indicated.

The process gradually progresses over the first 31 hours. One can clearly observe how the kinetics of the ion exchange is much faster in this case, since after 15 minutes of ion exchange $V/Z_{15\text{min}} = 222.5 \text{ \AA}^3$, whereas for the micro-size $\text{Na}_3\text{V}_2(\text{PO}_4)_2\text{F}_3$ it was $V/Z_{15\text{min}} = 220.0 \text{ \AA}^3$. After 105 min of ion exchange, $V/Z_{105\text{min}} = 224.6 \text{ \AA}^3$, comparable to the one obtained after 60 hours for micro-size $\text{Na}_3\text{V}_2(\text{PO}_4)_2\text{F}_3$ and characterized in the previous section. In this case, the ionic exchange is nearly complete after 31 hours. At this time, the unit cell reaches 225.9 \AA^3 . Further exchange, up to a final time of 97 hours, only slightly increases such value to 226.1 \AA^3 . These observations suggest that a solid

solution domain is present in $\text{Na}_{3-x}\text{Ag}_x\text{V}_2(\text{PO}_4)_2\text{F}_3$. We do not observe any miscibility gap (**Figure 4.6**), contrary to what was reported for the Li^+/Na^+ exchange [122]. The difference is likely due to the ionic radii of the cations ($R_{\text{Li}^+} = 0.76 \text{ \AA}$, $R_{\text{Na}^+} = 1.02 \text{ \AA}$, $R_{\text{Ag}^+} = 1.15 \text{ \AA}$) [155], since the size mismatch between Li^+ and Na^+ is much larger than the one between Ag^+ and Na^+ .

Table 4.3 : Unit cell parameters, volume and silver content (x) at different reaction times after the beginning of the Ag^+/Na^+ ion exchange in sub-micron $\text{Na}_3\text{V}_2(\text{PO}_4)_2\text{F}_3$. ICP-OES indicates a composition of $\text{Ag}_{3.1 \pm 0.12}\text{Na}_{0.12 \pm 0.05}\text{VPF}$ after 97 hours, close to full exchange.

| Time | a (Å) | b (Å) | c (Å) | V/Z (Å ³) |
|---------|-----------|-----------|------------|-------------------------|
| 0 | 9.028(3) | 9.042(3) | 10.741(3) | 219.2(1) |
| 15 min | 9.0639(3) | 9.0611(3) | 10.8389(2) | 222.56(6) |
| 45 min | 9.0769(3) | 9.0602(3) | 10.8863(3) | 223.82(6) |
| 105 min | 9.0857(3) | 9.0561(3) | 10.9187(3) | 224.60(5) |
| 5 h | 9.0923(2) | 9.0491(2) | 10.9501(3) | 225.24(4) |
| 10 h | 9.0968(2) | 9.0467(2) | 10.9668(3) | 225.63(4) |
| 31 h | 9.0986(2) | 9.0443(2) | 10.9797(2) | 225.88(4) |
| 55 h | 9.1004(2) | 9.0437(2) | 10.9842(2) | 226.00(4) |
| 97 h | 9.1007(5) | 9.0427(6) | 10.9880(2) | 226.08(6) |

The sample that had been ion-exchanged for 97 hours and with the largest unit cell (indicated as $\text{Ag}_3\text{V}_2(\text{PO}_4)_2\text{F}_3$, as obtained from the Rietveld refinement) was measured by SXRD and the resulting pattern was used to refine the structure by Rietveld method (**Figure 4.7**). No sodium is included in the refinement because ICP-OES only indicates the presence of only 0.12 $\text{Na}^+/\text{f.u.}$, and such a small amount of Na is difficult to localize. The long exchange in sub-micron $\text{Na}_3\text{V}_2(\text{PO}_4)_2\text{F}_3$ results in significantly larger unit cell parameters as compared to the pristine $\text{Na}_3\text{V}_2(\text{PO}_4)_2\text{F}_3$ (Table 1), with the SOF of Ag converging to a value of 2.85 $\text{Ag}/\text{f.u.}$ The fit quality (R_{Bragg}) of the sub-micron $\text{Ag}_3\text{V}_2(\text{PO}_4)_2\text{F}_3$ is worse than the one of micro-size $\text{Ag}_{2.71(6)}\text{Na}_{0.3(2)}\text{V}_2(\text{PO}_4)_2\text{F}_3$ (reported above) due to the broader reflections and the presence of additional small peaks, which are not indexed and might belong to a different unit cell symmetry. Note that no orthorhombic cell, even in the low-symmetry space group $Pmmm$, is able to index the extra observed peaks. At present we cannot be conclusive on whether such peaks belong to the phase (as a monoclinic distortion or a superstructure, for example), and this is currently object of further study.

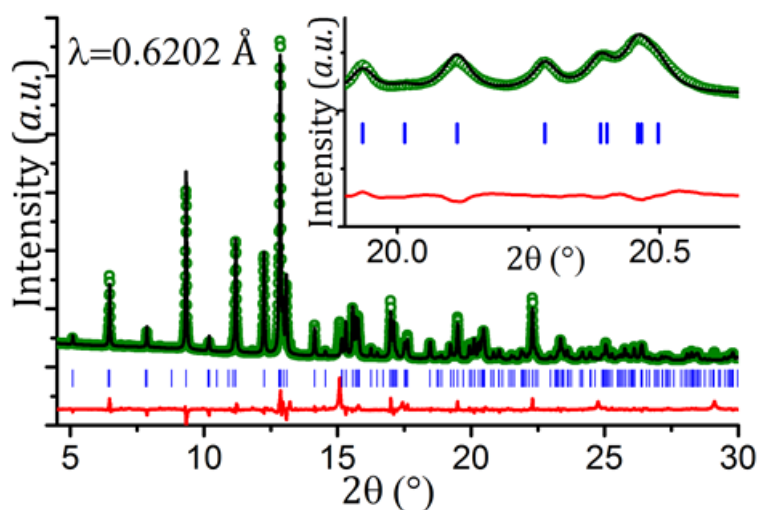


Figure 4.7 : Rietveld refinement of SXRD of $\text{Ag}_3\text{V}_2(\text{PO}_4)_2\text{F}_3$. Measured data are shown as green dots, Rietveld fit as a black line, their difference as a red line and Bragg positions as blue marks.

Table 4.4 : Structural parameters obtained from Rietveld refinement of SXRD data of sub-micron $\text{Ag}_3\text{V}_2(\text{PO}_4)_2\text{F}_3$. No Na is included in the refinement.

| $\text{Ag}_3\text{V}_2(\text{PO}_4)_2\text{F}_3$ | | | | | | |
|------------------------------------------------------------------------------------------|------------------|-----------------|-----------|-----------|---------|------------------|
| Space group : $Amam$; $Z = 4$ | | | | | | |
| $a = 9.1007(5) \text{ \AA}$, $b = 9.0427(6) \text{ \AA}$, $c = 10.9880(6) \text{ \AA}$ | | | | | | |
| $V = 904.26(9) \text{ \AA}^3$, $V/Z = 226.07(5) \text{ \AA}^3$ | | | | | | |
| $\chi^2 = 76.5$ | | | | | | |
| $R_{\text{bragg}} = 8.12\%$, $R_{\text{wp}} = 13.6\%$ | | | | | | |
| atom | Wyckoff position | Atomic position | | | Occ. | B_{iso} |
| | | x/a | y/b | z/c | | |
| V | 8g | ¼ | 0.2536(9) | 0.1801(7) | 1 | 0.4(2) |
| P | 8e | 0 | 0 | 0.240(1) | 1 | 1.4(3) |
| O1 | 16h | 0.101(2) | 0.094(3) | 0.155(2) | 1 | 1.2(6) |
| O2 | 16h | 0.094(2) | 0.405(3) | 0.175(2) | 1 | 1.4(6) |
| F1 | 4c | ¼ | 0.265(4) | 0 | 1 | 1.8(9) |
| F2 | 8g | ¼ | 0.739(3) | 0.141(2) | 1 | 0.6(5) |
| Ag1 | 4c | ¼ | 0.9592(9) | 0 | 0.95(2) | 2.5(3) |
| Ag2 | 8f | 0.962(2) | 0.788(3) | ½ | 0.51(5) | 1.2(4) |
| Ag3 | 8f | 0.943(2) | 0.853(3) | ½ | 0.44(5) | 1.5(5) |

To conclude, we have succeeded to obtain $\text{Ag}_3\text{V}_2(\text{PO}_4)_2\text{F}_3$ through Ag^+/Na^+ ion exchange into $\text{Na}_3\text{V}_2(\text{PO}_4)_2\text{F}_3$ and the as-obtained material can potentially be used as positive electrode in rechargeable silver-ion batteries.

IV.3. Fe-substitution into $\text{Na}_3(\text{VO})_2(\text{PO}_4)_2\text{F}$

IV.3.1. Sample preparation

$\text{Na}_3(\text{VO})\text{Fe}(\text{PO}_4)_2\text{F}_2$ was obtained through a sol-gel approach as inspired by the work of Qi *et al.* [138] by using NaF (Sigma-Aldrich; $\geq 99\%$), $\text{V}(\text{C}_5\text{H}_7\text{O}_2)_3$ (Sigma-Aldrich; $\geq 97\%$), $\text{Fe}(\text{NO}_3)_3 \cdot 9\text{H}_2\text{O}$ (Sigma-Aldrich; $\geq 98\%$), and $\text{NH}_4\text{H}_2\text{PO}_4$ (Sigma-Aldrich; $\geq 99.99\%$) precursors. The initial solution containing a mixture of NaF, $\text{V}(\text{C}_5\text{H}_7\text{O}_2)_3$, $\text{Fe}(\text{NO}_3)_3 \cdot 9\text{H}_2\text{O}$, and $\text{NH}_4\text{H}_2\text{PO}_4$, dissolved in 5 mL of Ethanol and 3 mL of Acetone, was dark red due to the dark color of $\text{V}(\text{C}_5\text{H}_7\text{O}_2)_3$. The solution was prepared for the synthesis of 2 g of final product. After a few hours under stirring in a closed vessel, the solution turned into a deep blue color as V^{3+} ions present in the solution were gradually oxidized into V^{4+} by oxygen in air. After two days under continuous stirring, the cap was opened in order to evaporate the solvent at ambient temperature, which leads to the formation of a yellow viscous gel. This gel was placed into a golden crucible and first annealed at 150°C during 3h to remove all the traces of solvent and then at 300°C during 3h in order to decompose all the nitrate and ammonium-containing sources. Afterwards, the resulting powder was finely ground in a mortar, pelletized, and finally calcined at 550°C during 3h under Ar atmosphere.

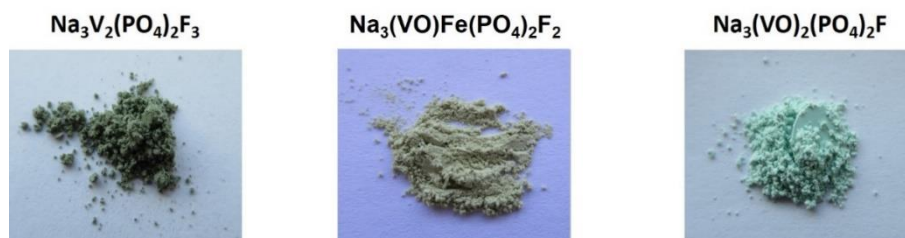


Figure 4.8 : A comparison of the color of the three samples: $\text{Na}_3\text{V}_2(\text{PO}_4)_2\text{F}_3$, $\text{Na}_3(\text{VO})\text{Fe}(\text{PO}_4)_2\text{F}_2$, and $\text{Na}_3(\text{VO})_2(\text{PO}_4)_2\text{F}$.

The analysis of the recorded XRD pattern revealed that all the observed diffraction peaks could be indexed in the $P4_2/mnm$ space group. No unindexed diffraction peak was detected. Comparing the obtained powder to $\text{Na}_3\text{V}_2(\text{PO}_4)_2\text{F}_3$ and $\text{Na}_3(\text{VO})_2(\text{PO}_4)_2\text{F}$, there is an obvious change in their color. $\text{Na}_3\text{V}_2(\text{PO}_4)_2\text{F}_3$ and $\text{Na}_3(\text{VO})_2(\text{PO}_4)_2\text{F}$ are dark grey and bluish green due to the presence of V^{3+} and V^{4+} respectively, whereas the synthesized $\text{Na}_3(\text{VO})\text{Fe}(\text{PO}_4)_2\text{F}_2$, with a $\text{V}^{4+}/\text{Fe}^{3+}$ ratio equals to 1, is beige (**Figure 4.8**). The ICP-OES analysis reveals a Na/V/Fe/P relative ratio of 2.9/1/1/2 in this final product, which

is in good agreement with the theoretical one. The SEM images of (**Figure 4.9**) show that the powder consists of well crystalline primary particles of ca. 500 nm.

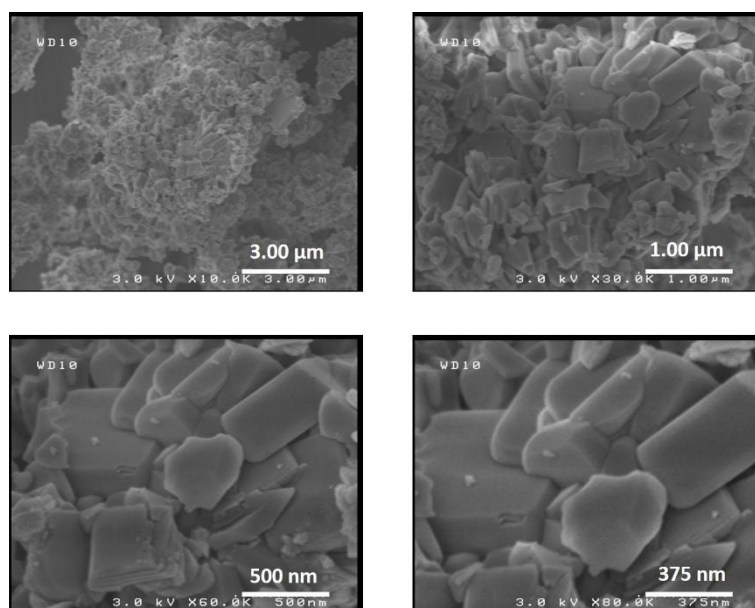


Figure 4.9 : SEM images of $\text{Na}_3(\text{VO})\text{Fe}(\text{PO}_4)_2\text{F}_2$ at different magnifications.

Besides the synthesis of $\text{Na}_3(\text{VO})\text{Fe}(\text{PO}_4)_2\text{F}_2$ we also explored the extended composition domain $\text{Na}_3(\text{VO})_{2-y}\text{Fe}_y(\text{PO}_4)_2\text{F}_{1+y}$ ($0 \leq y \leq 2$) by varying the $\text{V}(\text{C}_5\text{H}_7\text{O}_3)_3$: $\text{Fe}(\text{NO}_3)_3 \cdot 9\text{H}_2\text{O}$ molar ratio in the initial solution. The syntheses were performed in the same conditions as those already discussed, however the obtained powders were a mixture of NVPF- and NASICON-type phases. We also varied the thermal treatment conditions, but no pure phase was successfully obtained (**Figure 4.10** and **Figure 4.11**).

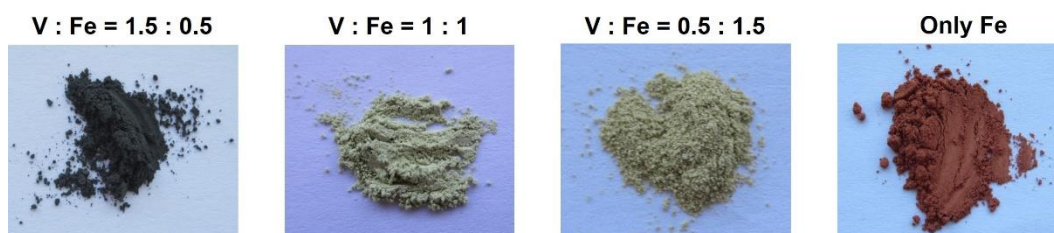


Figure 4.10 : Color of the powders obtained for different V : Fe ratios after a calcination at 550°C under Ar atmosphere during 3h.

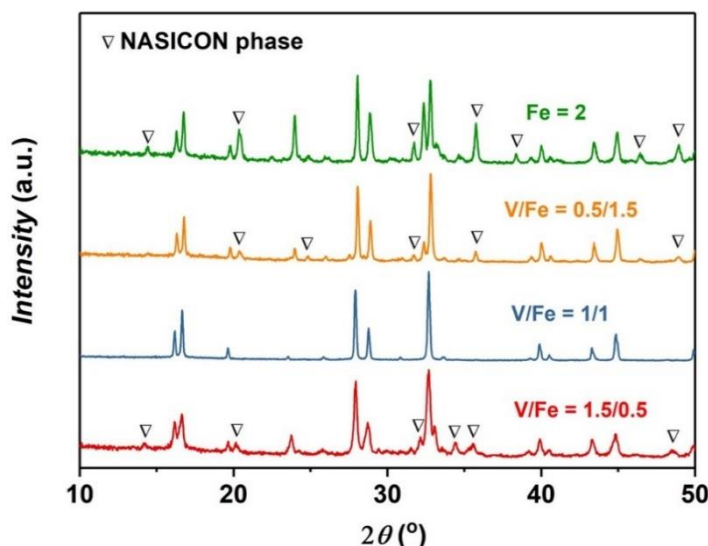


Figure 4.11 : XRD pattern collected using the Cu $K\alpha$ radiation for the products obtained for different V/Fe precursor ratios.

IV.3.2. Structural characterizations

The $\text{Na}_3\text{V}_2(\text{PO}_4)_2\text{F}_3$ parent composition presents a subtle orthorhombic distortion of the unit cell as detected by SXRD through the splitting of the (200)/(020) and (400)/(040) diffraction peaks and is now indexed in the $Amam$ space group.[83]. In this newly obtained Fe-substituted phase, no obvious separation of the (200)/(020) and (400)/(040) doublets is observed. Rietveld refinements were performed in the $P4_2/mnm$ space group (**Figure 4.12**) and also performed in the $Amam$ space group (**Figure 4.13**) in order to choose the best structural description for this newly obtained phase. As highlighted by a comparison of the profile fittings, the reliability factors, the cell parameters and the interatomic distances (**Figure 4.12**, **Figure 4.13**, and **Table 4.7**), no improvement of the fit was observed by considering the orthorhombic symmetry, and hence the tetragonal unit cell was thus retained. Three Na^+ positions are identified in the structure using Fourier difference maps. The atomic positions and the bond length values obtained are given in **Table 4.5** and **Table 4.6**, respectively. The M–F(2)/O(4) distance, which corresponds to the terminal bonds of the bioctahedron, is rather short (1.795(1) Å) and is equal to the average value between the V=O bond length in $\text{Na}_3(\text{VO})_2(\text{PO}_4)_2\text{F}$ and the terminal Fe–F bond length in $\text{Na}_3\text{Fe}_2(\text{PO}_4)_2\text{F}_3$ (1.626(1) Å and 1.92(1) Å, respectively) [82,135,144]. This observation strongly suggests the presence of V=O bonds in the structure of this newly obtained $\text{Na}_3(\text{VO})\text{Fe}(\text{PO}_4)_2\text{F}_2$ phase.

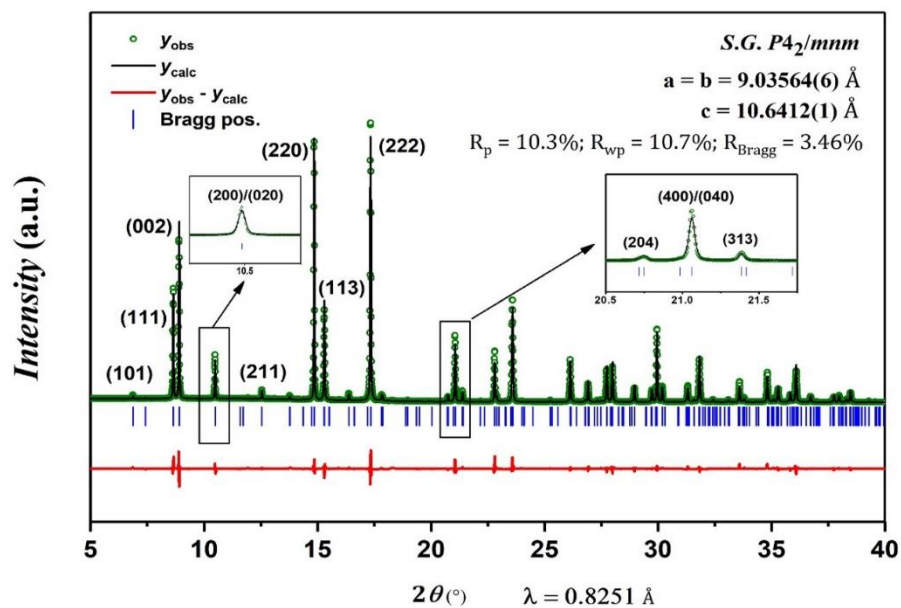


Figure 4.12 : Rietveld refinement from SXRD data recorded for $\text{Na}_3(\text{VO})\text{Fe}(\text{PO}_4)_2\text{F}_2$, performed in the $P4_2/mnm$ space group. Insets show enlargements of the (200)/(020) and (400)/(040) doublets.

Table 4.5 : Structural parameters of $\text{Na}_3(\text{VO})\text{Fe}(\text{PO}_4)_2\text{F}_2$ obtained from Rietveld refinement of synchrotron powder diffraction data collected at $\lambda = 0.8251 \text{ \AA}$.

| $\text{Na}_3(\text{VO})\text{Fe}(\text{PO}_4)_2\text{F}_2$ | | | | | | |
|------------------------------------------------------------------------------|------------------|-----------------|---------------|---------------|---------------|------------------|
| Space group : $P4_2/mnm$; $Z = 4$ | | | | | | |
| $a = b = 9.03564(6) \text{ \AA}$, $c = 10.6412(1) \text{ \AA}$ | | | | | | |
| $V/Z = 217.195(2) \text{ \AA}^3$ | | | | | | |
| $R_{\text{bragg}} = 3.46\%$, $R_p = 10.3\%$, $R_{\text{wp}} = 10.7\%$ | | | | | | |
| atom | Wyckoff position | Atomic position | | | Occ. | B_{iso} |
| | | x/a | y/b | z/c | | |
| V(1) | $8j$ | 0.7483(6) | 0.2517(6) | 0.1917(2) | $\frac{1}{2}$ | 0.96(6) |
| Fe(1) | $8j$ | 0.7483(6) | 0.2517(6) | 0.1917(2) | $\frac{1}{2}$ | 0.96(6) |
| P(1) | $4e$ | $\frac{1}{2}$ | $\frac{1}{2}$ | 0.253(2) | 1 | 0.9(1) |
| P(2) | $4d$ | $\frac{1}{2}$ | 0 | $\frac{1}{4}$ | 1 | 0.8(1) |
| O(1) | $16k$ | 0.595(2) | 0.094(2) | 0.162(1) | 1 | 0.78 |
| O(2) | $8j$ | 0.598(2) | 0.402(2) | 0.160(2) | 1 | 0.78 |
| O(3) | $8j$ | 0.402(2) | 0.402(2) | 0.330(2) | 1 | 0.78 |
| O(4) | $8j$ | $\frac{3}{4}$ | $\frac{1}{4}$ | 0.360(2) | $\frac{1}{2}$ | 1.0 |
| F(1) | $4g$ | $\frac{3}{4}$ | $\frac{1}{4}$ | 0 | 1 | 0.4 |
| F(2) | $8j$ | $\frac{3}{4}$ | $\frac{1}{4}$ | 0.360(2) | $\frac{1}{2}$ | 1.0 |
| Na(1) | $8i$ | 0.270(2) | 0.022(2) | 0 | 0.850(3) | 2.1(1) |
| Na(2) | $8i$ | 0.476(3) | 0.290(3) | 0 | 0.58(1) | 4.5(4) |
| Na(3) | $4f$ | 0.408(5) | 0.408(5) | 0 | 0.266(6) | 3.0(3) |

Table 4.6 : Bond length distances (\AA) describing the coordination polyhedra of each cation in $\text{Na}_3(\text{VO})\text{Fe}(\text{PO}_4)_2\text{F}_2$, from Rietveld refinement in the $P4_2/mnm$ space group of synchrotron X-ray powder diffraction data collected at $\lambda = 0.8251 \text{ \AA}$.

| $\text{Na}_3(\text{VO})\text{Fe}(\text{PO}_4)_2\text{F}_2$ | | | | | | |
|------------------------------------------------------------|-------------|-------------|-------------|-------------|------------|------------|
| | V/Fe | P(1) | P(2) | Na(1) | Na(2) | Na(3) |
| Coordination | 6 | 4 | 4 | 7 | 7 | 6 |
| Distances (\AA) | | | | | | |
| O(1) | 1.954(6) | 1.595(8) x2 | | 2.619(9) x2 | 2.27(1) x2 | 2.42(1) x4 |
| O(2) | 2.013(6) | | 1.529(6) x4 | | 2.70(1) x2 | |
| O(3) | 1.983(6) x2 | 1.493(8) x2 | | 2.351(7) x2 | | |
| F(1) | 2.040(1) | | | 2.464(7) | 2.50(1) | |
| F(2)/O(4) | 1.795(1) | | | 2.547(6) x2 | 2.55(1) x2 | 2.50(1) x2 |

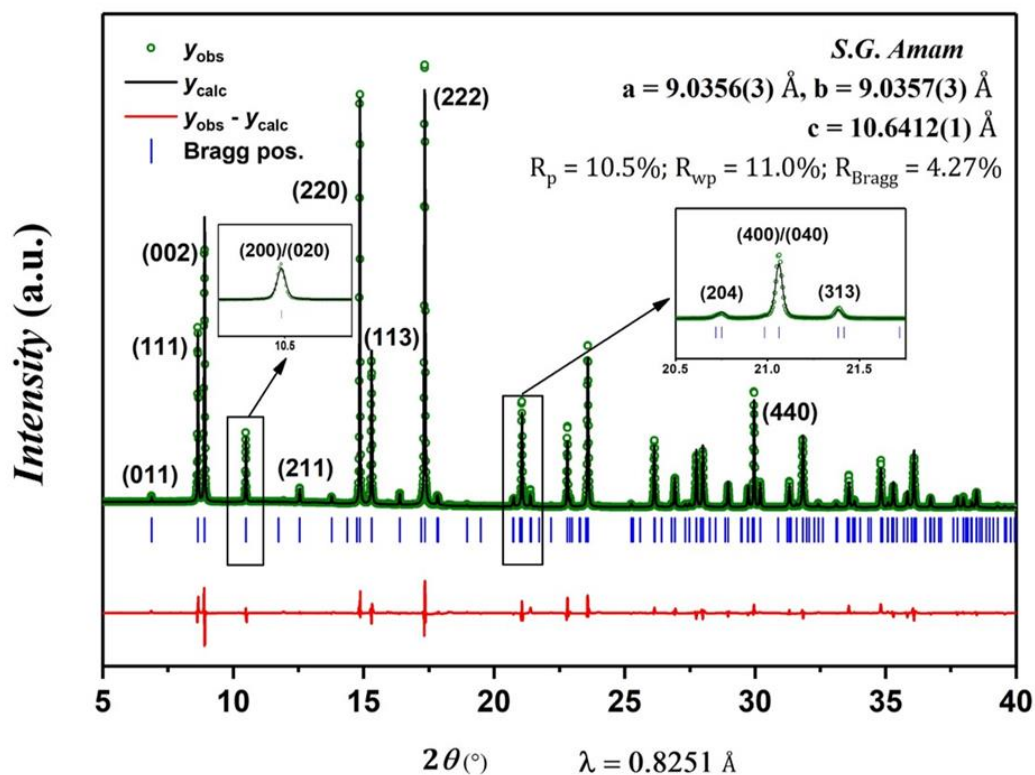


Figure 4.13 : Result of the Rietveld refinement performed in the *Amam* space group on the SXRD data recorded on the $\text{Na}_3(\text{VO})\text{Fe}(\text{PO}_4)_2\text{F}_2$ phase.

Table 4.7 : A comparison of the interatomic distances in $\text{Na}_3(\text{VO})\text{Fe}(\text{PO}_4)_2\text{F}_2$ obtained from Rietveld refinements by considering two structural descriptions: $A\bar{m}am$ and $P4_2/mnm$ space groups.

| <i>A$\bar{m}am$</i> | | <i>P4$_2$/mnm</i> | |
|--------------------------------|--------------|------------------------------|--------------|
| Interatomic distances (Å) | | Interatomic distances (Å) | |
| P(1)-O(1) | 1.582(6) x 2 | P(1)-O(1) | 1.529(6) x 4 |
| P(1)-O(2) | 1.490(7) x 2 | P(2)-O(2) | 1.595(8) x 2 |
| | | P(2)-O(3) | 1.493(8) x 2 |
| V/Fe-O(1) | 2.001(7) x 2 | V(1)-O(1) | 2.013(6) x 2 |
| V/Fe-O(2) | 1.993(7) x 2 | V(1)-O(2) | 1.954(6) |
| | | V(1)-O(3) | 1.983(6) |
| V/Fe-F(1) | 2.040(1) | V(1)-F(1) | 2.040(1) |
| V/Fe-F(2)/O(3) | 1.802(4) | V(1)-F(2)/O(4) | 1.795(1) |

The ^{57}Fe Mössbauer spectrum of $\text{Na}_3(\text{VO})\text{Fe}(\text{PO}_4)_2\text{F}_2$ exhibits a single quadrupole doublet (**Figure 4.14a**), with an isomer shift $\delta = 0.41(1) \text{ mm}\cdot\text{s}^{-1}$ and a mean quadrupole splitting $\Delta = 0.61 \text{ mm}\cdot\text{s}^{-1}$ corresponding to a six-fold coordinated high spin Fe^{3+} ion ($t_{2g}^3 e_g^2$) in a highly symmetric environment. The rather high value of the isomer shift is due to the high ionic character of the Fe–F and Fe–O bonds. The quadrupole splitting distribution is mono-modal and very narrow meaning that there is only one discrete site ($8j$) for Fe^{3+} ions with a regular and non-disordered local environment (**Figure 4.19**) [213].

X-ray absorption near edge structure (XANES) spectra at vanadium K-edge (5465 eV) and at iron K-edge (7112 eV) were used in order to determine the local environment as well as the oxidation state of vanadium and iron species. The edge energy of the XANES spectra recorded at vanadium and iron K-edges confirms the expected occurrence of V^{4+} and Fe^{3+} in the sample (**Figure 4.14b** and **c**). The low intensity of the pre-edge signal on the XANES spectrum at Fe K-edge confirms the symmetric octahedral environments of high-spin Fe^{3+} , while the high intensity of the pre-edge on the V K-edge spectrum implies that V local environment is highly distorted due to the presence of the highly covalent vanadyl bond, which is in agreement with the bond length values obtained from Rietveld refinement.

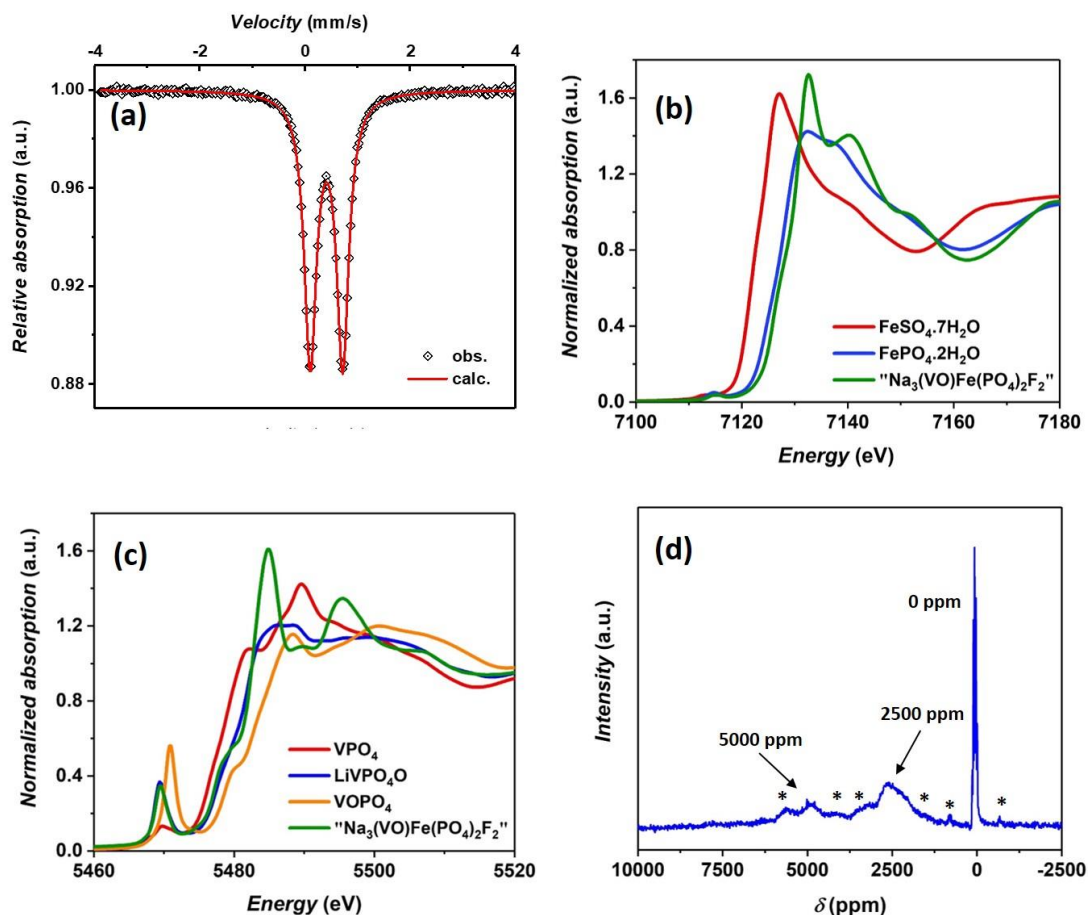


Figure 4.14 : (a) ^{57}Fe Mössbauer spectroscopy recorded at ambient temperature with a ^{57}Co source, (b) Fe K-edge XANES spectrum of $\text{Na}_3(\text{VO})\text{Fe}(\text{PO}_4)_2\text{F}_2$. Both $\text{Fe}^{2+}\text{SO}_4 \cdot 7\text{H}_2\text{O}$ and $\text{Fe}^{3+}\text{PO}_4 \cdot 2\text{H}_2\text{O}$ are used as references to determine the Fe oxidation state, (c) V K-edge XANES spectrum of $\text{Na}_3(\text{VO})\text{Fe}(\text{PO}_4)_2\text{F}_2$. The V^{3+}PO_4 , $\text{LiV}^{4+}\text{PO}_4\text{O}$ and $\text{V}^{5+}\text{OPO}_4$ XANES spectra are reported to determine the V oxidation state, (d) ^{31}P ss-NMR spectrum recorded at $B_0 = 2.35\text{T}$; $\nu_R = 30\text{ kHz}$. The excitation pulse was placed at 5000 ppm. The asterisks (*) indicate the rotational spinning sidebands.

While the V^{4+} and Fe^{3+} ions share the same Wyckoff position and hence cannot be distinguished by synchrotron X-ray diffraction, the EXAFS analysis at both V and Fe K-edges provides detailed information about the $\text{V}(\text{O},\text{F})_6$ and $\text{Fe}(\text{O},\text{F})_6$ local environments, even if oxygen and fluorine cannot be distinguished. The EXAFS analysis at Fe K-edge of the $\text{Na}_3(\text{VO})\text{Fe}(\text{PO}_4)_2\text{F}_2$ spectrum shows that the Fe^{3+} occupies an octahedral environment and is coordinated by four O atoms in a square plane at a distance of 2.00 Å and two O/F atoms on the axial positions at distances of 1.90 Å and 2.00 Å, with Debye-Waller factors of $4.99 \cdot 10^{-3} \text{ \AA}^2$. On the other hand, the $\text{V}^{4+}(\text{O},\text{F})_6$ octahedron is built by four equivalent oxygen atoms in a square plane at a V–O distance of $\sim 2.00 \text{ \AA}$, one O/F atom at 2.11 Å, and a closer O/F at 1.65 Å corresponding to the V=O vanadyl-type bond. Smaller Debye-Waller factors ($2.24 \cdot 10^{-3} \text{ \AA}^2$ vs $4.99 \cdot 10^{-3} \text{ \AA}^2$) are observed, which is in good agreement with a more covalent environment for V^{4+} than for

Fe^{3+} . Taking into account the stoichiometry as well as the vanadium and iron oxidation states, the structure of $\text{Na}_3(\text{VO})\text{Fe}(\text{PO}_4)_2\text{F}_2$ can be described as FeO_4F_2 and VO_5F octahedra which are sharing one common fluorine atom to form $\text{FO}_4\text{Fe}-\text{F}-\text{FeO}_4\text{F}$, $\text{FO}_4\text{Fe}-\text{F}-\text{VO}_5$, or $\text{O}_5\text{V}-\text{F}-\text{VO}_5$ bioctahedral units. Indeed, no superstructure corresponding to the $\text{V}^{4+}/\text{Fe}^{3+}$ ordering was detected in the SXRD data. The two ions are randomly distributed over all the transition metal sites in the structure.

The recorded ^{31}P *ss*-NMR spectrum shows a possible presence of several resonances in the range of 0 to 10000 ppm (**Figure 4.14d**). We have recently demonstrated that the presence of V^{4+} ion in highly distorted octahedral sites will cause no Fermi contact with the neighboring phosphorus nuclei as the orbital containing the electron spin of V^{4+} does not point towards the phosphorus sites and the ^{31}P resonance at ~ 0 ppm is associated to the $\text{P}(\text{OV}^{4+})_4$ local environment. Therefore, the ^{31}P paramagnetic resonances observed here can only be induced by the Fermi contact between Fe^{3+} and phosphorus nuclei.

Table 4.8 : A comparison of the cell parameters between the input model and the optimized structure of $\text{Na}_3\text{Fe}_2(\text{PO}_4)_2\text{F}_3$.

| | Input model | Structure optimized by GGA |
|----------|-------------|----------------------------|
| a (Å) | 9.029 | 9.148 |
| b (Å) | 9.024 | 9.196 |
| c (Å) | 10.747 | 10.778 |
| α | 90° | 90° |
| β | 90° | 90° |
| γ | 90° | 90° |

The Fermi contact between the unpaired electrons of Fe^{3+} and the phosphorus nuclei was studied through the $\text{Na}_3\text{Fe}_2(\text{PO}_4)_2\text{F}_3$ crystal structure and then extrapolated to the case of $\text{Na}_3(\text{VO})\text{Fe}(\text{PO}_4)_2\text{F}_2$. The crystal structure of $\text{Na}_3\text{Fe}_2(\text{PO}_4)_2\text{F}_3$ was reported by Le Meins *et al.*, and it contains six partially occupied Na sites [82], which cannot be taken into account in the DFT calculations. Furthermore, in this study, we only wanted to investigate the electron spin transfer between Fe^{3+} and its neighboring phosphorus nuclei, which is not influenced by the positions of Na^+ ions in the diffusion channels. An approximate $\text{Na}_3\text{Fe}_2(\text{PO}_4)_2\text{F}_3$ input model was constructed based on the crystal structure

of $\text{Na}_3\text{V}_2(\text{PO}_4)_2\text{F}_3$ by replacing all vanadium atoms in the unit cell by iron. The $\text{Na}_3\text{Fe}_2(\text{PO}_4)_2\text{F}_3$ input model was then relaxed by using the GGA method until the system reached its minimum energy. The spin density on each nucleus as well as the spin distribution map were calculated on the optimized structure. The theoretical ^{31}P paramagnetic shift is then computed from the electron spin density by using **Equation (3)**.

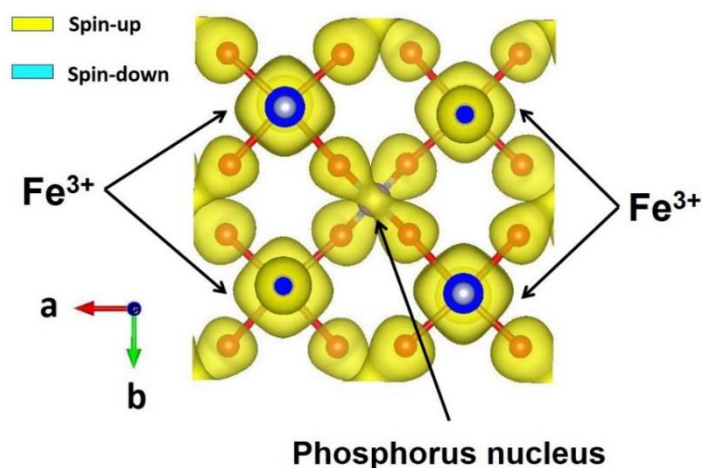


Figure 4.15 : Electron spin density calculated at an iso-surface value of $2 \cdot 10^{-3}$ electron $\cdot\text{\AA}^{-1}$ for $\text{Na}_3\text{Fe}_2(\text{PO}_4)_2\text{F}_3$. The ‘spin-up’ electrons are represented by the yellow region while the ‘spin down’ electrons are represented in blue.

The calculated spin distribution map shows that each phosphorus nucleus in the unit cell is surrounded by four Fe^{3+} ions and all these Fe^{3+} ions are in the high-spin state (**Figure 4.15**). Thanks to the orbital overlap between the $3d$ orbitals of Fe^{3+} and the sp^3 hybridized orbital of phosphorus, the spin electrons on Fe^{3+} can be transferred on the phosphorus site. The presence of the high density of the electron spin close to the phosphorus center will lead to a strong electron - nuclear spin interaction, resulting in the high paramagnetic shift on the ^{31}P NMR spectrum. All these four Fe^{3+} ions can transfer their electron spins on the phosphorus center and the calculated paramagnetic shift for this local environment is ~ 8400 ppm. In **Chapter III**, we have shown that the paramagnetic interaction in this structural framework is cumulative, which implies that the presence of one Fe^{3+} in the proximity of a phosphorus nuclei will contribute to a paramagnetic shift value of ~ 2100 ppm. We thus deduce that the $\text{P}(\text{OV}^{4+})_3(\text{OFe}^{3+})$, $\text{P}(\text{OV}^{4+})_2(\text{OFe}^{3+})_2$, and $\text{P}(\text{OV}^{4+})(\text{OFe}^{3+})_3$ local environments, if they exist in this crystal structure, should give rise to the ^{31}P NMR resonances at ~ 2100 ppm, 4200 ppm, and

6300 ppm, respectively. The experimental signals are indeed observed in this range, but they are unfortunately really broad due to a strong dipolar interaction between the five unpaired electrons of each Fe^{3+} and the phosphorus nucleus. These broad signals also overlap with the spinning side bands and the resolution of the recorded spectrum is not sufficient to detect all individual contributions.

The theoretical paramagnetic shift for this $\text{P}(\text{OFe}^{3+})_4$ local environment is ~ 8400 ppm. As we have recently demonstrated that there is no Fermi contact between V^{4+} and phosphorus nuclei in this structural framework, the magnitude of the Fermi contact will depend only on the presence of Fe^{3+} ions in the proximity of the phosphorus nucleus. Each Fe^{3+} will contribute to a shift value of ~ 2100 ppm while there is no contribution of V^{4+} to the paramagnetic shift of ^{31}P . In a recent work, we have reported that each V^{3+} ($3d^2$) in the proximity of a Phosphorus atom in this structural framework will contribute to a paramagnetic shift of ~ 1500 ppm due to the Fermi contact. In the case of Fe^{3+} , due to the presence of more unpaired electrons ($3d^5$), each Fe^{3+} can contribute to a shift of ~ 2100 ppm.

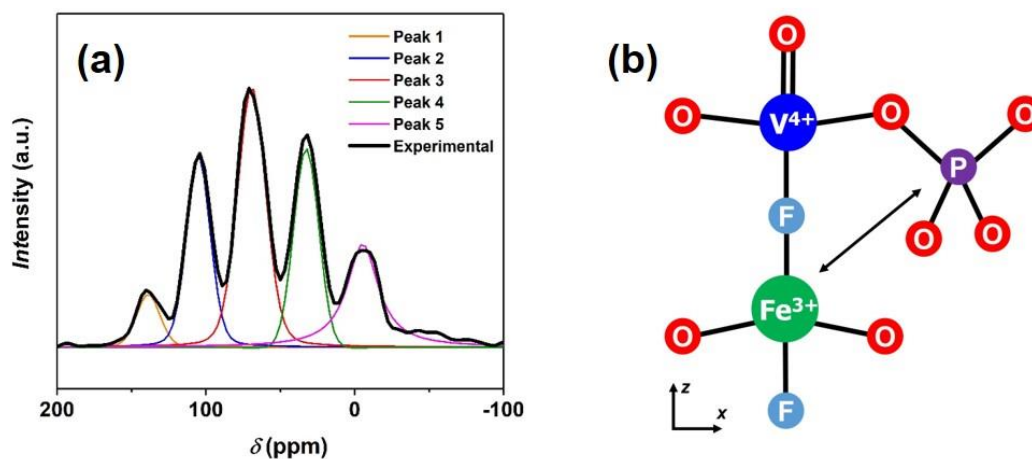


Figure 4.16 : (a) An enlargement of the ^{31}P NMR diamagnetic resonances (200 ppm to -100 ppm) recorded for the $\text{Na}_3(\text{VO})\text{Fe}(\text{PO}_4)_2\text{F}_2$ material. The five diamagnetic resonances in this material can be fitted by five different Gaussian/Lorentzian peak shape functions, (b) Illustration of the influence of the second neighboring metal ion belonging to the bioctahedral unit on the ^{31}P chemical shift value.

An enlargement on the ^{31}P NMR diamagnetic region associated to the $\text{P}(\text{OV}^{4+})_4$ environment (from -100 ppm to 200 ppm) reveals the presence of five diamagnetic resonances equally separated by ~ 35 ppm. They can be fitted by five different pseudo-Voigt peak shape functions (**Figure 4.16a**) and the corresponding values for the chemical shift, peak width and amplitude are compared in **Table 4.9**. As a V^{4+} ion induces almost

no Fermi contact with the neighboring P, these small shifts are associated to the presence of Fe^{3+} ions in the second coordination sphere of ^{31}P nucleus leading either to a weak Fermi contact shift or to small changes in the local atomic or electronic structure around V^{4+} resulting in such a small shift. These five ^{31}P NMR resonances correspond to $\text{P}(\text{OV}^{4+})_4$ local environments with different distribution of $\text{V}^{4+} : \text{Fe}^{3+}$ as second neighbors in the bioctahedral units (**Figure 4.18b**). We hence propose that each Fe^{3+} , as a second transition metal neighbor in the bioctahedra, contributes to a shift of ~ 35 ppm; therefore, the resonances at ~ 0 ppm, 33 ppm, 69 ppm, 105 ppm, and 139 ppm are assigned to $\text{P}(\text{OV}^{4+}-\text{F}-\text{V}^{4+})_{4-n}(\text{OV}^{4+}-\text{F}-\text{Fe}^{3+})_n$ local environments with $n = 0, 1, 2, 3, 4$, respectively. The relative intensities of the five diamagnetic resonances are in agreement with the values estimated considering a binomial distribution (**Table 4.9**). This shows that the $\text{V}^{4+}/\text{Fe}^{3+}$ distribution in the bioctahedral units is fully random and solely controlled by statistics.

Table 4.9 : The amplitude, chemical shift (δ), peak width, pseudo-Voigt peak shape function (η), and the relative contribution of each ^{31}P NMR resonance recorded in the diamagnetic region of $\text{Na}_3(\text{VO})\text{Fe}(\text{PO}_4)_2\text{F}_2$. The fitting was done using the DM-fit program.

| | Amplitude | δ (ppm) | Width (ppm) | η (Gaussian/Lorentzian) | Experimental contribution | Theoretical distribution |
|--------|-----------|----------------|-------------|------------------------------|---------------------------|--------------------------|
| Peak 1 | 6337 | 139 | 18.7 | 0.8 | 6.6% | 6.25% |
| Peak 2 | 22955 | 105 | 18.6 | 0.8 | 23.8% | 25% |
| Peak 3 | 31220 | 69 | 22.4 | 0.8 | 32.3% | 37.5% |
| Peak 4 | 23818 | 33 | 19.9 | 1.0 | 24.6% | 25% |
| Peak 5 | 12338 | -5 | 25.5 | 0 | 12.7% | 6.25% |

The ^{23}Na MAS NMR spectrum recorded for $\text{Na}_3(\text{VO})\text{Fe}(\text{PO}_4)_2\text{F}_2$ shows the presence of resonances at 300 ppm, 200 ppm and 80 ppm (**Figure 4.17**) corresponding to the $\text{Na}(\text{OFe}^{3+})_2$, $\text{Na}(\text{OFe}^{3+})(\text{OV}^{4+})$ and $\text{Na}(\text{OV}^{4+})_2$ local environment, respectively. The resonance at 200 ppm appears as a doublet while the one at 300 ppm appears as a triplet. The presence of Fe^{3+} ion in the proximity of Na nucleus seems to induce an additional interaction that results in the splitting of ^{23}Na resonance lines. Nonetheless, the nature of this additional interaction is still unclear.

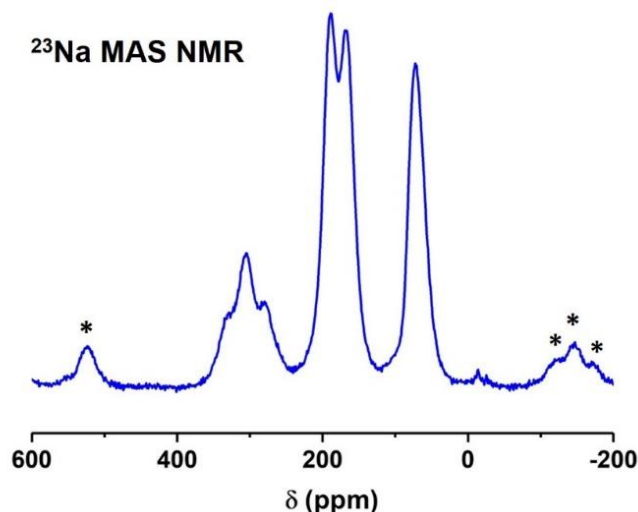


Figure 4.17 : ^{23}Na MAS NMR of $\text{Na}_3(\text{VO})\text{Fe}(\text{PO}_4)_2\text{F}_2$ recorded at $B_0 = 11.7$ T with $\nu_R = 50$ kHz. Rotational spinning sidebands are marked with asterisks.

All the information obtained by synchrotron X-ray powder diffraction, chemical analyses, as well as the local structure descriptions determined by ^{57}Fe Mössbauer, ^{31}P NMR and XAS at V and Fe K-edges spectroscopies, fully support the chemical formula $\text{Na}_3(\text{V}^{4+}\text{O})\text{Fe}^{3+}(\text{PO}_4)_2\text{F}_2$ for this new material.

IV.3.3. Electrochemical properties of $\text{Na}_3(\text{VO})\text{Fe}(\text{PO}_4)_2\text{F}_2$

$\text{Na}_3(\text{VO})\text{Fe}(\text{PO}_4)_2\text{F}_2$ was investigated as positive electrode in SIBs and cycled in the voltage window 2.5 - 4.3 V vs. Na^+/Na at the cycling rate of $C/10$ per Na^+ ; only one Na^+ can be reversibly extracted in this voltage window (**Figure 4.18a**). The first derivative curve for $\text{Na}_3(\text{VO})\text{Fe}(\text{PO}_4)_2\text{F}_2$ shows the presence of a broad peak at ~ 3.64 V vs. Na^+/Na (**Figure 4.18a**), which is comparable to the $\text{V}^{5+}/\text{V}^{4+}$ redox couple observed in the $\text{Na}_3(\text{VO})_2(\text{PO}_4)_2\text{F}$ counterpart [146].

Several intermediate phases, stabilized by the Na^+ -vacancy ordering, were detected during Na^+ deintercalation and re-intercalation from/in $\text{Na}_3(\text{VO})_2(\text{PO}_4)_2\text{F}$. In the case of $\text{Na}_3(\text{VO})\text{Fe}(\text{PO}_4)_2\text{F}_2$, the charge/discharge curve is very sloping suggesting a solid solution mechanism. Indeed, Fe^{3+} is randomly distributed among the transition metal sites, which thus prevents the formation of charge ordering on the transition metal sites as well as the Na^+ -vacancy ordering within the diffusion channels of the host structure.

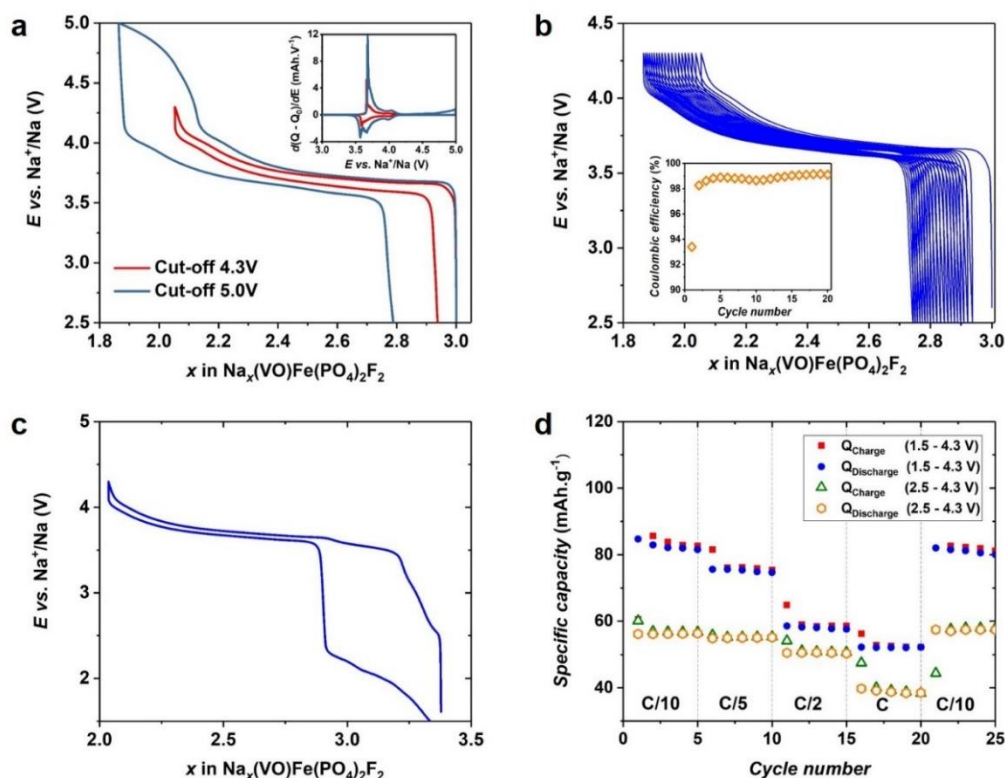


Figure 4.18 : (a) The charge/discharge curve of $\text{Na}_3(\text{VO})\text{Fe}(\text{PO}_4)_2\text{F}_2$ at the cycling rate of $C/10$ per Na^+ with the cutoff voltage of 4.3 and 5.0 V vs. Na^+/Na . Inset shows the first derivative charge/discharge curve as a function of the operational voltage, (b) The long-term evolution of the charge/discharge curves at the cycling rate of $C/10$ per Na^+ in the potential range of 2.5 - 4.3 V vs. Na^+/Na . Inset shows the evolution of the coulombic efficiency during the first twenty cycles, (c) The charge/discharge curve at the second cycle of $\text{Na}_3(\text{VO})\text{Fe}(\text{PO}_4)_2\text{F}_2$ at the cycling rate of $C/10$ per Na^+ in the potential range of 1.5 - 4.3 V vs. Na^+/Na , (d) The charge/discharge capacity of $\text{Na}_3(\text{VO})\text{Fe}(\text{PO}_4)_2\text{F}_2$ at different cycle rates in the potential ranges of 2.5 - 4.3 V and 1.5 - 4.3 V vs. Na^+/Na .

Extra capacity is observed when the upper cutoff voltage is increased up to 5.0 V vs. Na^+/Na ; nevertheless, this capacity is irreversible (**Figure 4.18a**). As this material contains only one V^{4+} ion per formula unit, the extraction of one Na^+ implies that all the vanadium ions are at the pentavalent state in $\text{Na}_2(\text{VO})\text{Fe}(\text{PO}_4)_2\text{F}_2$. Then, the extra capacity can either be attributed to the oxidation of Fe^{3+} into Fe^{4+} or to the electrolyte degradation. Nonetheless, the ^{57}Fe Mössbauer spectrum recorded on the sample recovered at 5.0 V only shows the presence of Fe^{3+} in its high-spin state (**Figure 4.19c**) confirming that Fe^{3+} was not oxidized into Fe^{4+} . We thus conclude that this irreversible extra capacity is attributed to the electrolyte decomposition.

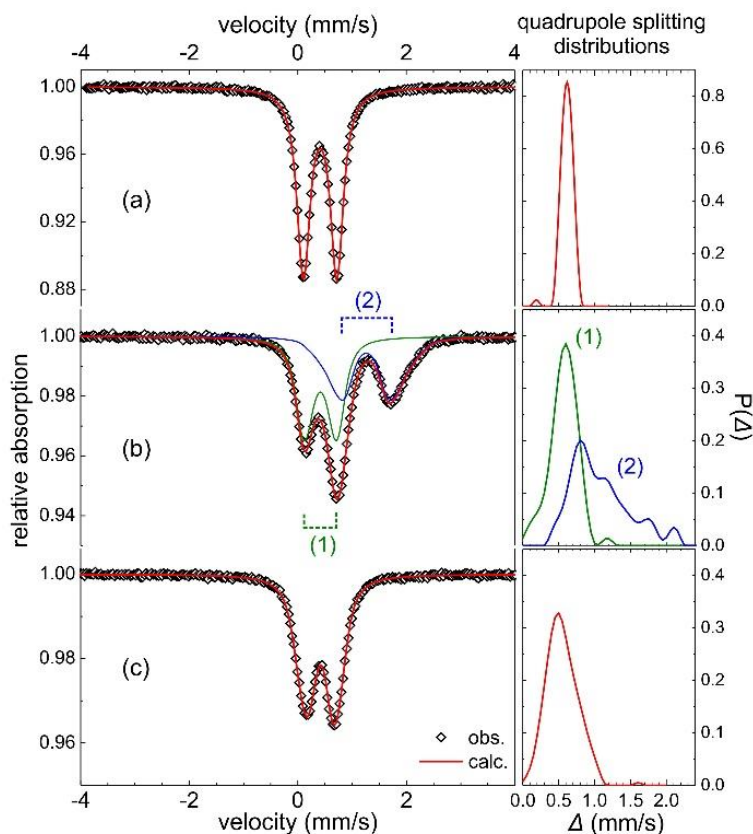


Figure 4.19 : Room temperature ^{57}Fe Mössbauer spectra of (a) pristine material $\text{Na}_3(\text{VO})\text{Fe}(\text{PO}_4)_2\text{F}_2$, (b) $\text{Na}_3(\text{VO})\text{Fe}(\text{PO}_4)_2\text{F}_2$ electrode discharged to 1.5 V vs. Na^+/Na and (c) $\text{Na}_3(\text{VO})\text{Fe}(\text{PO}_4)_2\text{F}_2$ electrode charged to 5.0 V vs. Na^+/Na . All sub-spectra were calculated using a distribution of the quadrupole splitting (Δ) hyperfine parameter shown in the right panel.

Table 4.10 : Refined room temperature ^{57}Fe Mössbauer hyperfine parameters for (i) pristine material $\text{Na}_3(\text{VO})\text{Fe}(\text{PO}_4)_2\text{F}_2$, (ii) $\text{Na}_3(\text{VO})\text{Fe}(\text{PO}_4)_2\text{F}_2$ electrode discharged to 1.5 V vs. Na^+/Na and (iii) $\text{Na}_3(\text{VO})\text{Fe}(\text{PO}_4)_2\text{F}_2$ electrode charged to 5.0 V vs. Na^+/Na . (δ isomer shift in respect to $\alpha\text{-Fe}$, Δ quadrupole splitting, Γ Lorentzian line width and A relative area). (*) mean value of the Δ distribution.

| Sample | sub. | δ (mm/s) | Δ (mm/s) | Γ (mm/s) | A (%) | assignment |
|--------------------|------|-----------------|-----------------|-----------------|-------|----------------------|
| Pristine | QD1 | 0.41(1) | 0.61(*) | 0.25(-) | 100 | HS- Fe^{3+} |
| Discharged (1.5 V) | QD1 | 0.42(1) | 0.57(*) | 0.25(-) | 53(3) | HS- Fe^{3+} |
| | QD2 | 1.26(1) | 1.08(*) | 0.25(-) | 47(3) | HS- Fe^{2+} |
| Charged (5 V) | QD1 | 0.42(1) | 0.55(*) | 0.25(-) | 100 | HS- Fe^{3+} |

Even without carbon-coating, this material shows very small polarization with limited capacity fading during electrochemical cycling (**Figure 4.18b Inset**). Indeed, comparing to a $\text{Na}/\text{Na}_3(\text{VO})_2(\text{PO}_4)_2\text{F}$ half-cell operating in the same conditions, the polarization observed for a $\text{Na}/\text{Na}_3(\text{VO})\text{Fe}(\text{PO}_4)_2\text{F}_2$ half-cell appears to be two times smaller (**Figure 4.20**). The cell parameters and the size of the diffusion channels of

$\text{Na}_3(\text{VO})\text{Fe}(\text{PO}_4)_2\text{F}_2$ are only $\sim 0.1\%$ bigger than those of $\text{Na}_3(\text{VO})_2(\text{PO}_4)_2\text{F}$; furthermore, the primary particles of $\text{Na}_3(\text{VO})\text{Fe}(\text{PO}_4)_2\text{F}_2$ are even bigger than those of $\text{Na}_3(\text{VO})_2(\text{PO}_4)_2\text{F}$ indicating that the easier diffusion cannot be attributed to shorter diffusion lengths. These results suggest that the smaller polarization observed for $\text{Na}_3(\text{VO})\text{Fe}(\text{PO}_4)_2\text{F}_2$ is due to an improvement in the intrinsic properties of the material. Dacek *et al.* reported that Na^+ diffusivity in $\text{Na}_3\text{M}_2(\text{PO}_4)_2\text{X}_3$ ($\text{M} = \text{Al}, \text{V}, \text{Ti}; \text{X} = \text{F}, \text{O}$) and in similar structures is unlikely affected by the size of the diffusion channels. It would rather depend strongly on the Na^+ -vacancy ordering and the Na^+ -defect formation energy [119,128].

A material with a high tendency to form Na^+ -vacancy ordering upon cycling, such as $\text{Na}_3\text{V}_2(\text{PO}_4)_2\text{F}_3$ and $\text{Na}_3(\text{VO})_2(\text{PO}_4)_2\text{F}$, will have a slower Na^+ diffusion process as extra activation energy is required to first break the Na^+ -vacancy ordering and then create local defects for the diffusion to occur. [119]. Any factor, such as cationic substitution on the vanadium site [119,128], that can prevent the formation of Na^+ -vacancy ordering during charge or lower the Na^+ -defect formation energy will thus be a driving force for the formation of off-stoichiometry compositions. Therefore, Fe^{3+} substitution for V with a random distribution of Fe^{3+} over V sites can be considered as an appropriate substituent or dopant that can be used to improve the Na^+ diffusivity in $\text{Na}_3\text{V}_2(\text{PO}_4)_2\text{F}_3$ and $\text{Na}_3(\text{VO})_2(\text{PO}_4)_2\text{F}$ -type materials.

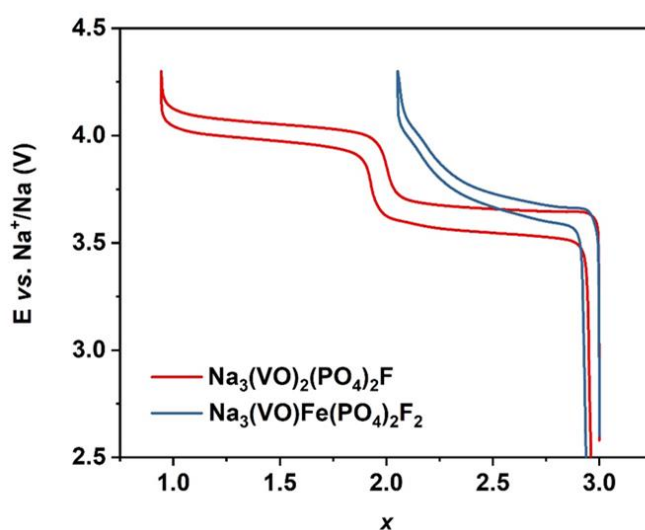


Figure 4.20 : Comparison of the electrochemical properties between $\text{Na}_3(\text{VO})_2(\text{PO}_4)_2\text{F}$ and $\text{Na}_3(\text{VO})\text{Fe}(\text{PO}_4)_2\text{F}_2$ cycled in the same condition.

Extra reversible capacity is obtained when the lower cutoff voltage is decreased to 1.5 V *vs.* Na^+/Na (**Figure 4.18c**), which could be due to the activation of the $\text{Fe}^{3+}/\text{Fe}^{2+}$ redox couple that had been reported earlier for the $\text{Na}_3\text{Fe}_2(\text{PO}_4)_2\text{F}_3$ composition [214]. The ^{57}Fe Mössbauer spectrum recorded on the material recovered at 1.5 V reveals the existence of 47% of Fe^{2+} (isomer shift $\delta = 1.26 \text{ mm}\cdot\text{s}^{-1}$) and 53% of Fe^{3+} ($\delta = 0.42 \text{ mm}\cdot\text{s}^{-1}$) in their high-spin state confirming the occurrence of the $\text{Fe}^{3+}/\text{Fe}^{2+}$ redox couple in this voltage region (**Figure 4.19b**). Other hyperfine parameters of these iron species are given in **Table 4.10**. The hyperfine parameters of Fe^{3+} in the pristine phase and in $\text{Na}_{3.5}(\text{VO})\text{Fe}(\text{PO}_4)_2\text{F}_2$ are very similar implying that there is little influence of the second coordination sphere on the Fe^{3+} sites. The reduction of 0.47 Fe^{3+} to Fe^{2+} corresponds to the insertion of ~ 0.5 extra Na^+ ions at the low voltage region to result in the composition $\text{Na}_{3.5}(\text{VO})\text{Fe}(\text{PO}_4)_2\text{F}_2$. The insertion of more than 0.5 Na^+ ions into the structure is not achieved, even at low cycling rates, most probably due to the strong $\text{Na}^+ - \text{Na}^+$ electrostatic repulsions within the channels of the structure that destabilizes the formation of the phases with more than 3.5 Na^+ per formula unit.

Zhang *et al.* reported that $\text{Na}_4\text{V}_2(\text{PO}_4)_2\text{F}_3$ could be synthesized mechanically by ball milling $\text{Na}_3\text{V}_2(\text{PO}_4)_2\text{F}_3$ with Na metal.[150]. Three Na^+ ions were electrochemically extracted from $\text{Na}_4\text{V}_2(\text{PO}_4)_2\text{F}_3$ upon charge; however, only two Na^+ ions could be reinserted into the structure during discharge to form $\text{Na}_3\text{V}_2(\text{PO}_4)_2\text{F}_3$. The initial phase, $\text{Na}_4\text{V}_2(\text{PO}_4)_2\text{F}_3$, was never recovered even though a very low cutoff voltage was applied [150]. These observations confirm our results that the $\text{Na}_3\text{V}_2(\text{PO}_4)_2\text{F}_3$ -like structure cannot accommodate so many Na^+ into its structural channels. The polarization increases greatly when the lower cutoff voltage is set at 1.5 V (**Figure 4.18c**), suggesting that the $\text{Fe}^{3+}/\text{Fe}^{2+}$ reduction and the extra Na^+ insertion processes are not energetically favorable; nevertheless, it appears that the presence of a huge polarization at low voltage does not affect the electrochemical mechanism involving the $\{\text{V}^{5+}=\text{O}\}^{3+}/\{\text{V}^{4+}=\text{O}\}^{2+}$ redox couple at the high voltage region. By opening the electrochemical window to 1.5 - 4.3 V, the $\text{Fe}^{3+}/\text{Fe}^{2+}$ redox couple can thus be activated, which leads to an increase of the reversible capacity of ca. 50% at $C/10$ (**Figure 4.18d**). Furthermore, it can recover its initial capacity delivered at $C/10$ after a series of electrochemical cycling at higher rates (**Figure 4.18d**).

IV.3.4. *Operando* structural characterization

Operando X-ray diffraction patterns recorded upon charging of an electrochemical $\text{Na}/\text{Na}_3(\text{VO})\text{Fe}(\text{PO}_4)_2\text{F}_2$ half-cell in the potential range of 2.5 - 4.3 V show a continuous evolution of the diffraction lines during the operation (**Figure 4.21**), which confirms the existence of a solid solution mechanism, as suggested by the S slope of the voltage profile (**Figure 4.18a**). As expected for a solid solution mechanism, the description of the structure in the tetragonal unit cell ($P4_2/mnm$ S.G.) remains valid all along the Na^+ deintercalation. The Le Bail fit of $\text{Na}_{2.54}(\text{VO})\text{Fe}(\text{PO}_4)_2\text{F}_2$ in the $P4_2/mnm$ space group, recorded at pattern #25, is given in **Figure 4.22**. The cell parameters of $\text{Na}_{3-x}(\text{VO})\text{Fe}(\text{PO}_4)_2\text{F}_2$ evolve slowly during the first five scans, which could be due to a delay in the reaction at the beginning of charge; nevertheless, a linear evolution is observed from the sixth scan until the end of charge (**Figure 4.23**).

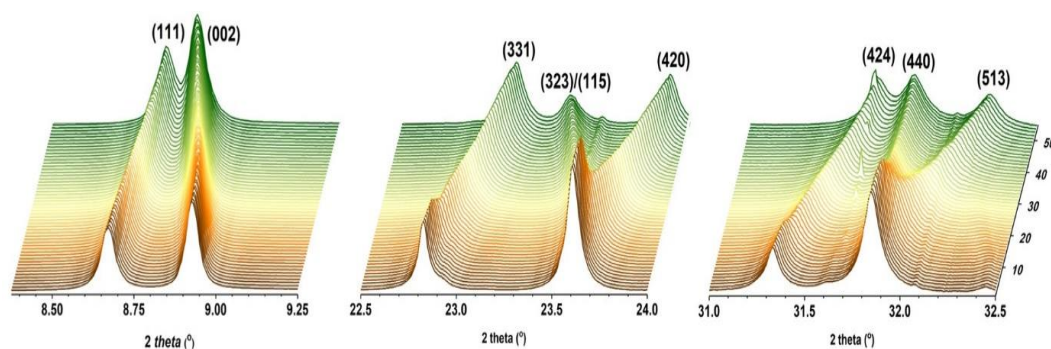


Figure 4.21 : The evolution of significant diffraction lines during Na^+ deintercalation from $\text{Na}_3(\text{VO})\text{Fe}(\text{PO}_4)_2\text{F}_2$. In situ XRD patterns were recorded upon cycling of a $\text{Na}/\text{Na}_3(\text{VO})\text{Fe}(\text{PO}_4)_2\text{F}_2$ half-cell at $\lambda = 0.8251 \text{ \AA}$.

The cell volume decreases with a contraction of the structure along a and b directions and an expansion along the c direction during charge (**Figure 4.23**). As expected, the oxidation of V^{4+} into V^{5+} with a smaller ionic radius leads to the decrease of a and b , whereas the Na^+ deintercalation decreases the screening effect between the terminal groups of two bioctahedral units pointing directly towards each other “through” the channel (**Figure 1.11a**) and thus results in an increase of the c parameter as a compensation effect. This anisotropic contraction/expansion of the unit cell during the Na^+ deintercalation reaction was also observed in $\text{Na}_3\text{V}_2(\text{PO}_4)_2\text{F}_3$, $\text{Na}_3(\text{VO})_2(\text{PO}_4)_2\text{F}$ as well as many NASICON materials [102,104,117,132,146].

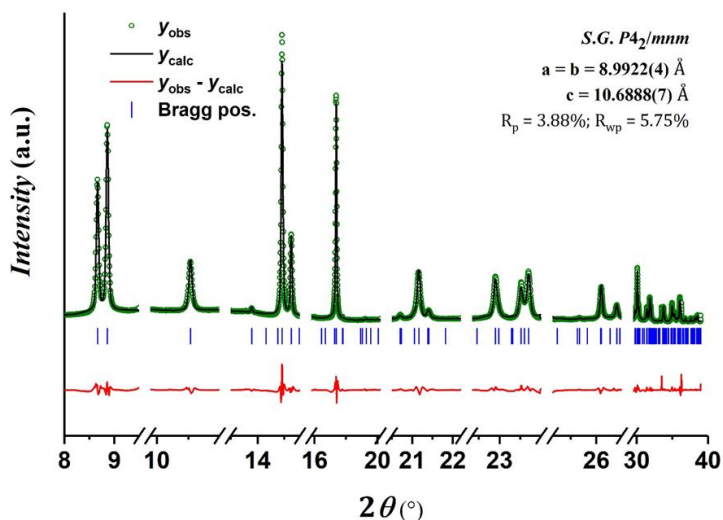


Figure 4.22 : Profile matching of $\text{Na}_{2.5}(\text{VO})\text{Fe}(\text{PO}_4)_2\text{F}_2$ recorded at pattern #25 on a $\text{Na} // \text{Na}_3(\text{VO})\text{Fe}(\text{PO}_4)_2\text{F}_2$ half-cell at $\lambda = 0.8251 \text{ \AA}$. The regions with the diffraction lines of Na metal, Be window, and Al current collector were excluded from the profile matching.

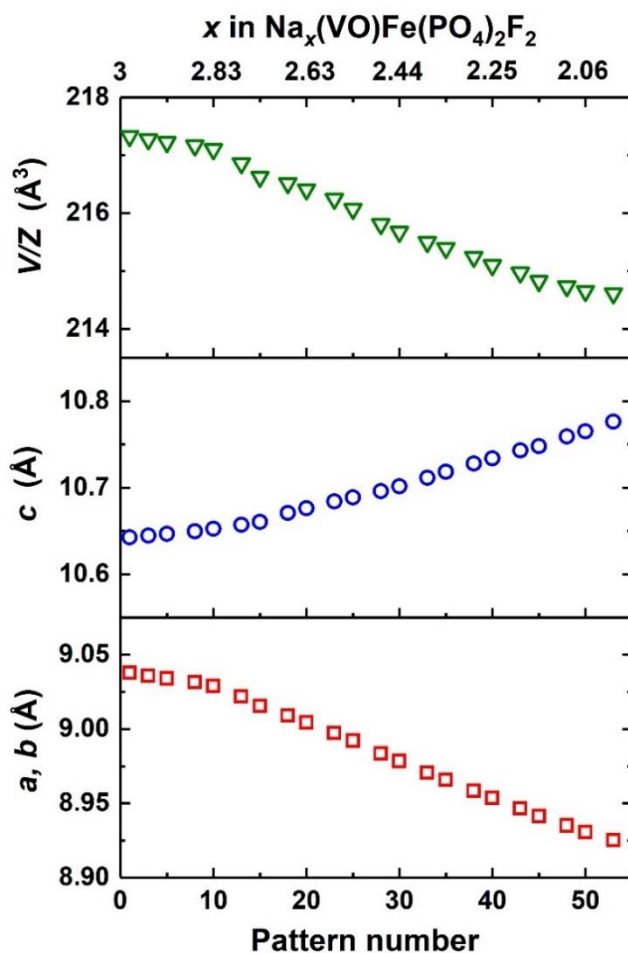


Figure 4.23 : The evolution of the cell parameters of $\text{Na}_3(\text{VO})\text{Fe}(\text{PO}_4)_2\text{F}_2$ during the Na^+ deintercalation reaction, determined from the Rietveld refinement of the SXRD patterns collected *operando* upon cycling of a cell $\text{Na} // \text{Na}_3(\text{VO})\text{Fe}(\text{PO}_4)_2\text{F}_2$.

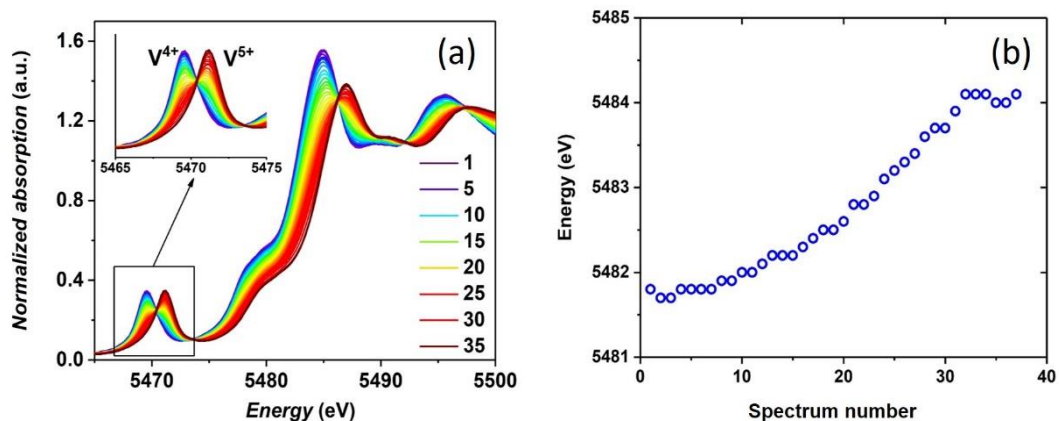


Figure 4.24 : *Operando* V K-edge XANES spectra recorded *operando* upon cycling of a $\text{Na}/\text{Na}_3(\text{VO})\text{Fe}(\text{PO}_4)_2\text{F}_2$ half-cell operating in the potential range of 2.5 - 4.5 V vs. Na^+/Na , and (b) The evolution of the energy of the absorption edge (taken at the normalized intensity = 0.8) of the Vanadium K-edge XANES spectra recorded *operando* a $\text{Na}/\text{Na}_3(\text{VO})\text{Fe}(\text{PO}_4)_2\text{F}_2$ half-cell.

Operando XAS spectra at vanadium K-edge were collected upon charging a $\text{Na}/\text{Na}_3(\text{VO})\text{Fe}(\text{PO}_4)_2\text{F}_2$ half-cell in the voltage range of 2.5 - 4.5 V at $C/10$ (**Figure 4.24a**); note that *operando* XAS experiment at Fe K-edge were not performed as ^{57}Fe Mössbauer measurements performed *ex situ* had already demonstrated that Fe^{3+} did not participate in the electrochemical reaction in the high voltage region. A linear evolution of the vanadium absorption edge is observed between 2.5 and 4.3 V (**Figure 4.24b**).

Above 4.3 V, no change in the shape or the absorption edge energy is observed. The edge energy in the initial state (5481.8 eV, taken at 80% of the maximum intensity of the edge) corresponds to the presence of V^{4+} while at the end of the charge only V^{5+} is detected (5484.1 eV) (**Figure 4.25**) supporting the speculation on the participation of the $\{\text{V}^{5+}=\text{O}\}^{3+}/\{\text{V}^{4+}=\text{O}\}^{2+}$ redox couple in this potential range.

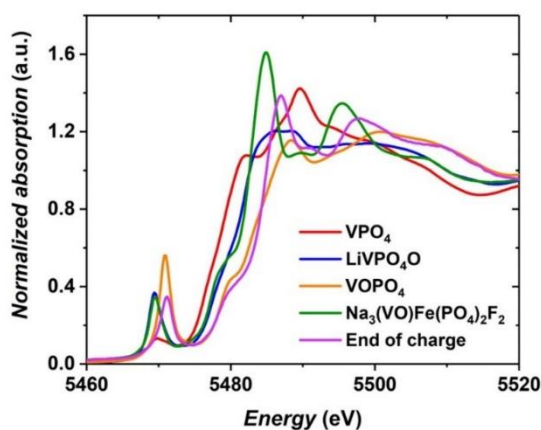


Figure 4.25 : Vanadium K-edge XANES spectra recorded on a $\text{Na}/\text{Na}_3(\text{VO})\text{Fe}(\text{PO}_4)_2\text{F}_2$ half-cell at the initial state and at the end of charge. The spectra of V^{3+}PO_4 , $\text{LiV}^{4+}\text{PO}_4\text{O}$ and $\text{V}^{5+}\text{OPO}_4$ were used as external references to determine the oxidation state of Vanadium.

The *operando* V K-edge XAS data set was globally analyzed using a chemometric approach, based on a combination of PCA and MCR-ALS methods [174]. The PCA results show that there are two components required to describe the whole system and the concentration profile of these two components is given in **Figure 4.26**. There is a delay in the electrochemical reaction as the vanadium oxidation state only started to change from the spectrum #5, and the electrochemical reaction involving the $\{\text{V}^{5+}=\text{O}\}^{3+}/\{\text{V}^{4+}=\text{O}\}^{2+}$ redox couple finished at spectrum #33, which corresponds to a voltage value of ~ 4.3 V vs. Na^+/Na . The reconstructed XAS spectra of these two components are identical to the spectrum #1 and spectrum #33 recorded experimentally.

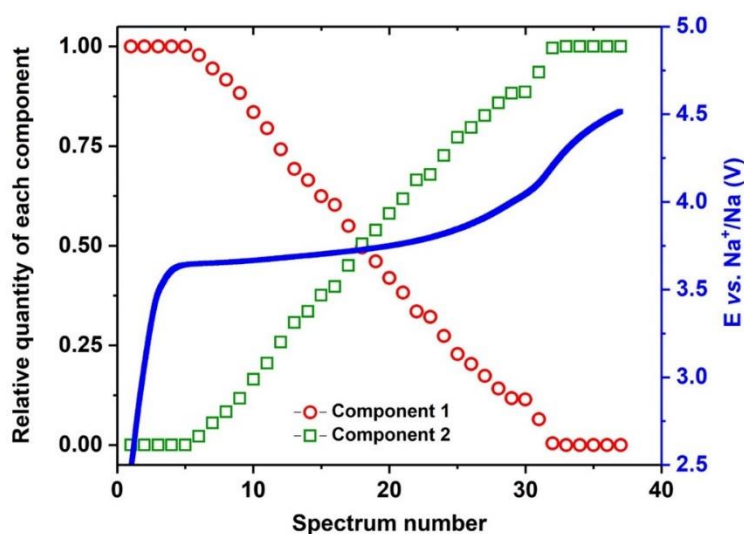


Figure 4.26 : The evolution of the concentration of the two principal components required to describe all the Vanadium K-edge XANES spectra recorded upon cycling of a $\text{Na}/\text{Na}_3(\text{VO})\text{Fe}(\text{PO}_4)_2\text{F}_2$ half-cell during charge.

The V local environments of the two principal components were obtained by analyzing the EXAFS oscillations of the reconstructed spectra. The local structure of the first component is identical to those of the pristine $\text{Na}_3(\text{VO})\text{Fe}(\text{PO}_4)_2\text{F}_2$ reported above, which is a highly distorted $\text{V}(\text{O}/\text{F})_6$ octahedral site due to the presence of a vanadyl bond. At the end of charge, $\text{V}^{4+}=\text{O}$ is fully oxidized into $\text{V}^{5+}=\text{O}$ and its local environment is even more distorted with a contraction of the bond lengths in the equatorial plane: two of the four equatorial V–O bonds are rather short (1.86 \AA) while the other two are at located at a distance of 1.98 \AA . The vanadyl bond ($d_{\text{V}=\text{O}} = 1.62 \text{ \AA}$) and the V–F bond ($d_{\text{V-F(axial)}} = 2.10 \text{ \AA}$) along the *c* axis are unlikely to be affected by the oxidation of V^{4+} to V^{5+} . The EXAFS analysis cannot distinguish whether the two contracted equatorial V–O bonds are in the *cis*- or in the *trans*-configuration; however, we here propose that the two short V–

O bonds would rather be formed on the *trans*-positions, which allows to minimize the electrostatic repulsion between the two oxygen atoms that are approaching the V^{5+} center as a result of the bond length contraction.

The substitution of Fe^{3+} into the structure of $\text{Na}_3(\text{VO})_2(\text{PO}_4)_2\text{F}$ was achieved through a solvent assisted synthesis approach; however, in this study only the $\text{Na}_3(\text{VO})\text{Fe}(\text{PO}_4)_2\text{F}_2$ composition was successfully obtained. In this newly obtained phase, V^{4+} and Fe^{3+} ions share the same Wyckoff position, and they are randomly distributed over all the lattice positions. This random $\text{V}^{4+}/\text{Fe}^{3+}$ distribution could be the origin of the absence of the Na^+ -vacancy ordering upon cycling, which might help to improve the Na^+ diffusivity during the sodiation and desodiation processes. Both $\{\text{V}^{5+}=\text{O}\}^{3+}/\{\text{V}^{4+}=\text{O}\}^{2+}$ and $\text{Fe}^{3+}/\text{Fe}^{2+}$ redox couples can be activated in $\text{Na}_3(\text{VO})\text{Fe}(\text{PO}_4)_2\text{F}_2$. Nonetheless, the reduction of Fe^{3+} into Fe^{2+} occurs at very low voltage together with a great polarization value that it cannot be used in any practical applications. One Na^+ can be electrochemically extracted in the high-voltage region due to the activation of the $\{\text{V}^{5+}=\text{O}\}^{3+}/\{\text{V}^{4+}=\text{O}\}^{2+}$ redox couple and the desodiation process occurs through a solid-solution mechanism with very low polarization.

IV.4. Al-substitution in $\text{Na}_3\text{V}_2(\text{PO}_4)_2\text{F}_3 - \text{Na}_3(\text{VO})_2(\text{PO}_4)_2\text{F}$

Bianchini and co-workers have recently reported the existence of a $\text{Na}_3\text{V}^{3+}_{2-z}\text{Al}_z(\text{PO}_4)_2\text{F}_3$ ($0 \leq z \leq 0.3$) solid solution [127]. These compositions can be obtained by a direct solid-state synthesis starting from a stoichiometric mixture of VPO_4 , AlPO_4 and NaF . Nonetheless, the authors in this work did not mention what had been obtained when the Al^{3+} content exceeded 0.3. In an independent work made by our group, we discovered that when the Al^{3+} content exceeded 0.3, the obtained products were a mixture of NASICON ($\text{Na}_3\text{V}^{3+}_{2-z}\text{Al}_z(\text{PO}_4)_3$) and $\text{Na}_3\text{V}^{3+}_{2-z}\text{Al}_z(\text{PO}_4)_2\text{F}_3$ phases; hence, by solid-state synthesis, the solubility of Al^{3+} in $\text{Na}_3\text{V}^{3+}_2(\text{PO}_4)_2\text{F}_3$ seemed to be limited to 0.3. All the as-obtained $\text{Na}_3\text{V}^{3+}_{2-z}\text{Al}_z(\text{PO}_4)_2\text{F}_3$ ($0 \leq z \leq 0.3$) materials can be indexed in the *Amam* space group with a subtle orthorhombic distortion in the (*ab*) plane, which is similar to the case of $\text{Na}_3\text{V}_2(\text{PO}_4)_2\text{F}_3$. In terms of electrochemistry, only $(2 - z)$ Na^+ ions in these $\text{Na}_3\text{V}_{2-z}\text{Al}_z(\text{PO}_4)_2\text{F}_3$ ($0 \leq z \leq 0.3$) phases can participate in the reversible electrochemical reaction. The same authors speculated that in these $\text{Na}_3\text{V}_{2-z}\text{Al}_z(\text{PO}_4)_2\text{F}_3$ phases only the $\text{V}^{4+}\text{-F}/\text{V}^{3+}\text{-F}$ redox couple can be electrochemically activated. When the V^{3+} ions in $\text{Na}_3\text{V}_2(\text{PO}_4)_2\text{F}_3$ are partially substituted by Al^{3+} , the number of V^{3+} redox centers and thus the number of Na^+ ions that can be extracted from the materials will decrease [127]. Even though the presence of Al^{3+} is detrimental to the electrochemical properties of $\text{Na}_3\text{V}_{2-z}\text{Al}_z(\text{PO}_4)_2\text{F}_3$ phases, it is still very interesting from the crystallographic point of view to know whether it is possible to increase the solubility of Al^{3+} in $\text{Na}_3\text{V}_2(\text{PO}_4)_2\text{F}_3$ by the use of other synthesis approaches or not.

In this study, we will report (i) the synthesis of $\text{Na}_3\text{V}^{3+}_{1.5}\text{Al}_{0.5}(\text{PO}_4)_2\text{F}_3$ composition, a new member of the $\text{Na}_3\text{V}^{3+}_{2-z}\text{Al}_z(\text{PO}_4)_2\text{F}_3$ family, that can be obtained by “sol-gel synthesis in acidic media” showing that the solid solution can be extended beyond $z = 0.3$, and (ii) the existence of a brand new material family, $\text{Na}_3(\text{V}^{4+}\text{O})_{2-z}\text{Al}_z(\text{PO}_4)_2\text{F}_{1+z}$ ($0 \leq z \leq 2$), that can be obtained by “sol-gel synthesis in basic media” or “solvent assisted synthesis approach”. Furthermore, an in-depth study by a combination of SXRD, ^{23}Na and ^{31}P solid-state NMR spectroscopy, infrared and XAS at Vanadium K-edge will help us to gain insightful information on the differences in the local and long-range crystal structures between the $\text{Na}_3\text{V}^{3+}_{2-z}\text{Al}_z(\text{PO}_4)_2\text{F}_3$ and the $\text{Na}_3(\text{V}^{4+}\text{O})_{2-z}\text{Al}_z(\text{PO}_4)_2\text{F}_{1+z}$ material families. Last but not least, the electrochemical properties of

$\text{Na}_3\text{V}^{3+}_{1.5}\text{Al}_{0.5}(\text{PO}_4)_2\text{F}_3$ will be compared with some representatives of the $\text{Na}_3(\text{V}^{4+}\text{O})_2\text{-Al}_z(\text{PO}_4)_2\text{F}_{1+z}$ compositions in order to gain insightful information on the nature of the redox couple as well as the role of Al^{3+} substituent on the electrochemical properties of each material family.

IV.4.1. Sol-gel synthesis of $\text{Na}_3\text{V}^{3+}_{1.5}\text{Al}_{0.5}(\text{PO}_4)_2\text{F}_3$

IV.4.1.1. Sample preparation

Citric acid monohydrate (Sigma-Aldrich; $\geq 99\%$), NH_4VO_3 (Merck; 99%) and $\text{Al}(\text{NO}_3)_3 \cdot 9\text{H}_2\text{O}$ (Sigma-Aldrich; $\geq 97\%$) with an appropriate molar ratio 2/1.5/0.5 were first dissolved in a Teflon beaker containing about 100 mL of water, then $\text{NH}_4\text{H}_2\text{PO}_4$ (Sigma-Aldrich; $\geq 99.99\%$) and NaF (Sigma-Aldrich; $\geq 99\%$) with 5% in excess, were successively and slowly added to the solution. Once the solution turned green, which corresponded to the reduction of V^{5+} to V^{3+} , it was heated overnight at 80°C under continuous stirring to obtain a beige/dark powder. This powder was finely ground, placed in a golden crucible, and heated at 350°C during 4h under Ar atmosphere to eliminate the volatile species and to decompose the nitrate and ammonium precursors. The as-obtained powder was subjected to a second calcination at 650°C during 10h under continuous Argon flow. Finally, the resulting black powder was washed in water during 4 days to eliminate possible impurities.

IV.4.1.2. Atomic and crystal structures characterization

The obtained powder was black due to the presence of carbon residue from the decomposition of citric acid at high temperature. The powder was soaked in concentrated HCl solution over one night in order to completely dissolve the phase product. The solution was filtered to eliminate the carbon residue and then subjected to ICP-OES analysis. The elemental analysis reveals the Na/V/Al/P ratio of 3/1.5/0.5/2.

The SXRD pattern shows that the obtained phase is pure and all the reflection peaks can be indexed in the *Amam* space group (**Figure 4.27**). In this phase, the orthorhombic splitting of (200)/(020) and (400)/(040) are no longer obvious; however, the (400)/(040) peaks are slightly asymmetric and the *Amam* space group is required to take into account this asymmetry (**Figure 4.27 Inset**).

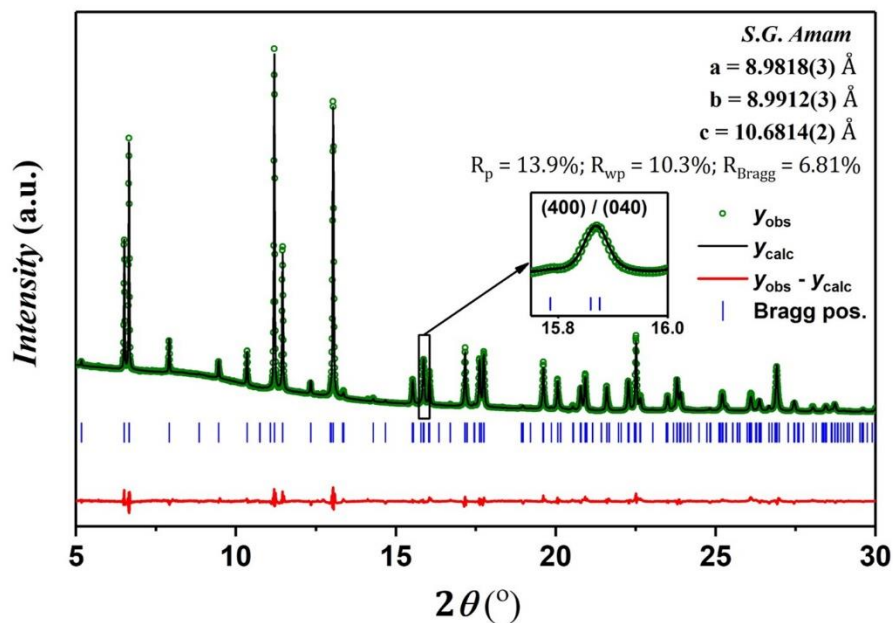


Figure 4.27 : Rietveld refinement performed in the *Amam* space group on the SXRD data recorded on the $\text{Na}_3\text{V}_{1.5}\text{Al}_{0.5}(\text{PO}_4)_2\text{F}_3$ powder ($\lambda = 0.6202 \text{ \AA}$). Inset shows a zoom on the (400)/(040) doublets.

Table 4.11 : Structural parameters of $\text{Na}_3\text{V}_{1.5}\text{Al}_{0.5}(\text{PO}_4)_2\text{F}_3$ obtained from Rietveld refinement of synchrotron powder diffraction data collected at $\lambda = 0.6202 \text{ \AA}$.

| $\text{Na}_3\text{V}_{1.5}\text{Al}_{0.5}(\text{PO}_4)_2\text{F}_3$ | | | | | | |
|------------------------------------------------------------------------------------------|------------------|-----------------|---------------|-----------|---------------|------------------|
| Space group: <i>Amam</i> ; $Z = 4$ | | | | | | |
| $a = 8.9818(3) \text{ \AA}$, $b = 8.9912(3) \text{ \AA}$, $c = 10.6814(2) \text{ \AA}$ | | | | | | |
| $V/Z = 216.7(3) \text{ \AA}^3$ | | | | | | |
| $R_{\text{bragg}} = 6.81\%$, $R_p = 13.9\%$, $R_{\text{wp}} = 10.3\%$ | | | | | | |
| atom | Wyckoff position | Atomic position | | | Occ. | B_{iso} |
| | | x/a | y/b | z/c | | |
| V(1) | 8g | $\frac{1}{4}$ | 0.248(1) | 0.1828(2) | $\frac{3}{4}$ | 0.85(6) |
| Al(1) | 8g | $\frac{1}{4}$ | 0.248(1) | 0.1828(2) | $\frac{1}{4}$ | 0.85(6) |
| P(1) | 8e | 0 | $\frac{1}{2}$ | 0.246(1) | 1 | 1.4(1) |
| O(1) | 16h | 0.090(3) | 0.097(2) | 0.160(2) | 1 | 0.3(1) |
| O(2) | 16h | 0.099(3) | 0.400(3) | 0.167(2) | 1 | 0.5(1) |
| F(1) | 4c | $\frac{1}{4}$ | $\frac{1}{2}$ | 0 | 1 | 0.4(1) |
| F(2) | 8g | $\frac{1}{4}$ | 0.247(1) | 0.363(1) | 1 | 1.2(1) |
| Na(1) | 4c | $\frac{3}{4}$ | 0.480(3) | 0 | 0.91(6) | 1.6(6) |
| Na(2) | 8f | 0.554(2) | 0.188(2) | 0 | 0.82(2) | 5.4(6) |
| Na(3) | 4c | $\frac{3}{4}$ | 0.02(7) | 0 | 0.45(6) | 3.1(5) |

The structural parameters of this newly obtained phase are summarized in **Table 4.11**. The cell parameters are contracted in all directions due to the smaller ionic radius of Al^{3+} as compared to V^{3+} ($R_{\text{Al}^{3+}} = 0.54 \text{ pm}$ vs. $R_{\text{V}^{3+}} = 0.64 \text{ pm}$). The Na^+ ions are distributed on three different Na sites with partial occupancies (**Table 4.11**). In this composition, the $\text{M}-\text{F}_{\text{terminal}}$ bond length has a value of $1.9267(9) \text{ \AA}$, which lies between bond length values of $\text{V}^{3+}-\text{F}_{\text{terminal}}$ ($1.968(6) \text{ \AA}$) in $\text{Na}_3\text{V}_2(\text{PO}_4)_2\text{F}_3$ and $\text{Al}^{3+}-\text{F}_{\text{terminal}}$ ($1.867(3) \text{ \AA}$) in $\text{Na}_3\text{Al}_2(\text{PO}_4)_2\text{F}_3$.

The SEM images show that the powder contains crystallites in different sizes embedded in a carbon matrix. Nonetheless, the sample is inhomogeneous with an irregular distribution of the carbon matrix: some regions in the sample are very porous (**Figure 4.28a** and **b**) while others are denser (**Figure 4.28c** and **d**).

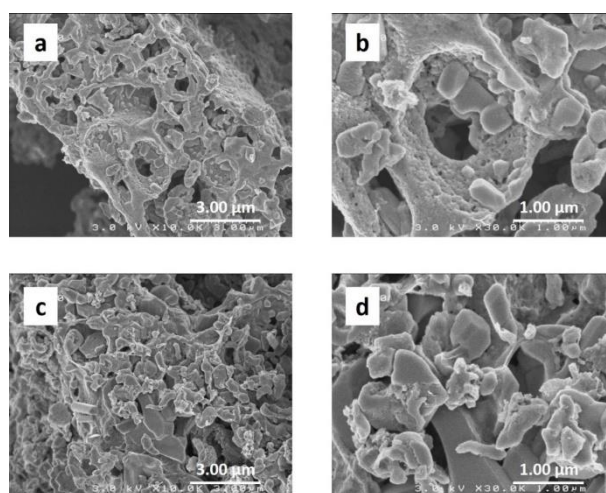


Figure 4.28 : SEM images of $\text{Na}_3\text{V}_{1.5}\text{Al}_{0.5}(\text{PO}_4)_2\text{F}_3$ powder taken at Zone 1 at the magnification of (a) x 10000 and (b) x 30000, and at Zone 2 at the magnification of (c) x 10000 and (d) x 30000.

The IR spectrum recorded on this composition shows an intense and characteristic stretching mode of P–O bonds (in PO_4^{3-}) at $\sim 1100 \text{ cm}^{-1}$ (**Figure 4.29a**). The characteristic stretching mode of the vanadyl group ($\text{V}^{4+}=\text{O}$) at $\sim 920 \text{ cm}^{-1}$ is completely absent in this composition, and thus implying that all vanadium ions are V^{3+} with the terminal $\text{V}^{3+}-\text{F}$ group. The Vanadium K-edge XANES spectrum of this phase was recorded and compared to those of VPO_4 , LiVPO_4O and VOPO_4 references in order to identify the vanadium oxidation state. The edge energy of this composition coincides with that of VPO_4 proving this new obtained phase contains only V^{3+} (**Figure 4.29b**). Furthermore, the low intensity of the pre-edge signal indicates that all vanadium ions reside in a highly

symmetric octahedral site, which is the preferential local environment of V^{3+} . The EXAFS analysis shows that the vanadium ion is coordinated by six equivalent V–F/O bonds with $d_{\text{V-F/O}} = 2.01 \text{ \AA}$ and a Debye-Waller factor of $3.33 \cdot 10^{-3} \text{ \AA}^2$. All the information obtained from ICP-OES, SXRD, IR, and XAS at Vanadium K-edge indicate that this composition contains only V^{3+} , and the exact chemical formula of this phase can thus be written as $\text{Na}_3\text{V}_{1.5}\text{Al}_{0.5}(\text{PO}_4)_2\text{F}_3$, as has been used since the beginning of this section.

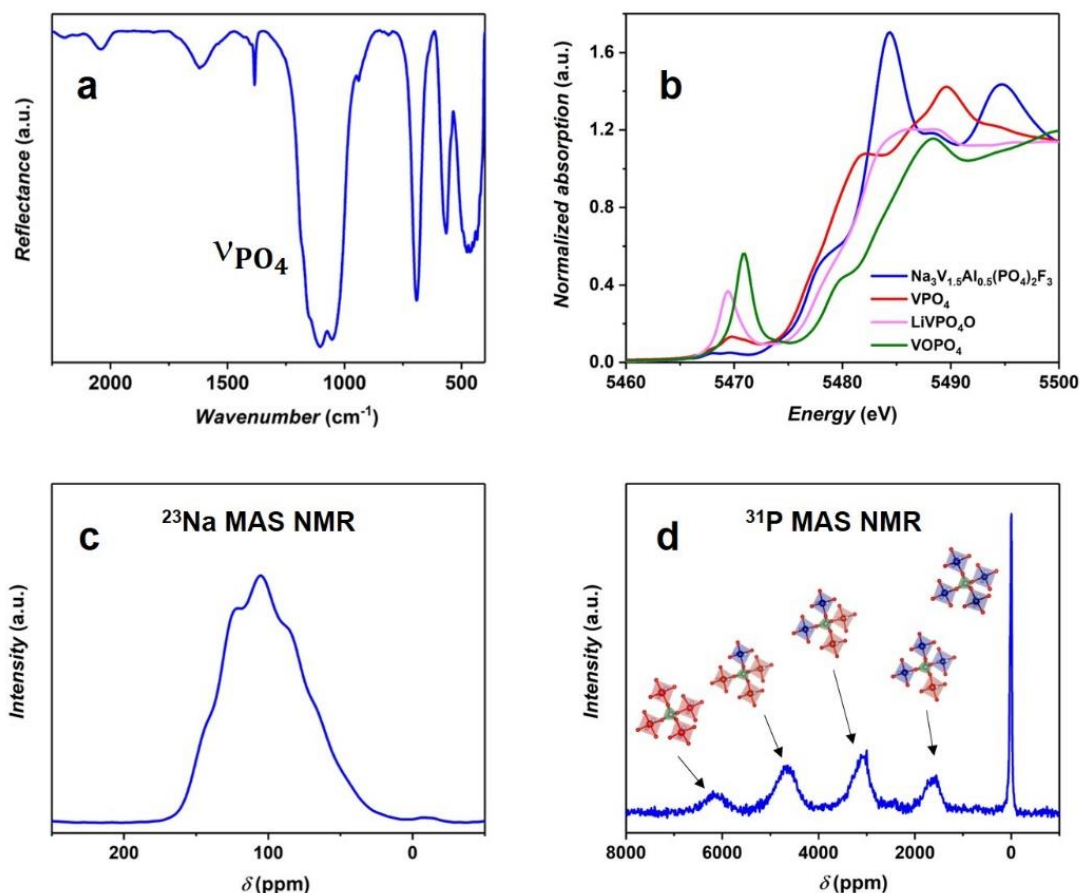


Figure 4.29 : (a) IR spectrum of $\text{Na}_3\text{V}_{1.5}\text{Al}_{0.5}(\text{PO}_4)_2\text{F}_3$ recorded in the wavenumber range of 400 - 2250 cm^{-1} , (b) Vanadium K-edge XANES spectrum of $\text{Na}_3\text{V}_{1.5}\text{Al}_{0.5}(\text{PO}_4)_2\text{F}_3$. V^{3+}PO_4 , $\text{LiV}^{4+}\text{PO}_4\text{O}$ and $\text{V}^{5+}\text{OPO}_4$ are used as references to determine V oxidation state, (c) ^{23}Na ss-NMR spectrum of $\text{Na}_3\text{V}_{1.5}\text{Al}_{0.5}(\text{PO}_4)_2\text{F}_3$ recorded at $B_0 = 11.7\text{T}$; $\nu_R = 30 \text{ kHz}$, (d) ^{31}P ss-NMR spectrum of $\text{Na}_3\text{V}_{1.5}\text{Al}_{0.5}(\text{PO}_4)_2\text{F}_3$ recorded at $B_0 = 2.35\text{T}$; $\nu_R = 30 \text{ kHz}$. The PO_4 tetrahedral units are in green while $\text{V}^{3+}\text{O}_4\text{F}_2$ and $\text{Al}^{3+}\text{O}_4\text{F}_2$ octahedral units are in red and blue, respectively.

The recorded ^{23}Na MAS NMR spectrum shows the presence of a very broad resonance at $\sim 100 \text{ ppm}$ (**Figure 4.29c**), indicating a distribution of several Na local environments. The signal is highly shifted due to the strong Fermi contact between the unpaired electrons of V^{3+} and the Na nuclei.

The ^{31}P MAS NMR spectrum recorded on $\text{Na}_3\text{V}_{1.5}\text{Al}_{0.5}(\text{PO}_4)_2\text{F}_3$ reveals the presence of five different resonances centered at 6000 ppm, 4500 ppm, 3000 ppm, 1500 ppm and 0 ppm (**Figure 4.29d**), and this is explained by the distribution of V^{3+} and Al^{3+} in the first coordination sphere created by M^{3+} with respect to the phosphorus site. As it has been discussed in **Chapter III**, each phosphorus in this structural framework is coordinated by four M^{3+} ions in their proximity. In $\text{Na}_3\text{V}^{3+}_{1.5}\text{Al}_{0.5}(\text{PO}_4)_2\text{F}_3$, V^{3+} and Al^{3+} co-exist, and a random distribution of these ions will lead to the formation of $\text{P}(\text{OV}^{3+})_4$, $\text{P}(\text{OV}^{3+})_3(\text{OAl}^{3+})$, $\text{P}(\text{OV}^{3+})_2(\text{OAl}^{3+})_2$, $\text{P}(\text{OV}^{3+})(\text{OAl}^{3+})_3$, and $\text{P}(\text{OAl}^{3+})_4$ local environments. As Al^{3+} does not possess any unpaired electron, there will be no spin interaction between Al^{3+} and its neighboring phosphorus nuclei, which is also illustrated by the spin distribution map obtained by DFT calculations (**Figure 4.30a**). Furthermore, the ^{31}P MAS NMR spectrum of $\text{Na}_3\text{V}^{3+}_{1.5}\text{Al}_{0.5}(\text{PO}_4)_2\text{F}_3$ is very similar to that of $\text{Na}_3\text{V}^{3+}_{1.6}\text{V}^{4+}_{0.4}(\text{PO}_4)_2\text{F}_{2.6}\text{O}_{0.4}$ (**Figure 4.30b**). This comparison thus reinforces our earlier studies that there is no spin transfer between V^{4+} and its neighboring phosphorus nuclei in $\text{Na}_3\text{V}_2(\text{PO}_4)_2\text{F}_3$ structural framework and each V^{3+} in the proximity of one phosphorus nucleus contributes to a Fermi contact shift of about 1500 ppm thanks to the delocalization mechanism.

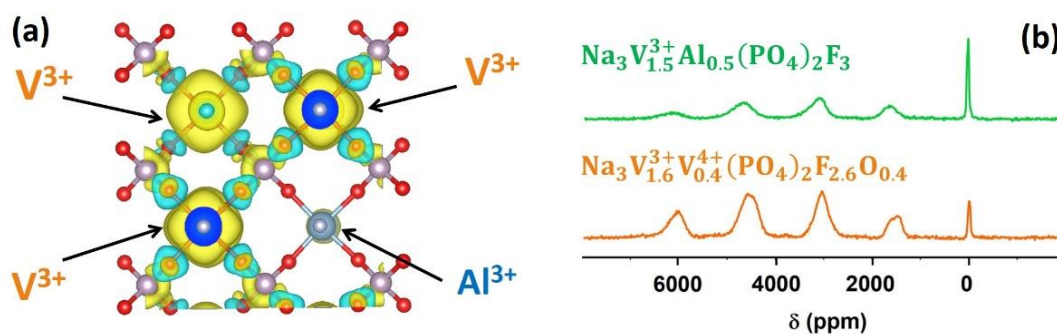


Figure 4.30 : (a) 3D calculated electronic spin map around a phosphorus nucleus when one of its neighboring V^{3+} is substituted by Al^{3+} , (b) ^{31}P MAS NMR spectra of $\text{Na}_3\text{V}_2(\text{PO}_4)_2\text{F}_{2.6}\text{O}_{0.4}$ and $\text{Na}_3\text{V}_{1.5}\text{Al}_{0.5}(\text{PO}_4)_2\text{F}_3$.

By the use of sol-gel method in acidic media, the solubility of Al^{3+} in $\text{Na}_3\text{V}_2(\text{PO}_4)_2\text{F}_3$ was extended up to $\text{Na}_3\text{V}_{1.5}\text{Al}_{0.5}(\text{PO}_4)_2\text{F}_3$, and the atomic and crystal structures of this newly obtained phase were carefully characterized by a combination of SXRD, IR spectroscopy, ^{23}Na and ^{31}P ss-NMR, and XAS at Vanadium K-edge. In this approach, an acidic media (citric acid) was used during the poly-condensation and evaporation steps. The solution however contained NaF , which could easily react with H^+ to generate the volatile HF species. In this acidic media, the loss of fluorine-containing

sources in form of HF depends strongly on the reaction conditions, such as the temperature of the dissolution process, the temperature and the heating rate of the solvent evaporation step, the temperature and the duration of the gel aging process. Besides these factors, the HF loss can also be influenced by the ambient conditions. Several attempts were made to reproduce the synthesis of $\text{Na}_3\text{V}_{1.5}\text{Al}_{0.5}(\text{PO}_4)_2\text{F}_3$ and to explore the Al^{3+} solubility at higher content. The as-obtained products were however a mixture of NASICON phase ($\text{Na}_3\text{V}_{2-z}\text{Al}_z(\text{PO}_4)_3$) with little presence of $\text{Na}_3\text{V}_{2-z}\text{Al}_z(\text{PO}_4)_2\text{F}_3$ composition. This was caused due to an uncontrollable loss of fluorine during the evaporation process. In order to prevent the fluorine loss, a buffer solution containing NH_3 was used to adjust the solution pH to ~ 9.2 . At this pH value, the fluorine exists in the solution in form of F^- and this ion cannot be lost during the evaporation process. Surprisingly, by moving from “sol-gel synthesis in acidic media” to “sol-gel synthesis in basic media”, a brand new material family with the general formula $\text{Na}_3(\text{V}^{4+}\text{O})_{2-z}\text{Al}_z(\text{PO}_4)_2\text{F}_{1+z}$ ($0 \leq z \leq 2$) was obtained. The details of the materials synthesis process as well as the structural and electrochemical characterizations of these phases will be given in the following section.

IV.4.2. The $\text{Na}_3(\text{V}^{4+}\text{O})_{2-z}\text{Al}_z(\text{PO}_4)_2\text{F}_{1+z}$ ($0 \leq z \leq 2$) material family

IV.4.2.1. Samples preparation

As was explained above, the Al^{3+} solubility in $\text{Na}_3\text{V}_2(\text{PO}_4)_2\text{F}_3$ could be extended up to $\text{Na}_3\text{V}^{3+}_{1.5}\text{Al}_{0.5}(\text{PO}_4)_2\text{F}_3$ through a “sol-gel synthesis approach in acidic media”. However, several difficulties were encountered during this approach mainly due to the volatility of fluorine species in acidic media. A modified sol-gel approach was thus developed in order to tackle this difficulty. The synthesis procedure was similar to the one described in **IV.4.1.1**, except that the NH_3 solution (28-30%) was slowly added to the solution in order to adjust its pH value to ~ 9.2 once all the initial reactants had been completely dissolved. Upon the addition of NH_3 , the solution changed into deep blue, the color of VO^{2+} ion, as the basic solution lowered the potential value of the $\text{VO}^{2+}/\text{V}^{3+}$ redox couple in aqueous media and thus V^{3+} ion can now be quickly oxidized by oxygen in air to generate VO^{2+} . The solution was slowly evaporated at 80°C under continuous stirring condition to result in a beige powder. This powder was subjected to a two-step thermal treatment, first at 350°C during 4h and then at 650°C in 10h under flowing Ar atmosphere.

The obtained powder after the calcination was bluish green. This method will be later called as “sol-gel synthesis in basic media”.

In parallel to the “sol-gel synthesis in basic media”, another synthesis approach was inspired by the work of Qi *et al.* [138], in which NaF (Sigma-Aldrich; $\geq 99\%$), $\text{V}(\text{C}_5\text{H}_7\text{O}_2)_3$ (Sigma-Aldrich; $\geq 97\%$), $\text{Al}(\text{NO}_3)_3 \cdot 9\text{H}_2\text{O}$ (Sigma-Aldrich; $\geq 97\%$), and $\text{NH}_4\text{H}_2\text{PO}_4$ (Sigma-Aldrich; $\geq 99.99\%$) were first dissolved in a closed vessel containing a mixture of ethanol and acetone. The initial solution was dark red due to the dark color of $\text{V}(\text{C}_5\text{H}_7\text{O}_2)_3$. After a few hours under continuous stirring condition, the initial dark red solution turned gradually into dark green and then deep blue color as V^{3+} ions were gradually oxidized into VO^{2+} by oxygen in air. After two days, the cap was opened and the solvent was evaporated at ambient temperature leading to the formation of a grey powder. This powder was placed into a golden crucible and first annealed at 150°C during 3h to remove all the traces of solvent and then at 300°C during 3h in order to decompose all the nitrate and ammonium-containing sources. Afterwards, the resulting powder was finely ground in a mortar, pelletized, and finally calcined at 550°C during 3h under Ar atmosphere. This method will further be called as “solvent assisted approach” in order to distinguish it from the other two methods described above.

IV.4.2.2. Phase identification

A comparison of the XRD patterns of the products obtained from the “sol-gel synthesis in basic media” and from the “solvent assisted synthesis approach” at different V/Al ratio is given in **Figure 4.31**.

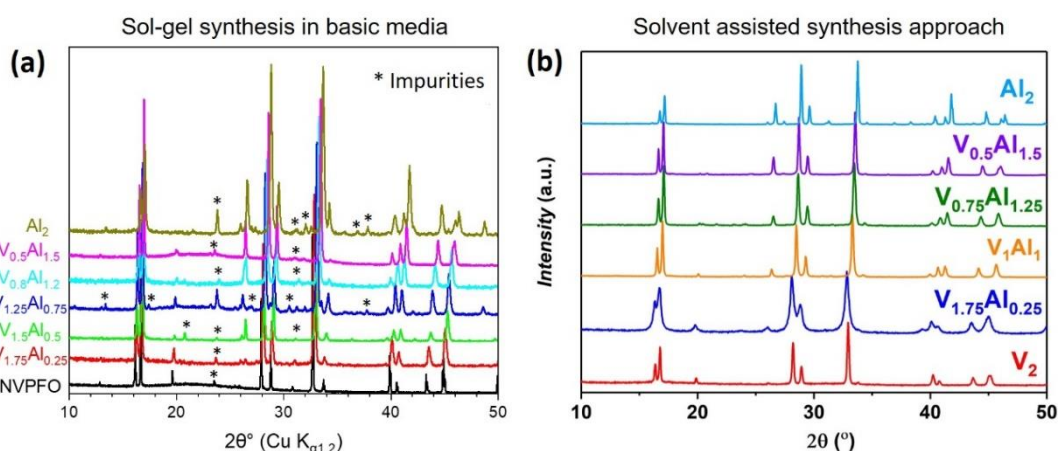


Figure 4.31 : XRD patterns recorded at $\text{Cu K}\alpha$ radiation of the products obtained from (a) sol-gel synthesis method in basic media, and (b) solvent assisted synthesis approach with different V/Al ratio. The NVPFO formula indicates $\text{Na}_3(\text{VO})_2(\text{PO}_4)_2\text{F}$.

The main product obtained from both synthesis approaches has a crystal structure similar to that of the $\text{Na}_3\text{V}_2(\text{PO}_4)_2\text{F}_{3-y}\text{O}_y$ compositions. Except for $\text{Na}_3\text{Al}_2(\text{PO}_4)_2\text{F}_3$, the main diffraction peaks observed can be indexed using a unit cell described in the $P4_2/mnm$ space group and the cell parameters obtained from the Le Bail fit are given in **Figure 4.32**. The crystal structure of $\text{Na}_3\text{Al}_2(\text{PO}_4)_2\text{F}_3$ is described in the $P4_2/mbc$ space group with $a = b = 12.3841(1) \text{ \AA}$ and $c = 10.3949(1) \text{ \AA}$ and this structural system can be transformed into the same setting as in the $P4_2/mnm$ space group through a transformation matrix as it will be explained later. By the use of IR spectroscopy, XAS at Vanadium K-edge and ^{31}P MAS NMR, we will later demonstrate that the main products obtained from both “sol-gel synthesis in basic media” and “solvent assisted synthesis approach” contain only V^{4+} and that the general chemical formula of all the obtained phases will be correctly written as $\text{Na}_3(\text{V}^{4+}\text{O})_{2-z}\text{Al}_z(\text{PO}_4)_2\text{F}_{1+z}$ ($0 \leq z \leq 2$). At this stage of the study, we have not identified the oxidation state of vanadium species, and the general chemical formula is thus simplified as $\text{Na}_3\text{V}_{2-z}\text{Al}_z(\text{PO}_4)_2(\text{F},\text{O})_3$ with $0 \leq z \leq 2$.

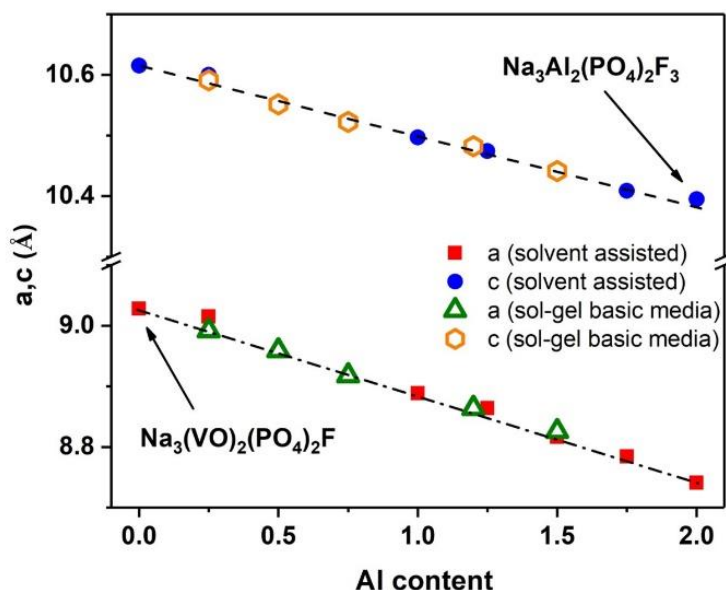


Figure 4.32 : A comparison of the cell parameters of the phases obtained from the “sol-gel synthesis in basic media” and from the “solvent assisted synthesis approach” when the Al content in the $\text{Na}_3\text{V}_{2-z}\text{Al}_z(\text{PO}_4)_2(\text{F},\text{O})_3$ substituted phases was varied from 0 to 2.

A linear evolution of the cell parameters was observed for all the main compositions obtained from “sol-gel synthesis in basic media” and “solvent assisted synthesis approach” (**Figure 4.32**). At some common compositions, such as $\text{Na}_3\text{V}_{1.75}\text{Al}_{0.25}(\text{PO}_4)_2(\text{F},\text{O})_3$ and $\text{Na}_3\text{V}_{0.5}\text{Al}_{1.5}(\text{PO}_4)_2(\text{F},\text{O})_3$, the cell parameters of the

phases are identical (**Figure 4.32**). Despite the difference in the nature of the synthesis approaches, the “sol-gel synthesis in basic media” and “solvent assisted synthesis approach” both lead to the formation of the same materials family, $\text{Na}_3\text{V}_{2-z}\text{Al}_z(\text{PO}_4)_2(\text{F},\text{O})_3$ with ($0 \leq z \leq 2$). However, each of these mentioned methods has its own limitations: In “sol-gel synthesis in basic media”, a continuous solid solution was observed for all the values of $0 \leq z \leq 2$, but all the phases were contaminated by impurities (**Figure 4.32a**). Except for $\text{Na}_3(\text{VO})_{1.5}\text{Al}_{0.5}(\text{PO}_4)_2\text{F}_{1.5}$ and $\text{Na}_3(\text{VO})_{0.5}\text{Al}_{1.5}(\text{PO}_4)_2\text{F}_{2.5}$ in which the main impurity is AlPO_4 , the rest of the samples contain several impurities whom we were not able to identify. The presence of these unknown impurities did not cause much trouble in XRD as the regions containing the impurities’ diffraction peaks can be excluded in the data analysis process, but it can disturb the signal of the main phase in the local-probing technique, such as XAS and *ss*-NMR. On the other hand, pure and well crystallized phases can be obtained by “solvent assisted synthesis approach” for the compositions with $z \geq 1$ (**Figure 4.32b**). When $z < 1$, the obtained product was not well crystallized as indicated by a broadening of all the diffraction peaks (*e.g.* $\text{Na}_3\text{V}_{1.75}\text{Al}_{0.25}(\text{PO}_4)_2(\text{F},\text{O})_3$). A higher calcination temperature (650°C) was applied on this composition in order to increase the crystallinity of the sample; unfortunately, it decomposed at this temperature to give a mixture of NASICON-structured and $\text{Na}_3(\text{VO})_2(\text{PO}_4)_2\text{F}$ -structured phases.

In order to obtain a precise description on the atomic local environment as well as the crystal structure and electrochemical properties of the phase of interest, only well crystallized compositions with the least presence of impurities will be subjected to further in-depth characterizations with SXRD, IR spectroscopy, XAS at Vanadium K-edge, *ss*-NMR and electrochemistry test, these include $\text{Na}_3\text{V}_{0.5}\text{Al}_{1.5}(\text{PO}_4)_2(\text{F},\text{O})_3$ from “sol-gel synthesis in basic media” and the $\text{Na}_3(\text{VO})_{2-z}\text{Al}_z(\text{PO}_4)_2\text{F}_{1+z}$ ($1 \leq z \leq 2$) series obtained from “solvent assisted synthesis approach”. Even though $\text{Na}_3\text{V}_{0.5}\text{Al}_{1.5}(\text{PO}_4)_2(\text{F},\text{O})_3$ was not obtained by the same synthesis approach as other samples, we have demonstrated that both “sol-gel synthesis in basic media” and “solvent assisted synthesis approach” led to the formation of the same material family, and thus all the structural and electrochemical information obtained from $\text{Na}_3\text{V}_{0.5}\text{Al}_{1.5}(\text{PO}_4)_2(\text{F},\text{O})_3$ can be extrapolated to its counterpart as if it had been obtained by the “solvent assisted synthesis approach” and vice versa.

IV.4.2.3. Structural characterization using high resolution SXRD

As it was spotted in section IV.4.2.2., except for the two ending members $\text{Na}_3(\text{VO})_2(\text{PO}_4)_2\text{F}$ and $\text{Na}_3\text{Al}_2(\text{PO}_4)_2\text{F}_3$, the laboratory XRD patterns of all the $\text{Na}_3\text{V}_{2-z}\text{Al}_z(\text{PO}_4)_2(\text{F},\text{O})_3$ ($0 < z < 2$) compositions can be indexed in the $P4_2/mnm$ space group with a linear evolution of the cell parameters. However, as it was shown in **Chapter II**, $\text{Na}_3\text{V}_2(\text{PO}_4)_2\text{F}_3$ - and $\text{Na}_3(\text{VO})_2(\text{PO}_4)_2\text{F}$ -related structures show a subtle orthorhombic distortion due to the triangular distribution of Na^+ ions in the (*ab*) plane and this distortion can only be detected by the use of high resolution SXRD since the *b/a* ratio is usually less than 1.002. Therefore, an investigation of the structure of $\text{Na}_3(\text{VO})_{2-z}\text{Al}_z(\text{PO}_4)_2\text{F}_{1+z}$ ($0 < z \leq 2$) by the use of SXRD is highly important as it will help us to examine (i) whether the subtle orthorhombic distortion exists in these compositions or not, and (ii) whether there would be a long-range charge ordering due to the co-existence of V^{4+} and Al^{3+} groups in a same phase or nor.

So far the simplified chemical formula $\text{Na}_3(\text{VO})_{2-z}\text{Al}_z(\text{PO}_4)_2\text{F}_{1+z}$ ($0 \leq z \leq 2$) was widely used. As it was mentioned above, we will later prove that the actual chemical formula of all the materials obtained by “sol-gel synthesis in basic media” and “solvent assisted synthesis approach” is $\text{Na}_3(\text{VO})_{2-z}\text{Al}_z(\text{PO}_4)_2\text{F}_{1+z}$ ($0 \leq z \leq 2$). In this part, whenever a Rietveld refinement is performed, the actual chemical formula of the corresponding material will also be given so as to provide a full description on the chemical formula and the crystal structure of the phase.

IV.4.2.3.1. $\text{Na}_3(\text{VO})_{2-z}\text{Al}_z(\text{PO}_4)_2\text{F}_{1+z}$ ($0 < z < 2$)

A detailed analysis of SXRD data show that all the $\text{Na}_3(\text{VO})_{2-z}\text{Al}_z(\text{PO}_4)_2\text{F}_{1+z}$ phases in the compositional range of $0 < z < 2$ adopt the same crystal structure and space group. An in-depth structural characterization by SXRD will be demonstrated for $\text{Na}_3(\text{VO})_{1.5}\text{Al}_{0.5}(\text{PO}_4)_2\text{F}_{1.5}$ as an example, but the same analysis strategy and results can be extrapolated for other compositions.

Figure 4.33 shows the Rietveld refinement performed on $\text{Na}_3(\text{VO})_{1.5}\text{Al}_{0.5}(\text{PO}_4)_2\text{F}_{1.5}$ in the $P4_2/mnm$ space group with a zoom on the (200)/(020) and (400)/(040) diffraction peaks (**Figure 4.33 Inset**). The splitting of the (200)/(020) or (400)/(040) doublets is unobservable and the (200)/(020) and (400)/(040) diffraction peaks can be fit with a pseudo-Voigt function, and thus exclude the possible presence of

the subtle orthorhombic distortion. The Na^+ ions are distributed over two different crystallographic sites: Na1 fully occupied and Na2 half occupied as in **Figure 3.4a**. The structural parameters of $\text{Na}_3(\text{VO})_{1.5}\text{Al}_{0.5}(\text{PO}_4)_2\text{F}_{1.5}$ are summarized in **Table 4.12**.

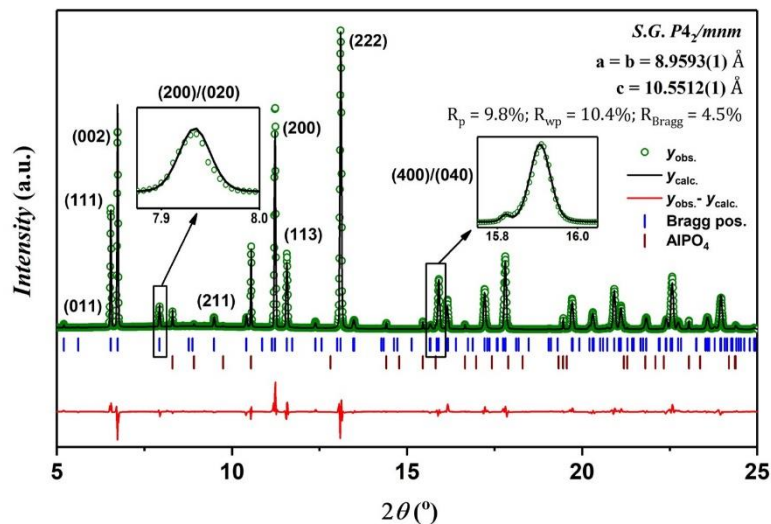


Figure 4.33 : Rietveld refinement performed in the $P4_2/mnm$ space group on the SXRD data recorded on the $\text{Na}_3(\text{VO})_{1.5}\text{Al}_{0.5}(\text{PO}_4)_2\text{F}_{1.5}$ powder ($\lambda = 0.6202 \text{ \AA}$).

Table 4.12 : Structural parameters of $\text{Na}_3(\text{VO})_{1.5}\text{Al}_{0.5}(\text{PO}_4)_2\text{F}_{1.5}$ obtained from Rietveld refinement of synchrotron powder diffraction data collected at $\lambda = 0.6202 \text{ \AA}$.

| $\text{Na}_3(\text{VO})_{1.5}\text{Al}_{0.5}(\text{PO}_4)_2\text{F}_{1.5}$ | | | | | | |
|----------------------------------------------------------------------------|------------------|-----------------|---------------|---------------|---------------|------------------|
| Space group: $P4_2/mnm$; $Z = 4$ | | | | | | |
| $a = b = 8.9593(1) \text{ \AA}$, $c = 10.5512(1) \text{ \AA}$ | | | | | | |
| $V/Z = 211.7(1) \text{ \AA}^3$ | | | | | | |
| $R_{\text{bragg}} = 4.5\%$, $R_p = 9.8\%$, $R_{\text{wp}} = 10.4\%$ | | | | | | |
| atom | Wyckoff position | Atomic position | | | Occ. | B_{iso} |
| | | x/a | y/b | z/c | | |
| V(1) | 8j | 0.2495(3) | 0.2495(3) | 0.1964(1) | $\frac{3}{4}$ | 0.85(6) |
| Al(1) | 8j | 0.2495(3) | 0.2495(3) | 0.1964(1) | $\frac{1}{4}$ | 0.85(6) |
| P(1) | 4d | 0 | $\frac{1}{2}$ | $\frac{1}{4}$ | 1 | 0.8(2) |
| P(2) | 4e | 0 | 0 | 0.2566(5) | 1 | 0.8(2) |
| O(1) | 16k | 0.0957(4) | 0.4056(5) | 0.1617(4) | 1 | 0.9(2) |
| O(2) | 8j | 0.0965(5) | 0.0965(5) | 0.1677(8) | 1 | 0.9(2) |
| O(3) | 8j | 0.4012(5) | 0.4012(5) | 0.1597(8) | 1 | 0.9(2) |
| F(1) | 4f | 0.2468(6) | 0.2468(6) | 0 | 1 | 0.85(7) |
| F(2)/O(4) | 8j | 0.2481(6) | 0.2481(6) | 0.3531(1) | 1 | 0.51(5) |
| Na(1) | 8i | 0.5174(5) | 0.2395(6) | 0 | 1 | 2.0(1) |
| Na(2) | 8i | 0.8013(6) | 0.0372(9) | 0 | $\frac{1}{2}$ | 3.9(3) |

We also performed the Rietveld refinement of the structure of $\text{Na}_3(\text{VO})_{1.5}\text{Al}_{0.5}(\text{PO}_4)_2\text{F}_{1.5}$ in the *Amam* space group, but it did not lead to any improvement in the quality of the fit and thus the structure of $\text{Na}_3(\text{VO})_{1.5}\text{Al}_{0.5}(\text{PO}_4)_2\text{F}_{1.5}$ is retained in the $P4_2/mnm$ space group. We also carefully examined the positions of all the diffraction peaks, but we did not detect any extra reflections due to the existence of a supercell or due to the ordering of $\text{V}^{4+}=\text{O}$ and $\text{Al}^{3+}-\text{F}$.

The structure of other $\text{Na}_3(\text{VO})_{2-z}\text{Al}_z(\text{PO}_4)_2\text{F}_{1+z}$ ($0 < z < 2$) compounds can also be indexed in the $P4_2/mnm$ space group and their atomic positions are similar to those reported in **Table 4.12**, except the relative occupancy of $\text{V}^{4+}/\text{Al}^{3+}$ site.

Table 4.13 : Cell parameters of $\text{Na}_3(\text{VO})_{2-z}\text{Al}_z(\text{PO}_4)_2\text{F}_{1+z}$ ($0.5 \leq z \leq 1.75$) compositions obtained from Rietveld refinement in the $P4_2/mnm$ space group.

| <i>z</i> value | Composition | Space group | <i>a</i> = <i>b</i> (Å) | <i>c</i> (Å) | <i>V</i> / <i>Z</i> (Å ³) |
|----------------|-------------------------------------------------------------------------------|---------------------------|-------------------------|--------------|---------------------------------------|
| 0.5 | $\text{Na}_3(\text{VO})_{1.5}\text{Al}_{0.5}(\text{PO}_4)_2\text{F}_{1.5}$ | <i>P4₂/mnm</i> | 8.9593(1) | 10.5512(1) | 211.7(1) |
| 1.0 | $\text{Na}_3(\text{VO})\text{Al}(\text{PO}_4)_2\text{F}_2$ | <i>P4₂/mnm</i> | 8.8889(2) | 10.4966(4) | 207.33(4) |
| 1.25 | $\text{Na}_3(\text{VO})_{0.75}\text{Al}_{1.25}(\text{PO}_4)_2\text{F}_{2.25}$ | <i>P4₂/mnm</i> | 8.8643(2) | 10.4740(5) | 205.75(5) |
| 1.50 | $\text{Na}_3(\text{VO})_{0.5}\text{Al}_{1.5}(\text{PO}_4)_2\text{F}_{2.5}$ | <i>P4₂/mnm</i> | 8.8170(2) | 10.4395(5) | 202.89(4) |
| 1.75 | $\text{Na}_3(\text{VO})_{0.25}\text{Al}_{1.75}(\text{PO}_4)_2\text{F}_{2.75}$ | <i>P4₂/mnm</i> | 8.7845(2) | 10.4087(2) | 200.80(5) |

The cell parameters of the $\text{Na}_3(\text{VO})_{2-z}\text{Al}_z(\text{PO}_4)_2\text{F}_{1+z}$ ($z = 0.5, 1.0, 1.25, 1.50$ and 1.75) phases obtained from Rietveld refinement are given in **Table 4.13**. A continuous shrinkage in the cell parameters is detected when V^{4+} is gradually substituted by Al^{3+} (**Figure 4.31**) as Al^{3+} is slightly smaller than V^{4+} ($R_{\text{V}^{4+}} = 0.58 \text{ \AA}$ vs. $R_{\text{Al}^{3+}} = 0.54 \text{ \AA}$) [155].

IV.4.2.3.2 $\text{Na}_3\text{Al}_2(\text{PO}_4)_2\text{F}_3$

We earlier explained that all the diffraction peaks of $\text{Na}_3\text{Al}_2(\text{PO}_4)_2\text{F}_3$ cannot be included in the $P4_2/mnm$ or *Amam* space group, but in $P4_2/mbc$. This indexation was based on an earlier study reported by Le Meins *et al.* [82]. At a temperature greater than 43°C , $\text{Na}_3\text{Al}_2(\text{PO}_4)_2\text{F}_3$ crystallizes in a tetragonal system with the *I4/mmm* space group ($\alpha\text{-Na}_3\text{Al}_2(\text{PO}_4)_2\text{F}_3$) and all the Na^+ ions are distributed on two different crystallographic sites. Upon cooling down below 43°C , the $\alpha \rightarrow \beta_1$ phase transition is observed which is

due to the redistribution of Na^+ ions, with eight different crystallographic Na sites in the β_1 phase [82].

In our study, all the main diffraction peaks can be indexed in the $P4_2/mbc$ space group ($\beta_1\text{-Na}_3\text{Al}_2(\text{PO}_4)_2\text{F}_3$) as proposed by Le Meins *et al.*; nevertheless, there are several peaks with lower intensity that cannot be included in this structural indexation, which could be due to a long-range Na^+ ordering that can only be detected by SXRD. Surprisingly, when moving to Rietveld refinement, the use of the $\beta_1\text{-Na}_3\text{Al}_2(\text{PO}_4)_2\text{F}_3$ structural model proposed by Le Meins *et al.* did not result in a satisfying fit, notably the Na^+ ions in the diffusion channels were not well localized. We thus relocated all the Na^+ positions in the structure by calculating Fourier difference maps with a retention of the structural framework in the $P4_2/mbc$ space group, the charge residues observed on the Fourier difference maps will indicate the Na^+ positions. Even with the use of SXRD data, the localization of Na^+ is still very complicated as (i) the unit cell of $\text{Na}_3\text{Al}_2(\text{PO}_4)_2\text{F}_3$ is too big ($a = b = 12.3841(1) \text{ \AA}$ and $c = 10.3949(1) \text{ \AA}$), and (ii) there are so many Na sites in this structure. We thus propose a new crystal structure for $\text{Na}_3\text{Al}_2(\text{PO}_4)_2\text{F}_3$ indexed in the $P4_2/mbc$ space group with the presence of eight Na sites (**Table 4.14**). The proposed structure is just an average one as the long-range Na^+ -vacancy is still unsolved and the intensities of several tiny peaks are not well fit (**Figure 4.34 Inset**).

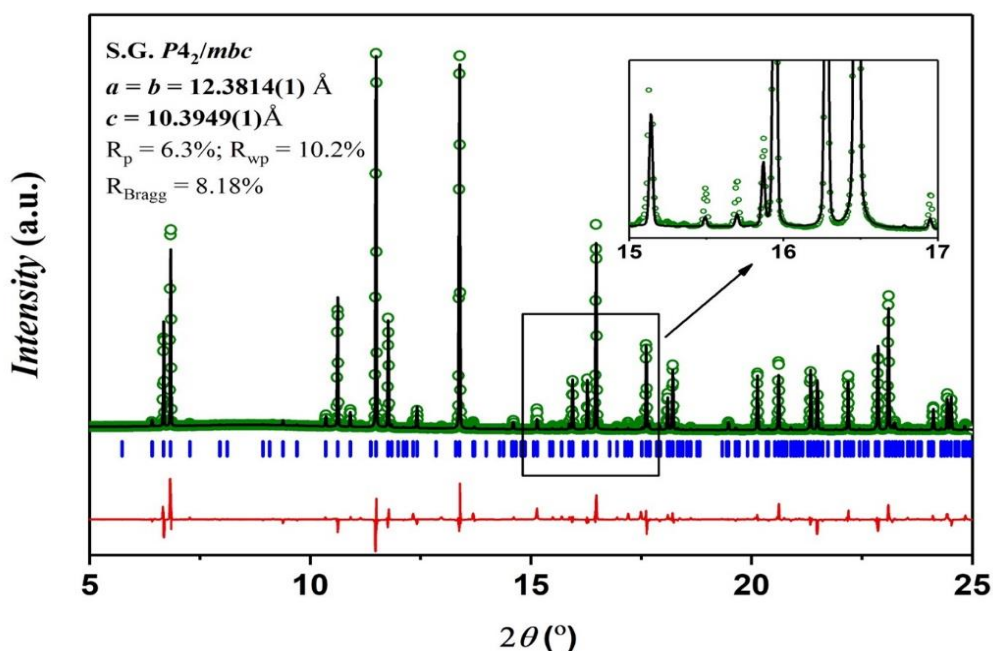


Figure 4.34 : Rietveld refinement results of $\text{Na}_3\text{Al}_2(\text{PO}_4)_2\text{F}_3$ by considering the $P4_2/mbc$ space group. The inset focuses on the diffraction lines between $15^\circ - 17^\circ$.

Table 4.14 : Structural parameters of $\text{Na}_3(\text{VO})_{1.5}\text{Al}_{0.5}(\text{PO}_4)_2\text{F}_{1.5}$ obtained from Rietveld refinement of synchrotron powder diffraction data collected at $\lambda = 0.6202 \text{ \AA}$.

| $\text{Na}_3\text{Al}_2(\text{PO}_4)_2\text{F}_3$ | | | | | | |
|------------------------------------------------------------------------|------------------|-----------------|---------------|---------------|---------|---------------------|
| Space group: $P4_2/mbc$; $Z = 8$ | | | | | | |
| $a = b = 12.3814(1) \text{ \AA}$, $c = 10.3949(1) \text{ \AA}$ | | | | | | |
| $V/Z = 199.2(1) \text{ \AA}^3$ | | | | | | |
| $R_{\text{bragg}} = 8.18\%$, $R_p = 6.3\%$, $R_{\text{wp}} = 10.2\%$ | | | | | | |
| atom | Wyckoff position | Atomic position | | | Occ. | B_{iso} |
| | | x/a | y/b | z/c | | |
| Al(1) | 16i | $\frac{1}{4}$ | 0 | 0.3221(1) | 1 | 1.0(1) ^o |
| P(1) | 4b | 0 | 0 | $\frac{1}{4}$ | 1 | 1.5(5) |
| P(2) | 4d | $\frac{1}{2}$ | 0 | $\frac{1}{4}$ | 1 | 1.0(1) |
| P(3) | 8g | $\frac{1}{4}$ | $\frac{1}{4}$ | $\frac{1}{4}$ | 1 | 1.0(1) |
| O(1) | 16i | 0 | 0.0975(2) | 0.1589(2) | 1 | 0.3(1) |
| O(2) | 16i | $\frac{1}{2}$ | 0.0992(2) | 0.1582(2) | 1 | 0.3(1) |
| O(3) | 16i | $\frac{1}{4}$ | 0.1500(2) | 0.3576(1) | 1 | 0.9(2) |
| O(4) | 16i | $\frac{1}{4}$ | 0.3449(4) | 0.3331(4) | 1 | 0.3(1) |
| F(1) | 8h | 0.2431(4) | 0.0116(5) | $\frac{1}{2}$ | 1 | 0.6(2) |
| F(2) | 16i | 0.5082(4) | 0.7461(5) | 0.3582(4) | 1 | 0.6(2) |
| Na(1) | 8h | 0.1069(5) | 0.4693(5) | 0 | 0.28(2) | 2.0(1) |
| Na(2) | 8h | 0.1215(3) | 0.0885(4) | 0 | 0.40(1) | 2.9(3) |
| Na(3) | 8h | 0.1981(5) | 0.3664(6) | 0 | 0.41(4) | 2.0(1) |
| Na(4) | 8h | 0.3582(3) | 0.1211(4) | 0 | 0.22(1) | 2.1(1) |
| Na(5) | 8h | 0.3450(5) | 0.3833(6) | 0 | 0.48(3) | 2.4(2) |
| Na(6) | 8h | 0.1353(6) | 0.4002(6) | 0 | 0.61(4) | 1.2(1) |
| Na(7) | 8h | 0.2462(5) | 0.1485(6) | 0 | 0.25(3) | 1.5(1) |
| Na(8) | 8h | 0.1079(6) | 0.0626(9) | 0 | 0.31(4) | 1.5(1) |

$\text{Na}_3\text{Al}_2(\text{PO}_4)_2\text{F}_3$ was indexed in the $P4_2/mbc$ space group and its unit cell is two times bigger than those of other $\text{Na}_3(\text{VO})_{2-z}\text{Al}_z(\text{PO}_4)_2\text{F}_{1+z}$ ($0 < z < 2$) compositions. Nevertheless, this is caused by a difference in Na^+ distribution in these phases and the cell parameters of $\text{Na}_3\text{Al}_2(\text{PO}_4)_2\text{F}_3$ can be converted to the same system as in $P4_2/mnm$ by an application of a transformation matrix, T :

$$T = \begin{pmatrix} \frac{1}{2} & \frac{1}{2} & 0 & 0 \\ \frac{1}{2} & -\frac{1}{2} & 0 & 0 \\ 0 & 0 & 1 & 0 \end{pmatrix}$$

The relationship between the unit cell of $\text{Na}_3\text{Al}_2(\text{PO}_4)_2\text{F}_3$ and $\text{Na}_3(\text{VO})_{2-z}\text{Al}_z(\text{PO}_4)_2\text{F}_{1+z}$ ($0 < z < 2$) is illustrated in **Figure 4.35**. The substitution of $\text{V}^{4+}=\text{O}$ groups into $\text{Na}_3\text{Al}_2(\text{PO}_4)_2\text{F}_3$ seems to disrupt the Na^+ distribution in the initial phase and results in a smaller unit cell.

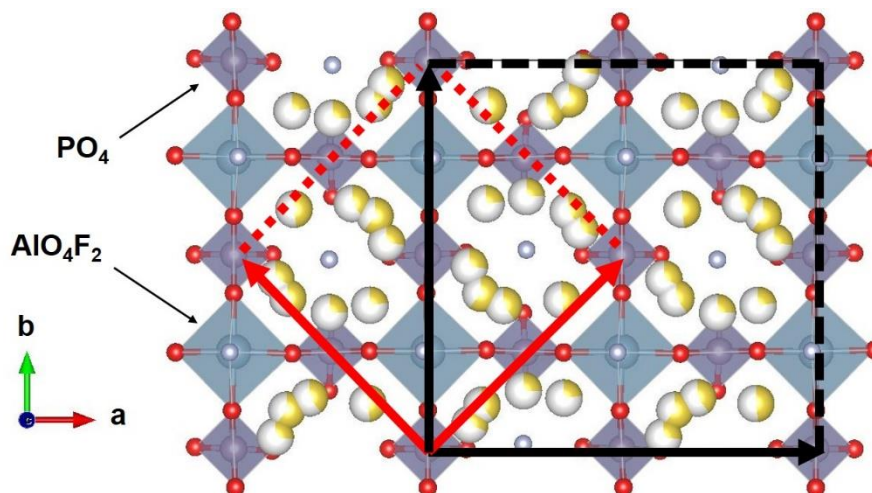


Figure 4.35 : The relationship between the cell vectors of $\text{Na}_3\text{Al}_2(\text{PO}_4)_2\text{F}_3$ (black vectors) and those of $\text{Na}_3(\text{VO})_{2-z}\text{Al}_z(\text{PO}_4)_2\text{F}_{1+z}$ ($0 < z < 2$) (red vectors).

Even though $\text{Na}_3\text{Al}_2(\text{PO}_4)_2\text{F}_3$ and $\text{Na}_3(\text{VO})_{2-z}\text{Al}_z(\text{PO}_4)_2\text{F}_{1+z}$ ($0 < z < 2$) are described in different space groups, they can be converted into the same system thanks to a transformation matrix, and a linear evolution of the cell parameters was observed for the whole composition range $\text{Na}_3(\text{VO})_{2-z}\text{Al}_z(\text{PO}_4)_2\text{F}_{1+z}$ ($0 \leq z \leq 2$). The Na^+ ions orderings in $\text{Na}_3(\text{VO})_2(\text{PO}_4)_2\text{F}$, $\text{Na}_3\text{Al}_2(\text{PO}_4)_2\text{F}_3$ and $\text{Na}_3(\text{VO})_{2-z}\text{Al}_z(\text{PO}_4)_2\text{F}_{1+z}$ ($0 < z < 2$) are different, but it does not prevent the formation of a solid solution.

IV.4.2.4. Vanadium oxidation state and chemical formula determination

All the obtained materials, except $\text{Na}_3\text{Al}_2(\text{PO}_4)_2\text{F}_3$, were bluish green, which is identical to the color of $\text{Na}_3(\text{VO})_2(\text{PO}_4)_2\text{F}$ (**Figure 2.9**). The Al^{3+} ion does not possess any electrons in the d orbitals, and thus it does not absorb any photons in the visible region. On the other hand, the presence of V^{3+} ions in this structure will lead to a dark color (**Figure 2.9**). Combining these two observations, we suspect that these phases contain V^{4+} and Al^{3+} .

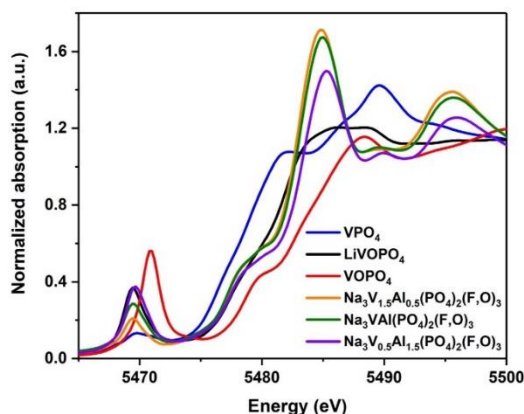


Figure 4.36 : Vanadium K-edge XANES spectra recorded on $\text{Na}_3\text{V}_{1.5}\text{Al}_{0.5}(\text{PO}_4)_2(\text{F},\text{O})_3$, $\text{Na}_3\text{V}_1\text{Al}_1(\text{PO}_4)_2(\text{F},\text{O})_3$ and $\text{Na}_3\text{V}_{0.5}\text{Al}_{1.5}(\text{PO}_4)_2(\text{F},\text{O})_3$ as compared to those of VPO_4 , LiVOPO_4 and VOPO_4 references.

Vanadium K-edge XANES spectra recorded on $\text{Na}_3\text{V}_{1.5}\text{Al}_{0.5}(\text{PO}_4)_2(\text{F},\text{O})_3$, $\text{Na}_3\text{V}_1\text{Al}_1(\text{PO}_4)_2(\text{F},\text{O})_3$ and $\text{Na}_3\text{V}_{0.5}\text{Al}_{1.5}(\text{PO}_4)_2(\text{F},\text{O})_3$ reveal that the edge energy of vanadium species in these compositions coincides with the edge energy of V^{4+} as in the $\text{LiV}^{4+}\text{OPO}_4$ reference, thus supporting the presence of V^{4+} . Furthermore, the pre-edge signal of all the recorded spectra are really intense, which is in agreement with the distorted local environment of V^{4+} ions due to the formation of vanadyl bonds (**Figure 4.36**).

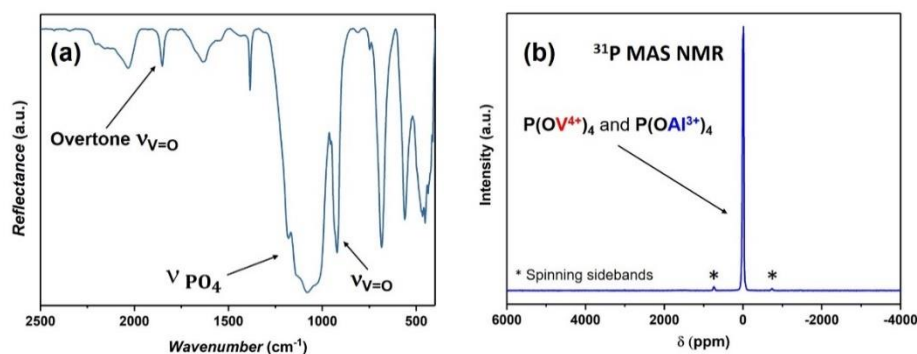


Figure 4.37 : (a) IR spectrum recorded on $\text{Na}_3\text{V}_{1.5}\text{Al}_{0.5}(\text{PO}_4)_2(\text{F},\text{O})_3$ and (b) ^{31}P MAS NMR spectrum recorded on $\text{Na}_3\text{V}_{1.5}\text{Al}_{0.5}(\text{PO}_4)_2(\text{F},\text{O})_3$ at $B_0 = 2.35\text{T}$; $\nu_R = 30\text{ kHz}$. The asterisks (*) indicate the rotational spinning sidebands.

The presence of vanadyl bonds can be detected directly by IR spectroscopy. **Figure 4.37a** shows the IR spectrum recorded on the $\text{Na}_3\text{V}_{1.5}\text{Al}_{0.5}(\text{PO}_4)_2(\text{F},\text{O})_3$ composition. An intense signal at 921 cm^{-1} with its second order harmonic at 1852 cm^{-1} are the clear evidences for the existence of $\text{V}^{4+}=\text{O}$ vanadyl bonds. Even though vanadium K-edge XANES spectrum and IR data support the presence of V^{4+} in form of vanadyl $\text{V}^{4+}=\text{O}$ groups, they do not exclude the possible presence of V^{3+} traces.

The whole **Chapter III** was dedicated to an investigation of $\text{V}^{3+}/\text{V}^{4+}$ electronic structure in $\text{Na}_3\text{V}_2(\text{PO}_4)_2\text{F}_3$ -related structural frameworks and their influence on the spin transfer mechanism between $\text{V}^{3+}/\text{V}^{4+}$ ions and their neighboring phosphorus nuclei. We have learnt that the presence of one V^{3+} ion in the proximity of phosphorus atom will contribute to a Fermi contact shift of 1500 ppm on the ^{31}P MAS NMR whereas V^{4+} does not induce any Fermi contact shift with its surrounding phosphorus nuclei. If the $\text{Na}_3\text{V}_{1.5}\text{Al}_{0.5}(\text{PO}_4)_2(\text{F},\text{O})_3$ composition contained any V^{3+} traces, there would be several paramagnetic resonances on the ^{31}P MAS NMR spectrum. The ^{31}P MAS NMR spectrum recorded on this composition reveals the extinction of all the paramagnetic resonances (**Figure 4.37b**) and thus indicates a total absence of V^{3+} ions. The EXAFS data recorded for this material can be fit with a single vanadium octahedral environment $\text{F}-\text{V}^{4+}\text{O}_4=\text{O}$, in which $d_{\text{V}-\text{O}} = 2.00 \text{ \AA} \times 4$, $d_{\text{V}-\text{F}} = 2.00 \text{ \AA}$, $d_{\text{V}=\text{O}} = 1.62 \text{ \AA}$ and $\sigma_{\text{O/F}} = 6.7 \cdot 10^{-3} \text{ \AA}^2$.

Even though XAS at Al K-edge was not performed, Al^{3+} local environment can be determined easily. As Al exhibits only one stable oxidation state (+3) and it does not have any tendency to form highly covalent bond, the chemical bond $\text{Al}^{3+}=\text{O}$ does not exist, the only possible Al^{3+} local environment in this structure is $\text{F}-\text{Al}^{3+}\text{O}_4-\text{F}$. Furthermore, the ICP-OES analysis performed on $\text{Na}_3\text{V}_{1.5}\text{Al}_{0.5}(\text{PO}_4)_2(\text{F},\text{O})_3$ shows a relative Na/V/Al/P ratio of 3/1.5/0.5/2. Combining all the analyses obtained from ICP-OES, IR spectroscopy, XAS at vanadium K-edge, ^{31}P MAS NMR and the charge compensation effect, the actual chemical formula of $\text{Na}_3\text{V}_{1.5}\text{Al}_{0.5}(\text{PO}_4)_2(\text{F},\text{O})_3$ will be written as $\text{Na}_3(\text{V}^{4+}\text{O})_{1.5}\text{Al}_{0.5}(\text{PO}_4)_2\text{F}_{1.5}$ or $\text{Na}_3\text{V}^{4+}_{1.5}\text{Al}_{0.5}(\text{PO}_4)_2\text{F}_{1.5}\text{O}_{1.5}$. The formation of this Al^{3+} substituted composition can be understood as follows: starting from the parental compound, $\text{Na}_3(\text{VO})_2(\text{PO}_4)_2\text{F}$, once the V^{4+} ion is substituted by Al^{3+} , the oxygen atom engaged in the vanadyl bond with this V^{4+} ion will be simultaneously replaced by fluorine in order to maintain the charge neutrality in the whole material, which leads to a double cationic-anionic substitution effect.

The determination of vanadium oxidation state and the deduction of the exact chemical formula for $\text{Na}_3(\text{V}^{4+}\text{O})_{1.5}\text{Al}_{0.5}(\text{PO}_4)_2\text{F}_{1.5}$ were done in a meticulous way in order to understand the nature of the ionic substitution. The same process was also applied to other compositions and we have discovered that all of them contained Al^{3+} and V^{4+} in form of $\text{V}^{4+}=\text{O}$. The general formula of this materials family is thus written as

$\text{Na}_3(\text{VO})_{2-z}\text{Al}_z(\text{PO}_4)_2\text{F}_{1+z}$ ($0 \leq z \leq 2$). This is an exciting discovery in the field of solid-state chemistry in which the double cationic-anionic can occur simultaneously and the resulted compositions form a continuous solid-solution.

IV.4.2.5. Solid-state NMR characterization

$\text{Na}_3\text{Al}_2(\text{PO}_4)_2\text{F}_3$ is an attractive Na^+ ionic conductor whose crystal structure is similar to that of $\text{Na}_3\text{V}_2(\text{PO}_4)_2\text{F}_3$ or $\text{Na}_3(\text{VO})_2(\text{PO}_4)_2\text{F}$, except for the Na^+ distribution in the diffusion channels [82,215]. Furthermore, $\text{Na}_3\text{Al}_2(\text{PO}_4)_2\text{F}_3$ can exist in form of two different polymorphs: α - $\text{Na}_3\text{Al}_2(\text{PO}_4)_2\text{F}_3$ (at the temperature greater than 43°C) and β_1 - $\text{Na}_3\text{Al}_2(\text{PO}_4)_2\text{F}_3$ (below 43°C). In α - $\text{Na}_3\text{Al}_2(\text{PO}_4)_2\text{F}_3$ there are two different Na crystallographic sites while there are eight Na sites in β_1 - $\text{Na}_3\text{Al}_2(\text{PO}_4)_2\text{F}_3$ [82]. This is a very interesting point in terms of solid-state chemistry and *ss*-NMR, as we would like to know whether it is possible to detect all the eight Na sites in β_1 - $\text{Na}_3\text{Al}_2(\text{PO}_4)_2\text{F}_3$ by the use of ^{23}Na *ss*-NMR or not, and whether it is possible to distinguish α - and β_1 - $\text{Na}_3\text{Al}_2(\text{PO}_4)_2\text{F}_3$ just by the use of ^{23}Na *ss*-NMR.

It has been shown earlier that $\text{Na}_3\text{Al}_2(\text{PO}_4)_2\text{F}_3$ and $\text{Na}_3(\text{VO})_2(\text{PO}_4)_2\text{F}$ form a continuous solid-solution with the general formula $\text{Na}_3(\text{V}^{4+}\text{O})_{2-z}\text{Al}_z(\text{PO}_4)_2\text{F}_{1+z}$ ($0 \leq z \leq 2$), in which a continuous evolution in the cell parameters was observed over the whole compositional range. In this case, *ss*-NMR spectroscopy is a powerful technique that will help us to follow the change in Na and P local environments when $\text{V}^{4+}=\text{O}$ groups in $\text{Na}_3(\text{VO})_2(\text{PO}_4)_2\text{F}$ are gradually substituted by $\text{Al}^{3+}-\text{F}$.

IV.4.2.5.1. Variable temperature ^{23}Na and ^{27}Al *ss*-NMR of $\text{Na}_3\text{Al}_2(\text{PO}_4)_2\text{F}_3$.

The ^{23}Na NMR spectrum of $\text{Na}_3\text{Al}_2(\text{PO}_4)_2\text{F}_3$ recorded at 47°C shows one diamagnetic resonance at $\delta = -25$ ppm. Even though there are two different Na sites in α - $\text{Na}_3\text{Al}_2(\text{PO}_4)_2\text{F}_3$, the Na^+ ions seem to have high mobility at this temperature and they can hop rapidly from one site to the other site, thus only one average resonance can be detected. At -13°C , the ^{23}Na resonance is very broad and the typical quadrupolar form of the signal is no longer observed. Even though XRD data shows the existence of eight different Na sites, the local environment and the chemical shift values of these Na sites are so close that they cannot be resolved in NMR spectroscopy (**Figure 4.38a**).

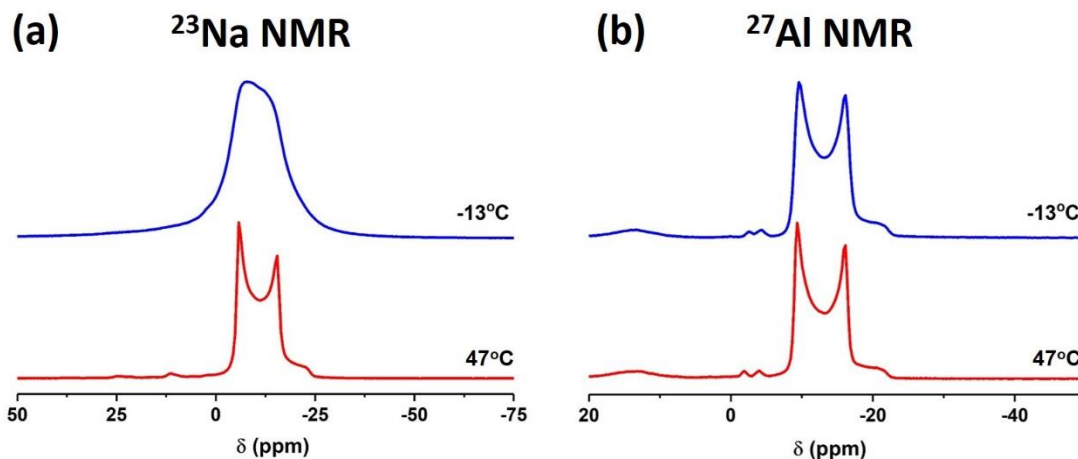


Figure 4.38 : (a) ^{23}Na MAS NMR spectra of $\text{Na}_3\text{Al}_2(\text{PO}_4)_2\text{F}_3$ recorded at $B_0 = 11.7\text{T}$ with $\nu_R = 30\text{ kHz}$ at -13°C and at 47°C , (b) ^{27}Al MAS NMR spectra of $\text{Na}_3\text{Al}_2(\text{PO}_4)_2\text{F}_3$ recorded at $B_0 = 11.7\text{T}$ with $\nu_R = 30\text{ kHz}$ at -13°C and at 47°C .

In $\text{Na}_3\text{Al}_2(\text{PO}_4)_2\text{F}_3$, the ^{27}Al resonance is diamagnetic and its line shape indicates a strong first-order quadrupolar coupling, which is characteristic for Al nucleus ($I = 5/2$), with a C_Q value equals to 0 as the Al sites in the structure are ‘quasi’-symmetric (**Figure 4.38b**). The tiny resonance observed at 15 ppm could be due to the presence of a negligible amount of impurity. The ^{27}Al MAS NMR spectra at low and high temperatures are identical proving that there is no change in Al local environment (**Figure 4.38b**).

IV.4.2.5.2. NMR study of $\text{Na}_3(\text{VO})_{2-z}\text{Al}_z(\text{PO}_4)_2\text{F}_{1+z}$ solid solution

The ^{23}Na MAS NMR spectra recorded on the $\text{Na}_3(\text{VO})_{2-z}\text{Al}_z(\text{PO}_4)_2\text{F}_{1+z}$ ($0 \leq z \leq 2$) compositions are given in **Figure 4.39a**. As discussed above, the ^{23}Na NMR spectrum of $\text{Na}_3\text{Al}_2(\text{PO}_4)_2\text{F}_3$ shows one quadrupole signal despite the presence of eight different crystallographic Na sites at ambient temperature (**Figure 4.38a**). In $\text{Na}_3(\text{VO})_{0.25}\text{Al}_{1.75}(\text{PO}_4)_2\text{F}_{2.75}$, the quadrupolar coupling on ^{23}Na nuclei can still be observed; however, this interaction is no longer obvious in $\text{Na}_3(\text{VO})_{0.5}\text{Al}_{1.5}(\text{PO}_4)_2\text{F}_{2.5}$ and it is now dominated by the Fermi contact between the electron spin of V^{4+} and ^{23}Na nuclei. The ^{23}Na resonances in $\text{Na}_3(\text{VO})_{0.5}\text{Al}_{1.5}(\text{PO}_4)_2\text{F}_{2.5}$ are rather broad with several contributions suggesting the presence of several Na local environments or Na^+ -vacancy orderings in the diffusion channels. All the ^{23}Na resonances in $\text{Na}_3(\text{VO})_{0.5}\text{Al}_{1.5}(\text{PO}_4)_2\text{F}_{2.5}$ are shifted to the positive values due to the Fermi contact between the unpaired electron of V^{4+} and the ^{23}Na nuclei. The more V^{4+} ions present in the structure, the Fermi contact

is stronger and the ^{23}Na resonances are shifted toward the positive direction. The ^{23}Na NMR shift reaches its maximum value when all the Al^{3+} ions in the structure are replaced by V^{4+} as in $\text{Na}_3(\text{V}^{4+}\text{O})_2(\text{PO}_4)_2\text{F}$ (**Figure 4.39a**).

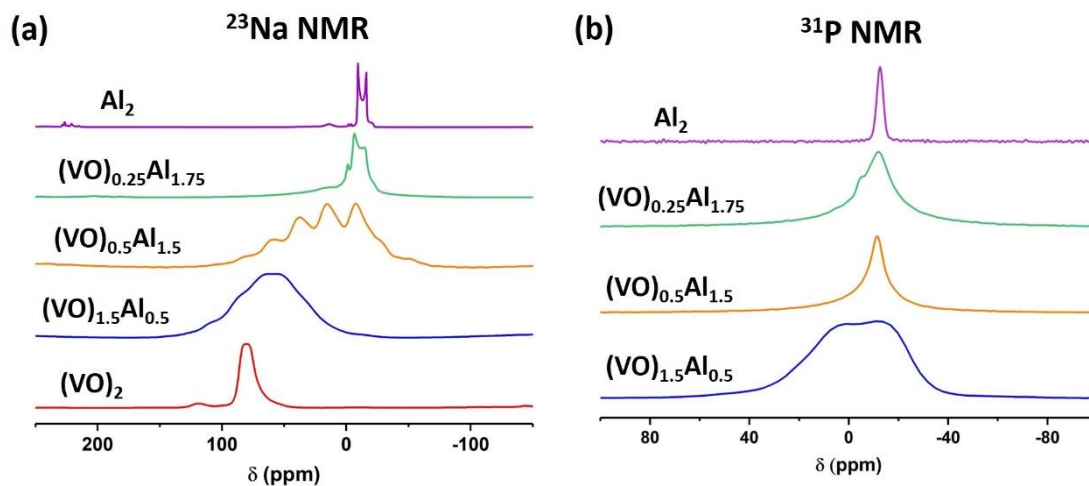


Figure 4.39 : (a) ^{23}Na MAS NMR spectra of $\text{Na}_3(\text{VO})_{2-z}\text{Al}_z(\text{PO}_4)_2\text{F}_{1+z}$ ($0 \leq z \leq 2$) recorded at $B_0 = 11.7$ T with $\nu_R = 30$ kHz, (b) ^{31}P MAS NMR spectra of $\text{Na}_3(\text{VO})_{2-z}\text{Al}_z(\text{PO}_4)_2\text{F}_{1+z}$ ($0 \leq z \leq 2$) recorded at $B_0 = 2.35$ T with $\nu_R = 30$ kHz.

The ^{31}P MAS NMR spectrum of $\text{Na}_3\text{Al}_2(\text{PO}_4)_2\text{F}_3$ shows the presence of a narrow resonance at $\delta = -10$ ppm corresponding to the unique $\text{P}(\text{OAl}^{3+}\text{—F})_4$ local environment in this composition. When Al^{3+} and V^{4+} co-exist in the same structure, more phosphorus local environments, such as $\text{P}(\text{OAl}^{3+}\text{—F})_3(\text{OV}^{4+}\text{=O})$, $\text{P}(\text{OAl}^{3+}\text{—F})_2(\text{OV}^{4+}\text{=O})_2$, $\text{P}(\text{OAl}^{3+}\text{—F})(\text{OV}^{4+}\text{=O})_3$ and $\text{P}(\text{OV}^{4+}\text{=O})_4$ are generated. The co-existence of these five phosphorus local environments broadens the ^{31}P NMR resonances recorded on $\text{Na}_3(\text{VO})_{2-z}\text{Al}_z(\text{PO}_4)_2\text{F}_{1+z}$ ($0 \leq z \leq 2$) phases (**Figure 4.39b**). In $\text{Na}_3(\text{VO})_{1.5}\text{Al}_{0.5}(\text{PO}_4)_2\text{F}_{1.5}$, the ^{31}P NMR signal ranging from -40 ppm to 40 ppm is very broad. This could be due to the presence of different domains in the particle where one is Al^{3+} -rich while the other is V^{4+} -rich, and thus leading to the preferential formation of $\text{P}(\text{OAl}^{3+}\text{—F})_4$ and $\text{P}(\text{OV}^{4+}\text{=O})_4$ local environments, respectively. In $\text{Na}_3(\text{VO})_2(\text{PO}_4)_2\text{F}$, two ^{31}P NMR resonances are observed at 92 ppm, which corresponds to two different phosphorus crystallographic sites. Therefore, V^{4+} ions with the formal charge +4 tend to induce a higher shift on the ^{31}P signals than the neighboring Al^{3+} ions.

IV.4.3. Electrochemistry of Al^{3+} substituted phases

As was shown above, Al^{3+} can be substituted into $\text{Na}_3\text{V}^{3+}_2(\text{PO}_4)_2\text{F}_3$ to form $\text{Na}_3\text{V}^{3+}_{2-z}\text{Al}_z(\text{PO}_4)_2\text{F}_3$ ($0 \leq z \leq 0.5$) or it can be also substituted into $\text{Na}_3(\text{V}^{4+}\text{O})_2(\text{PO}_4)_2\text{F}$ to form $\text{Na}_3(\text{V}^{4+}\text{O})_{2-z}\text{Al}_z(\text{PO}_4)_2\text{F}_{1+z}$ ($0 \leq z \leq 2$). It would be interesting to know how the Al^{3+} -substituent can affect the electrochemical properties of V^{3+} and V^{4+} in $\text{Na}_3\text{V}^{3+}_{2-z}\text{Al}_z(\text{PO}_4)_2\text{F}_3$ and $\text{Na}_3(\text{V}^{4+}\text{O})_{2-z}\text{Al}_z(\text{PO}_4)_2\text{F}_{1+z}$, respectively. **Figure 4.40** compares the charge/discharge signatures of $\text{Na}_3\text{V}^{3+}_{1.5}\text{Al}_{0.5}(\text{PO}_4)_2\text{F}_3$, $\text{Na}_3(\text{V}^{4+}\text{O})_{1.5}\text{Al}_{0.5}(\text{PO}_4)_2\text{F}_{1.5}$ and those obtained for the carbon-coated $\text{Na}_3\text{V}^{3+}_2(\text{PO}_4)_2\text{F}_3$ and $\text{Na}_3(\text{V}^{4+}\text{O})_2(\text{PO}_4)_2\text{F}$.

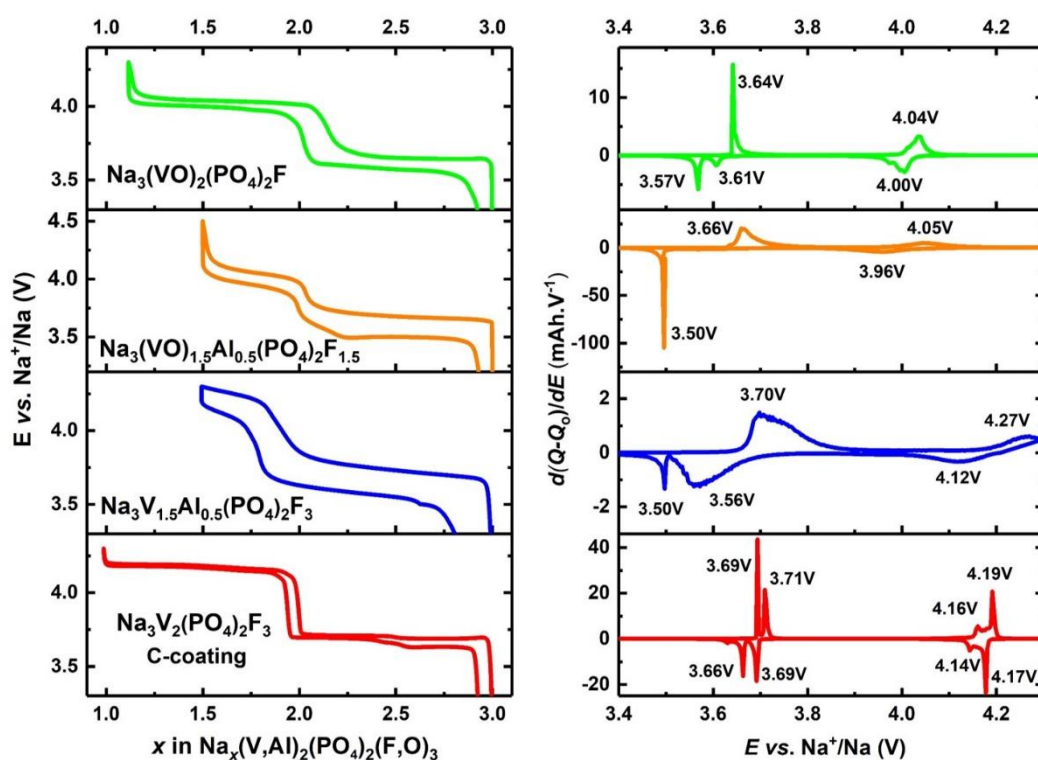


Figure 4.40 : (Left) Electrochemical charge/discharge curves of $\text{Na}_3\text{V}_{1.5}\text{Al}_{0.5}(\text{PO}_4)_2\text{F}_3$ and $\text{Na}_3(\text{VO})_{1.5}\text{Al}_{0.5}(\text{PO}_4)_2\text{F}_{1.5}$ in sodium half-cells at the cycling rate of $C/10$ per Na^+ ion as compared to those obtained for the carbon-coated $\text{Na}_3\text{V}_2(\text{PO}_4)_2\text{F}_3$ and $\text{Na}_3(\text{VO})_2(\text{PO}_4)_2\text{F}$, (Right) The first derivatives of the corresponding electrochemical curves.

In $\text{Na}_3\text{V}^{3+}_2(\text{PO}_4)_2\text{F}_3$ and $\text{Na}_3(\text{V}^{4+}\text{O})_2(\text{PO}_4)_2\text{F}$, two Na^+ ions can be reversibly extracted/reinserted in the potential range of 2.5 - 4.3 V vs. Na^+/Na whereas in the same cycling conditions only 1.5 Na^+ ions can be extracted from $\text{Na}_3\text{V}^{3+}_{1.5}\text{Al}_{0.5}(\text{PO}_4)_2\text{F}_3$ and $\text{Na}_3(\text{V}^{4+}\text{O})_{1.5}\text{Al}_{0.5}(\text{PO}_4)_2\text{F}_{1.5}$ (**Figure 4.40**). A higher cutoff voltage, e.g. 5.0 V vs. Na^+/Na was also applied on these two Al^{3+} substituted phases, but the charge curve just went up steeply without any evidence of extra Na^+ extraction at the high-voltage region. For the two families of materials $\text{Na}_3\text{V}^{3+}_{2-z}\text{Al}_z(\text{PO}_4)_2\text{F}_3$ and $\text{Na}_3(\text{V}^{4+}\text{O})_{2-z}\text{Al}_z(\text{PO}_4)_2\text{F}_{1+z}$, the

number of Na^+ ions that can participate in the reversible electrochemical reaction is only $(2 - z)$.

In $\text{Na}_3\text{V}^{3+}_2(\text{PO}_4)_2\text{F}_3$, the desodiation occurs through a series of biphasic reaction as indicated by the presence of two “composition-voltage” plateau together with a gradual oxidation of $\text{V}^{3+}-\text{F}$ into $\text{V}^{4+}-\text{F}$ (**Chapter II**). For $\text{Na}_3\text{V}^{3+}_{1.5}\text{Al}_{0.5}(\text{PO}_4)_2\text{F}_3$, the charge curve is characterized by two sloping curves at average potentials of 3.70 V and 4.27 V vs. Na^+/Na , which correspond to the extraction of 1 and 0.5 Na^+ ions, respectively (**Figure 4.40**). The sloping nature of the voltage-composition profile and the “broad peaks” observed on the first derivative curve indicate that desodiation from $\text{Na}_3\text{V}^{3+}_{1.5}\text{Al}_{0.5}(\text{PO}_4)_2\text{F}_3$ occurs through a solid-solution mechanism without the formation of Na^+ -vacancy ordering. The random distribution of Al^{3+} over V^{3+} sites could be the reason for the disappearance of the charge ordering during cycling. The positions of the signatures observed in the first derivative curves of $\text{Na}_3\text{V}^{3+}_2(\text{PO}_4)_2\text{F}_3$ and $\text{Na}_3\text{V}^{3+}_{1.5}\text{Al}_{0.5}(\text{PO}_4)_2\text{F}_3$ are identical, meaning that the Na^+ extraction from $\text{Na}_3\text{V}^{3+}_{1.5}\text{Al}_{0.5}(\text{PO}_4)_2\text{F}_3$ also occurs through the oxidation of $\text{V}^{3+}-\text{F}$ to $\text{V}^{4+}-\text{F}$. In a recent theoretical study, it was predicted that the presence of a foreign ion in the framework of $\text{Na}_3\text{V}^{3+}_2(\text{PO}_4)_2\text{F}_3$ can trigger a local structural distortion, and thus disrupt the formation of Na^+ -vacancy ordering during charge and promote the activation of the $\text{V}^{5+}-\text{F}/\text{V}^{4+}-\text{F}$ at the high voltage region, hence more Na^+ ions can be extracted from the materials [119]. In $\text{Na}_3\text{V}^{3+}_{1.5}\text{Al}_{0.5}(\text{PO}_4)_2\text{F}_3$, no formation of Na^+ -vacancy ordering was detected during charge but no extra capacity or the activation of $\text{V}^{5+}-\text{F}/\text{V}^{4+}-\text{F}$ redox couple was observed in the high-voltage range.

The electrochemical signature of $\text{Na}_3(\text{V}^{4+}\text{O})_{1.5}\text{Al}_{0.5}(\text{PO}_4)_2\text{F}_{1.5}$ is characterized by two “sloping curves” corresponding to the reversible extraction of ~ 1 Na^+ and 0.5 Na^+ ions at average potentials of ~ 3.66 and 4.05 V vs. Na^+/Na respectively. Compared to $\text{Na}_3(\text{V}^{4+}\text{O})_2(\text{PO}_4)_2\text{F}$, the Na^+ extraction voltage in $\text{Na}_3(\text{V}^{4+}\text{O})_{1.5}\text{Al}_{0.5}(\text{PO}_4)_2\text{F}_{1.5}$ is not affected by the presence of Al^{3+} ion, and the Na^+ extraction in this case also occur through the activation of the $\{\text{V}^{5+}=\text{O}\}^{3+}/\{\text{V}^{4+}=\text{O}\}^{2+}$ redox couple

In the two cases, $\text{Na}_3\text{V}^{3+}_{1.5}\text{Al}_{0.5}(\text{PO}_4)_2\text{F}_3$ and $\text{Na}_3(\text{V}^{4+}\text{O})_{1.5}\text{Al}_{0.5}(\text{PO}_4)_2\text{F}_{1.5}$, the electrochemical profile of the Al^{3+} substituted phases is very sloping and the peaks on its

derivative curve are highly broadened indicating that the Na^+ desodiation occurs through a solid solution mechanism, which was also confirmed by *operando* SXR experiment. The Al^{3+} substitution in both cases prevents the charge ordering upon cycling. On the other hand, the substitution does not have any effect on the Na^+ extraction voltages. Even though Al^{3+} ions are randomly distributed over all the M^{3+} sites in the structure, it seems that the presence of Al^{3+} does not induce a great influence on the crystal field of the V^{3+} or V^{4+} ion opposite to it in the same bioctahedral unit.

IV.5. Conclusions

The ionic exchange between Na and Ag within the structural framework of the electrode material $\text{Na}_3\text{V}_2(\text{PO}_4)_2\text{F}_3$ was investigated in details in this study. The exchange proceeds close to completion in roughly 30 hours if the submicron particle size was used. On the other hand, the ion exchange into the microcrystalline $\text{Na}_3\text{V}_2(\text{PO}_4)_2\text{F}_3$ cannot be finished even after 60 hours due to kinetic limitations. Although the XRD and NPD patterns look significantly different after the exchange because of the high atomic weight of silver compared to sodium, the Rietveld refinement shows that all the silver-exchanged compounds adopt the same structure as $\text{Na}_3\text{V}_2(\text{PO}_4)_2\text{F}_3$ with a subtle orthorhombic distortion, and this distortion is more pronounced in the phases with higher Ag^+ content. This observation supports the fact that the framework of $\text{Na}_3\text{V}_2(\text{PO}_4)_2\text{F}_3$ is capable of exhibiting high ionic conductivity and can support the presence of different monovalent ions. Finally, the $\text{Ag}_{2.7}\text{V}_2(\text{PO}_4)_2\text{F}_3$ obtained by Ag^+/Na^+ ion exchange into microcrystalline $\text{Na}_3\text{V}_2(\text{PO}_4)_2\text{F}_3$ undergoes an order-disorder transition upon heating, which transforms the symmetry from orthorhombic to tetragonal as a consequence of Ag^+ disordering. This transition occurs close to 600 K while a similar one in $\text{Na}_3\text{V}_2(\text{PO}_4)_2\text{F}_3$ occurs at 400 K, showing that Ag is less prone to disordering than sodium within this framework. **$\text{Ag}_3\text{V}_2(\text{PO}_4)_2\text{F}_3$** is possibly a new polyanionic framework capable of Ag^+ ionic conduction, which could be used as a positive electrode material in rechargeable or primary silver-based batteries.

$\text{Na}_3(\text{VO})\text{Fe}(\text{PO}_4)_2\text{F}_2$ was obtained by an original sol-gel method and the structure of this newly obtained phase was described in the $P4_2/mnm$ space group. Only one Na^+ can be reversibly extracted in the potential range of 2.5 - 4.3 V vs. Na^+/Na , which corresponds to the oxidation of all V^{4+} ions into V^{5+} . Limited polarization value and good capacity retention was observed upon cycling, even if the reversible capacity decreased as the $\text{Fe}^{4+}/\text{Fe}^{3+}$ redox couple could not be activated. On the contrary, extra 0.5 Na^+ could be reversibly inserted into the structure by activating the $\text{Fe}^{3+}/\text{Fe}^{2+}$ redox couple, but at very low voltage (~ 1.5 V vs. Na^+/Na). *Operando* synchrotron X-ray powder diffraction revealed there was no formation of Na^+ -vacancy ordering during charge (*i.e.* Na^+ deintercalation), which was contrary to what had been observed for $\text{Na}_3\text{V}_2(\text{PO}_4)_2\text{F}_3$ and $\text{Na}_3(\text{VO})_2(\text{PO}_4)_2\text{F}$. Their suppression would lower the Na^+ -defect formation energy, and hence increase the Na^+ ionic conductivity in the diffusion channels, and could explain the low polarization value observed for this material when used at the positive electrode in a sodium cell. Fe^{3+} could be a promising substituent or dopant that needs to be extensively studied in order to enhance the electrochemical performance of $\text{Na}_3\text{V}_2(\text{PO}_4)_2\text{F}_3$, $\text{Na}_3(\text{VO})_2(\text{PO}_4)_2\text{F}$ and similar phases.

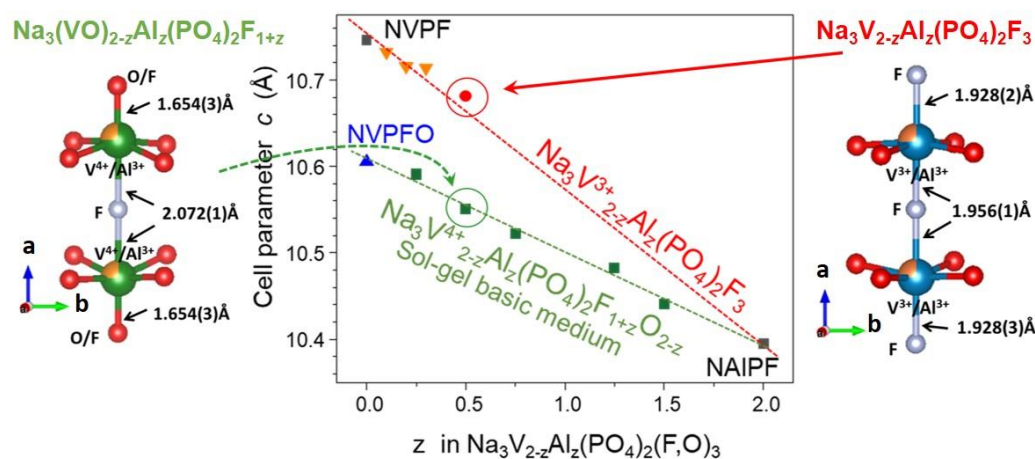


Figure 4.41 : Comparisons of cell parameters between $\text{Na}_3\text{V}_{2-z}\text{Al}_z(\text{PO}_4)_2\text{F}_3$ ($0 \leq z \leq 0.5$) and $\text{Na}_3(\text{VO})_{2-z}\text{Al}_z(\text{PO}_4)_2\text{F}_{1+z}$ ($0 \leq z \leq 2$).

Two different Al-substituted materials, $\text{Na}_3\text{V}_{2-z}\text{Al}_z(\text{PO}_4)_2\text{F}_3$ and $\text{Na}_3(\text{VO})_{2-z}\text{Al}_z(\text{PO}_4)_2\text{F}_{1+z}$, were obtained by the use of several synthesis approaches. In the case of $\text{Na}_3\text{V}_{2-z}\text{Al}_z(\text{PO}_4)_2\text{F}_3$, the solid solution was limited to $z = 0.3$ by solid-state reaction, however the solubility of Al^{3+} in $\text{Na}_3\text{V}_2(\text{PO}_4)_2\text{F}_3$ can be extended up to $z = 0.5$ by the use of sol-gel reaction in acidic media. All the obtained $\text{Na}_3\text{V}_{2-z}\text{Al}_z(\text{PO}_4)_2\text{F}_3$ ($0 \leq z \leq 0.5$) phases were indexed in the $Amam$ space group with a subtle orthorhombic

distortion. By altering the acidic media into basic media or by the use of a solvent assisted method, $\text{Na}_3(\text{VO})_{2-z}\text{Al}_z(\text{PO}_4)_2\text{F}_{1+z}$ ($0 \leq z \leq 2$) compositions with the presence of V^{4+} in the structure were achieved (**Figure 4.41**). The use of an acidic environment seems to reserve vanadium ions in the V^{3+} oxidation state while V^{3+} ions in a basic media or organic environment tends to be quickly oxidized to V^{4+} by oxygen in the atmosphere, which results in the formation of $\text{Na}_3(\text{VO})_{2-z}\text{Al}_z(\text{PO}_4)_2\text{F}_{1+z}$. In these newly obtained phases, $\text{Na}_3\text{Al}_2(\text{PO}_4)_2\text{F}_3$ formed unlimited solid solution with $\text{Na}_3(\text{VO})_2(\text{PO}_4)_2\text{F}$. This is one of the rare example in solid-state chemistry where both cationic and anionic substitutions occur simultaneously. The orthorhombic distortion was completely suppressed in these phases and their structure can be indexed in the $P4_2/mnm$ space group. At the atomic level the V^{4+} ions in $\text{Na}_3(\text{VO})_{2-z}\text{Al}_z(\text{PO}_4)_2\text{F}_{1+z}$ are characterized by the presence of a short vanadyl bond (1.62 Å) on the terminal position while the vanadium ions in $\text{Na}_3\text{V}_{2-z}\text{Al}_z(\text{PO}_4)_2\text{F}_3$ are in the +3 oxidation state and their local environments are completely symmetric with six equivalent V–F/O bonds (**Figure 4.41**). As the terminal V^{3+} –F bond is longer than the terminal V^{4+} –O bond and the ionic radius of V^{3+} is slightly bigger than V^{4+} , hence at the same Al^{3+} content, such as $\text{Na}_3\text{V}^{3+}_{1.5}\text{Al}_{0.5}(\text{PO}_4)_2\text{F}_3$ vs. $\text{Na}_3(\text{V}^{4+}\text{O})_{1.5}\text{Al}_{0.5}(\text{PO}_4)_2\text{F}_{1.5}$, the cell parameters of the $\text{Na}_3\text{V}_{2-z}\text{Al}_z(\text{PO}_4)_2\text{F}_3$ composition are slightly bigger than its $\text{Na}_3(\text{VO})_{2-z}\text{Al}_z(\text{PO}_4)_2\text{F}_{1+z}$ counterpart (**Figure 4.41**). Furthermore, these two Al^{3+} substituted series have a common composition at $\text{Na}_3\text{Al}_2(\text{PO}_4)_2\text{F}_3$ ($z = 2$), we thus expect that a linear extrapolation of the cell parameters of these families will have a convergence at $z = 2$ (**Figure 4.41**).

In terms of electrochemistry, the presence of Al^{3+} seems to decrease the reversible capacity and increase the polarization of the material upon cycling. Furthermore, the $\text{V}^{4+}/\text{V}^{3+}$ redox couple in $\text{Na}_3\text{V}_{2-z}\text{Al}_z(\text{PO}_4)_2\text{F}_3$ and the $\{\text{V}^{5+}=\text{O}\}^{3+}/\{\text{V}^{4+}=\text{O}\}^{2+}$ redox couple in $\text{Na}_3(\text{VO})_{2-z}\text{Al}_z(\text{PO}_4)_2\text{F}_{1+z}$ are unlikely to be affected by the Al^{3+} substitution. The long distance between two metal sites in the same bioctahedral unit (~ 4.2 Å) and the closed-shell electronic structure of Al^{3+} seems to prevent it from having any significant interaction with its opposite transition-metal site. Combining these observations, it seems that Al^{3+} substitution would be detrimental to the electrochemical performance of $\text{Na}_3\text{V}_2(\text{PO}_4)_2\text{F}_3$ and $\text{Na}_3(\text{VO})_2(\text{PO}_4)_2\text{F}$, nonetheless the experience in layered oxides has shown that Al^{3+} substitution is required to improve the stability of the structure. First of all, Al^{3+} has a closed-shell electronic structure whose electrons are highly localized in its proximity, and hence the Al^{3+} –O bonds are highly ionic, which prevents the formation of

oxygen, especially at the high-voltage region. Secondly, the presence of a small amount of Al^{3+} in layered oxide materials such as $\text{Li}[\text{Ni}_{0.8}\text{Co}_{0.15}\text{Al}_{0.05}]\text{O}_2$ (NCA) has improved significantly the thermal runaway temperature - the temperature at which the released heat is accelerated and can lead to cell explosion. In $\text{Na}_3\text{V}_2(\text{PO}_4)_2\text{F}_3$ and $\text{Na}_3(\text{VO})_2(\text{PO}_4)_2\text{F}$, the desodiation and sodiation processes occur through many bi-phasic reactions with the presence of many 'composition-voltage' plateaus on the electrochemical profile and these processes are accompanied by a great amount of heat dissipation. Upon Al^{3+} substitution, these 'composition-voltage' plateaus are suppressed and the electrochemical reactions occur through solid-solution mechanism with less heat release during the electrochemical cycling. Furthermore, the electrochemical profile has an 'S-shape' which is desirable for the design of 'Battery Management System' (BMS), a system controlling the operation of the batteries in the multiple-cell design.

Last but not least, the discovery of Al^{3+} and Fe^{3+} substitution in $\text{Na}_3\text{V}_2(\text{PO}_4)_2\text{F}_3$ and/or $\text{Na}_3(\text{VO})_2(\text{PO}_4)_2\text{F}$ may open the door to the development of a new generation of polyanionic material for SIBs with the general formula $\text{Na}_3(\text{V,Al,Fe})_2(\text{PO}_4)_2(\text{F,O})_3$ where the optimized content of Al^{3+} and Fe^{3+} will help to improve the stability and the Na^+ diffusivity in the materials.

Chapter V

General Conclusions

In this Ph.D work, several derivatives from $\text{Na}_3\text{V}_2(\text{PO}_4)_2\text{F}_3$ and $\text{Na}_3(\text{VO})_2(\text{PO}_4)_2\text{F}$ were obtained through different synthesis approaches, such as solid-state reaction and sol-gel methods in different pH media, and the crystal structure of these phases were determined by high resolution synchrotron XRD. These derivatives can be classified into three groups: (i) cationic substitution, (ii) anionic substitution, (iii) cationic and anionic substitutions, and the structural relationship between are summarized in **Figure 5.1**.

The pristine material, $\text{Na}_3\text{V}_2(\text{PO}_4)_2\text{F}_3$, crystallizes in the *Amam* space group with a subtle orthorhombic distortion and the Na^+ ions are distributed over three different crystallographic sites in a triangular arrangement. Upon oxygen substitution, the oxygen and fluorine atoms are randomly distributed over the terminal positions. This random anionic distribution influences significantly the Na^+ arrangement in the diffusion channels: The charge residue corresponding to the presence of Na^+ calculated by difference Fourier transformation map is more diffuse and the Na^+ ions are supposed to be distributed over four different Na^+ sites for the $\text{Na}_3\text{V}^{3+}_{2-y'}\text{V}^{4+}_{y'}(\text{PO}_4)_2\text{F}_{3-y'}\text{O}_{y'}$ phases with $0 < y' < 2$, and this disordered distribution of Na^+ in oxygen-substituted phases seemed to minimize the orthorhombic distortion of the unit cell. In $\text{Na}_3(\text{VO})_2(\text{PO}_4)_2\text{F}$, all the terminal fluorine atoms are substituted by oxygen and a complex Na^+ -vacancy ordering was observed. A monoclinic cell with the presence of a modulated vector was required to describe the absolute structure of $\text{Na}_3(\text{VO})_2(\text{PO}_4)_2\text{F}$.

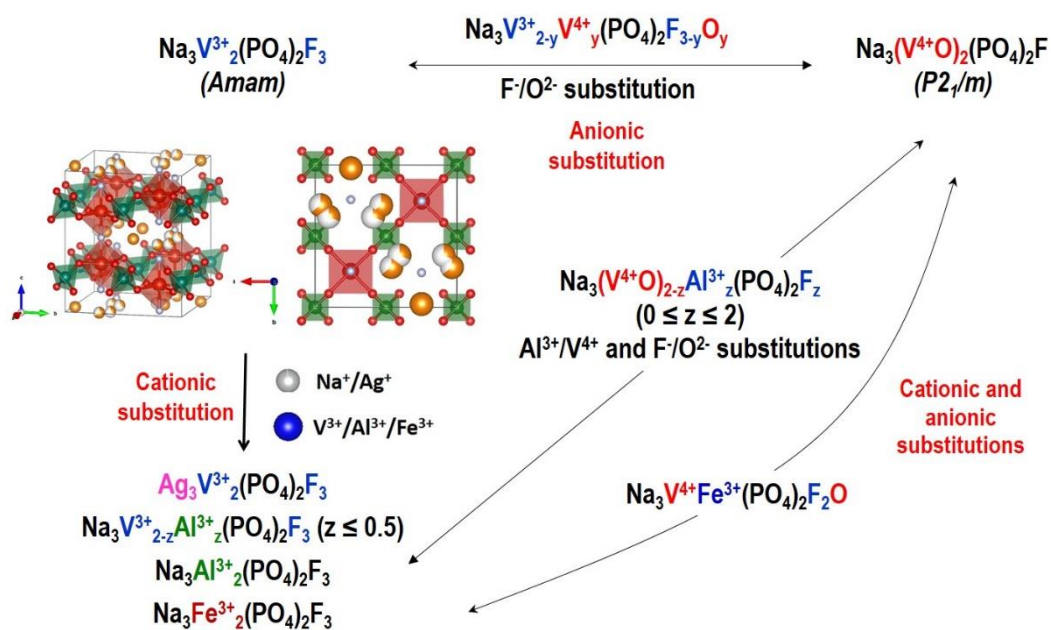


Figure 5.1 : Structural relationship between $\text{Na}_3\text{V}_2(\text{PO}_4)_2\text{F}_3$, $\text{Na}_3(\text{VO})_2(\text{PO}_4)_2\text{F}$ and their derivatives.

The Na^+ ions in $\text{Na}_3\text{V}_2(\text{PO}_4)_2\text{F}_3$ are relatively mobile and they can be replaced by Li^+ , K^+ or Ag^+ leading to the formation of $\text{Li}_3\text{V}_2(\text{PO}_4)_2\text{F}_3$, $\text{K}_3\text{V}_2(\text{PO}_4)_2\text{F}_3$ and $\text{Ag}_3\text{V}_2(\text{PO}_4)_2\text{F}_3$, respectively. These new materials adopt the same structure as similar to that of $\text{Na}_3\text{V}_2(\text{PO}_4)_2\text{F}_3$ with a subtle orthorhombic distortion, nonetheless this distortion is more pronounced in $\text{Ag}_3\text{V}_2(\text{PO}_4)_2\text{F}_3$ than in other homologues. This observation proved that the arrangement of monovalent ions in the diffusion channels is the origin of the orthorhombic distortion.

The V^{3+} ion in $\text{Na}_3\text{V}_2(\text{PO}_4)_2\text{F}_3$ can be replaced by Cr^{3+} , Al^{3+} , Fe^{3+} and Ga^{3+} leading to the formation of $\text{Na}_3\text{Cr}_2(\text{PO}_4)_2\text{F}_3$, $\text{Na}_3\text{Al}_2(\text{PO}_4)_2\text{F}_3$, $\text{Na}_3\text{Fe}_2(\text{PO}_4)_2\text{F}_3$ and $\text{Na}_3\text{Ga}_2(\text{PO}_4)_2\text{F}_3$, respectively. The structural framework of these phases were constructed by the interconnection between $\text{M}_2\text{O}_8\text{F}_3$ bioctahedra and PO_4 groups, but their structures at ambient temperature were indexed in different space groups due to a difference in the Na^+ distribution. In this study, a solid solution between $\text{Na}_3\text{V}_2(\text{PO}_4)_2\text{F}_3$ and $\text{Na}_3\text{Al}_2(\text{PO}_4)_2\text{F}_3$ was discovered and the solubility of Al^{3+} in $\text{Na}_3\text{V}_2(\text{PO}_4)_2\text{F}_3$ was limited to $z = 0.5$ (**Figure 5.1**), and all these Al^{3+} -substituted $\text{Na}_3\text{V}_{2-z}\text{Al}_z(\text{PO}_4)_2\text{F}_3$ presented a subtle orthorhombic distortion.

Cationic and anionic substitutions can occur simultaneously on the crystal structure of $\text{Na}_3(\text{VO})_2(\text{PO}_4)_2\text{F}$, and this lead to the formation of two different kinds of materials $\text{Na}_3(\text{VO})\text{Fe}(\text{PO}_4)_2\text{F}_2$ and $\text{Na}_3(\text{VO})_{2-z}\text{Al}_z(\text{PO}_4)_2\text{F}_{1+z}$ ($0 \leq z \leq 2$). In the case of Fe^{3+} substitution, only one composition was achieved whereas a full-range solid solution was obtained for Al^{3+} . These are the rare examples in the field of solid-state chemistry where a double cationic-anionic substitution can occur at the same time. The orthorhombic distortion was completely suppressed in these phases and their structures were indexed in a tetragonal cell. The random distribution of the anion and cation in this case seemed to be the reason for the suppression of the orthorhombic distortion.

In terms of electrochemistry, two Na^+ ions can be extracted and reinserted reversibly for all the $\text{Na}_3\text{V}^{3+}_{2-y'}\text{V}^{4+}_{y'}(\text{PO}_4)_2\text{F}_{3-y'}\text{O}_{y'}$ ($0 \leq y' \leq 2$) phases. Among them, $\text{Na}_3\text{V}_2(\text{PO}_4)_2\text{F}_3$ had the highest Na^+ extraction voltage. Upon oxygen substitution, the vanadyl bond was formed together with a shift of the Na^+ extraction voltage to a lower value. The Na^+ extraction from $\text{Na}_3\text{V}_2(\text{PO}_4)_2\text{F}_3$ and $\text{Na}_3(\text{VO})_2(\text{PO}_4)_2\text{F}$ occurred through bi-phasic mechanism with the formation of several intermediate phases. In the oxygen-

substituted compositions, the voltage evolved continuously upon charge with no formation of any Na^+ -vacancy ordering. The random distribution of oxygen and fluorine on the terminal positions could be the main reason for the disruption of Na^+ -vacancy ordering in the diffusion channels. When going to the high-voltage region, an irreversible structural modification was observed for $\text{Na}_3\text{V}_2(\text{PO}_4)_2\text{F}_3$ while all the other phases were completely stable even though the same floating time were applied for all the compositions. Therefore, the presence of the vanadyl bond could be considered as a crucial factor to stabilize these structural frameworks.

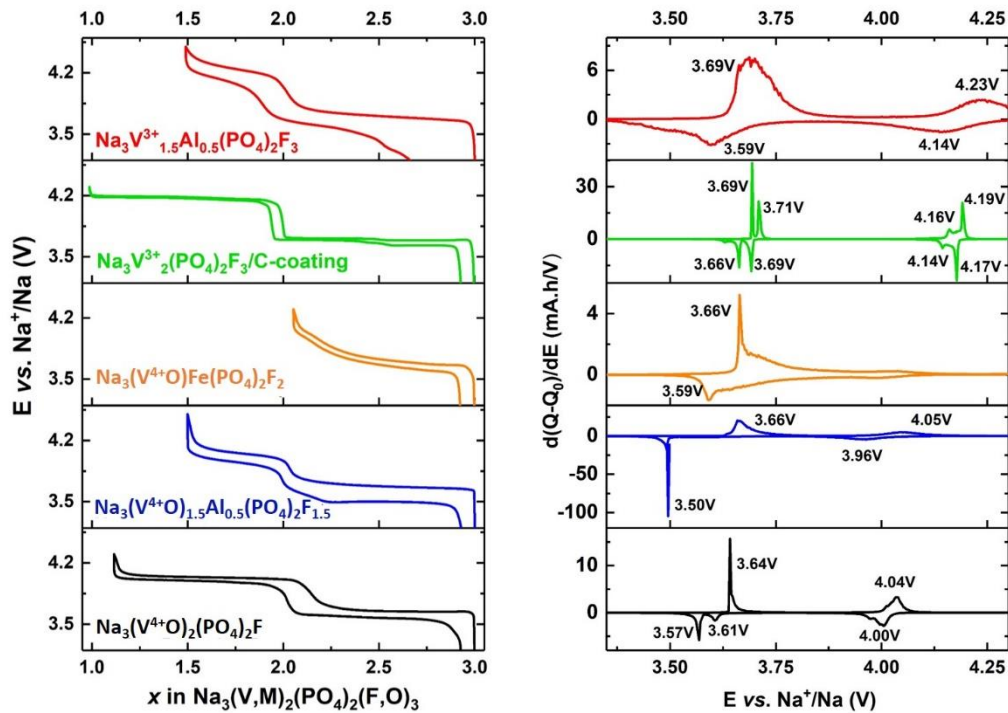


Figure 5.2 : Comparing the electrochemical properties of different $\text{Na}_3(\text{V},\text{M})_2(\text{PO}_4)_2(\text{F},\text{O})_3$ phases.

In $\text{Na}_3\text{V}_{2-z}\text{Al}_z(\text{PO}_4)_2\text{F}_3$ ($0 \leq z \leq 0.5$), only the $\text{V}^{4+}/\text{V}^{3+}$ redox couple could be activated while the electroactivity of $\{\text{V}^{5+}=\text{O}\}^{3+}/\{\text{V}^{4+}=\text{O}\}^{2+}$ was detected for $\text{Na}_3(\text{VO})\text{Fe}(\text{PO}_4)_2\text{F}_2$ and $\text{Na}_3(\text{VO})_{2-z}\text{Al}_z(\text{PO}_4)_2\text{F}_{1+z}$ ($0 \leq z \leq 2$). The redox potential of the $\text{V}^{4+}/\text{V}^{3+}$ and $\{\text{V}^{5+}=\text{O}\}^{3+}/\{\text{V}^{4+}=\text{O}\}^{2+}$ couples appeared to be unlikely affected by the presence of the foreign ions, such as Al^{3+} or Fe^{3+} . The long distance between two metal sites in the same bioctahedra ($\sim 4.2 \text{ \AA}$) might prevent a foreign metal ion from having significant influence on the electronic structure of the opposite vanadium site. In all these compositions, the Na^+ extraction occurred through solid solution mechanism and the random distribution of the anion and cations in these cases could even prevent the charge

ordering upon cycling. The presence of Fe^{3+} seemed to enhance the Na^+ diffusivity while the Al^{3+} substitution might increase the ionicity of its chemical bonds and thus enhance the stability of the structure. Combining these effects, one might expect the existence of the $\text{Na}_3(\text{V},\text{Al},\text{Fe})_2(\text{PO}_4)_2(\text{F},\text{O})_3$ composition with an optimized content of Al^{3+} and Fe^{3+} that might result in a superior electrochemical performance than that of $\text{Na}_3\text{V}_2(\text{PO}_4)_2\text{F}_3$ or $\text{Na}_3(\text{VO})_2(\text{PO}_4)_2\text{F}$.

References:

- [1] D. Zhang, Q. Liu, Y. Li, Design of flow battery, Elsevier B.V., 2014. doi:10.1016/B978-0-444-59566-9.00003-X.
- [2] T.M. Lim, M. Ulaganathan, Q. Yan, Advances in membrane and stack design of redox flow batteries (RFBs) for medium- and large-scale energy storage, Elsevier Ltd., 2014. doi:10.1016/B978-1-78242-013-2.00014-5.
- [3] US Department of Energy, Storing Energy, Vanadium Redox Flow Batteries, Elsevier Inc., 2012. doi:10.1016/B978-0-12-803440-8/00012-9.
- [4] M. Kwiecien, P. Schröer, M. Kuipers, D.U. Sauer, Current research topics for lead-acid batteries, *Lead-Acid Batter. Futur. Automob.* (2017) 133–146. doi:10.1016/B978-0-444-63700-0.00004-0.
- [5] C. Chumchal, D. Kurzweil, Lead-acid battery operation in micro-hybrid and electrified vehicles, Elsevier B.V., 2017. doi:10.1016/B978-0-444-63700-0.00013-1.
- [6] J. Meiwes, Current distribution in lead/acid and nickel/cadmium accumulators, 27 (1989) 45–58.
- [7] <https://biodiversitylibrary.org/page/6194528>.
- [8] L.A. Parnell, S. Szpak, Thermal behaviour of Li/SOCl₂ batteries of thin cell design, *Electrochim. Acta.* 30 (1985) 913–922.
- [9] A.A. Butakov, D.A. Vaganov, V.B. Solomonov, Mechanism of explosions of Li/SOCl₂ power sources, *J. Power Sources.* 39 (1992) 375–377.
- [10] M.S. Whittingham, A.H. Thompson, Intercalation and lattice expansion in titanium disulfide, *J. Chem. Phys.* 62 (1975) 1588.
- [11] M.S. Whittingham, Electrical Energy Storage and Intercalation Chemistry, *Science* (80-.). 192 (1976) 1126–1127.
- [12] K. Mizushima, P.C. Jones, P.J. Wiseman, J.B. Goodenough, Li_xCoO₂ (0 < x ≤ 1): A new cathode material for batteries of high energy density, *Mater. Res. Bull.* 15 (1980) 783–789.
- [13] A. Yoshino, K. Sanechika, T. Nakajima, Secondary battery, US4668595A, US Patent. <https://patentimages.storage.googleapis.com/09/af/76/745061503b5807/US4668595.pdf>.
- [14] https://www.nissan-global.com/EN/TECHNOLOGY/OVERVIEW/li_ion_ev.html.
- [15] L. Croguennec, M.R. Palacin, Recent achievements on inorganic electrode materials for lithium-ion batteries, *J. Am. Chem. Soc.* 137 (2015) 3140–3156.
- [16] J. B. Goodenough, K.-S. Park, The Li-Ion Rechargeable Battery: A Perspective, *J. Am. Chem. Soc.* 135 (2013) 1167–1176.
- [17] A. Ponrouch, M.R. Palacin, On the road toward calcium-based batteries, *Curr. Opin. Electrochem.* 9 (2018) 1–7.
- [18] A. Ponrouch, J. Bitenc, R. Dominko, N. Lindahl, P. Johansson, M.R. Palacin, Multivalent rechargeable batteries, *Energy Storage Mater.* 20 (2019) 253–262.
- [19] R. Attias, M. Salama, B. Hirsch, Y. Goffer, D. Aurbach, Anode-Electrolyte Interfaces in Secondary Magnesium Batteries, *Joule.* 3 (2019) 27–52.
- [20] R. Liu, Z. Liang, Z. Gong, Y. Yang, Research Progress in Multielectron Reactions in Polyanionic Materials for Sodium-Ion Batteries, *Small Methods.* 3 (2019) 1800221.
- [21] D. Kundu, E. Talaie, V. Duffort, L.F. Nazar, The emerging chemistry of sodium ion batteries for electrochemical energy storage, *Angew. Chemie - Int. Ed.* 54 (2015) 3432–3448. doi:10.1002/anie.201410376.
- [22] V. Palomares, P. Serras, I. Villaluenga, K.B. Hueso, J. Carretero-González, T. Rojo, Na-ion batteries, recent advances and present challenges to become low cost energy storage systems, *Energy Environ. Sci.* 5 (2012) 5884–5901.
- [23] D. Larcher, J.-M. Tarascon, Towards greener and more sustainable batteries for electrical energy storage., *Nat. Chem.* 7 (2015) 19–29.

- [24] C.P. Grey, J.M. Tarascon, Sustainability and in situ monitoring in battery development, *Nat. Mater.* 16 (2016) 45–56.
- [25] J.W. Choi, D. Aurbach, Promise and reality of post-lithium-ion batteries with high energy densities, *Nat. Rev. Mater.* 1 (2016).
- [26] <https://natron.energy/>.
- [27] <https://www.faradion.co.uk/>.
- [28] <http://www.hinabattery.com/en/>.
- [29] <http://www.tiamat-energy.com/>.
- [30] J.-Y. Hwang, S.-T. Myung, Y.-K. Sun, Sodium-ion batteries: present and future, *Chem. Soc. Rev.* 46 (2017) 3529–3614.
- [31] <https://www.estabanell.cat/>.
- [32] <https://www.naiades.eu/>.
- [33] W. Luo, L. Hu, Na metal anode: “Holy Grail” for room-temperature Na-ion batteries?, *ACS Cent. Sci.* 1 (2015) 420–422.
- [34] B. Jache, P. Adelhelm, Use of graphite as a highly reversible electrode with superior cycle life for sodium-ion batteries by making use of co-intercalation phenomena, *Angew. Chemie - Int. Ed.* 53 (2014) 10169–10173.
- [35] K. Westman, R. Dugas, P. Jankowski, W. Wiczczyk, G. Gachot, M. Morcrette, E. Irisarri, A. Ponrouch, M.R. Palacín, J.M. Tarascon, P. Johansson, Diglyme Based Electrolytes for Sodium-Ion Batteries, *ACS Appl. Energy Mater.* 1 (2018) 2671–2680.
- [36] E. Irisarri, A. Ponrouch, M.R. Palacin, Review—Hard Carbon Negative Electrode Materials for Sodium-Ion Batteries, *J. Electrochem. Soc.* 162 (2015) A2476–A2482.
- [37] Z. Li, Z. Jian, X. Wang, I.A. Rodríguez-Pérez, C. Bommier, X. Ji, Hard carbon anodes of sodium-ion batteries: undervalued rate capability, *Chem. Commun.* 53 (2017) 2610–2613.
- [38] K. Wang, Y. Jin, S. Sun, Y. Huang, J. Peng, J. Luo, Q. Zhang, Y. Qiu, C. Fang, J. Han, Low-Cost and High-Performance Hard Carbon Anode Materials for Sodium-Ion Batteries, *ACS Omega.* 2 (2017) 1687–1695.
- [39] B. Shen, Y. You, Y. Niu, Y. Li, C. Dai, L. Hu, B. Guo, J. Jiang, S. Bao, M. Xu, Improving the Performance of Hard Carbon//Na₃V₂O₂(PO₄)₂F Sodium-Ion Full Cells by Utilizing the Adsorption Process of Hard Carbon, *ACS Appl. Mater. Interfaces.* 10 (2018) 16581–16587.
- [40] K. Xu, A. Von Cresce, Interfacing electrolytes with electrodes in Li ion batteries, *J. Mater. Chem.* 21 (2011) 9849–9864.
- [41] K. Xu, Electrolytes and interphases in Li-ion batteries and beyond, *Chem. Rev.* 114 (2014) 11503–11618.
- [42] K. Li, J. Zhang, D. Lin, D.W. Wang, B. Li, W. Lv, S. Sun, Y.B. He, F. Kang, Q.H. Yang, L. Zhou, T.Y. Zhang, Evolution of the electrochemical interface in sodium ion batteries with ether electrolytes, *Nat. Commun.* 10 (2019) 1–10.
- [43] S. Komaba, T. Ishikawa, N. Yabuuchi, W. Murata, A. Ito, Y. Ohsawa, Fluorinated ethylene carbonate as electrolyte additive for rechargeable Na batteries, *ACS Appl. Mater. Interfaces.* 3 (2011) 4165–4168.
- [44] N. Yabuuchi, K. Kubota, M. Dahbi, S. Komaba, Research development on sodium-ion batteries, *Chem Rev.* 114 (2014) 11636–11682.
- [45] S. Komaba, W. Murata, T. Ishikawa, N. Yabuuchi, T. Ozeki, T. Nakayama, A. Ogata, K. Gotoh, K. Fujiwara, Electrochemical Na insertion and solid electrolyte interphase for hard-carbon electrodes and application to Na-ion batteries, *Adv. Funct. Mater.* 21 (2011) 3859–3867.
- [46] A. Ponrouch, R. Dedryvere, D. Monti, A.E. Demet, J.M. Ateba Mba, L. Croguennec, C. Masquelier, P. Johansson, M.R. Palacin, Towards high energy density sodium ion batteries through electrolyte optimization, *Energy Environ. Sci.* 6 (2013) 2361–2369.
- [47] J. Zheng, Y. Zhao, X. Feng, W. Chen, Y. Zhao, Novel safer phosphonate-based gel polymer electrolytes for sodium-ion batteries with excellent cycling performance, *J. Mater. Chem. A.* 6

- (2018) 6559–6564.
- [48] E. Bekaert, L. Buannic, U. Lassi, A. Llordés, J. Salminen, *Electrolytes for Li- and Na-Ion Batteries: Concepts, Candidates, and the Role of Nanotechnology*, Elsevier Inc., 2017. doi:10.1016/B978-0-323-42977-1.00001-7.
- [49] Y. Wang, S. Song, C. Xu, N. Hu, J. Molenda, L. Lu, Development of solid-state electrolytes for sodium-ion battery – A short review, *Nano Mater. Sci.* 1 (2019) 91–100.
- [50] C. Delmas, J.-J. Braconnier, C. Fouassier, P. Hagenmuller, Electrochemical intercalation of sodium in Na_xCO_2 bronzes, *Solid State Ionics.* 3–4 (1981) 165–169.
- [51] C. Delmas, Sodium and Sodium-Ion Batteries: 50 Years of Research, *Adv. Energy Mater.* 8 (2018) 1–9.
- [52] Q. Bai, L. Yang, H. Chen, Y. Mo, Computational Studies of Electrode Materials in Sodium-Ion Batteries, *Adv. Energy Mater.* 8 (2018) 1–29.
- [53] A.J. Toumar, S.P. Ong, W.D. Richards, S. Dacek, G. Ceder, Vacancy Ordering in O3-Type Layered Metal Oxide Sodium-Ion Battery Cathodes, *Phys. Rev. Appl.* 4 (2015) 1–9.
- [54] X. Li, X. Ma, D. Su, L. Liu, R. Chisnell, S.P. Ong, H. Chen, A. Toumar, J.C. Idrobo, Y. Lei, J. Bai, F. Wang, J.W. Lynn, Y.S. Lee, G. Ceder, Direct visualization of the Jahn-Teller effect coupled to Na ordering in $\text{Na}_{5/8}\text{MnO}_2$, *Nat. Mater.* 13 (2014) 586–592.
- [55] H. Wang, B. Yang, X.Z. Liao, J. Xu, D. Yang, Y.S. He, Z.F. Ma, Electrochemical properties of P2- $\text{Na}_{2/3}[\text{Ni}_{1/3}\text{Mn}_{2/3}]\text{O}_2$ cathode material for sodium ion batteries when cycled in different voltage ranges, *Electrochim. Acta.* 113 (2013) 200–204.
- [56] Y. Liu, X. Fang, A. Zhang, C. Shen, Q. Liu, H.A. Enaya, C. Zhou, Layered P2- $\text{Na}_{2/3}[\text{Ni}_{1/3}\text{Mn}_{2/3}]\text{O}_2$ as high-voltage cathode for sodium-ion batteries: The capacity decay mechanism and Al_2O_3 surface modification, *Nano Energy.* 27 (2016) 27–34.
- [57] D. Yuan, X. Liang, L. Wu, Y. Cao, X. Ai, J. Feng, H. Yang, ChemInform Abstract: A Honeycomb-Layered $\text{Na}_3\text{Ni}_2\text{SbO}_6$: A High-Rate and Cycle-Stable Cathode for Sodium-Ion Batteries. , *ChemInform.* 45 (2014) no-no. doi:10.1002/chin.201446013.
- [58] J. Ma, S.H. Bo, L. Wu, Y. Zhu, C.P. Grey, P.G. Khalifah, Ordered and disordered polymorphs of $\text{Na}(\text{Ni}_{2/3}\text{Sb}_{1/3})\text{O}_2$: Honeycomb-ordered cathodes for Na-ion batteries, *Chem. Mater.* 27 (2015) 2387–2399.
- [59] W. Schmidt, R. Berthelot, A.W. Sleight, M.A. Subramanian, Solid solution studies of layered honeycomb-ordered phases $\text{O}_3\text{-Na}_3\text{M}_2\text{SbO}_6$ (M=Cu, Mg, Ni, Zn), *J. Solid State Chem.* 201 (2013) 178–185.
- [60] H. Xu, S. Guo, H. Zhou, Review on anionic redox in sodium-ion batteries, *J. Mater. Chem. A.* (2019). doi:10.1039/c9ta06389g.
- [61] B. Mortemard De Boisse, G. Liu, J. Ma, S.I. Nishimura, S.C. Chung, H. Kiuchi, Y. Harada, J. Kikkawa, Y. Kobayashi, M. Okubo, A. Yamada, Intermediate honeycomb ordering to trigger oxygen redox chemistry in layered battery electrode, *Nat. Commun.* 7 (2016) 1–9.
- [62] M.H.N. Assadi, M. Okubo, A. Yamada, Y. Tateyama, Oxygen redox promoted by Na excess and covalency in hexagonal and monoclinic $\text{Na}_{2-x}\text{RuO}_3$ polymorphs, *J. Electrochem. Soc.* 166 (2019) A5343–A5348.
- [63] H. Koga, L. Croguennec, M. Menetrier, K. Douhil, S. Belin, L. Bourgeois, E. Suard, F. Weill, C. Delmas, Reversible Oxygen Participation to the Redox Processes Revealed for $\text{Li}_{1.20}\text{Mn}_{0.54}\text{Co}_{0.13}\text{Ni}_{0.13}\text{O}_2$, *J. Electrochem. Soc.* 160 (2013) A786–A792.
- [64] H. Koga, L. Croguennec, M. Ménétrier, P. Mannesiez, F. Weill, C. Delmas, S. Belin, Operando X-ray Absorption Study of the Redox Processes Involved upon Cycling of the Li-Rich Layered Oxide $\text{Li}_{1.20}\text{Mn}_{0.54}\text{Co}_{0.13}\text{Ni}_{0.13}\text{O}_2$ in Li Ion Batteries, *J. Phys. Chem. C.* 118 (2014) 5700–5709.
- [65] H. Koga, L. Croguennec, M. Ménétrier, P. Mannesiez, F. Weill, C. Delmas, Different oxygen redox participation for bulk and surface: A possible global explanation for the cycling mechanism of $\text{Li}_{1.20}\text{Mn}_{0.54}\text{Co}_{0.13}\text{Ni}_{0.13}\text{O}_2$, *J. Power Sources.* 236 (2013) 250–258.
- [66] C. Genevois, H. Koga, L. Croguennec, M. Ménétrier, C. Delmas, F. Weill, Insight into the atomic structure of cycled lithium-rich layered oxide $\text{Li}_{1.20}\text{Mn}_{0.54}\text{Co}_{0.13}\text{Ni}_{0.13}\text{O}_2$ using HAADF STEM and electron nanodiffraction, *J. Phys. Chem. C.* 119 (2015) 75–83.

- [67] P.F. Wang, Y. You, Y.X. Yin, Y.G. Guo, Layered Oxide Cathodes for Sodium-Ion Batteries: Phase Transition, Air Stability, and Performance, *Adv. Energy Mater.* 8 (2018) 1–23.
- [68] Y.N. Zhou, P.F. Wang, X.D. Zhang, L.B. Huang, W.P. Wang, Y.X. Yin, S. Xu, Y.G. Guo, Air-Stable and High-Voltage Layered P3-Type Cathode for Sodium-Ion Full Battery, *ACS Appl. Mater. Interfaces.* 11 (2019) 24184–24191.
- [69] J. Deng, W. Bin Luo, X. Lu, Q. Yao, Z. Wang, H.K. Liu, H. Zhou, S.X. Dou, High Energy Density Sodium-Ion Battery with Industrially Feasible and Air-Stable O3-Type Layered Oxide Cathode, *Adv. Energy Mater.* 8 (2018) 1–9.
- [70] S. Chu, H. Sun, G. Chen, Y. Chen, W. Zhou, Z. Shao, Rationally designed Water-Insertable Layered Oxides with Synergistic Effect of Transition-Metal Elements for High-Performance Oxygen Evolution Reaction, *ACS Appl. Mater. Interfaces.* 11 (2019) 25227–25235.
- [71] S. Boyd, R. Dhall, J.M. Lebeau, V. Augustyn, Charge storage mechanism and degradation of P2-type sodium transition metal oxides in aqueous electrolytes, *J. Mater. Chem. A.* 6 (2018) 22266–22276.
- [72] M. Duffiet, M. Blangero, P.E. Cabelguen, C. Delmas, D. Carlier, Influence of the Initial Li/Co Ratio in LiCoO_2 on the High-Voltage Phase-Transitions Mechanisms, *J. Phys. Chem. Lett.* 9 (2018) 5334–5338.
- [73] J. Gopalakrishnan, K. Kasthuri Rangan, $\text{V}_2(\text{PO}_4)_3$: A Novel NASICON-Type Vanadium Phosphate Synthesized by Oxidative Deintercalation of Sodium from $\text{Na}_3\text{V}_2(\text{PO}_4)_3$, *Chem. Mater.* 4 (1992) 747–749.
- [74] J.-N. Chotard, G. Rousse, R. David, O. Mentré, M. Courty, C. Masquelier, Discovery of a Sodium-Ordered Form of $\text{Na}_3\text{V}_2(\text{PO}_4)_3$ below Ambient Temperature, *Chem. Mater.* 27 (2015) 5982–5987.
- [75] L. Sharma, K. Nakamoto, R. Sakamoto, S. Okada, P. Barpanda, $\text{Na}_2\text{FePO}_4\text{F}$ Fluorophosphate as Positive Insertion Material for Aqueous Sodium-Ion Batteries, *ChemElectroChem.* 6 (2019) 444–449.
- [76] R. Ling, S. Cai, S. Shen, X. Hu, D. Xie, F. Zhang, X. Sun, N. Yu, F. Wang, Synthesis of carbon coated $\text{Na}_2\text{FePO}_4\text{F}$ as cathode materials for high-performance sodium ion batteries, *J. Alloys Compd.* 704 (2017) 631–640.
- [77] C. Masquelier, L. Croguennec, Polyanionic (phosphates, silicates, sulfates) frameworks as electrode materials for rechargeable Li (or Na) batteries, *Chem. Rev.* 113 (2013) 6552–6591.
- [78] J.-M.A. Mba, L. Croguennec, N.I. Basir, J. Barker, C. Masquelier, Lithium Insertion or Extraction from/into Tavorite-Type LiVPO_4F : An In Situ X-ray Diffraction Study, *J. Electrochem. Soc.* 159 (2012) A1171–A1175.
- [79] K. Trad, D. Carlier, L. Croguennec, A. Wattiaux, M. Ben Amara, C. Delmas, $\text{Na}_3\text{Fe}_3(\text{PO}_4)_3$ Alluaudite Phase: Synthesis, Structure, and Electrochemical Properties As Positive Electrode in Lithium and Sodium Batteries, *Chem. Mater.* 22 (2010) 5554–5562.
- [80] K.H. Ha, S.H. Woo, D. Mok, N.S. Choi, Y. Park, S.M. Oh, Y. Kim, J. Kim, J. Lee, L.F. Nazar, K.T. Lee, $\text{Na}_{4-\alpha}\text{M}_{2+\alpha/2}(\text{P}_2\text{O}_7)_2$ ($2/3 \leq \alpha \leq 7/8$, $\text{M} = \text{Fe}, \text{Fe}_{0.5}\text{Mn}_{0.5}, \text{Mn}$): A promising sodium ion cathode for na-ion batteries, *Adv. Energy Mater.* 3 (2013) 770–776.
- [81] S.M. Oh, S.T. Myung, J. Hassoun, B. Scrosati, Y.K. Sun, Reversible NaFePO_4 electrode for sodium secondary batteries, *Electrochem. Commun.* 22 (2012) 149–152.
- [82] J.-M. Le Meins, M.-P. Crosnier-Lopez, A. Hemon-Ribaud, G. Courbion, Phase Transitions in the $\text{Na}_3\text{M}_2(\text{PO}_4)_2\text{F}_3$ family ($\text{M} = \text{Al}^{3+}, \text{V}^{3+}, \text{Cr}^{3+}, \text{Fe}^{3+}, \text{Ga}^{3+}$): Synthesis, Thermal, Structural, and Magnetic Studies, *J. Solid State Chem.* 148 (1999) 260–277.
- [83] M. Bianchini, N. Brisset, F. Fauth, F. Weill, E. Elkaim, E. Suard, C. Masquelier, L. Croguennec, $\text{Na}_3\text{V}_2(\text{PO}_4)_2\text{F}_3$ revisited: A high-resolution diffraction study, *Chem. Mater.* 26 (2014) 4238–4247.
- [84] A.J. Fernández-Ropero, M. Zarrabeitia, M. Reynaud, T. Rojo, M. Casas-Cabanas, Toward Safe and Sustainable Batteries: $\text{Na}_4\text{Fe}_3(\text{PO}_4)_2\text{P}_2\text{O}_7$ as a Low-Cost Cathode for Rechargeable Aqueous Na-Ion Batteries, *J. Phys. Chem. C.* 122 (2018) 133–142.
- [85] J.M. Clark, P. Barpanda, A. Yamada, M.S. Islam, Sodium-ion battery cathodes $\text{Na}_2\text{FeP}_2\text{O}_7$ and $\text{Na}_2\text{MnP}_2\text{O}_7$: diffusion behaviour for high rate performance, *J. Mater. Chem. A.* 2 (2014) 11807–11812.

- [86] A. Manthiram, J.B. Goodenough, Lithium insertion into $\text{Fe}_2(\text{MO}_4)_3$ frameworks: Comparison of $\text{M} = \text{W}$ with $\text{M} = \text{Mo}$, *J. Solid State Chem.* 71 (1987) 349–360.
- [87] A.K. Padhi, V. Manivannan, J.B. Goodenough, Tuning the position of the redox couples in materials with NASICON structure by anionic substitution, *J. Electrochem. Soc.* 145 (1998) 1518–1520.
- [88] A. Manthiram, J.B. Goodenough, Lithium Insertion into $\text{Fe}_2(\text{SO}_4)_3$ Frameworks, *J. Power Sources.* 26 (1989) 403–408.
- [89] C. Housecroft, A. Sharpe, *Inorganic Chemistry*, 2005.
- [90] C. Masquelier, A.K. Padhi, K.S. Nanjundaswamy, J.B. Goodenough, New Cathode Materials for Rechargeable Lithium Batteries : The 3-D Framework Structures $\text{Li}_3\text{Fe}_2(\text{XO}_4)_3$ ($\text{X} = \text{P}, \text{As}$), *J. Solid State Chem.* 234 (1998) 228–234.
- [91] A.K. Padhi, K.S. Nanjundaswamy, C. Masquelier, J.B. Goodenough, Mapping of transition metal redox energies in phosphates with NASICON structure by lithium intercalation, *J. Electrochem. Soc.* 144 (1997) 2581–2586.
- [92] A.K. Padhi, Effect of Structure on the $\text{Fe}^{3+}/\text{Fe}^{2+}$ Redox Couple in Iron Phosphates, *J. Electrochem. Soc.* 144 (1997) 1609.
- [93] C.C. Torardi, E. Prince, Structure of the lithium insertion compound $\text{Li}_2\text{Fe}_2(\text{MoO}_4)_3$ from neutron powder diffraction data, *Mater. Res. Bull.* 21 (1986) 719–726.
- [94] G. Barim, P. Cottingham, S. Zhou, B.C. Melot, R.L. Brutchey, Investigating the Mechanism of Reversible Lithium Insertion into Anti-NASICON $\text{Fe}_2(\text{WO}_4)_3$, *ACS Appl. Mater. Interfaces.* 9 (2017) 10813–10819.
- [95] K.S. Nanjundaswamy, A.K. Padhi, J.B. Goodenough, S. Okada, H. Ohtsuka, H. Arai, J. Yamaki, Synthesis, redox potential evaluation and electrochemical characteristics of NASICON-related-3D framework compounds, *Solid State Ionics.* 92 (1996) 1–10.
- [96] H. Ben Yahia, R. Essehli, R. Amin, K. Boulahya, T. Okumura, I. Belharouak, Sodium intercalation in the phosphosulfate cathode $\text{NaFe}_2(\text{PO}_4)(\text{SO}_4)_2$, *J. Power Sources.* 382 (2018) 144–151.
- [97] K. Shiva, P. Singh, W. Zhou, J.B. Goodenough, $\text{NaFe}_2\text{PO}_4(\text{SO}_4)_2$: A potential cathode for a Na-ion battery, *Energy Environ. Sci.* 9 (2016) 3103–3106.
- [98] L.H.B. Nguyen, T. Broux, P.S. Camacho, D. Denux, L. Bourgeois, S. Belin, A. Iadecola, F. Fauth, D. Carlier, J. Olchowka, C. Masquelier, L. Croguennec, Stability in water and electrochemical properties of the $\text{Na}_3\text{V}_2(\text{PO}_4)_2\text{F}_3 - \text{Na}_3(\text{VO})_2(\text{PO}_4)_2\text{F}$ solid solution, *Energy Storage Mater.* 20 (2019).
- [99] P. Serras, V. Palomares, A. Goñi, I. Gil de Muro, P. Kubiak, L. Lezama, T. Rojo, High voltage cathode materials for Na-ion batteries of general formula $\text{Na}_3\text{V}_2\text{O}_{2x}(\text{PO}_4)_2\text{F}_{3-2x}$, *J. Mater. Chem.* 22 (2012) 22301.
- [100] Y. Park, D. Seo, H. Kwon, B. Kim, J. Kim, H. Kim, I. Kim, H. Yoo, K. Kang, A New High-Energy Cathode for a Na-Ion Battery with Ultrahigh Stability, *J. Am. Chem. Soc.* 135 (2013) 13870–13878.
- [101] Y.U. Park, D.H. Seo, H. Kim, J. Kim, S. Lee, B. Kim, K. Kang, A family of high-performance cathode materials for Na-ion batteries, $\text{Na}_3(\text{VO}_{1-x}\text{PO}_4)_2\text{F}_{1+2x}$ ($0 \leq x \leq 1$): Combined first-principles and experimental study, *Adv. Funct. Mater.* 24 (2014) 4603–4614.
- [102] F. Chen, V.M. Kovrugin, R. David, O. Mentré, F. Fauth, J. Chotard, C. Masquelier, A NASICON-Type Positive Electrode for Na Batteries with High Energy Density: $\text{Na}_4\text{MnV}(\text{PO}_4)_3$, *Small Methods.* 1800218 (2018) 1800218.
- [103] W. Zhou, L. Xue, X. Lü, H. Gao, Y. Li, S. Xin, G. Fu, Z. Cui, Y. Zhu, J.B. Goodenough, $\text{Na}_x\text{MV}(\text{PO}_4)_3$ ($\text{M} = \text{Mn}, \text{Fe}, \text{Ni}$) Structure and Properties for Sodium Extraction, *Nano Lett.* 16 (2016) 7836–7841.
- [104] A.M. Abakumov, M. V. Zakharkin, O.A. Drozhzhin, E. V. Antipov, D. Chernyshov, I. V. Tereshchenko, K.J. Stevenson, Enhancing Na^+ Extraction Limit through High Voltage Activation of the NASICON-Type $\text{Na}_4\text{MnV}(\text{PO}_4)_3$ Cathode, *ACS Appl. Energy Mater.* 1 (2018) 5842–5846.
- [105] J. Barker, M.Y. Saidi, J.L. Swoyer, A Comparative Investigation of the Li Insertion Properties of the Novel Fluorophosphate Phases, NaVPO_4F and LiVPO_4F , *J. Electrochem. Soc.* 151 (2004) A1670.

- [106] H. Zhuo, X. Wang, A. Tang, Z. Liu, S. Gamboa, P.J. Sebastian, The preparation of $\text{NaV}_{1-x}\text{Cr}_x\text{PO}_4\text{F}$ cathode materials for sodium-ion battery, *J. Power Sources*. 160 (2006) 698–703.
- [107] N. Kosova, D. Rezepova, $\text{Na}_{1+y}\text{VPO}_4\text{F}_{1+y}$ ($0 \leq y \leq 0.5$) as Cathode Materials for Hybrid Na/Li Batteries, *Inorganics*. 5 (2017) 19.
- [108] M. Law, P. Balaya, NaVPO_4F with high cycling stability as a promising cathode for sodium-ion battery, *Energy Storage Mater.* 10 (2018) 102–113.
- [109] J. Zhao, J. He, X. Ding, J. Zhou, Y. Ma, S. Wu, R. Huang, A novel sol-gel synthesis route to NaVPO_4F as cathode material for hybrid lithium ion batteries, *J. Power Sources*. 195 (2010) 6854–6859.
- [110] L. Li, Y. Xu, X. Sun, R. Chang, Y. Zhang, X. Zhang, J. Li, Fluorophosphates from Solid-State Synthesis and Electrochemical Ion Exchange: NaVPO_4F or $\text{Na}_3\text{V}_2(\text{PO}_4)_2\text{F}_3$?, *Adv. Energy Mater.* 8 (2018) 1–9.
- [111] E. Boivin, J.N. Chotard, T. Bamine, D. Carlier, P. Serras, V. Palomares, T. Rojo, A. Iadecola, L. Dupont, L. Bourgeois, F. Fauth, C. Masquelier, L. Croguennec, Vanadyl-type defects in Tavorite-like NaVPO_4F : From the average long range structure to local environments, *J. Mater. Chem. A*. 5 (2017) 25044–25055.
- [112] C. Delmas, R. Olazcuaga, F. Cherkaoui, R. Brochu, G. Le Flem, A new family of phosphates with the formula $\text{Na}_3\text{M}_2(\text{PO}_4)_3$ ($\text{M} = \text{Ti}, \text{V}, \text{Cr}, \text{Fe}$), *C. R. Seances Acad. Sci., Ser. C*. 287 (1978) 169–174.
- [113] F. Lalère, V. Seznec, M. Courty, R. David, J.N. Chotard, C. Masquelier, Improving the energy density of $\text{Na}_3\text{V}_2(\text{PO}_4)_3$ -based positive electrodes through V/Al substitution, *J. Mater. Chem. A*. 3 (2015) 16198–16205.
- [114] W. Ren, Z. Zheng, C. Xu, C. Niu, Q. Wei, Q. An, K. Zhao, M. Yan, M. Qin, L. Mai, Self-sacrificed synthesis of three-dimensional $\text{Na}_3\text{V}_2(\text{PO}_4)_3$ nanofiber network for high-rate sodium-ion full batteries, *Nano Energy*. 25 (2016) 145–153.
- [115] Z. Jian, L. Zhao, H. Pan, Y.S. Hu, H. Li, W. Chen, L. Chen, Carbon coated $\text{Na}_3\text{V}_2(\text{PO}_4)_3$ as novel electrode material for sodium ion batteries, *Electrochem. Commun.* 14 (2012) 86–89.
- [116] Z. Jian, W. Han, X. Lu, H. Yang, Y.S. Hu, J. Zhou, Z. Zhou, J. Li, W. Chen, D. Chen, L. Chen, Superior electrochemical performance and storage mechanism of $\text{Na}_3\text{V}_2(\text{PO}_4)_3$ cathode for room-temperature sodium-ion batteries, *Adv. Energy Mater.* 3 (2013) 156–160.
- [117] F. Lalère, V. Seznec, M. Courty, J.N. Chotard, C. Masquelier, Coupled X-ray diffraction and electrochemical studies of the mixed Ti/V-containing NASICON: $\text{Na}_2\text{TiV}(\text{PO}_4)_3$, *J. Mater. Chem. A*. 6 (2018) 6654–6659.
- [118] R. Jalem, R. Natsume, M. Nakayama, T. Kasuga, First-Principles Investigation of the Na+Ion Transport Property in Oxyfluorinated Titanium(IV) Phosphate $\text{Na}_3\text{Ti}_2\text{P}_2\text{O}_{10}\text{F}$, *J. Phys. Chem. C*. 120 (2016) 1438–1445.
- [119] S.T. Dacek, W.D. Richards, D.A. Kitchaev, G. Ceder, Structure and Dynamics of Fluorophosphate Na-Ion Battery Cathodes, *Chem. Mater.* 28 (2016) 5450–5460.
- [120] J. Barker, R.K.B. Gover, P. Burns, A.J. Bryan, Hybrid-Ion, *Electrochem. Solid-State Lett.* 9 (2006) A190.
- [121] R.K.B. Gover, A. Bryan, P. Burns, J. Barker, The electrochemical insertion properties of sodium vanadium fluorophosphate, $\text{Na}_3\text{V}_2(\text{PO}_4)_2\text{F}_3$, *Solid State Ionics*. 177 (2006) 1495–1500.
- [122] Y.U. Park, J. Bai, L. Wang, G. Yoon, W. Zhang, H. Kim, S. Lee, S.W. Kim, J.P. Looney, K. Kang, F. Wang, In Situ Tracking Kinetic Pathways of Li^+/Na^+ Substitution during Ion-Exchange Synthesis of $\text{Li}_x\text{Na}_{1.5-x}\text{VOPO}_4\text{F}_{0.5}$, *J. Am. Chem. Soc.* 139 (2017) 12504–12516.
- [123] N. V. Kosova, D.O. Rezepova, S.A. Petrov, A.B. Slobodyuk, Electrochemical and Chemical Na^+/Li^+ Ion Exchange in Na-Based Cathode Materials: $\text{Na}_{1.56}\text{Fe}_{1.22}\text{P}_2\text{O}_7$ and $\text{Na}_3\text{V}_2(\text{PO}_4)_2\text{F}_3$, *J. Electrochem. Soc.* 164 (2017) A6192–A6200.
- [124] N. V. Kosova, D.O. Rezepova, Mixed sodium-lithium vanadium fluorophosphates $\text{Na}_{3-x}\text{Li}_x\text{V}_2(\text{PO}_4)_2\text{F}_3$: The origin of the excellent high-rate performance, *J. Power Sources*. 408 (2018) 120–127.
- [125] M. Bianchini, F. Lalère, H.B.L. Nguyen, F. Fauth, R. David, E. Suard, L. Croguennec, C.

- Masquelier, $\text{Ag}_3\text{V}_2(\text{PO}_4)_2\text{F}_3$, a new compound obtained by Ag^+/Na^+ ion exchange into the $\text{Na}_3\text{V}_2(\text{PO}_4)_2\text{F}_3$ framework, *J. Mater. Chem. A*. 6 (2018) 10340–10347.
- [126] X. Lin, J. Huang, H. Tan, J. Huang, B. Zhang, $\text{K}_3\text{V}_2(\text{PO}_4)_2\text{F}_3$ as a robust cathode for potassium-ion batteries, *Energy Storage Mater.* 16 (2019) 97–101.
- [127] M. Bianchini, P. Xiao, Y. Wang, G. Ceder, Additional Sodium Insertion into Polyanionic Cathodes for Higher-Energy Na-Ion Batteries, *Adv. Energy Mater.* 7 (2017) 1700514.
- [128] I.L. Matts, S. Dacek, T.K. Pietrzak, R. Malik, G. Ceder, Explaining Performance-Limiting Mechanisms in Fluorophosphate Na-Ion Battery Cathodes through Inactive Transition-Metal Mixing and First-Principles Mobility Calculations, *Chem. Mater.* 27 (2015) 6008–6015.
- [129] M. Xu, P. Xiao, S. Stauffer, J. Song, G. Henkelman, J.B. Goodenough, Theoretical and experimental study of vanadium-based fluorophosphate cathodes for rechargeable batteries, *Chem. Mater.* 26 (2014) 3089–3097.
- [130] R.A. Shakoor, D.H. Seo, H. Kim, Y.U. Park, J. Kim, S.W. Kim, H. Gwon, S. Lee, K. Kang, A combined first principles and experimental study on $\text{Na}_3\text{V}_2(\text{PO}_4)_2\text{F}_3$ for rechargeable Na batteries, *J. Mater. Chem.* 22 (2012) 20535–20541.
- [131] T. Broux, F. Fauth, N. Hall, Y. Chatillon, M. Bianchini, T. Bamine, J. Leriche, E. Suard, D. Carlier, Y. Reynier, L. Simonin, C. Masquelier, L. Croguennec, High Rate Performance for Carbon-Coated $\text{Na}_3\text{V}_2(\text{PO}_4)_2\text{F}_3$ in Na-Ion Batteries, *Small Methods*. 3 (2019) 1800215.
- [132] M. Bianchini, F. Fauth, N. Brisset, F. Weill, E. Suard, C. Masquelier, Croguen, Comprehensive Investigation of the $\text{Na}_3\text{V}_2(\text{PO}_4)_2\text{F}_3$ – $\text{NaV}_2(\text{PO}_4)_2\text{F}_3$ System by Operando High Resolution Synchrotron X-ray Diffraction, *Chem. Mater.* 27 (2015) 3009–3020.
- [133] T. Broux, T. Bamine, L. Simonelli, L. Stievano, F. Fauth, M. Ménétrier, D. Carlier, C. Masquelier, L. Croguennec, V IV Disproportionation Upon Sodium Extraction From $\text{Na}_3\text{V}_2(\text{PO}_4)_2\text{F}_3$ Observed by Operando X-ray Absorption Spectroscopy and Solid-State NMR, *J. Phys. Chem. C*. 121 (2017) 4103–4111.
- [134] W. Massa, O. V. Yakubovich, O. V. Dimitrova, Crystal structure of a new sodium vanadyl(IV) fluoride phosphate $\text{Na}_3\{\text{V}_2\text{O}_2\text{F}[\text{PO}_4]_2\}$, *Solid State Sci.* 4 (2002) 495–501.
- [135] A.A. Tsirlin, R. Nath, A.M. Abakumov, Y. Furukawa, D.C. Johnston, M. Hemmida, H.A. Krug Von Nidda, A. Loidl, C. Geibel, H. Rosner, Phase separation and frustrated square lattice magnetism of $\text{Na}_{1.5}\text{VOPO}_4\text{F}_{0.5}$, *Phys. Rev. B - Condens. Matter Mater. Phys.* 84 (2011) 2–13.
- [136] F. Sauvage, E. Quarez, J.M. Tarascon, E. Baudrin, Crystal structure and electrochemical properties vs. Na^+ of the sodium fluorophosphate $\text{Na}_{1.5}\text{VOPO}_4\text{F}_{0.5}$, *Solid State Sci.* 8 (2006) 1215–1221.
- [137] P. Serras, V. Palomares, P. Kubiak, L. Lezama, T. Rojo, Enhanced electrochemical performance of vanadyl (IV) $\text{Na}_3(\text{VO})_2(\text{PO}_4)_2\text{F}$ by ex-situ carbon coating, *Electrochem. Commun.* 34 (2013) 344–347.
- [138] Y. Qi, L. Mu, J. Zhao, Y. Hu, H. Liu, S. Dai, Superior Na-Storage Performance of Low-Temperature-Synthesized $\text{Na}_3(\text{VO}_{1-x}\text{PO}_4)_2\text{F}_{1+2x}$ ($0 \leq x \leq 1$) Nanoparticles for Na-Ion Batteries, *Angew. Chemie*. 127 (2015) 10049–10054.
- [139] Z.Y. Gu, J.Z. Guo, Y. Yang, H.Y. Yu, X.T. Xi, X.X. Zhao, H.Y. Guan, X. He, X.L. Wu, Precisely controlled preparation of an advanced $\text{Na}_3\text{V}_2(\text{PO}_4)_2\text{O}_2\text{F}$ cathode material for sodium ion batteries: The optimization of electrochemical properties and electrode kinetics, *Inorg. Chem. Front.* 6 (2019) 988–995.
- [140] J.-Z. Guo, P.-F. Wang, X.-L. Wu, X.-H. Zhang, Q. Yan, H. Chen, J.-P. Zhang, Y.-G. Guo, High-Energy/Power and Low-Temperature Cathode for Sodium-Ion Batteries: In Situ XRD Study and Superior Full-Cell Performance, *Adv. Mater.* 29 (2017) 1701968.
- [141] Z. Mao, R. Wang, B. He, Y. Gong, H. Wang, Large-Area, Uniform, Aligned Arrays of $\text{Na}_3(\text{VO})_2(\text{PO}_4)_2\text{F}$ on Carbon Nanofiber for Quasi-Solid-State Sodium-Ion Hybrid Capacitors, *Small*. 3 (2019) 1902466.
- [142] Y. Qi, L. Mu, J. Zhao, Y.-S. Hu, H. Liu, S. Dai, Superior Na-Storage Performance of Low-Temperature-Synthesized $\text{Na}_3(\text{VO}_{1-x}\text{PO}_4)_2\text{F}_{1+2x}$ ($0 \leq x \leq 1$) Nanoparticles for Na-Ion Batteries, *Angew. Chemie Int. Ed.* 54 (2015) 9911–9916.
- [143] T. Broux, T. Bamine, F. Fauth, L. Simonelli, W. Olszewski, C. Marini, M. Ménétrier, D. Carlier, C. Masquelier, L. Croguennec, Strong Impact of the Oxygen Content in $\text{Na}_3\text{V}_2(\text{PO}_4)_2\text{F}_{3-y}\text{O}_y$ ($0 \leq y$

- ≤ 0.5) on Its Structural and Electrochemical Properties, *Chem. Mater.* 28 (2016) 7683–7692.
- [144] L.H.B. Nguyen, T. Broux, P.S. Camacho, D. Denux, L. Bourgeois, S. Belin, A. Iadecola, F. Fauth, D. Carlier, J. Olchowka, C. Masquelier, L. Croguennec, Stability in water and electrochemical properties of the $\text{Na}_3\text{V}_2(\text{PO}_4)_2\text{F}_3 - \text{Na}_3(\text{VO})_2(\text{PO}_4)_2\text{F}$ solid solution, *Energy Storage Mater.* 20 (2019) 324–334.
- [145] C. Li, M. Shen, X. Lou, B. Hu, Unraveling the Redox Couples of $\text{V}^{\text{III}}/\text{V}^{\text{IV}}$ Mixed-Valent $\text{Na}_3\text{V}_2(\text{PO}_4)_2\text{O}_{1.6}\text{F}_{1.4}$ Cathode by Parallel-Mode EPR and In Situ/Ex Situ NMR, *J. Phys. Chem. C.* 122 (2018) 27224–27232.
- [146] N. Sharma, P. Serras, V. Palomares, H.E.A. Brand, J. Alonso, P. Kubiak, M.L. Fdez-gubieda, T. Rojo, Sodium Distribution and Reaction Mechanisms of a $\text{Na}_3\text{V}_2\text{O}_2(\text{PO}_4)_2\text{F}$ Electrode during Use in a Sodium-Ion Battery, *Chem. Mater.* 26 (2014) 3391–3402.
- [147] T. Broux, B. Fleutot, R. David, A. Brüll, P. Veber, F. Fauth, M. Courty, L. Croguennec, C. Masquelier, Temperature Dependence of Structural and Transport Properties for $\text{Na}_3\text{V}_2(\text{PO}_4)_2\text{F}_3$ and $\text{Na}_3\text{V}_2(\text{PO}_4)_2\text{F}_{2.5}\text{O}_{0.5}$, *Chem. Mater.* 30 (2018) 358–365.
- [148] P.R. Kumar, Y.H. Jung, C.H. Lim, D.K. Kim, $\text{Na}_3\text{V}_2\text{O}_{2x}(\text{PO}_4)_2\text{F}_{3-2x}$: a stable and high-voltage cathode material for aqueous sodium-ion batteries with high energy density, *J. Mater. Chem. A Mater. Energy Sustain.* 3 (2015) 6271–6275.
- [149] S. Liu, L. Wang, J. Liu, M. Zhou, Q. Nian, Y. Feng, Z. Tao, L. Shao, $\text{Na}_3\text{V}_2(\text{PO}_4)_2\text{F}_3$ -SWCNT: a high voltage cathode for non-aqueous and aqueous sodium-ion batteries, *J. Mater. Chem. A.* 7 (2019) 248–256.
- [150] B. Zhang, R. Dugas, G. Rousse, P. Rozier, A.M. Abakumov, J.-M. Tarascon, Insertion compounds and composites made by ball milling for advanced sodium-ion batteries, *Nat. Commun.* 7 (2016) 10308.
- [151] M. Peng, D. Zhang, X. Wang, D. Xia, Y. Sun, G. Guo, Three-electron reversible redox for a high-energy fluorophosphate cathode: $\text{Na}_3\text{V}_2\text{O}_2(\text{PO}_4)_2\text{F}$, *Chem. Commun.* 55 (2019) 3979–3982.
- [152] G. Yan, S. Mariyappan, G. Rousse, Q. Jacquet, M. Deschamps, R. David, B. Mirvaux, J.W. Freeland, J. Tarascon, Higher energy and safer sodium ion batteries via an electrochemically made disordered $\text{Na}_3\text{V}_2(\text{PO}_4)_2\text{F}_3$ material, *Nat. Commun.* 10 (2019) 585.
- [153] H. Xiong, Y. Liu, H. Shao, Y. Yang, Understanding the electrochemical mechanism of high sodium selective material $\text{Na}_3\text{V}_2(\text{PO}_4)_2\text{F}_3$ in Li^+/Na^+ dual-ion batteries, *Electrochim. Acta.* 292 (2018) 234–246.
- [154] L.H.B. Nguyen, J. Olchowka, S. Belin, P. Sanz Camacho, M. Duttine, A. Iadecola, F. Fauth, D. Carlier, C. Masquelier, L. Croguennec, Monitoring the Crystal Structure and the Electrochemical Properties of $\text{Na}_3(\text{VO})_2(\text{PO}_4)_2\text{F}$ through Fe^{3+} Substitution, *ACS Appl. Mater. Interfaces.* 11 (2019) 38808–38818.
- [155] R.D. Shannon, C.T. Prewitt, Effective ionic radii in oxides and fluorides, *Acta Crystallogr. Sect. B Struct. Crystallogr. Cryst. Chem.* 25 (1969) 925–946.
- [156] J. Barker, R.K.B. Gover, P. Burns, A.J. Bryan, $\text{Li}_{4/3}\text{Ti}_{5/3}\text{O}_4 \parallel \text{Na}_3\text{V}_2(\text{PO}_4)_2\text{F}_3$: An example of a hybrid-ion cell using a non-graphitic anode, *J. Electrochem. Soc.* 154 (2007) 882–887.
- [157] N. Hall, S. Boulineau, S. Launois, L. Simonin, L. Croguennec, C. Masquelier, Method for preparing a $\text{Na}_3\text{V}_2(\text{PO}_4)_2\text{F}_3$ particular material, French Patent 2016.
- [158] J. Rodríguez-Carvajal, Recent advances in magnetic structure determination by neutron powder diffraction, *Phys. B Condens. Matter.* 192 (1993) 55–69.
- [159] V. Petříček, M. Dušek, L. Palatinus, Crystallographic Computing System JANA2006: General features, *Z. Krist.* 229 (2014) 345–352.
- [160] K. Momma, F. Izumi, VESTA: A three-dimensional visualization system for electronic and structural analysis, *J. Appl. Crystallogr.* 41 (2008) 653–658.
- [161] D. Massiot, F. Fayon, M. Capron, I. King, S. Le Calvé, B. Alonso, J. Durand, B. Bujoli, Z. Gan, G. Hoatson, Modelling one- and two-dimensional solid-state NMR spectra, *Magn. Reson. Chem.* 40 (2002) 70–76.
- [162] V. Briois, C. La Fontaine, S. Belin, L. Barthe, T. Moreno, V. Pinty, A. Carcy, R. Girardot, E. Fonda, ROCK: The new Quick-EXAFS beamline at SOLEIL, *J. Phys. Conf. Ser.* 712 (2016).

- [163] E. Fonda, A. Rochet, M. Ribbens, L. Barthe, S. Belin, V. Briois, The SAMBA quick-EXAFS monochromator: XAS with edge jumping, *J. Synchrotron Radiat.* 19 (2012) 417–424.
- [164] J.B. Leriche, S. Hamelet, J. Shu, M. Morcrette, C. Masquelier, G. Ouvrard, M. Zerrouki, P. Soudan, S. Belin, E. Elkaïm, F. Baudalet, An Electrochemical Cell for Operando Study of Lithium Batteries Using Synchrotron Radiation, *J. Electrochem. Soc.* 157 (2010) A606.
- [165] C. Lesage, E. Devers, C. Legens, G. Fernandes, O. Roudenko, V. Briois, High pressure cell for edge jumping X-ray absorption spectroscopy: Applications to industrial liquid sulfidation of hydrotreatment catalysts, *Catal. Today.* 336 (2019) 63–73.
- [166] J. Wong, F.W. Lytle, R.P. Messmer, D.H. Maylotte, K-edge absorption spectra of selected vanadium compounds, *Phys. Rev. B - Condens. Matter Mater. Phys.* 30 (1984).
- [167] B. Poumellec, V. Kraizman, Y. Aifa, R. Cortès, A. Novakovich, R. Vedrinskii, Experimental and theoretical studies of dipole and quadrupole contributions to the vanadium, *Phys. Rev. B - Condens. Matter Mater. Phys.* 58 (1998) 6133–6146.
- [168] Z.Y. Wu, D.C. Xian, T.D. Hu, Y.N. Xie, Y. Tao, C.R. Natoli, E. Paris, A. Marcelli, Quadrupolar transitions and medium-range-order effects in metal K -edge x-ray absorption spectra of 3 d transition-metal compounds, *Phys. Rev. B - Condens. Matter Mater. Phys.* 70 (2004) 1–4.
- [169] E. Boivin, R. David, J.-N. Chotard, T. Bamine, A. Iadecola, L. Bourgeois, E. Suard, F. Fauth, D. Carlier, C. Masquelier, L. Croguennec, $\text{LiVPO}_4\text{F}_{1-y}\text{O}_y$ Tavorite-Type Compositions : Influence of the Concentration of Vanadyl-Type Defects on the Structure and Electrochemical Performance, *Chem. Mater.* 30 (2018) 5682–5693.
- [170] B. Ravel, M. Newville, ATHENA, ARTEMIS, HEPHAESTUS: Data analysis for X-ray absorption spectroscopy using IFEFFIT, *J. Synchrotron Radiat.* 12 (2005) 537–541.
- [171] M.E. Tuckerman, A. Chandra, D. Marx, Structure and Dynamics of OH^- (aq), *Acc. Chem. Res.* 39 (2006) 151–158.
- [172] P. Serras, J. Alonso, N. Sharma, J. Miguel, P. Kubiak, M.L. Fdez-Gubieda, T. Rojo, Electrochemical Na Extraction/Insertion of $\text{Na}_3\text{V}_2\text{O}_{2x}(\text{PO}_4)_2\text{F}_{3-2x}$, *Chem. Mater.* 25 (2013) 4917–4925.
- [173] H. Deng, J. Wang, R. Callender, W.J. Ray, Relationship between Bond Stretching Frequencies and Internal Bonding for $[\text{}^{16}\text{O}_4]^-$ and $[\text{}^{18}\text{O}_4]^-$ Phosphates in Aqueous Solution, *J. Phys. Chem. B.* 102 (1998) 3617–3623.
- [174] D.L. Massart, B.G.M. Vandeginste, L.M.C. Buydens, S.D. Jong, P.J. Lewi, J. Smeyers-Verbeke, *Handbook of Chemometrics and Qualimetrics: Part A*, Elsevier: Amsterdam, 1997.
- [175] M. Fehse, A. Iadecola, M.T. Sougrati, P. Conti, M. Giorgetti, L. Stievano, Applying chemometrics to study battery materials: Towards the comprehensive analysis of complex operando datasets, *Energy Storage Mater.* 18 (2019) 328–337.
- [176] A. Darwiche, F. Murgia, M. Fehse, A. Mahmoud, A. Iadecola, S. Belin, C. La Fontaine, V. Briois, R.P. Hermann, B. Fraisse, R. Berthelot, M.T. Sougrati, L. Monconduit, L. Stievano, Operando X-ray absorption spectroscopy applied to battery materials at ICGM: The challenging case of BiSb's sodiation, *Energy Storage Mater.* 21 (2019) 1–13.
- [177] M. Garrido, M.S. Larrechi, F.X. Rius, R. Tauler, Calculation of band boundaries of feasible solutions obtained by Multivariate Curve Resolution–Alternating Least Squares of multiple runs of a reaction monitored by NIR spectroscopy, *Chemom. Intell. Lab. Syst.* 76 (2005) 111–120.
- [178] J. Jaumot, A. de Juan, R. Tauler, MCR-ALS GUI 2.0: New features and applications, *Chemom. Intell. Lab. Syst.* 140 (2015) 1–12.
- [179] H.R. Keller, D.L. Massart, Evolving factor analysis, *Chemom. Intell. Lab. Syst.* 12 (1991) 209–224.
- [180] W. Windig, Two-Way Data Analysis: Detection of Purest Variables, *Compr. Chemom.* 2 (2009) 275–307.
- [181] M. Maeder, A. de Juan, Two-Way Data Analysis: Evolving Factor Analysis, *Compr. Chemom.* 2 (2009) 261–274.
- [182] L.H.B. Nguyen, P. Sanz Camacho, T. Broux, C. Masquelier, L. Croguennec, D. Carlier, DFT-assisted ^{31}P and ^{23}Na MAS-NMR Study of the $\text{Na}_3\text{V}_2(\text{PO}_4)_2\text{F}_3 - \text{Na}_3\text{V}_2(\text{PO}_4)\text{FO}_2$ solid solution:

- unravelling the local structure and electronic structure, in: ECS 235th Meet., 2019.
- [183] E. Boivin, A. Iadecola, F. Fauth, J.-N. Chotard, C. Masquelier, L. Croguennec, Redox Paradox of Vanadium in Tavorite $\text{LiVPO}_4\text{F}_{1-y}\text{O}_y$, *Chem. Mater.* 31 (2019) 7367–7376.
- [184] E. Boivin, J.-N. Chotard, M. Ménétrier, L. Bourgeois, T. Bamine, D. Carlier, F. Fauth, C. Masquelier, L. Croguennec, Oxidation under Air of Tavorite LiVPO_4F : Influence of Vanadyl-Type Defects on Its Electrochemical Properties, *J. Phys. Chem. C.* 120 (2016) 26187–26198.
- [185] L.H.B. Nguyen, P. Sanz Camacho, T. Broux, J. Olchowka, C. Masquelier, L. Croguennec, D. Carlier, DFT-assisted ^{31}P and ^{23}Na MAS-NMR Study of the $\text{Na}_3\text{V}_2(\text{PO}_4)_2\text{F}_3 - \text{Na}_3\text{V}_2(\text{PO}_4)_2\text{FO}_2$ Solid Solution: Unravelling its Local and Electronic Structures, *Chem. Mater.* (2019), Submitted.
- [186] M. Murakami, Y. Noda, Y. Koyama, K. Takegoshi, H. Arai, Y. Uchimoto, Z. Ogumi, Local Structure and Spin State of Cobalt Ion at Defect in Lithium Overstoichiometric LiCoO_2 As Studied by ^{67}Li Solid-State NMR Spectroscopy, *J. Phys. Chem. C.* 118 (2014) 15375–15385.
- [187] D. Carlier, M. Ménétrier, C.P. Grey, C. Delmas, G. Ceder, Understanding the NMR shifts in paramagnetic transition metal oxides using density functional theory calculations, *Phys. Rev. B.* 67 (2003) 174103.
- [188] S. Levasseur, M. Ménétrier, Y. Shao-Horn, L. Gautier, A. Audemer, G. Demazeau, A. Largeteau, C. Delmas, Oxygen Vacancies and Intermediate Spin Trivalent Cobalt Ions in Lithium-Overstoichiometric LiCoO_2 , *Chem. Mater.* 15 (2003) 348–354.
- [189] M. Ménétrier, Y. Shao-Horn, A. Wattiaux, L. Fournès, C. Delmas, Iron Substitution in Lithium-Overstoichiometric “ $\text{Li}_{1.1}\text{CoO}_2$ ”: Combined ^{57}Fe Mössbauer and ^7Li NMR Spectroscopies Studies, *Chem. Mater.* 17 (2005) 4653–4659.
- [190] Y.J. Lee, F. Wang, C.P. Grey, ^6Li and ^7Li MAS NMR Studies of Lithium Manganate Cathode Materials, *J. Am. Chem. Soc.* 120 (1998) 12601–12613.
- [191] J. Kim, D.S. Middlemiss, N.A. Chernova, B.Y.X. Zhu, C. Masquelier, C.P. Grey, Linking Local Environments and Hyperfine Shifts: A Combined Experimental and Theoretical ^{31}P and ^7Li Solid-State NMR Study of Paramagnetic Fe(III) Phosphates, *J. Am. Chem. Soc.* 132 (2010) 16825–16840.
- [192] T. Bamine, E. Boivin, F. Boucher, R.J. Messinger, E. Salager, M. Deschamps, C. Masquelier, L. Croguennec, M. Ménétrier, D. Carlier, Understanding Local Defects in Li-Ion Battery Electrodes through Combined DFT/NMR Studies: Application to LiVPO_4F , *J. Phys. Chem. C.* 121 (2017) 3219–3227.
- [193] R.J. Messinger, M. Ménétrier, E. Salager, A. Boulineau, M. Duttine, D. Carlier, J.M. Ateba Mba, L. Croguennec, C. Masquelier, D. Massiot, M. Deschamps, Revealing Defects in Crystalline Lithium-Ion Battery Electrodes by Solid-State NMR: Applications to LiVPO_4F , *Chem. Mater.* 27 (2015) 5212–5221.
- [194] M. Zhou, A. Ahmad, Synthesis, processing and characterization of nasicon solid electrolytes for CO_2 sensing applications, *Sensors Actuators, B Chem.* 122 (2007) 419–426.
- [195] K. Shimoda, M. Murakami, D. Takamatsu, H. Arai, *Electrochimica Acta* In situ NMR observation of the lithium extraction/insertion from, *Electrochim. Acta.* 108 (2013) 343–349.
- [196] O. Pecher, P.M. Bayley, H. Liu, Z. Liu, N.M. Trease, C.P. Grey, Automatic Tuning Matching Cyclor (ATMC) in situ NMR spectroscopy as a novel approach for real-time investigations of Li- and Na-ion batteries, *J. Magn. Reson.* 265 (2016) 200–209.
- [197] F. Poli, J.S. Kshetrimayum, L. Monconduit, M. Letellier, *Electrochemistry Communications* New cell design for in-situ NMR studies of lithium-ion batteries, *Electrochem. Commun.* 13 (2011) 1293–1295.
- [198] O. Pecher, J. Carretero-Gonzalez, K.J. Griffith, C.P. Grey, Materials’ methods: NMR in battery research, *Chem. Mater.* 29 (2017) 213–242.
- [199] K. Ogata, E. Salager, C.J. Kerr, A.E. Fraser, C. Ducati, A.J. Morris, S. Hofmann, C.P. Grey, Revealing lithium-silicide phase transformations in nano-structured silicon-based lithium ion batteries via in situ NMR spectroscopy, *Nat. Commun.* 5 (2014) 1–11.
- [200] A.J. Pell, G. Pintacuda, C.P. Grey, Progress in Nuclear Magnetic Resonance Spectroscopy Paramagnetic NMR in solution and the solid state, *Prog. Nucl. Magn. Reson. Spectrosc.* 111 (2019) 1–271.

- [201] Z. Liu, Y. Hu, M.T. Dunstan, H. Huo, X. Hao, H. Zou, G. Zhong, Y. Yang, C.P. Grey, Local Structure and Dynamics in the Na Ion Battery Positive Electrode Material $\text{Na}_3\text{V}_2(\text{PO}_4)_2\text{F}_3$, *Chem. Mater.* 26 (2014) 2513–2521.
- [202] G. Kresse, J. Furthmüller, Efficiency of ab-initio total energy calculations for metals and semiconductors using a plane-wave basis set, *Comput. Mater. Sci.* 6 (1996) 15–50.
- [203] P.E. Blöchl, First-principles calculations of defects in oxygen-deficient silica exposed to hydrogen, *Phys. Rev. B - Condens. Matter Mater. Phys.* 62 (2000) 6158–6179.
- [204] J.A. Dean, Lange's Handbook of Chemistry, *Mater. Manuf. Process.* (1998) 1291. doi:10.1080/10426919008953291.
- [205] A. Castets, D. Carlier, Y. Zhang, F. Boucher, N. Marx, L. Croguennec, M. Ménétrier, Multinuclear NMR and DFT Calculations on the LiFePO_4OH and $\text{FePO}_4\cdot\text{H}_2\text{O}$ Homeotypic Phases, *J. Phys. Chem. C.* 115 (2011) 16234–16241.
- [206] W. Liu, H. Yi, Q. Zheng, X. Li, H. Zhang, Y-Doped $\text{Na}_3\text{V}_2(\text{PO}_4)_2\text{F}_3$ compounds for sodium ion battery cathodes: electrochemical performance and analysis of kinetic properties, *J. Mater. Chem. A.* 5 (2017) 10928–10935.
- [207] Y. Zhang, S. Guo, H. Xu, Synthesis of uniform hierarchical $\text{Na}_3\text{V}_{1.95}\text{Mn}_{0.05}(\text{PO}_4)_2\text{F}_3$ @C hollow microspheres as a cathode material for sodium-ion batteries, *J. Mater. Chem. A.* 6 (2018) 4525–4534.
- [208] A. Daidouh, C. Durio, C. Pico, M.L. Veiga, N. Chouaibi, A. Ouassini, Structural and electrical study of the alluaudites $(\text{Ag}_{1-x}\text{Na}_x)_2\text{FeMn}_2(\text{PO}_4)_3$ ($x = 0, 0.5$ and 1), *Solid State Sci.* 4 (2002) 541–548.
- [209] E. Quarez, O. Mentré, K. Djellab, C. Masquelier, Crystal structures and sodium/silver distributions within the ionic conductors $\text{Na}_5\text{Ag}_2\text{Fe}_3(\text{As}_2\text{O}_7)_4$ and $\text{Na}_2\text{Ag}_5\text{Fe}_3(\text{P}_2\text{O}_7)_4$, *New J. Chem.* 34 (2010) 287–293.
- [210] E. Quarez, O. Mentré, Y. Oumellal, C. Masquelier, Crystal structures of new silver ion conductors $\text{Ag}_7\text{Fe}_3(\text{X}_2\text{O}_7)_4$ ($X = \text{P}, \text{As}$), *New J. Chem.* 33 (2009) 998–1005.
- [211] C. Masquelier, F. d'Yvoire, E. Bretey, P. Berthet, C. Peytour-Chansac, A new family of sodium ion conductors: the diphosphates and diarsenates $\text{Na}_7\text{M}_3(\text{X}_2\text{O}_7)_4$; ($M = \text{Al}, \text{Ga}, \text{Cr}, \text{Fe}$; $X = \text{P}, \text{As}$), *Solid State Ionics.* 67 (1994) 183–189.
- [212] C. Zhu, C. Wu, C. Chen, P. Kopold, P.A. van Aken, J. Maier, Y. Yu, A High Power–High Energy $\text{Na}_3\text{V}_2(\text{PO}_4)_2\text{F}_3$ Sodium Cathode: Investigation of Transport Parameters, Rational Design and Realization, *Chem. Mater.* 29 (2017) 5207–5215.
- [213] E. Bill, ^{57}Fe -Mössbauer Spectroscopy and Basic Interpretation of Mössbauer Parameters, in: *Pract. Approaches to Biol. Inorg. Chem.*, Elsevier, 2013: pp. 109–130.
- [214] K. Chihara, A. Kitajou, I.D. Gocheva, S. Okada, J.I. Yamaki, Cathode properties of $\text{Na}_3\text{M}_2(\text{PO}_4)_2\text{F}_3$ [$M = \text{Ti}, \text{Fe}, \text{V}$] for sodium-ion batteries, *J. Power Sources.* 227 (2013) 80–85.
- [215] J.-M. Le Meins, O. Bohnke, G. Courbion, Ionic conductivity of crystalline and amorphous $\text{Na}_3\text{Al}_2(\text{PO}_4)_2\text{F}_3$, *Solid State Ionics.* 111 (1998) 67–75.

Résumé:

Les batteries Na-ion se développent comme une nouvelle alternative aux batteries Li-ion. Parmi le grand nombre de matériaux déjà étudiés à l'électrode positive, $\text{Na}_3\text{V}_2(\text{PO}_4)_2\text{F}_3$ et $\text{Na}_3(\text{VO})_2(\text{PO}_4)_2\text{F}$ sont les plus performants grâce à des capacités théoriques élevées, des potentiels d'extraction des ions Na^+ élevés, et la stabilité de la structure lors de cyclages longues durées. De plus, la structure et les propriétés électrochimiques des matériaux $\text{Na}_3\text{V}_2(\text{PO}_4)_2\text{F}_3$ et $\text{Na}_3(\text{VO})_2(\text{PO}_4)_2\text{F}$ peuvent être modulées par un effet de substitution cationique ou anionique. Ce travail de thèse a pour but d'explorer la cristalochimie de nouveaux matériaux dérivés de $\text{Na}_3\text{V}_2(\text{PO}_4)_2\text{F}_3$ et $\text{Na}_3(\text{VO})_2(\text{PO}_4)_2\text{F}$. Dans un premier temps, différents modes de synthèse (voies tout solide, céramique assistée par sol-gel, et broyage mécanique) sont explorées pour réaliser des substitutions cationiques et anioniques. La structure tridimensionnelle à longue distance de ces matériaux est déterminée par diffraction des rayons X synchrotron, tandis que les environnements locaux sont ensuite décrits finement en combinant des techniques de spectroscopies (résonance magnétique nucléaire à l'état solide, absorption des rayons X, et infra-rouge) dont l'interprétation est appuyée par des calculs théoriques. Les diagrammes de phases et les processus d'oxydoréduction impliqués lors des réactions de dés-intercalation et de ré-intercalation des ions Na^+ de la structure hôte sont étudiés pour chacune des compositions, *operando* (cad. lors du fonctionnement de la batterie) en diffraction et absorption des rayons X synchrotron. Une compréhension des mécanismes structuraux et redox impliqués au cours du cyclage permet d'identifier les limitations de ces phases et de nous guider pour proposer des nouveaux matériaux dérivés présentant de meilleures performances.

Mots clés: Batteries Na-ion, Matériaux polyanioniques, Diffraction des rayons X, RMN de l'état solide, Calculs DFT, Absorption des rayons X synchrotron.

Abstract:

Na-ion batteries are currently developed as a future alternative to the conventional Li-ion batteries. Among all the polyanion materials studied as positive electrodes for Na-ion batteries, $\text{Na}_3\text{V}_2(\text{PO}_4)_2\text{F}_3$ and $\text{Na}_3(\text{VO})_2(\text{PO}_4)_2\text{F}$ are the two promising compositions thanks to their high theoretical capacity, high Na^+ -extraction voltage, and especially the high stability of their structural framework upon long-term cycling. Furthermore, the crystal structure and the electrochemical properties of these materials can be greatly modulated through an effect of cationic or anionic substitution. This PhD work aims at exploring the diversity in crystal chemistry of $\text{Na}_3\text{V}_2(\text{PO}_4)_2\text{F}_3$, $\text{Na}_3(\text{VO})_2(\text{PO}_4)_2\text{F}$ and their derivatives obtained through different synthesis methods. The three-dimensional long range crystal structure of these phases is determined by the use of high resolution synchrotron X-ray powder diffraction whereas their local atomic and electronic structures are investigated through a combination of solid-state nuclear magnetic resonance supported by first-principles theoretical calculations, synchrotron X-ray absorption spectroscopy and infrared spectroscopy. Thereafter, the phase diagram and the redox processes involved in the Na^+ deintercalation and intercalation are established thanks to *operando* synchrotron X-ray diffraction and absorption. An in-depth understanding on the crystal structure as well as the involved redox couples for each composition helps us to determine the limitations of these vanadium fluorinated oxy-phosphates and sheds light to the development of new materials with better performance based on their structure.

Keywords: Na-ion batteries, Polyanion materials, Synchrotron X-ray diffraction, Solid-state NMR, DFT calculations, Synchrotron X-ray absorption.